NOISE MINIMAL & GREEN TRAJECTORY AND FLIGHT PROFILE OPTIMIZATION FOR HELICOPTERS

A THESIS SUBMITTED TO
THE GRADUATE SCHOOL OF NATURAL AND APPLIED SCIENCES
OF
MIDDLE EAST TECHNICAL UNIVERSITY

BY

ARDA YÜCEKAYALI

IN PARTIAL FULFILLMENT OF THE REQUIREMENTS
FOR
THE DEGREE OF DOCTOR OF PHILOSOPHY
IN
AEROSPACE ENGINEERING

JULY 2020

Approval of the thesis:

NOISE MINIMAL & GREEN TRAJECTORY AND FLIGHT PROFILE OPTIMIZATION FOR HELICOPTERS

submitted by **Arda Yücekayalı** in partial fulfillment of the requirements for the degree of **Doctor of Philosophy in Aerospace Engineering, Middle East Technical University** by,

Prof. Dr. Halil Kalıpçılar
Dean, Graduate School of **Natural and Applied Sciences** _____

Prof. Dr. İsmail Hakkı Tuncer
Head of the Department, **Aerospace Engineering** _____

Asst. Prof. Dr. Ali Türker Kutay
Supervisor, **Aerospace Engineering, METU** _____

Examining Committee Members:

Prof. Dr. Yusuf Özyörük
Aerospace Engineering, METU _____

Asst. Prof. Dr. Ali Türker Kutay
Aerospace Engineering, METU _____

Prof. Dr. Kemal Özgören
Mechanical Engineering, METU _____

Asst. Prof. Dr. Mustafa Kaya
Aerosapce Engineering, AYBU _____

Asst. Prof. Dr. Onur Baş
Mechanical Engineering, TEDU _____

Date: 16.07.2020

I hereby declare that all information in this document has been obtained and presented in accordance with academic rules and ethical conduct. I also declare that, as required by these rules and conduct, I have fully cited and referenced all material and results that are not original to this work.

Name, Last name: Arda Yücekayalı

Signature :

ABSTRACT

NOISE MINIMAL & GREEN TRAJECTORY AND FLIGHT PROFILE OPTIMIZATION FOR HELICOPTERS

Yücekayalı, Arda
Doctor of Philosophy, Aerospace Engineering
Supervisor: Asst. Prof. Dr. Ali Türker Kutay

July 2020, 282 pages

The main aim of this study is to provide a multi-disciplinary optimization and track environment to generate acoustic optimal trajectories through waypoints that ensures the rotorcraft of interest can follow at practical effort, safety, fuel consumption and speed. Rotorcraft noise annoyance remains as a challenge to solve complex, three dimensional and coupled rotary wing aerodynamics, aeroacoustics and flight dynamics interactively. Two essential paths can be acknowledged in order to reduce annoyance. One is the more sophisticated option, optimized new rotorcraft design, whereas the other option is to benefit from the directivity characteristic of sound and perform trajectory optimization to minimize noise impact at noise sensitive premises. This study focuses on the second yet with consideration of the potential trade-offs between low noise signature and other performance parameters. Eventually, the main aim of this study is to develop a trajectory optimization and track framework for rotorcrafts providing minimal noise, low emission i.e. lower fuel consumption, safe and trackable, in other words “green” flight profiles. In this scope, a Lagrangian CFD solver specialized for rotor/propellers is developed, coupled with rotorcraft mathematical model and an aeroacoustics solver to build a high fidelity, accuracy and resolution rotorcraft comprehensive modeling environment. The developed

methodology is validated with wind tunnel, whirl tower test data, PIV results and benchmark commercial tools. The developed comprehensive tool provides free flight trim, high fidelity modeling and analysis capability for conventional and unconventional rotorcraft configurations with unsteady wake dynamics covering blade-vortex, rotor-wake and rotor-rotor interactions. Further in the study, the comprehensive model is extended into a real-time computable simulation model. Then a model predictive control -an optimal control- approach is developed to simultaneously optimize the trajectory and control input to track the generated trajectory. The multi-disciplinary objective function including acoustics, performance, fuel, safety, comfort and mission concerns provides the so called "green" trajectory with reduced noise impact at desired locations. Various simulations were performed to further test the aerodynamic modeling, aeroacoustics analysis and trajectory optimization capabilities of the developed framework. It is concluded that the proof of concept, i.e. the potential of reduced noise impact and fuel consumption over the same mission through trajectory optimization, is achieved. Developed methodology can be utilized to generate optimal flight routes and procedures specific to rotorcraft configuration, which are currently rather generic for all types of rotorcrafts, especially for booming e-VTOL platforms that will mostly operate over urban areas or for re-planning of legacy flight routes.

Keywords: Rotorcraft Aeroacoustics, Green Trajectory, Modeling

ÖZ

HELİKOPTERLER İÇİN GÜRÜLTÜ MİNİMAL & "YEŞİL" YÖRÜNGE VE UÇUŞ PROFİLİ ENİYİLEMESİ

Yücekayalı, Arda
Doktora, Havacılık ve Uzay Mühendisliği
Tez Yöneticisi: Asst. Prof. Dr. Ali Türker Kutay

Temmuz 2020, 282 sayfa

Dönerkanatlı hava araçlarının toplum üzerindeki gürültü rahatsızlığı, karmaşık, üç-boyutlu ve akuple döner kanat aerodinamiği, aeroakustiği ve uçuş dinamiğininin birlikte çözümünü gerektirdiğinden, ilgi uyandırıcı bir alan olarak devam etmektedir. Gürültü rahatsızlığını azaltmanın temelde iki yolu olduğu kabul edilebilir. Bunlardan biri daha sofistike, en iyileştirilmiş yeni döner kanat tasarımları, diğeri ise, uçuş esnasında yerleşim yerleri, hastaneler, yoğun nüfüslü yerler gibi gürültüye hassas yerlerden, aeroakustiğin yönelim karakteristiğinden faydalanarak uçuş profili en iyilemesi üzerinden gürültü kaçınımı ile rahatsızlığın azaltılması olarak gösterilebilir. Bu çalışma ikinci yaklaşım üzerine eğilmektedir. Bu kapsamda, bu çalışmanın temel amacı, uçuş yörüngesi/profili en iyilemesi ve takibinin sağlanması, gürültü kaçınımı ve/veya azaltımı sağlanırken, yakıt tüketimi, performans, güvenlik, komfor ve görev isterleri gibi diğer konular arasında denge sağlanmasıdır. Düşük gürültülü ve yakıt tüketimli en iyilenmiş bu uçuş profillerine "yeşil" yörünge adı verilmiştir. Bu amaçla öncelikle rotor ve pervanelere özelleşmiş Lagrangian hesaplamalı akışkanlar dinamiği çözücüsü geliştirilmiş, döner kanat uçuş dinamiği modeli ve aeroakustik çözücü ile akuple edilmiştir. Bu sayede, yüksek gerçeklikte, doğrulukta ve çözünürlükte, döner kanat tümleşik matematik modelleme ortamı

geliştirilmiştir. Geliştirilen tümleşik model, literatürde bulunan rüzgar tüneli ve rotor kulesi test verileri ile, akış görselleştirme testleri ile ve ticari kıstas yazılımlar ile kıyaslanmış ve doğrulanmıştır. Geliştirilen tümleşik model multi-copter, tiltrotor, eş-eksenli vb dahil herhangi bir döner kanatlı hava aracı için modelleme, serbest uçuş denge analizlerini yapabilmekte, daimi ve daimi olmayan art akış, pal-girdap, rotor-art akış ve rotor-rotor etkileşimlerini yüksek çözünürlük ve doğrulukta hesaba katabilmektedir. Çalışmanın devamında, tümleşik model, gerçek zamanlı çalışma kabiliyetine sahip bir simulasyon modeline dönüştürülmüş, optimal kontrol tabanlı, model tahminli kontrol yaklaşımı ile simultane olarak hem yörünge & uçuş profili eniyilemesi hem de bunun takibi için gerekli kontrol girdilerini çözen bir sistem oluşturulmuştur. Multi-disipliner eniyiyleme hedef fonksiyonu, akustik, perfomans, yakıt tüketimi, güvenlik, konfor ve görev gereksinimlerinden beslenmekte, "yeşil" yörünge ve uçuş profili en iyilemesi ile hava aracı yerde gürültü etkisinin istenilen yerlerde azaltımını sağlamaktadır. Geliştirilen çatı modelin kabiliyetleri çeşitli analizler ile test edilmiş, aerodinamik modelleme, aeroakustik analiz ve yörünge & uçuş profili en iyileme performansı değerlendirilmiştir. Sonuç olarak, bu çalışma ile önerilen yöntemin konsept doğrulaması yapılmış, aynı görevin icra edilmesine karşın, istenilen yerlerde daha düşük gürültü etkisi ve toplamda daha düşük yakıt tüketimi sağlanabilmiştir. Geliştirilen bu yaklaşım, en iyilenmiş uçuş rotaları belirlenmesinde, günümüzde tüm döner kanatlı hava araçları için jenerik ve en kötü duruma göre oluşturulan uçuş rotalarının hava aracı spesifik güncellenmesinde kullanılabilir. Özellikle de kullanıma alındığında çoğunlukle yerleşim yerleri etrafında kullanılacak, hızla yükselen e-VTOL platformları için uçuş rotası ve hava trafiği planlamasına katkı sağlayacağı değerlendirilmektedir.

Anahtar Kelimeler: Aeroakustik, Yörünge, Uçuş Profili Eniyilemesi

To my love Başak and to my joy Ela

ACKNOWLEDGMENTS

The author would like to thank to all members of doctoral defense committee: Prof. Dr. Yusuf Özyörük, Asst. Prof. Dr. Ali Türker Kutay, Prof. Dr. Kemal Özgören, Asst. Prof. Dr. Onur Baş, Assoc. Prof. Yıldırım Kemal Yıllıkçı and Dr. Mustafa Kaya for their valuable feedbacks.

The author would like to declare his gratitude to the valuable thesis progress committee Prof. Dr. Kemal Özgören, Prof. Dr. Yusuf Özyörük and Asst. Prof. Dr. Ali Türker Kutay for their substantial feedbacks from the very beginning of the study.

The author would like thank to Gökhan Virlan, retired Branch Head at Land Forces Headquarters, Army Aviation Plans and Operations, Turkish Aerospace helicopter experimental test pilot and a PhD candidate like himself, for educational chats, sharing of valuable experiences and for reminding the author significance of lifelong development.

The author would like to show gratitude to his manager since day one, Yüksel Ortakaya, for his support, trust, valuable discussions, and feedbacks since the very beginning of the author's career.

The author would like to acknowledge Murat Şenipek, for his support, inputs, and companionship throughout the development and implementation of this study.

The author would like to appreciate his mother and father, Esin and Ferhat, for their endless support, faith and lead for finishing this dissertation.

The author would like to appreciate his spouse Başak, for her never-ending patience, support, faith, love and for making everything extremely easy for him throughout this study, or simply for her existence in his life.

TABLE OF CONTENTS

ABSTRACT.....v

ÖZ vii

ACKNOWLEDGMENTS x

TABLE OF CONTENTS..... xi

LIST OF TABLES.....xv

LIST OF FIGURES xvi

CHAPTERS

1 INTRODUCTION 1

1.1 Aerodynamic Model 7

1.2 Aeroacoustics Model.....9

1.3 Simulation/Mathematical Model 11

1.4 Trajectory Optimization and Track.....14

2 LITERATURE REVIEW 17

2.1 Aerodynamic Model 17

2.2 Aeroacoustics Model.....19

2.3 Simulation/Mathematical Model 21

2.4 Trajectory Optimization and Track 25

3 METHOD 29

3.1 Organization of Dissertation 35

4 AERODYNAMICS MODULE 37

4.1 Viscous Vortex Particle Method (VVPM) 39

4.2 Rotor Dynamics 49

4.3 Trim 55
4.4 Validation 59
4.5 Further Qualitative Assessment/Exploration 70
4.5.1 Main Rotor – Tail Rotor Interaction 70
4.5.2 Co-axial Rotor Evaluation 73
4.5.3 Intermeshing 77
4.5.4 Tilting Prop-rotor 81
4.6 Verification Check 82
5 AEROACOUSTICS MODEL 87
5.1 Fundamentals and Governing Equations 88
5.2 Aeroacoustics Solver 94
5.3 High Resolution Wake for Acoustic Simulations 98
5.4 Aerodynamics-Aeroacoustics Models Interface 101
5.5 Validation 109
5.6 Further Exploration of VVPAM 113
5.6.1 Acoustic Contour at Ground for a Level Flight Condition 113
5.6.2 Full Helicopter BVI Noise Study 114
6 SIMULATION MODEL 121
6.1 Comprehensive Mathematical Model 122
6.1.1 Trim 126
6.1.2 SAS 130
6.2 Noise Model / Surrogate Model 135
6.2.1 Multiple Rotor Acoustics 145
6.2.2 Sphere Database 150

6.2.3 Verification 152
6.3 Terrain Model 154
6.4 Simulation Model 157
6.5 Development Environment 161
7 TRAJECTORY OPTIMIZATION AND TRACK 163
7.1 Method – MPC 164
7.2 Objective Function 168
7.2.1 Acoustic 169
7.2.2 Performance 171
7.2.3 Safety & Comfort 173
7.2.4 Avoid regions 174
7.2.5 Mission & Waypoints 177
7.3 Constraints 181
7.4 Optimization Algorithm 183
7.5 Trajectory Optimization 186
7.6 Prediction & Control Horizons 188
8 RESULTS 191
8.1 Full Helicopter Trim Acoustic Analysis 192
8.2 Flyover Acoustic Simulation 200
8.3 Multi-rotor sample and acoustic analysis 205
8.3.1 Hovering Flight Condition 206
8.3.2 20 knots transition flight 208
8.3.3 50 knots post-transition flight 210
8.3.4 100 knots fixed-wing mode 211

8.3.5 Acoustic Analysis for Hovering Flight Condition 212
8.4 Trajectory optimizations 214
8.4.1 Jump Take-off and Acceleration 214
8.4.2 360 Turn 217
8.5 Green Trajectory optimizations 220
8.5.1 Accelerate and Flyover Mission 220
8.5.2 Horseshoe Turn and climb Mission 227
9 CONCLUSION 233
10 FUTURE WORKS 247
REFERENCES 249
APPENDICES
A. Greens function 267
B. Lighthill's Acoustic Analogy 270
C. Validation of Aeroacoustics Solver with Commercial Tools 271
D. Model Predictive Control for SAS 275
E. VVPM for Fuselage Interaction 276
F. Trajectory Optimization for Multiple Rotorcrafts 277
CURRICULUM VITAE 279

LIST OF TABLES

TABLES

Table 4.1 Biot-Savart Kernel regularization functions 44
Table 4.2 S76 Wind Tunnel Forward Flight Trim Parameters (Shinoda, 1996) 66
Table 4.3 Co-axial test model rotor parameters 68
Table 5.1 HART-II test case model 109
Table 6.1 Performance comparison of sphere approach and acoustic simulation 153
Table 7.1 Configuration parameters for “fmincon” (The MathWorks, 2012) 186
Table 8.1 Conventional helicopter analysis model 193
Table 8.2 Optimization trade-off results for accelerate and flyover mission..... 225
Table 8.3 Optimization trade-off results for horseshoe turn and climb 230

LIST OF FIGURES

FIGURES

Figure 1.1 Volocopter 2X, E-Hang 184, Joby S2 2
Figure 1.2 Lilium Jet, Kitty Hawk Cora, ZeeAero Z-P2 2
Figure 3.1 Flow chart of the proposed methodology 30
Figure 3.2 Flow chart for aerodynamics module 31
Figure 3.3 Flow chart for aeroacoustics module 32
Figure 3.4 Flow chart of the simulation model 33
Figure 3.5 Trajectory optimization flow chart 34
Figure 4.1 A sample VVPM solution for a conventional helicopter at quartering flight 37
Figure 4.2 Regularization functions 43
Figure 4.3 Illustration of sectional aerodynamic force and moments 52
Figure 4.4 Illustration of sectional inertial force and moments 52
Figure 4.5 Coordinate frames (left: body and hub non rotating frames, right: hub rotating, blade and segment frames) (Şenipek, 2017) 53
Figure 4.6 Filtering for rotor hub force and moments 58
Figure 4.7 Thrust&torque test and analysis comparison for S76 main rotor 60
Figure 4.8 Convergence, wake evolution and vorticity field for sample case (10deg collective) 60
Figure 4.9 Vorticity contour and tip vortex trajectory comparison with commercial CFD 61
Figure 4.10 Caradonna-Tung Test Case (Caradonna et al., 1980) 62
Figure 4.11 Spanwise load distribution comparison between VVPM, CAMRAD, CHARM, CFD and Test data 63
Figure 4.12 Spanwise lift coefficient comparison between VVPM, CAMRAD, CHARM, CFD and Test data 63
Figure 4.13 Model and test parameters (left); performance comparisons (right) 64

Figure 4.14 Flow variation (just above rotor plane) in time and its mean for a specific spanwise location 65
Figure 4.15 Mean inflow distribution Test (PIV) vs VVPM comparison 65
Figure 4.16 S76 Wind tunnel test versus CAMRAD II and VVPM comparison ... 66
Figure 4.17 Induced velocity contour, wake structure, thrust and torque oscillations for 0.2 advance ratio..... 67
Figure 4.18 HART-II test case rotor load comparison at section r/R=0.85 68
Figure 4.19 Sample co-axial rotor vorticity iso-surface and thrust convergence ... 69
Figure 4.20 Co-axial rotor aerodynamic performance test comparison..... 69
Figure 4.21 Vorticity iso-surface and particle distributions for quartering flight... 71
Figure 4.22 Vorticity iso surface and vorticity contour at a plane passing from the center of the tail rotor..... 72
Figure 4.23 Vorticity contours at cross-planes 72
Figure 4.24 Main – tail rotor wakes with and without vortex particles 73
Figure 4.25 Co-axial rotor particle distribution at hover 74
Figure 4.26 Coaxial rotor spanwise Fz and effective AoA distribution for hover . 74
Figure 4.27 Coaxial rotor vorticity iso-surface and contour at a slice x=0..... 75
Figure 4.28 Coaxial rotor wake evolution at 80 knots forward speed 75
Figure 4.29 Vorticity contours at cross-planes and streamlines at 80 knots forward speed 76
Figure 4.30 Vorticity iso-surface and contour at cross-plane with streamlines at 80 knots forward speed 76
Figure 4.31 Coaxial upper and lower rotor loads distributed over the discs and variation with rotor revolution at 80 knots forward speed..... 77
Figure 4.32 Non-dimensional airloads distribution and vorticity iso-surfaces for an intermeshing rotor at hover flight condition 78
Figure 4.33 Vorticity contour over x-z and y-z contours at hover condition 78
Figure 4.34 Vorticity iso-surface colored with total air speed in 50 knots forward flight condition..... 79

Figure 4.35 Vorticity iso-surface colored with total air speed in 50 knots forward flight condition 79
Figure 4.36 Intermeshing rotor particle distribution in forward flight 1st rev. 80
Figure 4.37 Intermeshing rotor particle distribution in forward flight 2nd rev. 80
Figure 4.38 Intermeshing rotor particle distribution in forward flight 3rd rev. 80
Figure 4.39 Tilting prop-rotor simulation 81
Figure 4.40 Tilting prop-rotor simulation 82
Figure 4.41 Tilting prop-rotor simulation 82
Figure 4.42 Wakes for moving and floating configuration, initial cond. 83
Figure 4.43 Wakes for moving and floating configuration, 1st main rotor rev. 83
Figure 4.44 Wakes for moving and floating configuration, 2nd main rotor rev. 84
Figure 4.45 Wakes for moving and floating configuration, 3rd main rotor rev. 84
Figure 4.46 Thrust and torque variation of moving and floating main rotors 85
Figure 4.47 Thrust and torque variation of moving and floating tail rotors 85
Figure 5.1 Acoustic wave propagation on ground surface (height:150m) for a quartering conventional helicopter configuration 87
Figure 5.2 Illustration of the integral solution for FWH 96
Figure 5.3 Increased wake and airloads resolution for aeroacoustics data 99
Figure 5.4 Increased wake and airloads resolution for aeroacoustics data 99
Figure 5.5 Sensitivity analysis for different spanwise & azimuth-wise resolutions. 100
Figure 5.6 Total velocity vector and effective angle of attack illustration for blade sections 102
Figure 5.7 Blade surface geometry and surface mesh 102
Figure 5.8 Airfoil surface pressure distribution stored as pressure database 103
Figure 5.9 Chordwise pressure distribution at each blade section 103
Figure 5.10 Pressure distributed over the blade geometry 104
Figure 5.11 Blade geometric representation with different number of chordwise elements 105

Figure 5.12 Blade geometric representation with different number of chordwise elements 106
Figure 5.13 Comparison of distributed pressure over the blade geometry at different number of chordwise elements 106
Figure 5.14 Rotor total thrust variation comparison determined with VVPM and Pressure integration over the blade surface..... 107
Figure 5.15 Blade pressure distribution at each azimuth location 107
Figure 5.16 Variable step wake evolution, starts with 7.5 azimuth steps, ends with 1-degree azimuth steps 110
Figure 5.17 Load distribution on disc and test vs analysis comparison at a section at r/R=0.86 110
Figure 5.18 Acoustic pressure time variation, test vs analysis comparison..... 111
Figure 5.19 SPL contour at a plane below rotor disc, test (left) vs analysis (right) comparison 111
Figure 5.20 Thickness and loading noise frequency spectrum for HART-II case 112
Figure 5.21 Frequency spectrum comparison of analysis with HART-II test data113
Figure 5.22 Acoustic wave propagation on a ground surface below 150m..... 114
Figure 5.23 Acoustic wave propagation on a ground surface below 150m..... 114
Figure 5.24 BVI condition full helicopter trim 116
Figure 5.25 Main rotor thickness and loading noise, acoustic pressure response 116
Figure 5.26 Main rotor total acoustic pressure response 117
Figure 5.27 Acoustic pressure response for a single blade for one full revolution and identified BVI instances..... 118
Figure 5.28 1st BVI instance, advancing side 118
Figure 5.29 2nd BVI instance, around 180° azimuth..... 119
Figure 5.30 3rd BVI instance, around retreating side 119
Figure 5.31 4th BVI instance, around retreating side 120
Figure 5.32 5th BVI instance, around 350° azimuth 120
Figure 6.1 Rotorcraft comprehensive model equipped with acoustic sphere 121
Figure 6.2 Illustration of modular structure..... 123

Figure 6.3 Main components of a typical rotorcraft – conventional configuration (Şenipek, 2017).....124
Figure 6.4 Left: Class diagram of BaseObject Class and its child objects, Right: Dynamic system inputs, integrator and output classes (Şenipek, 2017) 126
Figure 6.5 Trim switch from dynamic inflow to VVPM at hover.....129
Figure 6.6 Filtered rotor loads for utilization in trim iteration 129
Figure 6.7 Conventional configuration helicopter hover trim.....130
Figure 6.8 SAS on and off simulation, control angles 131
Figure 6.9 SAS on and off simulation, Euler angles 131
Figure 6.10 SAS on and off simulations for longitudinal cyclic step input 132
Figure 6.11 SAS on and off simulations for longitudinal cyclic step input 132
Figure 6.12 SAS on and off simulations for pedal step input 133
Figure 6.13 SAS on and off simulations for pedal step input 133
Figure 6.14 SAS on and off simulations for collective step input.....134
Figure 6.15 SAS on and off simulations for collective step input.....134
Figure 6.16 Acoustic sphere noise contour for a typical flight 136
Figure 6.17Acoustic sphere cut into half for a typical flight condition.....137
Figure 6.18 Typical acoustic pressure time variation at an observer location 138
Figure 6.19 Projection of frequency spectrum from sphere surface to observer location 141
Figure 6.20 Instantaneous SPL contour on ground (terrain) surface.....142
Figure 6.21 SEL contour at t=0 seconds for hovering helicopter.....143
Figure 6.22 SEL contour at t=25 seconds for hovering helicopter.....143
Figure 6.23 SEL contour at t=50 seconds for hovering helicopter.....144
Figure 6.24 SEL contour at t=100 seconds for hovering helicopter.....144
Figure 6.25 Main rotor acoustic analysis output signal and re-sampled signal.....146
Figure 6.26 Main rotor acoustic analysis output signal and re-sampled signal.....146
Figure 6.27 Tail rotor acoustic analysis output signal and re-sampled signal.....147
Figure 6.28 Tail rotor acoustic analysis output signal and re-sampled signal.....147
Figure 6.29 Full helicopter acoustic signature at flyover condition.....148

Figure 6.30 Full helicopter acoustic signature at flyover condition 148
Figure 6.31 Main rotor only and tail rotor only acoustic spheres at level flight... 149
Figure 6.32 Full rotorcraft acoustic sphere at level flight..... 149
Figure 6.33 Acoustic sphere database illustration for constant C_T/σ..... 151
Figure 6.34 Acoustic sphere database illustration for constant C_T/σ..... 152
Figure 6.35 Comparison sphere approach with direct acoustic simulation 153
Figure 6.36 6 degrees approach/descending flight condition 154
Figure 6.37 Interpolated acoustic sphere (left), direct calculated acoustic sphere (right) 154
Figure 6.38 Terrain mesh and observer (node) illustration..... 155
Figure 6.39 Representative map and 3-D cad model for Prague 156
Figure 6.40 Default terrain model..... 157
Figure 6.41 Illustration for the simulation model 158
Figure 6.42 Simulation Model Visual in Simulink Environment 160
Figure 7.1 A sample output for the noise impact on ground during take-off (rotorcraft geometry is up scaled for illustration) 163
Figure 7.2 Sample Slalom and teardrop maneuvers with model predictive control (Yücekayali, Şenipek, & Ortakaya, 2019) 164
Figure 7.3 Illustration of MPC scheme..... 165
Figure 7.4 Prediction horizon, control horizon and acoustic horizon illustration. 166
Figure 7.5 Flow chart of trajectory optimization and track framework..... 167
Figure 7.6 MPC structure in the simulation model..... 167
Figure 7.7 Prediction model Simulink flow diagram..... 168
Figure 7.8 Illustration for maximum permitted noise level, bumper limit and instantaneous noise level during simulation. 170
Figure 7.9 Typical performance cruise chart for conventional helicopter (Federal Aviation Administration (FAA), 2019) 173
Figure 7.10 Definition of bumper region 175
Figure 7.11 A sample trajectory optimization with bumper region (solid line : with bumper region, dotted line : without bumper region) 176

Figure 7.12 A sample trajectory optimization with bumper region (solid line : with bumper region, dotted line : without bumper region).....176
Figure 7.13 A sample trajectory optimization with bumper region (solid line : with bumper region, dotted line : without bumper region).....177
Figure 7.14 Illustration for position cost of objective 178
Figure 7.15 Illustration for direction cost function 179
Figure 7.16 Illustration of waypoint switching conditions.....180
Figure 7.17 Flow chart for waypoint switching decision 180
Figure 7.18 Avoid regions in the vicinity of Columbia Airport (*Noise Sensitive Areas*, n.d.) 182
Figure 7.19 An example for dedicated flight corridors and routes (Behr & Reindel, 2008).....182
Figure 7.20 Illustration for prediction stage response and plant response 187
Figure 7.21 Illustration for prediction stage response and plant response 187
Figure 7.22 NED speeds, MPS future predictions and Plant response 188
Figure 7.23 Comparison of different prediction to control horizon ratios 189
Figure 7.24 Comparison of different prediction to control horizon ratios 189
Figure 7.25 Comparison of different prediction to control horizon ratios 189
Figure 7.26 Comparison of different prediction to control horizon ratios 190
Figure 8.1 Conventional helicopter analysis model 192
Figure 8.2 Conventional helicopter level flight trim q-criterion iso-surface.....193
Figure 8.3 Hover trim variables & inputs convergence history 194
Figure 8.4 Hover trim total SPL contour, in plane & out of plane acoustic pressure variation of thickness (upper) and loading (lower) noise components.....195
Figure 8.5 Moderate speed trim variables & inputs convergence history.....196
Figure 8.6 Moderate speed trim total SPL contour, in plane & out of plane acoustic pressure variation of thickness (upper) and loading (lower) noise components ...197
Figure 8.7 High speed trim variables & inputs convergence history 198
Figure 8.8 High speed trim total SPL contour, in plane & out of plane acoustic pressure variation of thickness (upper) and loading (lower) noise components ...199

Figure 8.9 Flyover flight profile for noise certification of helicopters 201
Figure 8.10 Instantaneous acoustic pressure contour for flyover simulation 201
Figure 8.11 Instantaneous acoustic pressure contour for flyover simulation 202
Figure 8.12 Instantaneous acoustic pressure contour for flyover simulation 202
Figure 8.13 SPL variation for flyover 203
Figure 8.14 Thickness noise acoustic pressure variation for flyover case 204
Figure 8.15 Loading noise acoustic pressure variation for flyover case 204
Figure 8.16 Multi-rotor analysis model for demonstration 205
Figure 8.17 Multi-rotor analysis model for demonstration 205
Figure 8.18 Multi-rotor hover trim, vortex particles and vorticity iso-surface 206
Figure 8.19 Multi-rotor hover trim vorticity contour in cross-plane 207
Figure 8.20 Thrust convergence variation with simulation step 207
Figure 8.21 Power convergence variation with simulation step 208
Figure 8.22 Multi-rotor 20 knots trim, vortex particles and vorticity iso-surface 208
Figure 8.23 Multi-rotor 20 knots trim vorticity contour in cross-plane 209
Figure 8.24 Thrust convergence variation with simulation step 209
Figure 8.25 Power convergence variation with simulation step 210
Figure 8.26 Multi-rotor 50 knots trim vorticity iso-surface and vorticity contour over in-plane 210
Figure 8.27 Multi-rotor 50 knots trim vorticity iso-surface and streamlines 211
Figure 8.28 100 knots trim, vortex particles and vorticity iso-surface 211
Figure 8.29 100 knots trim, in-plane & cross-plane vorticity contours 212
Figure 8.30 Multi-rotor acoustic analysis 213
Figure 8.31 Jump Take-off and acceleration flight path 214
Figure 8.32 Jump Take-off and acceleration flight path 215
Figure 8.33 Jump take-off total SEL contour on ground 215
Figure 8.34 Jump Take-off SPL contour on city model 216
Figure 8.35 Jump take-off control inputs and NED velocity histories 216
Figure 8.36 Jump take-off Euler angle and rates history 217
Figure 8.37 360 turn trajectory optimization and track results 218

Figure 8.38 Acoustic spheres for 360 turn 218
Figure 8.39 360 turn control inputs and NED velocity histories 219
Figure 8.40 360 turn Euler angle and rates history 219
Figure 8.41 SEL contour with OBJ1 for acceleration and flyover mission 221
Figure 8.42 SEL contour with OBJ2 for acceleration and flyover mission 221
Figure 8.43 SEL contour with OBJ3 for acceleration and flyover mission 221
Figure 8.44 Optimized trajectories with OBJ1, OBJ2 and OBJ3 for acceleration and flyover mission 222
Figure 8.45 Optimized trajectories with OBJ1, OBJ2 and OBJ3 for acceleration and flyover mission 223
Figure 8.46 SELdB and SPLdB with OBJ1, OBJ2 and OBJ3 for acceleration and flyover mission 224
Figure 8.47 OBJ1, OBJ2 and OBJ3 control inputs and NED velocity histories for acceleration and flyover mission 225
Figure 8.48 OBJ1, OBJ2 and OBJ3 Euler angle and rates history for acceleration and flyover mission 226
Figure 8.49 Horseshoe turn and climb mission 227
Figure 8.50 Horseshoe turn and climb mission acoustic contour on city model 228
Figure 8.51 Acoustic contour and flight profile for OBJ1 and OBJ2 228
Figure 8.52 Acoustic contour and flight profile for OBJ3 229
Figure 8.53 Comparison of SPL time variation and SEL at observer location 229
Figure 8.54 Euler angles and rates for horseshoe turn and climb mission 231
Figure 8.55 Control angles and velocity components for horseshoe turn and climb mission 231
Figure 9.1 Cross-plane vorticity contour for a typical rotor 235
Figure 9.2 Vorticity iso-surface for a typical rotor 236
Figure 9.3 Solution with viscous diffusion on (left) and off (right) 237
Figure 9.4 Solution with viscous diffusion on (left) and off (right) 237
Figure 9.5 Comparison of acoustic analysis results of 5 different institutes, VVPAM and test data 240

Figure 9.6 Blade loads comparison with test data (left: 5 institutes vs test, right: VVPM vs test)..... 240
Figure 11.1 HART-II test case configuration and CHARM wake output 271
Figure 11.2 Test vs PSU-WOPWOP comparison..... 272
Figure 11.3 Test vs TACO initial comparison..... 272
Figure 11.4 Wake re-construction..... 273
Figure 11.5 Test vs TACO + CHARM validation..... 273
Figure 11.6 Gust simulation at hover. SAS is off for grey, SAS is on for red helicopters. Left : t=0 seconds, Right: t=1.0 seconds 275
Figure 11.7 Gust simulation at hover. SAS is off for grey, SAS is on for red helicopters. Left : t=2.0 seconds, Right: t=3.0 seconds 275
Figure 11.8 Local air speed distribution of rotor induced airflow on fuselage..... 276
Figure 11.9 Multiple helicopter trajectory optimization – pirouette maneuver.... 277
Figure 11.10 Multiple helicopter trajectory optimization – pirouette maneuver.. 278

CHAPTER 1

INTRODUCTION

Unsurprisingly rotorcrafts dominate civil air space and civil operations with a wide range of applications, users, and operators. In fact, users such as police and media benefit from the low speed agility, maneuverability and hovering capabilities of rotorcrafts for surveillance, monitoring and chase purposes while off shore oil platform, medical and transportation focused operators rely on vertical and runway free take-off/landing as well as cruise, endurance and range capabilities. Besides, effective, and efficient usage in search and rescue, firefighting, medical help delivery, ambulance purposes and operations, makes helicopters indispensable for today's society.

Considering the operation purposes and areas; flight conditions and maneuvers covering the flight spectrum and envelope for rotorcrafts are being performed over residential or noise sensitive areas. As a result, noise signature and impacts for most of the flight regimes such as take-off/landing, cruise, climb, descent, hover and high-speed forward flight are being experienced by the public on ground and contribute to annoyance. The growth of civil and commercial rotorcraft operations around urban, residential areas and city centers has eventually brought higher public awareness and annoyance on helicopter noise. Perceiving the public pressure, civil regulatory authorities such as Federal Aviation Administration (FAA) and International Civil Aviation Organization (ICAO) are imposing more and more severe requirements for civil certifications. When historical development of the certification requirements for helicopters is evaluated starting from the first issue of ICAO Annex 16 at 1981, a pressurizing decrease in maximum permitted noise levels is observed for the last decade causing a great number of legacy helicopters remain over limits. In parallel, helicopter operations are being increasingly curtailed in major operating cities in Europe and USA. As a matter of fact, as both public and

regulatory authorities emphasis solely on noise rather than efficiency and consumption (Brentner & Farassat, 2003), the legacy flight paths for rotorcrafts around urban areas are being re-planned considering worst case i.e. noisiest rotorcrafts, resulting in longer flight distances, increased fuel consumption, emission and cost that even the newest rotorcrafts obliged to undertake.

Moreover, considering the e-VTOL industry, which figuratively boomed with the initiative of UBER in 2016 (Holden & Goel, 2016), a broad range of multi-rotor rotorcraft configurations potentially with combination co-axial, prop-rotor, propeller and rotors are about to dominate the civil airspace. More than 130 e-VTOL configurations(Bacchini & Cestino, 2019) have been committed, a bunch of remarkable examples are illustrated in Figure 1.1 and Figure 1.2, and so many of them have already being produced prototypes, started flight tests or even started certification tests.

Figure 1.1 Volocopter 2X, E-Hang 184, Joby S2

Figure 1.2 Lilium Jet, Kitty Hawk Cora, ZeeAero Z-P2

All those unique e-VTOL configurations would eventually have their own unique noise characteristics and signature. Considering the fact that they are all electric driven, operating in urban areas, premises, and metropoles, without engine and transmission noise, the overall noise signature will be all shaped by aeroacoustics.

Eventually, already booming civil rotorcraft operations will even increase with the eVTOL leap with even more usage around urban areas, metropolitans, residential

areas, helipads, and airports. Meanwhile air traffic will still remain as the most annoying transportation type considering the noise generated; as the study of the European Commission revealed; amongst rail, road and air transportations, even when physically exposed at the same noise levels, air transportation is the one with the highest percentage of annoyed people (Dose/Effect– & WG2, 2002). Thus, increasing public annoyance and imposed challenging certification requirements revealed the importance of helicopter aeroacoustics, such that noise signature of a rotorcraft has become one of the leading features for public acceptance and prevailing design considerations. Therefore, to study the impact and public annoyance of helicopter noise, a better understanding of the physical mechanisms of noise generation and an engineering approach to evaluate and manipulate noise signature of a helicopter is essential.

Rotorcraft noise reveals the complex aeromechanical nature of rotor aerodynamics and dynamics combined with the wide maneuverability, flight envelope and flight condition range, resulting in a complex and significantly diverse acoustic characteristic. As the aerodynamic noise is basically a consequence of the aerodynamic forces such as lift, thrust and propulsion which are essentials of flight dynamics, cancelling it completely is not possible. Yet, by acoustically optimal designs or altering usage and flight decisions, performing trade-offs with other performance parameters and design considerations, it is possible to alleviate or manipulate or direct the noise impact on ground

One way to alleviate the noise annoyance of helicopters is performing more advanced, optimized new designs. Utilizing higher fidelity aerodynamic and aeroacoustics estimation methodologies and enhancing the new designs in terms of noise by adding aeroacoustics as one of the design parameters and generating feedbacks through the design phase, preferable or favorable new design may be generated. However, it is important to anticipate that enhancing noise characteristics may require a trade-off between other design and performance parameters and the noise problem would remain unchanged for legacy helicopters.

Another way to alleviate the noise annoyance is to estimate helicopters' instantaneous noise levels and the impact on ground, take advantage of noise directivity, frequency and attenuation characteristics and manipulate them accordingly. It has been shown that, relatively small modifications in flight parameters and their time variations result in significant changes in noise impact at specific locations on ground and exposed sound levels over a wide area (Greenwood, 2017). There have been various studies to provide noise optimal trajectories, generally specific only to a certain part of the mission such as approach, landing or take-off and with acoustic concern only. Previous studies (Cruz et al., 2012; Hartjes & Visser, 2019; Padula et al., 2019; Tsuchiya et al., 2009) revealed the potential of identifying quieter paths through trajectory optimization yet only for landing or approach missions

Indeed, as discussed in the report of FAA to Congress, (Federal Aviation Administration (FAA), 2004), on helicopter urban noise study revealed that most frequently expressed operational issues for helicopter usage are operational routes, routing design guidelines and noise abatement procedures involve optimal helicopter route planning to avoid noise sensitive areas that require a comprehensive evaluation. This study concentrates on the second approach; optimizing the full trajectory by altering the usage/flight characteristics with addition of fuel consumption, speed, safety and mission waypoints concerns, to manipulate the acoustic signature of a helicopter. At this point it is important to clarify what by "trajectory" is meant. "Trajectory" and "path" are generally used as interchangeable in the literature but principally they shall be different with a distinct characteristic. In this study, by "path" optimization; generating an optimal route in other words x,y and z coordinates at earth frame to track is meant. On the other hand, by "trajectory" optimization; addition to generating an optimal "path", optimization of how the aircraft should be flown through that "path" is intended such as the instantaneous velocity profile i.e. total airspeed, sideslip and angle of attack and/or attitude profile such as heading, pitch and roll angles. In this sense, trajectory optimization represents optimization of flight path and flight profile together.

A trajectory optimization problem with acoustic concern only would lack in noise impact assessment on noise sensitive regions, therefore as discussed in Morris's study, (Morris et al., 2015) terrain combined with noise sensitive area information is essential to provide an actual noise minimal path. Therefore, a generic ground model is implemented into the optimization cost function so that annoyance at noise sensitive regions and residential areas can be alleviated while having a so-called green trajectory.

The main aim of this study is to provide a multi-disciplinary optimization and track environment to generate acoustic optimal trajectories through waypoints that ensures the rotorcraft of interest can follow at practical effort, safety, fuel consumption and speed. In this scope, a non-linear rotorcraft mathematical model is coupled with an acoustic model to estimate instantaneous noise signature on ground. A trajectory optimization and optimal control loop operates over the mathematical and noise model to simultaneously optimize and track the generated trajectory, minimizing noise impact at desired locations on ground while considering fuel consumption, speed & safety, waypoints to reach. A terrain model provides required information to optimization function including height above ground level, noise sensitive regions and obstructions present in the domain.

As a matter of fact, the helicopter route planning or re-planning would be possible to be optimized/improved specifically to each rotorcraft design and noise signature. This would simultaneously decrease noise annoyance and optimize emission as well as consumption compared to current approach where all types of flight procedures are generic in nature independent of associated aircraft or engine designs (Khardi, 2014).

The utilized approach provides trajectory generation and path following with a foresight of future dynamic response of the plant. This feedforward feature ensures high noise impact flight regimes such as blade-vortex dominated conditions are avoided or noise is directed away from sound sensitive locations over urban areas.

Proposed methodology provides a multi-disciplinary trajectory optimization environment combining aspects from different disciplines such as aerodynamics,

aeroacoustics, flight dynamics, control, optimization, and comprehensive modeling. To provide such capability; a rotor aerodynamic solver capable of estimating high fidelity airloads, wake dynamics and interaction is developed first. The aerodynamic solver is coupled with a rotor dynamics module which provides individual blade dynamic response under isolated or full helicopter free flight conditions. Then, an interface approach is proposed and developed, which provides aeromechanical data such as time variation of kinematics and pressure distribution of each blade that is utilized in aeroacoustics solver. The rotor model is than coupled with a rotorcraft comprehensive mathematical model so that full rotorcraft free flight trim and simulations can be performed with full wake and loads interaction between each rotor on the configuration. High fidelity rotorcraft model is then transformed into a simulation model to provide real time simulation with non-linear aerodynamic and flight dynamics. The simulation model is operated by a model predictive control approach with optimization objective consisting of cost from various disciplines such as acoustics, emission, performance, safety, and comfort.

Eventually, a trajectory optimization and track framework has been developed with this study providing reduced noise impact and fuel consumption while considering safety, comfort and mission requirements. The comprehensive rotorcraft model developed through coupling the Lagrangian CFD solver, VVPM, with rotorcraft mathematical model and aeroacoustics solver, is validated with wind tunnel and whirl tower test data, PIV, and commercial benchmark tools results. Developed framework is further tested to evaluate aerodynamics and aeroacoustics analysis, and trajectory optimization capabilities. In this scope, conventional helicopter free flight trim and aeroacoustics analysis are performed and fly over noise signature is studied. Then a multi-rotor configuration with combination of co-axial rotors, pro-rotors, propellers and wings is generated and analyzed in various flight conditions including hover, transition and high-speed forward flight. Then various trajectory optimization and track studies are performed with mission only, acoustics only and comprehensive objective functions.

It is concluded that the proof of concept, i.e. the potential of reduced noise impact and fuel consumption over the same mission through trajectory optimization, is achieved. Developed methodology can be utilized to generate optimal flight routes and procedures specific to rotorcraft configuration, which are currently rather generic for all types of rotorcrafts, especially for booming e-VTOL platforms that will mostly operate over urban areas or for re-planning of legacy flight routes. The study is essentially a combination of four disciplines therefore introduction for each of the four modules, aerodynamics model, aeroacoustics model, simulation model and trajectory optimization framework, are given separately with the following sub-chapters.

1.1 Aerodynamic Model

Typically a rotor in axial and forward flight or interfering with other rotors, experiences unsteady and complex three-dimensional aerodynamic features such as vortex formations, reverse flow regions, blade-wake, blade-vortex and rotor-rotor interactions, which altogether constitutes the rotor wake dynamics. Being the main driver of the time dependent blade induced flow, the accurate prediction of the rotor wake is essential to estimate rotor aeromechanical behavior including blade dynamic response, unsteady loads, rotor performance, trim and acoustic signature. Therefore, a better estimation of rotor wake dynamics is the fundamental scope of rotorcraft comprehensive modeling.

State-of-the-art approach for accurate rotor wake predictions is utilization of classical CFD to solve Navier-Stokes rotor flow field. However, computational cost, high-resolution mesh requirements to avoid numerical diffusion and limitations which arise with a grid-based approach; restrict the ability to model dynamic behavior of rotor blades under majority of flight condition/maneuver. Parallel drawbacks limits coupling CFD with multi-body approach to trim the rotor. Correspondingly, the flexibility of BEM codes combined with vortex wake methods brings the ability to estimate rotor dynamic response, however, the nature of these

tools requires modeling the flow behavior with simplified mathematical models depending on various empirical correlation factors. As discussed in literature (Conlisk, 2001; Okulov et al., 2014) the vortex-wake methods widely implemented in the comprehensive codes rely on empirical formulations for tip vortex location, vortex decay, core size and wake geometry due to the potential flow assumption.

At this point, viscous vortex particle methods (VVPM) utilized for rotor wake estimations have shown promising potential in the last decade. A typical VVPM solves the velocity-vorticity form of incompressible Navier-Stokes equations with a Lagrangian approach for a grid-free simulation. Therefore, limitations of potential flow assumption, empirical corrections and simplifications of vortex-wake methods and mesh requirements, numerical dissipation and computational cost drawbacks of grid-based CFD methods can be eliminated.

Moreover, when the e-VTOL configurations are considered, multiple rotors all interacting with each other and complex free flight dynamics, require solution of all aerodynamic interactions and complex wake dynamics and produce feedback to flight dynamics modeling for free flight simulation and trim. Still, such an approach is only a pre-requisite to generate required aeromechanical data for further acoustic calculations. Current state-of-the art modeling capabilities are either awfully expensive and de-coupled from flight dynamics or uncapable of solving unconventional rotor configurations without tuning through flight tests. The VVPM coupled comprehensive model developed in this study on the other hand, inherently can perform such comprehensive analysis for any rotorcraft configuration including multi-rotors, conventional and unconventional such as co-axial, intermeshing, tiltrotors etc.

In this study, VVPM approach is coupled with a rotor dynamics model for comprehensive rotorcraft modeling purposes. The coupling is achieved through vorticity generation and induced velocity information exchange. Each time step, induced velocity computed with VVPM is utilized by the airloads model to determine required vorticity sources to be released into the domain. Convection and viscous diffusion for the vorticity field is then re-computed with VVPM. In this

setup, VVPM is responsible from flow field and induced velocity computation whereas rotor model is responsible of blade/rotor aerodynamic, dynamic and inertial load computations as well as total integrated loads that are transferred to the fuselage for further flight dynamics calculations. Developed tool is validated with whirl tower and wind tunnel test data for S76 helicopter main rotor (Jepson et al., 1983; Johnson, 1980; Shinoda, 1996), well-known Caradonna-Tung (Caradonna et al., 1980; Joulain et al., 2017), NASA test models (Ramasamy et al., 2010) and HART-II wind tunnel test case (Wall, 2003). Commercial comprehensive modeling tools CAMRAD-II and CHARM as well as grid based commercial CFD are utilized as a benchmark. Comparisons are performed in terms of rotor total aerodynamic performance i.e. thrust to torque variations, rotor spanwise and azimuth-wise load variations, tip vortex trajectories and vorticity contours. Then VVPM is explored for further rotorcraft applications such as unconventional configurations i.e. intermeshing, co-axial rotors and tilting proprotors. Being coupled with rotor dynamics, the VVPM tool has the potential to replace legacy vortex-wake based models in terms of flight dynamics analysis, interactional aerodynamics, rotor loads and rotor noise predictions.

1.2 Aeroacoustics Model

Aeroacoustics is a multi-disciplinary field combining principles of fluid mechanics and acoustics. Rotorcraft aeroacoustics on the other hand, is an outcome of blade spanwise and azimuth wise load variations, kinematic motion, blade-wake and blade-blade interactions as well as rotor total aerodynamic characteristics and wake dynamics. Solution or modeling of aeroacoustics response of a rotor requires solution of coupled aerodynamics, rotor dynamics and wake dynamics together. Moreover, simulation of a realistic flight or operating condition, full helicopter trim is essential. The state-of-the-art approach to solve solid-fluid interaction and the pressure distribution along the blade surface might seem to be the CFD methods. Yet, despite the increase of computational infrastructure and the maturation of CFD applications,

the necessity of solving rotor and helicopter dynamics in a tight coupled manner is the main drawback that leads unsatisfactory acoustic estimations (Brentner & Farassat, 2003). Instead, analysis or simulation of a rotor aeroacoustics is most of the time performed with hybrid methods.

Hybrid methods generally treat near and far field with different principles such that; the near field is solved with high fidelity aerodynamic simulations, whereas noise signature is propagated to an arbitrary distance of interest with wave equation combining advantageous aspects of numerical schemes. Like most of the hybrid methods in the literature, solution of Ffowcs Williams – Hawking (FWH) equation is practiced in this study. The FWH equation is a generalized formulation of Lighthill's acoustic analogy and copes with the sound propagation from arbitrarily moving surfaces with pressure variations on the surface (Brentner & Farassat, 2003). The integral formulation of FWH equation requires solid body surface i.e. in this case, rotor blade kinematics as well as unsteady pressure distribution for which aerodynamics, rotor dynamics and flight dynamics coupled comprehensive modeling is essential. Although the multi-disciplinary nature of the helicopter operating environment requires a comprehensive analysis to predict aeromechanical state of the rotors, most of the time, pressure distribution over the blade is not the concern but the concentrated load variation is. Therefore, a pressure distribution methodology is proposed with this study to project spanwise concentrated loads calculated with comprehensive codes to chordwise pressure distribution along the blade.

Aeroacoustics solver utilized in this study solves FWH equation Farasat 1A integral formulation which has been validated by the author with commercial comprehensive rotorcraft models (Yücekayali, Şenipek, Ortakaya, et al., 2019). The high fidelity and resolution aeromechanical data is generated with the developed aerodynamic model. The concentrated loads are then transformed into chordwise and spanwise pressure distribution and projected over real blade geometry at each azimuth angle with the developed pressure database methodology. Then, aeroacoustics solver performs noise analysis at desired observer locations. Consequently, as the VVPM is coupled

with a comprehensive rotorcraft model, full rotorcraft trim and simulation can be performed for further acoustic assessments. The infrastructure developed in this scope enables to perform high accuracy and resolution acoustic simulation for any rotorcraft configuration of interest without a need for any exterior tool or code.

Developed aeroacoustics analysis scheme is validated with wind tunnel test data (Wall, 2003) present in the literature in terms of acoustic pressure time variation from different microphone locations and sound pressure level contour below the rotor disc.

The methodology provides acoustic pressure time data at any observer location on which fast Fourier transform (FFT) analysis can be performed for further frequency spectra evaluations. Besides, sound pressure level and sound exposure level metrics can be calculated. Developed methodology benefits from the linearizable property of the acoustic estimations to superimpose multiple rotor noise signatures with proper interpolation approaches. Trimmed, steady or unsteady flight conditions or maneuver acoustic simulations are available which provide an environment to perform maneuvering rotorcraft noise analysis.

1.3 Simulation/Mathematical Model

The simulation model developed in this study covers rotorcraft comprehensive mathematical model, surrogate noise model and the terrain model. Combined together, it provides real time flight dynamics simulation with acoustic calculations on the ground/terrain field of interest. The optimization module operates over the simulation model to generate optimal trajectories; therefore, the realization of the generated trajectories depends on the accuracy, fidelity and representation capability of the simulation model.

Accurate rotorcraft analysis and simulation require a well-established aerodynamics, rotor dynamics and flight dynamics representation. One of the biggest challenges in rotorcraft industry is therefore to develop a flight dynamics model providing accurate estimation of the complex aeromechanical environment the rotors are operating in

during a free flight trim, steady or unsteady maneuver. Additionally, the modular structure providing flexible modeling capability for multi-rotors or unconventional configurations supported by proper and competent aerodynamics model covering loads, wake dynamics and interactions, is essential. On the other hand, the balance between fidelity, complexity and computational burden shall be adjusted such that it enables calculations to be performed fast enough for simulation or in this case optimization of the trajectory through mimicking the trajectory in great numbers at background.

The comprehensive mathematical model utilized in the simulation model in this dissertation is a modular, variable fidelity and coupled aeromechanics model; developed with an object-oriented manner, providing simulating multi-rotors and unconventional configurations. This modular structure enables to elaborate any desired rotorcraft configuration with components at varying desired fidelity representations. Components such as aerodynamic surfaces, landing gears, auxiliary bodies, stores, propellers and rotors each at variable fidelity and complexity constitute the modular structure. Besides, the mathematical model ensures simulation at a fidelity high enough to estimate instantaneous performance parameters, safety and comfort constraints which are essential variables for a green trajectory optimization purpose. Providing fast/real time simulation capability, the mathematical model enables utilization of predictive algorithms through multi-disciplinary and multi-variable optimization framework.

The non-linear representation of a rotorcraft, which sometimes can even be dynamically unstable depending on the configuration, is stabilized with a closed loop feedback constituting a SAS environment.

The surrogate noise model on the other hand, is constituted by a database of pre-complied high-fidelity acoustic solution stored on an acoustic sphere. The aeromechanical and acoustic solution at observers at equal distances from rotor center establishing a sphere covering the rotorcraft of interest are performed and stored in a database. Considering the atmospheric attenuation and spreading losses,

the noise level on observers or ground surface/terrain can be determined through projecting over acoustic rays. This approach is demonstrated to have the utmost accuracy compared to a typical rotor acoustic analysis, in terms of sound pressure level and frequency spectra, while providing a real time noise calculation even for whole ground surface consisting hundreds of observers (Yücekayali & Ortakaya, 2015b). Unlike the general trend in literature (Hartjes & Visser, 2019; Morris et al., 2015; WANG et al., 2018; Yücekayali & Ortakaya, 2015b), a full sphere contour instead of a hemi-sphere contour is utilized in this study. The main reason for this is that the aim of this study is to generate optimized trajectories over a terrain such as a residential area or city, and within such an optimized trajectory, large pitch and roll angles might occur, which results in digression from the hemi-sphere contour, that requires extrapolation and results in loss of accuracy. This may even occur at slight Euler rotations when the distances to observer locations are high. Utilization of a full acoustic sphere eliminates the need of extrapolation.

Acoustic sphere database is then generated through coupling of VVPM, aeroacoustics solver and mathematical model at trimmed flight conditions with different weight, descent, climb and sideslip conditions.

Terrain model is another crucial component of the simulation model which contains landform, noise sensitive regions, obstructions and airspace regulation information and is essential to determine noise signature of a rotorcraft on ground surface. The terrain is included as a surface mesh and each node represents an observer location for which acoustic calculations are performed for. Sound pressure levels (SPL) are calculated instantaneously during simulation or trajectory optimization and track, then are utilized to calculate sound exposure levels (SEL) at desired locations on terrain/map. SPL standing for instantaneous noise signature and SEL standing for time averaged noise signature on ground are both utilized in the trajectory optimization cost function to generate noise optimal trajectory/path to be tracked.

In conclusion, the simulation model covers the comprehensive rotorcraft mathematical model, noise model and a terrain model, provides a real time

simulation capability at a fidelity high enough to utilize in trajectory optimization and track purposes.

1.4 Trajectory Optimization and Track

In complex trajectory track problems, achieving a single objective is, most of the time, not enough. The system shall achieve a set of performance parameters or states while tracking the desired path. Moreover, if the path to track is considered within the optimization problem, ensuring the generated trajectory is both optimal and trackable, requires a multi-disciplinary approach.

The aim of this study is to provide an optimization framework for noise minimal trajectory generation while keeping lower fuel consumption. Besides, assuring the flight profile is safe, comfortable and it complies with platform and civil airspace constraints. Therefore, the essence of the methodology is waypoint tracking with additional set of performance and optimality requirements.

When combined with waypoints, fuel and speed goals; the optimization objective function i.e. minimizing the noise impact on ground, becomes highly non-linear and sensitive to inputs. Therefore, accurate objective cost estimation cannot be achieved without flight simulation through the generated trajectory. In this scope, a model predictive control is evaluated as a proper approach, as control and trajectory optimization can be achieved through previously simulating all possible paths to provide foresight for the objective function.

Typically for a model predictive control (MPC), an optimization stage is combined with a model representing the plant and the control input is obtained with solution of the optimization problem exposed to specific constraints and cost (Y. Wang & Boyd, 2010). Classically, MPC acts as a tracking algorithm to pursue the predefined trajectory providing optimal control law utilizing the state feedback information (Castillo et al., 2007; Kunz et al., 2013; Neunert et al., 2016). However, there are many studies in the literature that combines trajectory optimization and tracking problem through model predictive control (Lapp & Leena, 2004).

In this study on the other hand, noise signature, fuel consumption, comfort and waypoints are included in the objective function as additional costs, so that trajectory and the control history to track the trajectory are simultaneously optimized with bounds do not directly appear in the output of the MPC. The accuracy of the generated trajectory and track performance through the optimized control history depends on the fidelity of the dynamic model of the plant to be controlled. The performance of MPC, which is already a complex control framework, is expected to be improved with higher fidelity dynamic model of the plant (Ngo & Sultan, 2016). Combination of costs from various disciplines in objective function introduces the utmost complexity, therefore the addition to linearized model, the exact non-linear replica of the plant to be controlled is also utilized as the prediction model.

Having a detailed overall objective function still does not eliminate the need of constraints for the optimization function. These constraints are generally incorporated with platform specific limitations that shall not be violated throughout the simulation, such as ‘never exceed speed’, roll & pitch attitude limitation, wind-azimuth envelope, altitude limits, power available or transmission limits, control limits or rates. Additionally, helicopter maneuverability may be restricted in terms of passenger or pilot comfort aspects through constraints on translational and rotational accelerations and attitude limitations. Further constraints may be required when operating around airports, helipads, and urban areas, where there are confined civil airspace or flight corridors. Therefore, specific constraints are combined with the objective function in order to achieve an optimization and well-behaved track of the trajectory.

CHAPTER 2

LITERATURE REVIEW

The methodology proposed in this dissertation is a trajectory optimization and track framework which combines multiple disciplines such as aerodynamics, aeroacoustics, fight dynamics and control. For each discipline, a module is developed and tightly inserted in the overall framework. In this scope, literature review is grouped under four chapters. The aerodynamic chapter covers literature review in terms of rotor aerodynamic modeling, simulation, and wake dynamics. Aeroacoustics chapter covers literature review in terms of rotorcraft aeroacoustics solvers and methodologies. Simulation/mathematical model chapter covers flight dynamics modeling of rotorcraft, simplified noise models and terrain models. Trajectory optimization and track chapter covers literature review in terms of trajectory optimization, track algorithms and control approaches.

2.1 Aerodynamic Model

Considering the advances in efficient vortex algorithms, the increase of interest for higher fidelity comprehensive modeling and the bottlenecks of grid based CFD for full helicopter modeling with all rotor dynamics and flight mechanics features included; VVPM for helicopter rotors revealed itself as a valuable alternative. Yet, VVPM relies on either near body CFD or lifting line to calculate lift and drag values of an airfoil accurately. However, in terms of rotor unsteady wake dynamics and accurate rotor loads, VVPM combines advantageous aspects of CFD and blade element methods (BEM), and discards the drawbacks such as fidelity level, cost, and implementation limits. Therefore, VVPM possess potential for comprehensive modeling approaches, interactional aerodynamics, and exploitation in design loop, flight dynamics and rotor dynamics applications.

Vortex methods have been studied for fluid dynamics applications for many years. However, the entry of vortex methods into rotorcraft industry effectively, is observed within the last decade. He (He & Zhao, 2009) was one of the frontiers to couple VVPM with a comprehensive rotor model for vorticity generation to estimate unsteady blade airloads. Then Zhao (J. Zhao & He, 2012) extended the model for further ground effect and interference analysis of rotor wake with ship decks. Tan (Tan & Wang, 2013) developed a similar VVPM model for helicopter rotors but instead of an actuator line approach at rotor model end, a panel method coupled BEM is utilized. Alvarez's work (Alvarez & Ning, 2018) is one of the studies that explore wake interaction of multiple rotors, although the study considers propellers with non-zero advance ratio. Propeller interaction have also been explored in other studies (J. Calabretta, 2010; J. S. Calabretta & McDonald, 2010; H. B. Wang, 2017) where VVPM is utilized to investigate propulsion-airframe and propulsion-wing interactions. As VVPM is flexible to simulate multiple rotors and their mutual interaction (Alvarez & Ning, 2019), it is moreover advantageous to study unconventional configurations. In this scope, examples of VVPM to investigate wake, load and interaction calculations for co-axial (Singh & Friedmann, 2018b, 2018a), tiltrotor (Ho & Yeo, 2017) and side-by-side overlapping (Avera, 2017) rotors. In another study, VVPM is utilized to identify state-space induced flow model for flight dynamics and control applications, which enables to describe inflow mathematical model for advanced/new configurations where test data is absent and grid-based CFD simulations are expensive (He et al., 2017). An essential alternative usage of VVPM is the field of wind energy, where wake methods have been extensively utilized at varying fidelities (Vermeer et al., 2013). Parallel to that, due to the ability to model multiple rotor and rotor-rotor, rotor-tower interactions, affordable computational cost, suitable accuracy, fidelity and ease of coupling with structural models, VVPM received broad attention for wind turbine/farm modeling, analysis and design of vertical (Chatelain et al., 2016) and horizontal (Hu et al., 2015) axis wind turbines.

Further application of VVPM observed in the literature is coupling with grid based CFD for high-resolution near body solution of lifting surfaces. By doing so, Lagrangian particles track the rotor wake while compressible flow simulation near body region can be performed with Eulerian approach which eliminates the diffusive and dampening behavior of grid based CFD for high vorticial flow structures in far wake. Utilization of such a hybrid method (Stock et al., 2010) is proposed to compare grid based CFD and VVPM vorticity contours for tip vortex of a finite wing and model rotor wakes in forward flight. On the other hand, Ma (Ma et al., 2018) utilized VVPM/CFD coupling to study rotor aerodynamic characteristics and loads for an individual blade control application.

In terms of rotor aerodynamic modeling, the author has previously published studies at various fidelities for rotor aerodynamic modeling (Tamer et al., 2010; Yücekayali & Ortakaya, 2010), analysis (Dülgar et al., 2019; Yücekayali et al., 2018), design (Baslamisli et al., 2014; Şenipek et al., 2015; Tamer et al., 2011), test & evaluation (Yücekayali et al., 2013) and assessment of interactional aerodynamics purposes (Yücekayali & Ortakaya, 2019), which all provided infrastructure and knowledge in the scope of this dissertation.

2.2 Aeroacoustics Model

Aeroacoustics is a multi-disciplinary field combining principles of fluid mechanics and acoustics. Aeroacoustics basically stands for aerodynamically generated noise, and as in its form considered in this dissertation, is a consequence of solid body kinematics and unsteady pressure fluctuations on the solid surface. Starting with Lighthill's acoustic analogy (Lighthill, 1952), rotorcraft noise evaluation methodologies evolved within the years and converged to three fundamental methods namely: Ffowcs Williams-Hawking, Kirchhoff and Collapsing sphere. Amongst the alternatives, like most of the rotorcraft noise estimation codes in the literature, Ffowcs Williams-Hawking (FWH) approach is implemented in this study.

The FWH equation is a generalized formulation of Lighthill's acoustic analogy and copes with the sound propagation from arbitrarily moving surfaces with pressure variations on the surface (Williams & Hawkings, 1969). In their study, Ffowcs Williams and Hawkings re-arranged the Navier-Stokes equations into an inhomogeneous wave equation, which is then re-formulated in integral form for ease of numerical solution and implementation for noise evaluations of aerodynamically generated sound from propellers and rotors (Brentner & Farassat, 2003). The report published by Brentner and Farasat (Brentner & Farassat, 1994) is the utmost useful source providing historical perspective and method assessment on helicopter noise prediction. Utilization of FWH equation provides a hybrid approach to resolve wave propagation from nearfield to far field i.e. observer, which benefits numerical solution methods and computational efficiency (Mishra et al., 2016). FWH is an appropriate approach for analysis of aerodynamically generated noise and today almost all deterministic rotor noise prediction tools are based on the time-domain integral formulation of the FWH equation (Brentner & Farassat, 2003; Casalino, 2003; Martinussen, 2010; Mishra et al., 2016; Morgans et al., 2005; Opoku et al., 2002; Ortun et al., 2014; Özyörük et al., 2017; Prieur & Splettstoesser, 1999).

In terms of aerodynamically generated rotorcraft noise; the author has previously published studies for noise computations with inhouse developed tools (Yucekayali et al., 2019; Yücekayali, Şenipek, Ortakaya, et al., 2019) and commercial tools (Yücekayali et al., 2015), in design optimization (Yücekayali & Ortakaya, 2015a), in interactional acoustics (Atalay, Yücekayalı, et al., 2019) and for test&evaluation concerns (Ezertaş & Yücekayali, 2013; Yücekayali, Ayan, et al., 2014; Yücekayali, Baslamisli, et al., 2014; Yücekayali et al., 2013), which all provides infrastructure and knowledge for this dissertation.

2.3 Simulation/Mathematical Model

Rotorcraft simulation/mathematical models provide a variety of assessment areas such as performance, controllability and stability analyses, piloted simulations and handling quality evaluations, comprehensive modeling and design activities. Fidelity and complexity of the flight dynamics treatment varies according to the purpose of the mathematical models.

In general, rotorcraft mathematical models vary in fidelity, in terms of inflow models, rotor dynamics and unsteady wake dynamics modeling capabilities. A great deal of studies and a few commercial comprehensive mathematical models exist in literature.

A typical rotorcraft simulation/mathematical model consists of 6 DoF equations of motions, and the contributions of each rotorcraft component such as rotors, wing, fuselage and empennage, are calculated individually and integrated at the center of gravity of the platform. Utilization of momentum theory in terms determination of the inflow distribution, provides a simple dynamic representation of a rotorcraft. Such a modeling technique is utilized by Cvetkovic (Cvetkovic et al., 2002) to study decoupled i.e. longitudinal and lateral responses, although it is not considered as a feasible approach (Johnson, 1994). Talbot's study (Talbot et al., 1982) is another utilization of simple momentum theory which is combined with coupled flapping rotor dynamics response for piloted simulations. Another flapping only rotor dynamics, coupled with a momentum theory was developed by Salazar (Salazar, 2010).

More advanced rotor dynamics representations are achieved by taking not only flapping but also lead-lag response of blades into consideration; as well as hub dynamics such as hinge and related restraints. Takahashi (Takahashi, 1990) has coupled such rotor dynamics model with a three-state nonlinear dynamic inflow model to estimate the induced velocity distribution over the rotor disc. One of the most extensively used momentum theory implemented mathematical model is the

Minimum Complexity Model, developed by Heffley and Mnich (Heffley & Mnich, 1988) providing component buildup method and enables the user to be able to model with only basic data for a specific helicopter. Minimum complexity has been used in several studies for the past 20 years as a base model on which researchers are implementing specific improvements for further flight dynamic analyses (Hilbert, 1984; Luca Vigano, 2006; Munzinger, 1998; Yilmaz, 2008). Despite its simplicity, momentum theory can be especially useful when coupled with mathematical models providing a general understanding of the dynamic response of a rotorcraft. On the other hand, the reason why momentum theory provides the lowest fidelity estimation is that, it suggests a uniform induced velocity distribution over the rotor disc, which, in reality is extremely non-uniform under influence of strong tip and root vortices, wake and blade interaction. In this scope, instead of utilizing a uniform inflow model, several researchers have implemented tip loss functions such as Prandtl function to include tip losses to some extent (Klesa, 2008; Sankar, 2001; Todorov, 2011; Vladimir et al., 2006). However, the non-uniformity of forward flight induced velocity distribution cannot be achieved with a simple tip loss function, instead, inherently non-uniform induced velocity models are essential. In this manner, there are studies, that utilize Drees gradient formula generated from the wake geometry of a simple cylindrical vortex wake, depends on both wake skew and advance ratio (Gennaretti et al., 2009; Masarati, 2017; Shen, 2003). Another non-uniform inflow model significantly implemented in the past is Mangler&Squire's (Leishman, 2006) inflow model which is based on potential theory and with the modifications of Bramwell (Bramwell et al., 2001) can be used from hover to high advance ratio flight conditions. Mangler&Squire's inflow model found place in studies related with blade-vortex interaction, neural networks and system identification (Gläßel et al., 2004), as well as initial condition for prescribed wake models in terms of induced velocity (Castles & de Leeuw, 1953).

The finite state dynamic inflow formulation developed by Peters and He (Peters et al., 1987; Peters & He, 1989, 1995) have replaced the momentum theory to provide a higher fidelity non-uniform inflow model. The configurable fidelity, computational

low cost and accuracy of the Peters-He inflow model resulted in being one of the most extensively used inflow models by the studies on rotor aerodynamics, rotor aerodynamic mathematical models, helicopter flight dynamics mathematical models that are also used in simulators even at contemporary studies (Goulos, 2016; Yücekayali, 2011).

Simple harmonic or finite state dynamic wake models have been extensively used for flight dynamics, performance, and simulation purposes (Chen, 1990). Yet, more accurate, and higher fidelity mathematical models are essential for more advanced evaluations and designs providing more reliable, lighter, maneuverable and safe platforms. Huh's study (Huh, 1988) is one the first examples of more sophisticated and advanced mathematical models, including prescribed and free wake method in terms of inflow model for hovering helicopter rotor. Another example is Liu's study (Liu, 2008) where a comprehensive rotorcraft analysis methodology is coupled with the vortex wake methods. Such refined aerodynamic models including wake dynamics and induced velocity prediction with vortex wake methods for further flight dynamics applications are utilized by Theodore (Theodore & Celi, 2002) and Reddy (Reddy & Stewart, 2009) to investigate blade and rotor elastic & dynamic responses.

Except from the academic or research studies, there are a few commercial comprehensive modeling tools providing build-up and user selective options to generate mathematical models of the rotorcraft configuration of interest. FLIGHTLAB (Advanced Rotorcraft Technology, 2008) built in a modular structure where each module corresponds to a physical or logical subsystem of the aircraft model, can be pointed as one of the well-known low-cost, selective high fidelity, reconfigurable and high productivity simulation and analysis tool. Flight dynamics analyses, such as trim conditions, linear and nonlinear response of the helicopter can be studied with a selective fidelity level. CAMRAD JA/II (Johnson, 1988a, 1988b) on the other hand, is a comprehensive model of rotorcraft aerodynamics and dynamics, combines structural, inertial and aerodynamic models in order to analyze

rotor and helicopter performance, loads and dynamic responses with free wake option.

Finally, in his master thesis (Yücekayali, 2011), the author has studied prescribed wake models (Egolf & Landgrebe, 1982; Landgrebe, 1971), vortex core size and its evolution (Young, 1997) as well as free and fixed wake models (Beddoes, 1985; Szymendera, 2002) which provided experience, capability and background for the methodology proposed with this dissertation in terms of rotor wake dynamics, inflow dynamics and mathematical modeling as well as simulation.

To provide a real time simulation model in terms of acoustic calculations, a sphere approach that estimates instantaneous noise signature on ground is developed and implemented. The approach utilizes previously generated acoustic spheres consisting of acoustic pressure frequency spectra at locations on a sphere surface with a radius large enough to assume whole rotorcraft as a point acoustic source. In this method, noise level on an observer location outside the sphere is calculated through propagation of the acoustic pressure level from sphere surface up to the observer location while considering atmospheric absorption and spreading losses.

Similar approaches under different names such as acoustic mapping, radiation spheres, sound spheres and second level acoustic model (Hartjes & Visser, 2019; Morris et al., 2015; WANG et al., 2018; Yücekayali & Ortakaya, 2015b) have been implemented in literature. Once different flight regimes are stored as a database, interpolation between spheres provides an approximate acoustic solution of the instantaneous flight condition. The database dependent parameters as a rule of thumb are generally thrust level, flight speed and flight path angles as discussed in the literature (Bernardini et al., 2015; Tsuchiya et al., 2009).

In terms of utilization of acoustic sphere model coupled aircraft mathematical models, which can compute real time acoustic response on ground; the author has previously published two studies; one for rotorcrafts (Yücekayali & Ortakaya, 2015b) and the other for propeller aircrafts (Şenipek et al., 2017).

The landform has a direct effect on acoustic impact of an aircraft on ground as the terrain governs the acoustic emission distance. Morris's (Morris et al., 2015) work can be an example of the terrain model implemented in the acoustic calculations.

2.4 Trajectory Optimization and Track

Trajectory optimization and track are generally considered for unmanned air vehicles (UAVs) for which acoustics concerns are insignificant. An example for such trajectory optimization problems is the work of Gatzke (Gatzke, 2010) where a direct method, a pseudo spectral method, is utilized for optimal control and optimization is performed for path planning where control input profile is precomputed and fed into the simulation as a function of time. As the trajectory generation and control input profile are determined offline, any disturbance during real flight would result in a deviation from the desired path. A similar problem is expected to be encountered in the work of Dauer (Dauer et al., 2013) where path is optimized on ground, time dependent velocity and attitude references are generated offline and fed to the system during the real flight. On the other hand, there are few examples for trajectory optimization problem of full helicopters and even fewer examples of trajectory optimization with the concern of noise. One trajectory optimization example for full helicopter is the work of Dugar (Dugar et al., 2017), which takes the advantage of decoupling path and velocity, attitude, optimizations with velocity tracker at the inner loop and position tracker at the outer loop. When noise is the concern for trajectory optimization, Visser's work (Visser et al., 2009) is an example of optimizing rotorcraft trajectories which was formally a fixed-wing tool transformed into a rotorcraft tool. The study utilizes an offline approach i.e. direct collocation method therefore computation cost highly depends on the grid size. This might be the reason that only approach trajectories are considered with a noise model that ignores directivity characteristics of rotorcraft noise. A rare example of online trajectory optimization with noise concern is Ikaida's work (IKAIDA et al., 2010) where trajectory optimization is performed for stages with defined duration and

while aircraft tracking the optimized path, trajectory is generated for the next stage i.e. 40 seconds. While this study steps forward as being online, it is not exactly real time, instead it uses stage division approach and a very simplified helicopter mathematical model, a point mass model, is utilized which would lead discrepancy between desired trajectory optimization, tracking and noise characteristics and the test environment.

Being built on optimal control theory and having facility to combine with different optimization methods, MPC gained popularity. The increase in computational capabilities with the advances in technology and efficient algorithm developments influenced the number and application areas of MPC. Recent examples of MPC are found in a wide range of applications such as robotics (Erez et al., 2013), chemical process, industrial control and economics (Y. Wang & Boyd, 2010). In terms of aerospace, there are application examples in fully autonomous UAVs as MPC satisfies the optimal control demand especially for rotorcrafts (Neunert et al., 2016). Furthermore, it is evaluated that the ability to employ hard constraints and to estimate future behavior under current action for feedforward drives are the significant aspects of MPC for trajectory tracking purposes.

The potential of trajectory optimization and track with optimal control has been revealed with studies of Chen (Chen & Zhao, 1996), Zhao (Y. Zhao et al., 1996), Okuno (OKUNO & Kawachi, 1994) and Botasso (Bottasso et al., 2004) before. In this study on the other hand, built on optimal control basis, model predictive control is utilized to generate optimal noise minimal and green trajectories for rotorcrafts.

In terms of trajectory optimization and track, the author has previously published various studies which are the outcomes or extensions of the optimal control and trajectory optimization methodology proposed with this dissertation. In his study, where optimal guidance model is developed for conventional helicopters (Yücekayali et al., 2017), reference states desired to be followed are generated through an optimization stage, then an LQR controller tracks the reference states while simultaneously stabilizing the plant. The author also implemented trajectory optimization and track principles to define an agility metric as a helicopter main rotor

performance parameter to utilize agility in design optimization studies in his successive publications (Şenipek et al., 2019; Yücekayali, Şenipek, & Ortakaya, 2019). Additionally, author utilized model predictive control approach to perform and assess maneuver airloads for a conventional helicopter configuration (Atalay, Şenipek, et al., 2019).

CHAPTER 3

METHOD

The optimal trajectory generation and track framework proposed with this study essentially is composed of four sub-systems related with each other through tight/loose coupling, direct data transfer or model representation i.e. surrogate or superior model. Rotor aerodynamics module covers the rotor dynamics coupled aerodynamic and wake modeling approach to provide the desired rotor aeromechanical data and colored as grey in Figure 3.1. A VVPM approach is developed to provide induced velocity distribution along the blade span and wake dynamics which is then utilized by the rotor dynamics model to calculate blade loads. Aeroacoustics module covers the aeroacoustics solver, interface between aeromechanics and acoustics models and their application to full rotorcraft configurations, colored red in Figure 3.1. The aeromechanical data produced by the aerodynamic module is transformed into blade pressure distribution and along with the blade kinematics information, acoustics solver copes with the acoustic pressure, sound pressure level (SPL) and frequency spectrum at desired observer locations. Third module is the simulation model, covering the rotorcraft mathematical model, acoustic surrogate model, terrain model and simulation environment, colored blue in Figure 3.1. The coupled aerodynamics and aeroacoustics modules are operated to estimate SPL and frequency spectrum on observers located on a spherical surface enveloping the rotorcraft. Multiple rotor overlapping is performed, and sphere database is generated to provide real time noise estimation on the terrain. Rotorcraft comprehensive mathematical model equipped with the acoustic sphere is then transformed into the simulation model for further applications. Finally, colored green in Figure 3.1, trajectory optimization and track module covers the optimal control approach, optimization algorithm and the multi point – multi disciplinary objective function. A model predictive control scheme operates the simulation model, to

generate optimal trajectory and inputs required for tracking. A multi-objective cost function assures waypoint tracking, safety, comfort, minimum emission and minimum noise at desired regions on the terrain.

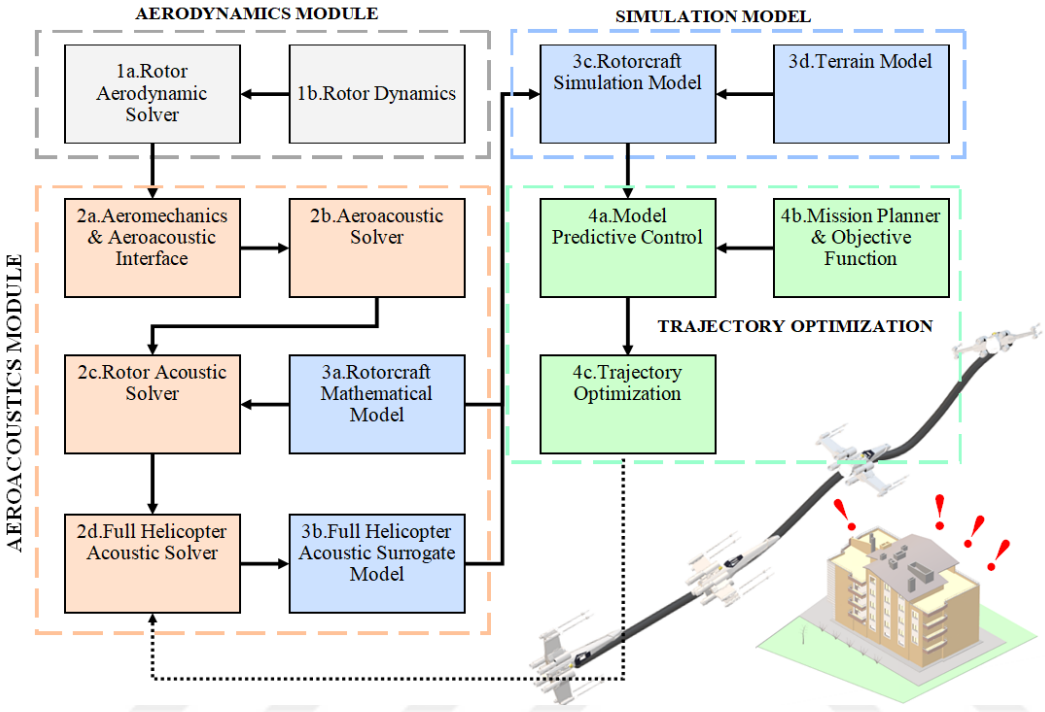

Figure 3.1 Flow chart of the proposed methodology

The flow chart for the aerodynamic module is given in Figure 3.2. Aerodynamics module basically is composed of VVPM and rotor dynamics module tightly coupled together, exchanging induced velocity and blade aerodynamic loads information at each time step. As the wake dynamics evolve in time, induced flow on each blade is calculated through the VVPM. Then the aerodynamics load distribution over each blade is updated with taking blade dynamic response, platform motion and relative air velocity into account. Updated aerodynamic load distribution is utilized in bound and trailed circulation calculations according to which new viscous particles are generated for the next time step. As the rotor dynamic response is solved simultaneously; wake dynamics, all the blade-vortex, rotor-wake and rotor-rotor interactions are included in the calculations inherently. The aerodynamic coefficients of the profiles are determined from the airfoil database stored in terms of effective

angle of attack and Mach number. At each time step, according to the instantenous effective angle of attack and Mach number, cl, cd and cm coefficients are interpolated from the database.

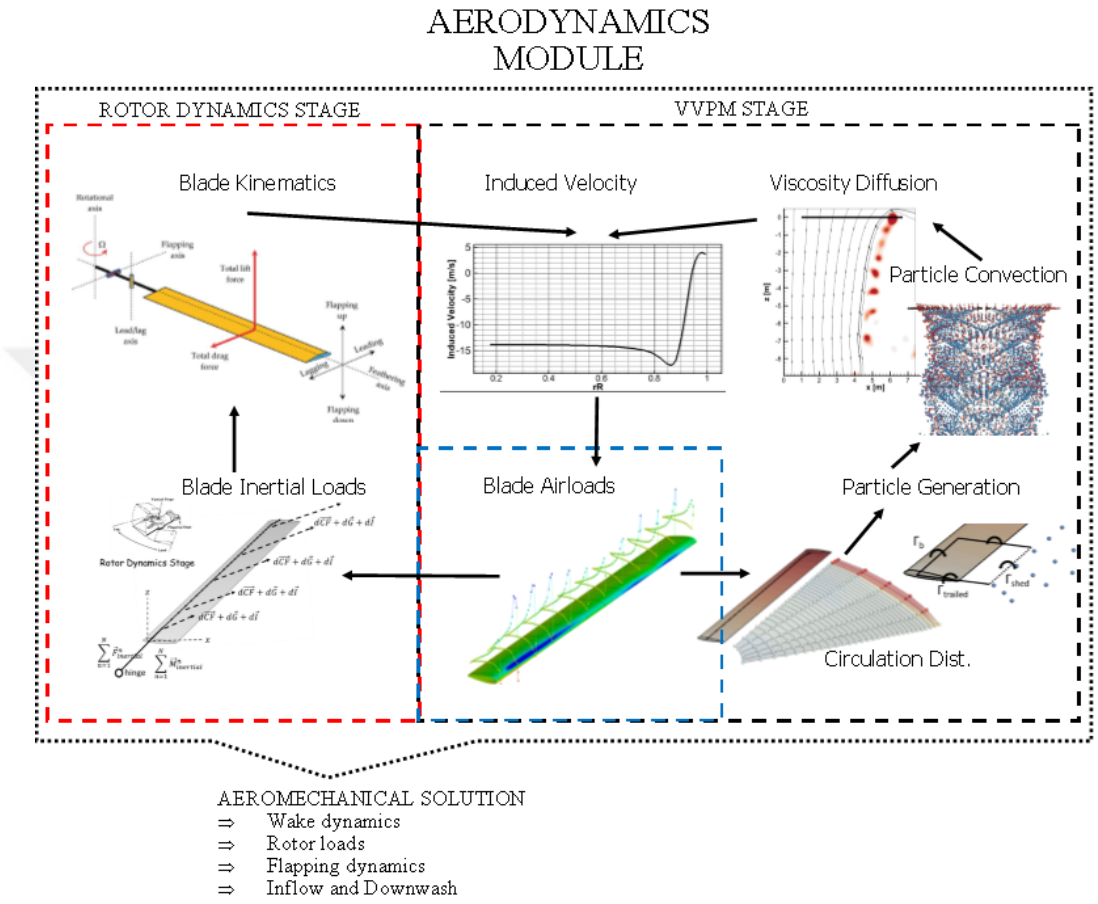

Figure 3.2 Flow chart for aerodynamics module

The flow chart for the aeroacoustics module is given in Figure 3.3. The wake solution generated through aerodynamics module is further extended to provide high resolution aeromechanical data for at least one or more revolutions with increments smaller than 1 degree's azimuth steps. With the help of pressure database previously generated for each airfoil, the concentrated loads along the blade span are transformed into chordwise pressure Cp distributions. Then aerodynamic loads are projected as pressure distribution over the blade geometry in terms of surface mesh and data. The interface algorithm prepares blade pressure distribution at each

azimuth angle and provides required kinematics data for further acoustic analysis. The aeroacoustics solver utilized in this study had been developed within industry-academy co-operation program by Prof. Özyörük from Middle East Technical University (Özyörük et al., 2017) and funded by Turkish Aerospace Industries. After the acoustics analysis at desired observer locations post process algorithms summarizes acoustic pressure variation, prepares SPL calculations and contour and then performs frequency spectrum analysis.

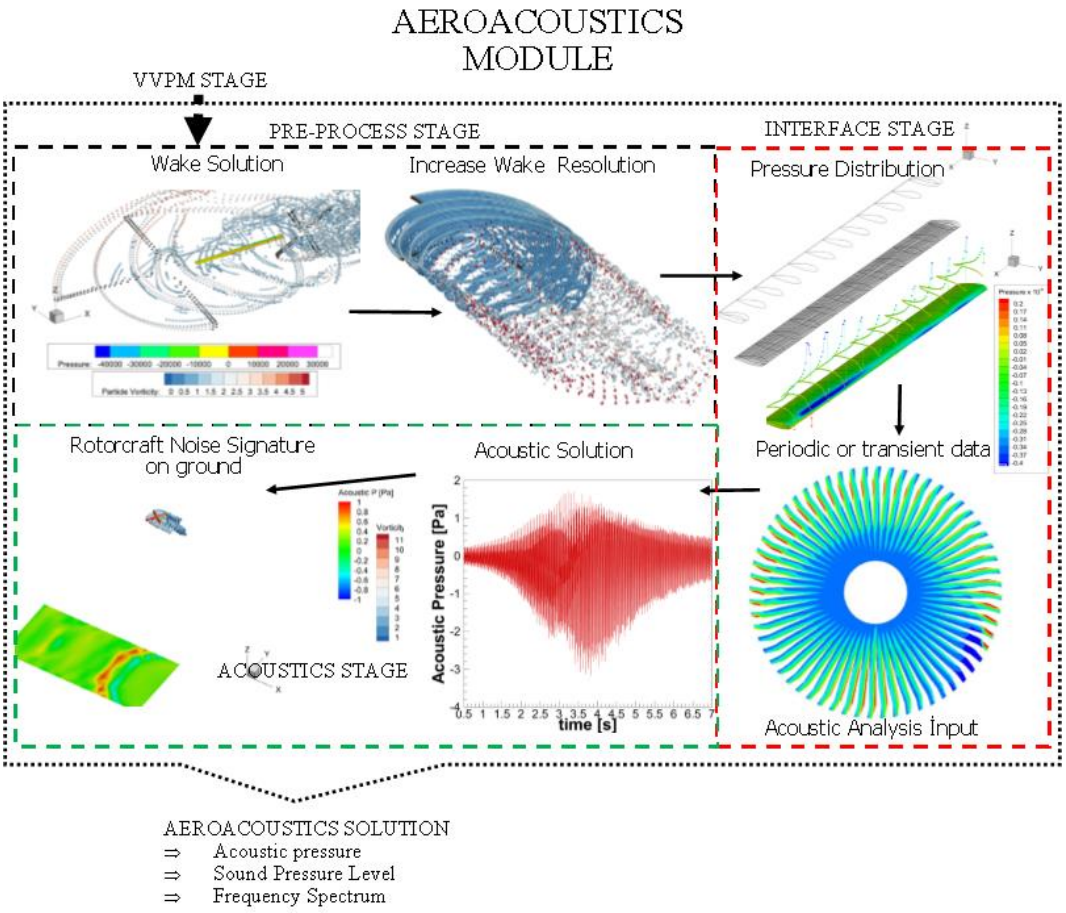

Figure 3.3 Flow chart for aeroacoustics module

Flow chart for the simulation model is given in Figure 3.4. Simulation model covers rotorcraft comprehensive mathematical model, acoustic surrogate model (noise model) and the terrain model and provides real time flight dynamics simulation coupled with real time acoustic/noise signature calculation on the ground surface.

Real time computation is achieved through performing trim and noise analysis with the coupled aerodynamics and aeroacoustics solver beforehand and through storing the results on a spherical observer grid at various flight conditions to generate the acoustic sphere database. Then, the sphere database is coupled with the flight dynamics and terrain models so that SPL contours on a ground surface independent from the dimensions generated at least 100 Hz. The acoustic sphere database is continuously expanding for different flight conditions therefore gradually covers larger portion of the flight envelope.

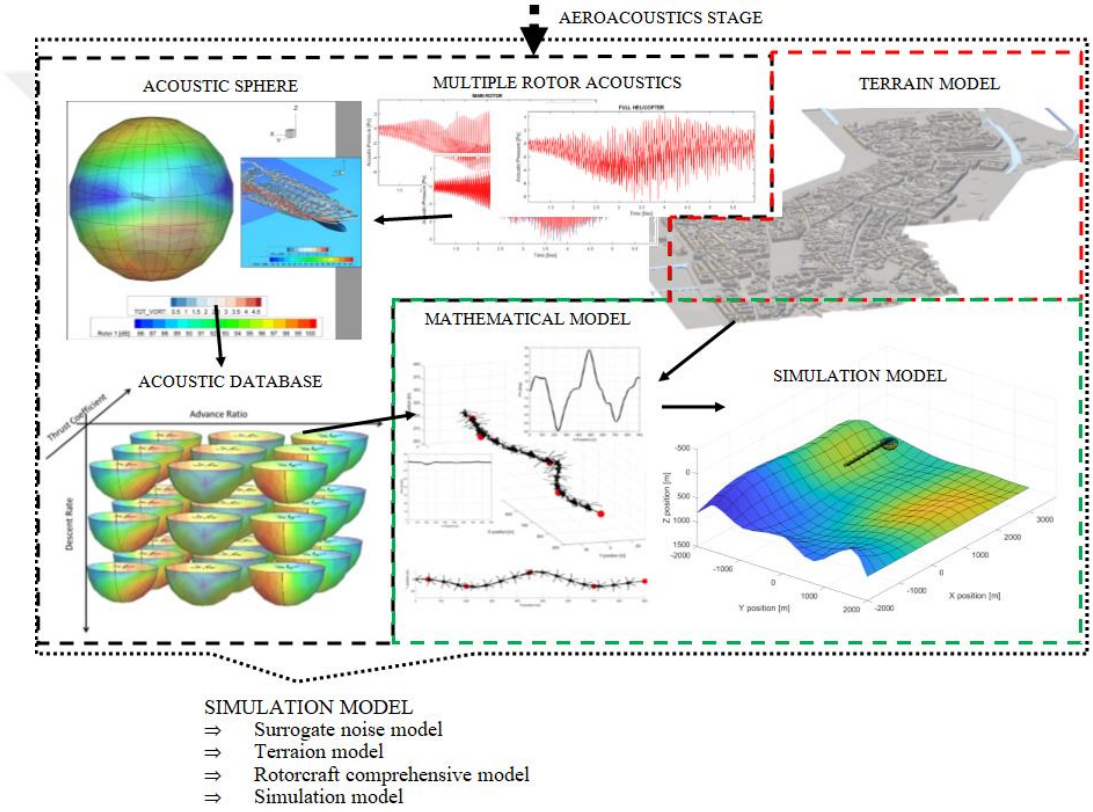

Figure 3.4 Flow chart of the simulation model

Trajectory optimization flow chart is given in Figure 3.5. Trajectory optimization framework wakes the simulation model as both plant and predictive model and utilizes a model predictive control scheme to simultaneously optimize the trajectory and the control inputs to track the generated path. MPC optimizes the trajectory along the prediction horizon yet the control inputs are fed into the plant along control

horizon which is generally much smaller interval. This brings a feedforward feature to the system and enables to control the plant with simpler models. Although the main aim of this study is to generate noise minimal and green (minimum emission & fuel consumption) trajectories, safety, comfort, trackability and mission fulfillments are essential. Moreover, mission and platform specific constraints are required when operating in civil airspace. All those concerns contribute to the global cost function and an optimization algorithm seeks for an optimal trajectory. Trajectory module input is the simulation model, and output is noise minimal trajectory and control history with additional performance, safety, comfort and mission concerns.

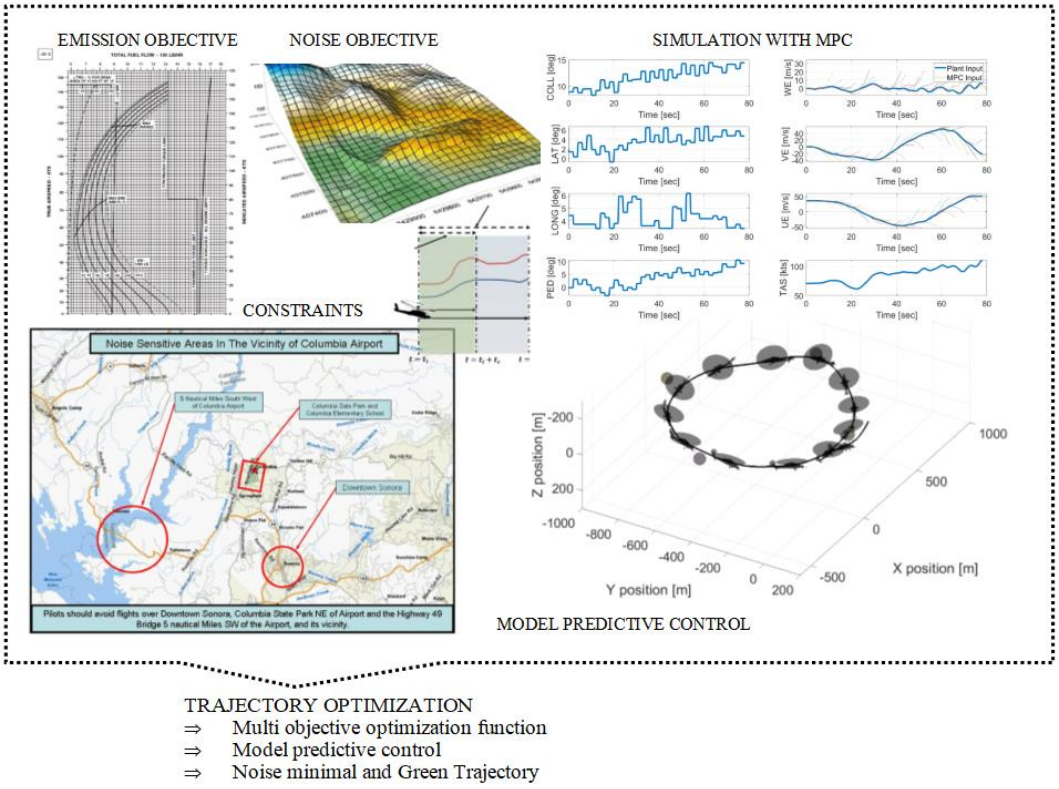

Figure 3.5 Trajectory optimization flow chart

3.1 Organization of Dissertation

The main structure of the dissertation is divided into four main chapters each representing a module, followed by results and conclusion chapters.

Aerodynamics module chapter, CHAPTER 4, discusses the development of the viscous vortex particle model (VVPM) and coupling with rotor dynamics module to provide high fidelity rotor aerodynamics, loads and wake dynamics model which is ready to couple with acoustics solver and comprehensive rotorcraft mathematical model. Trim algorithm is introduced in terms of isolated rotor trim. Then validation activities are presented in chapter 4.4. Total thrust to torque variation comparisons, flow field, tip vortices trajectory and rotor loads comparisons with test data existing in the literature are given. Moreover, co-axial rotor simulations are performed and validated with wind tunnel test data. Finally, the developed VVPM tool is further qualitatively explored for unconventional rotorcraft configurations such as lift offset, intermeshing, and tilting prop-rotor.

The aeroacoustics model chapter, CHAPTER 5, discusses the fundamentals and governing equations for the aeroacoustics solver utilized in this study and the interface developed to directly couple the VVPM with the noise computations. High resolution wake generation algorithm is summarized then the validation study of the developed viscous vortex particle acoustic model (VVPAM) is presented where blade load, acoustic pressure and sound pressure contours are compared with HART-II wind tunnel test data. Finally, further exploration of the VVPAM is performed for full helicopter trimmed level flight condition and full helicopter BVI noise investigation.

Simulation model chapter, CHAPTER 6, covers the comprehensive rotorcraft mathematical model, surrogate noise model, terrain model and coupling of those to provide real time flight dynamics model with acoustic signature computation on whole ground surface or multiple observer locations. Full helicopter trim methodology and stability augmentation system (SAS) algorithms are summarized.

Then surrogate noise model i.e. acoustic sphere approach, verification and acoustic sphere database are introduced. The implementation approach of the terrain model is discussed and the fully coupled flight dynamics simulation model is presented.

Trajectory optimization and track chapter, ,CHAPTER 7, presents the model predictive control approach, the overall cost function with objective contributions from acoustics & performance disciplines, safety, comfort and mission tasks. The developed and commercial optimization algorithms that are implemented in this study are introduced. Then, sample trajectory optimization and track results are presented to discuss the accuracy, performance and capability of the developed trajectory optimization and track framework.

The results chapter, CHAPTER 8, presents analysis results determined with the developed tool. Various evaluations with different test purposes are performed on the developed comprehensive modeling, aeroacoustics analysis and trajectory optimization & track approaches. Each evaluation is performed to test, evaluate and demonstrate a different capability of the overall developed methodology.

Conclusion chapter, CHAPTER 9, summarizes the study, presents the outcomes of the study and discusses the potential of the current state.

Future works chapter, CHAPTER 10, discusses potential improvements and application fields of the developed approaches.

CHAPTER 4

AERODYNAMICS MODULE

Aerodynamics module covers development of a viscous vortex particle method as a flow solver specifically implemented to estimate rotor/propeller unsteady wake dynamics, airloads, blade-vortex, blade-wake, and rotor-rotor interactions. The purpose of the aerodynamics module is the achieve high fidelity rotor modeling and airloads data at high resolution and accuracy, interactional wake dynamics and provide required aeromechanical data for further acoustic calculations and comprehensive rotorcraft modeling. A sample analysis for a conventional helicopter configuration with well-known generic helicopter fuselage ROBIN (Freeman & Mineck, 1979; Kunze, 2013) at quartering flight condition is given in Figure 4.1, where vorticity iso-surface colored with total air speed and vortex particles colored with particle strengths are demonstrated.

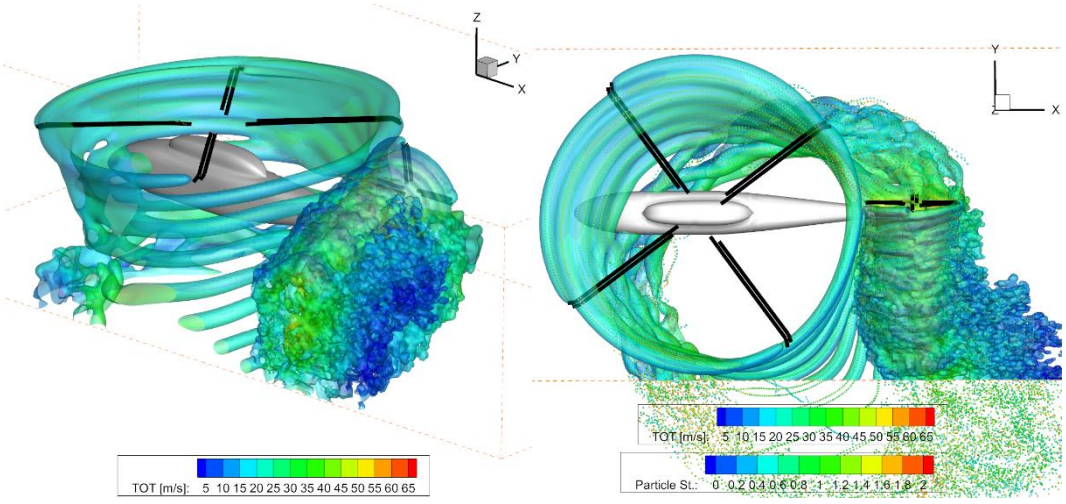

Figure 4.1 A sample VVPM solution for a conventional helicopter at quartering flight

The VVPM operates as a Lagrangian flow solver provides particle induced velocity along the blade span which is then coupled with rotor dynamics models to estimate

blade dynamic responses and calculate a realistic trim condition. The VVPM coupled rotor dynamics algorithm i.e. the aerodynamics model developed in this study, combines advantages of classical Eulerian CFD methods and blade element codes with inflow or vortex models (prescribed, fixed, or free wake). Advantages such as fidelity, accuracy, estimation capability of vortex convection, diffusion and stretching of CFD, and flexibility to implement within comprehensive codes for full rotorcraft trim and simulation of BEM are collated. Whereas, the disadvantages of CFD such as computational cost, high-resolution mesh requirements to avoid numerical diffusion and limitations arise with a grid-based approach and the disadvantages of BEM codes such as simplifications in aerodynamics, dependence on various empirical correlation factors and the necessity to tune with test data especially for unconventional and new configurations, are eliminated.

VVPM rotor aerodynamic model can be broken down into two parts. First part; development of a VVPM approach for rotor/propeller aeromechanics which intends to eliminate inflow models or wake methods requiring numerous empiric/analytic user define parameters within comprehensive modeling tools. Second part is coupling with the rotor dynamics which is the junction point with comprehensive modeling, solves local air velocities determined from superposition of wake induced velocity, free stream air velocity including flight and wind vector, relative velocities resulting from rotorcraft angular rates, rotor-blade flapping and lead-lagging rates. Instantaneous airloads, circulation and local air velocity information is exchanged with the comprehensive model at a proper degree of freedom for each blade element. Comprehensive model then manages the time integration to determine rotor dynamic behavior and response for force and moment integration of rotorcraft at center of gravity for further flight dynamics considerations such as free flight trim or maneuver analysis. This chapter presents the methodology, implementation, validation and further exploration of the developed aerodynamics module of the comprehensive rotorcraft model developed in this study.

First theory and implementation of the VVPM is discussed, then coupling with rotor dynamics model where determination of rotor hub loads through integration of all

aerodynamic and inertial force and moments is presented. Then trim approach is discussed. Finally, validation with whirl tower, wind tunnel and benchmark analysis tools data existing in the literature as well as further qualitative assessment for unconventional configurations are presented.

4.1 Viscous Vortex Particle Method (VVPM)

The governing equations for VVPM approach are determined by re-writing incompressible Navier-Stokes equations in velocity-vorticity. Then the vorticity field can be resolved using a Lagrangian approach so that only the vorticity-dominated regions of interest can be solved without grid generation effort (He et al., 2017).

For an incompressible Newtonian fluid with uniform viscosity, the Navier-Stokes momentum term is given with equation (1).

$$\rho \frac{\partial u}{\partial t} + \rho u \nabla u = -\nabla p + \rho f + \mu \nabla^2 u \tag{1}$$

Where ρ is density, u is velocity vector, p is scalar pressure, f is conservative force field such as gravitational field and μ is the viscosity. The with the definition of vorticity, equation (2), the vector identity given with equation (3) is inserted into equation (1) to determine equation (4).

$$\omega = \nabla \times u \tag{2}$$

$$\nabla^2 u = \nabla(\nabla \cdot u) - \nabla \times \omega \tag{3}$$

$$\rho \frac{\partial u}{\partial t} + \rho \left\{ \nabla \frac{u^2}{2} - u \times \omega \right\} = -\nabla p + \rho f + \mu \nabla^2 u \tag{4}$$

Keeping in mind the two additional identities given with equations (5) and (6);

$$\nabla^2 \omega = -\nabla \times (\nabla \times \omega) \tag{5}$$

$$\nabla \times (u \times \omega) = (\omega \cdot \nabla)u - (u \cdot \nabla)\omega \quad (6)$$

Curl of the equation (4) is taken to eliminate the pressure term and determine the vorticity transport equation given with equation (7).

$$\frac{\partial \omega}{\partial t} + (u \cdot \nabla)\omega = \frac{d\omega}{dt} = v\nabla^2\omega + (\omega \cdot \nabla)u \quad (7)$$

Note that the viscous diffusion is defined through kinematic viscosity, and incompressible and Newtonian fluid assumption is done with this approach. Substituting the circulation contained in the vorticial fluid element $\alpha_i = \int_{\Omega_i} \omega_i(x)dx$, i.e. Helmholtz's first theorem (Georges-henri cottet, 2001), into (7) vortex particle convection diffusion and stretching with viscous diffusion models are determined as (8)

$$\frac{dx}{dt} = u(x,t) \quad and \quad \frac{d\alpha}{dt} = \nabla u \cdot \alpha + v\nabla^2\alpha \quad (8)$$

Convection and viscous diffusion equations given with (8) are considered as the governing equations and are solved separately which is called viscous splitting (Stock, 2007). The total velocity of a vortex particle is decomposed into vector summation of uniform free-stream field,u_∞ velocity induced by the lifting surfaces (blades in this case), u_{bl} and velocity induced by all the vorticity particles in the domain. Uniform free-stream field is represented with the wind and flight velocity vector and all the rotor blades contributes to the velocity induced as the lifting surfaces. Velocity induced by each vortex particle, u_i is calculated with Biot-Savart law (Georges-henri cottet, 2001) and superimposed for total particle induction.

The strength of vortex particle methods stems from the representation of the whole vorticity field with discrete Lagrangian vortex particles. If the vorticity field of a domain is represented by $\omega(\vec{x}, t)$, and there exists N number of vortex particles each of which has a vector valued vorticity ω_i and a volume V_i then the field can be constructed through equation (9).

$$\omega(\vec{x},t)=\sum_{i=1}^{N}\omega_i V_i\delta(\vec{x}-\vec{x}_i) \tag{9}$$

Where δ is the three-dimensional Dirac delta function. Representation of vorticity field with such point vortices (or vortons) is called singular vortex particle method (Chorin, 1973, 1980; van Rees et al., 2011; Winckelmans & A., 1993) as the singularity condition i.e. $\vec{x}=\vec{x}_i$results in a non-divergence-free particle field.

Considering the incompressibility $(\nabla\cdot u=0)$ and vorticity $(\nabla\times u=\omega)$ definitions, the relation between the velocity and vorticity is constituted through a streamfunction $\nabla^2\varphi(x,t)=-\omega(x,t)$ and $u(x,t)=\nabla\times\varphi(x,t)$ (Anderson, 2012)

Then the relation between the streamfunction and the vorticity for unbounded domain is constituted by equation (10) (Winckelmans & A., 1993)

$$\varphi(x,t)=G(x)*\omega(x,t)=\sum_{i=1}^{N}G(\vec{x}-\vec{x}_i)\,\omega_i V_i \tag{10}$$

Likewise, the relation between the streamfunction and local velocity is constituted by equation (11).

$$u(x,t)=\nabla\times\varphi(x,t)=\sum_{i=1}^{N}\nabla(G(\vec{x}-\vec{x}_i))\times\omega_i V_i \tag{11}$$

Keeping in mind that Green's function for $-\nabla^2$ is $G(x)={}^{1}/_{4\pi|x|}$, (Winckelmans & A., 1993) and $\alpha_i=\int_{\Omega_i}\omega_i(x)dx$, the velocity field is determined by equation (12).

$$u(x,t)=-\frac{1}{4\pi}\sum_{i=1}^{N}\frac{1}{|\vec{x}-\vec{x}_i|^3}(\vec{x}-\vec{x}_i)\times\alpha_i \tag{12}$$

Equation (12) provides a velocity field induced by N number of vorticity particles, however the formulation yields to singularity at $\vec{x}=\vec{x}_i$ as the vortons are defined as point vortices. Where $-\frac{1}{4\pi}\sum_{i=1}^{N}\frac{1}{|\vec{x}-\vec{x}_i|^3}(\vec{x}-\vec{x}_i)$ is defined as the singular Biot-Savart Kernel. Regularization of vortex methods has been extensively implemented in the literature. Regularization of the kernel is extensively done in the literature through

defining the vortex as a vortex blob with a smoothing radius or cut-off functions. Chorin's (Chorin, 1973) work was one of the first examples where the kernel value tends to return to zero towards vortex center with utilization of cut-off functions. Winckelmans's (Winckelmans & A., 1993) high order algebraic function is one of the widely used regularization, which is also utilized in the studies done by Calabretta (J. Calabretta, 2010) and Alvarez (Alvarez & Ning, 2018).

Regularization is generally performed through definition of the vorticity field, $\omega(\vec{x}, t)$ by replacing the Dirac function, δ which basically introduces the singularity with a regularization function ζ_σ as given with equation (13).

$$\omega(\vec{x}, t) = \sum_{i=1}^{N} \omega_i V_i \zeta_\sigma(\vec{x} - \vec{x}_i) \tag{13}$$

where σ is the smoothing radius, a cut-off length or core radius. In this study on the other hand, σ is defined specifically for each particle related with its initial discretization so that smoothing radius became a function of resolution that is governed with minimum flow field resolution. If selected large enough, it guarantees convergence and zero norm error between vorticity and velocity (Singh & Friedmann, 2018a)

Setting $\alpha_i = \int_{\Omega_i} \omega_i(x) dx$, vorticity field is defined as equation (14).

$$\omega(\vec{x}, t) = \sum_{i=1}^{N} \alpha_i \zeta_\sigma(\vec{x} - \vec{x}_i) \tag{14}$$

The relationship between vorticity field, vortex particles and velocity field are determined similarly, utilizing Green's function. Derivation requires straightforward mathematical operations which are skipped here for simplicity, yet summarized in Appendix A. Having defined regularization function ζ_σ the velocity field is obtained with equation (15)

$$u_\sigma(\vec{x}, t) = -\sum_{i=1}^{N} \frac{q_\sigma(\vec{x} - \vec{x}_i)}{|\vec{x} - \vec{x}_i|^3} (\vec{x} - \vec{x}_i) \times \alpha_i \tag{15}$$

where q_σ(x) is a function of the regularization function ζ_σ and Green's function G defined as $q_\sigma(x) = q(|x|/\sigma)$. A Gaussian regularization function is implemented in this study imposes a Gaussian vorticity distribution close to vortex center. Gaussian regularization utilized in this study is analogous with the works of He (He & Zhao, 2009), Zhao (J. Zhao & He, 2012) and Tan (Tan & Wang, 2013).

Defining $\rho = \frac{|\vec{x}-\vec{x}_i|}{\sigma_i}$, a non-dimensional distance parameter, in Figure 4.2 how Gaussian employs as a regularization function is studied and compared with singular core, Winckelman's low and high order regularization functions (Winckelmans & A., 1993). Additionally, Gauss, high and low order algebraic regularization functions $\zeta(\rho)$and their corresponding $G(\rho)$ and $q(\rho)$ functions are presented with Table 4.1.

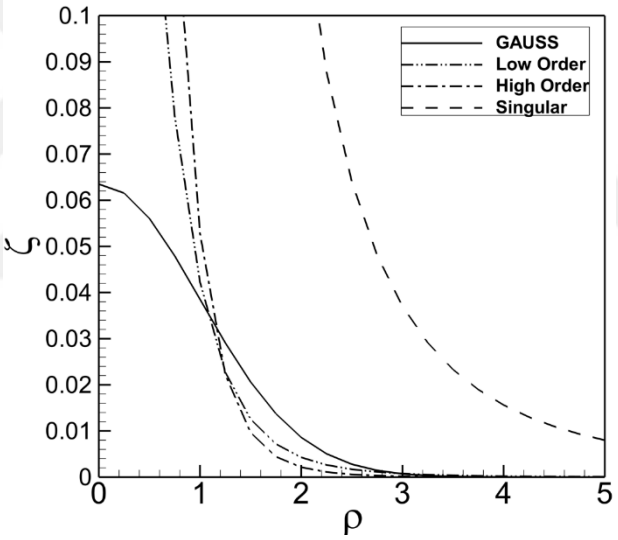

Figure 4.2 Regularization functions

Table 4.1 Biot-Savart Kernel regularization functions

Type	$\boldsymbol{\zeta(\rho)}$	
Gauss	$\frac{1}{4\pi}\left(\frac{2}{\pi}\right)^{1/2} e^{-\rho^2/2}$	
Low Order	$\frac{3}{4\pi(\rho^2+1)^{5/2}}$	
High Order	$\frac{15/2}{4\pi(\rho^2+1)^{7/2}}$	
Type	$\boldsymbol{G(\rho)}$	
Gauss	$\frac{1}{4\pi\rho} erf\left(\frac{\rho}{\sqrt{2}}\right)$	
Low Order	$\frac{1}{4\pi\sqrt{(\rho^2+1)}}$	
High Order	$\frac{(\rho^2+3/2)}{4\pi(\rho^2+1)^{3/2}}$	
Type	$\boldsymbol{q(\rho)}$	
Gauss	$\frac{1}{4\pi}\left(erf\left(\frac{\rho}{\sqrt{2}}\right)-\left(\frac{2}{\pi}\right)^{1/2}\rho e^{-\rho^2/2}\right)$	$G(\rho)\rho-\zeta(\rho)\rho$
Low Order	$\frac{\rho^3}{4\pi(\rho^2+1)^{3/2}}$	
High Order	$\frac{\rho^3\left(\rho^2+5/2\right)}{4\pi(\rho^2+1)^{5/2}}$	

Having regularized the Biot-Savart Kernel, particle convection and vortex strength vector with diffusion and vortex stretching through equation (16).

$$\frac{dx}{dt} = u_\sigma(x,t) \quad and \quad \frac{d\alpha}{dt} = \nabla u_\sigma \cdot \alpha + v\nabla^2\alpha \tag{16}$$

Once induction from all vortex particles are determined, convection term (left) in equation (16) is solved with an Adams-Moulton scheme given in equation (17) Herier (Hairer et al., 1993) .

$$y_{n+2} = y_{n+1} + h\left({}^{5}/_{12}\, f(t_{n+2}, y_{n+2}) + {}^{8}/_{12}\, f(t_{n+1}, y_{n+1}) - {}^{1}/_{12}\, f(t_n, y_n)\right) \tag{17}$$

For the convection term, y is the position of the particle, x and f is the velocity vector of the particle, $u(x,t)$. Then the Adams-Moulton scheme for particle convection becomes equation (18) with initial conditions $u_0, u_{-1} = 0$

$$x_{t+1} = x_t + dt\left(\frac{5}{12}u_{t+1} + \frac{8}{12}u_t - \frac{1}{12}u_{t-1}\right) \tag{18}$$

Now, going back to equation (16), i.e. the governing equation for the vortex dynamics, the first term in the diffusion equation $\nabla u_\sigma \cdot \alpha$ is the vortex stretching term which describes vortex lengthening due to velocity gradient in three dimensional flows. Due to conservation of angular momentum, the vorticity strength increases in parallel with the stretching direction.

Utilizing the classical scheme, the vortex stretching is handled through directly multiplying the velocity gradient with particle vorticity. Now, the vorticity time derivative due to vortex stretching is defined through velocity gradient with equation (19).

$$\left(\frac{d\vec{\alpha}^p}{dt}\right)_{Stretching} = \alpha^p \cdot \nabla\vec{u} = \alpha_i^p \frac{\partial u_i}{\partial x_i} \tag{19}$$

where superscript p represents the particle index. Note that, the vector variables are now written with subscript i in vector indices for ease of mathematical representation. Remembering that $u^p(x,t) = \sum_{p=1}^{N} \nabla(G(\vec{x} - \vec{x}^p)) \times \alpha^p$, the vortex stretching of a particle due to all other vortex particles in the domain is written in vectoral indices form as equation (20).

$$\frac{d\alpha_i{}^p}{dt} = \alpha_i^p \frac{\partial}{\partial x_i}\left[\sum_{q=1}^{N} \varepsilon_{ijk} \frac{\partial}{\partial x_j} G_\sigma(\vec{x}^p - \vec{x}^q)\alpha_k^q\right] \tag{20}$$

Recalling from Appendix A the relations given with equations (21), (22) and (23),

$$\rho = \frac{|\vec{x}|}{\sigma} \tag{21}$$

$$\frac{\partial \rho}{\partial x_i} = \frac{x_i}{\sigma^2}\rho \tag{22}$$

$$-\left(\frac{1}{\rho}\right)\left(\frac{dG}{d\rho}\right) = \frac{q(\rho)}{\rho^3} \tag{23}$$

The Laplacian of the Greens function, $\frac{\partial}{\partial x_i}\frac{\partial}{\partial x_j} G_\sigma(x)$, is determined and implemented in equation (20) to determined equation (24) as (Winckelmans & A., 1993)

$$\begin{aligned}\frac{d}{dt}\alpha_i^p = \sum_{q=1}^{N} \varepsilon_{ijk} \frac{1}{\sigma^3} \alpha_i^p \alpha_k^q \Bigg[& -\frac{q(\rho)}{\rho^3}\delta_{ij} \\ & + \frac{1}{\sigma^2}\left(-\frac{1}{\rho}\frac{d}{d\rho}\left(\frac{q(\rho)}{\rho^3}\right)\right)\left(x_j^p - x_j^q\right)\left(x_i^p - x_i^q\right)\Bigg]\end{aligned} \tag{24}$$

Again recalling from Appendix A the equation (25) and implementing into equation (24),

$$-\frac{1}{\rho}\frac{d}{d\rho}\left(\frac{q(\rho)}{\rho^3}\right) = \frac{1}{\rho^2}\left(3\frac{q(\rho)}{\rho^3} - \zeta(\rho)\right) \tag{25}$$

The vortex stretching term of the diffusion model is determined as equation (26) where kernel regularization functions given with Table 4.1 are utilized to determine the numerical value.

$$\frac{d}{dt}\alpha_i^p = \sum_{q=1}^{N} \varepsilon_{ijk} \frac{1}{\sigma^3} \alpha_i^p \alpha_k^q \left[-\frac{q(\rho)}{\rho^3} \delta_{ij} + \frac{1}{\sigma^2}\frac{1}{\rho^2}\left(3\frac{q(\rho)}{\rho^3} - \zeta(\rho)\right)\left(x_j^p - x_j^q\right)\left(x_i^p - x_i^q\right)\right] \tag{26}$$

As suggested by Stock (Stock, 2007) the vortex stretching might generate high local vorticities, which produces unrealistic results and discontinuities in the flow field. This was also experienced in this study. Going back to the governing equation for vorticity change in a vortex particle with time, equation (16), the second term, $v\nabla^2\alpha$ is the viscous diffusion term. Viscous diffusion acts as a physical mechanism due to viscosity to distribute localized high vortices and is essential to be included in the governing equations. Viscous diffusion can be managed through re-distribution of the particle strength vectors, $\vec{\alpha}^p$, within other particles. From a set of viscous diffusion methods present in the literature, a commonly utilized "Particle Strength Exchange" (PSE) method is implemented (He & Zhao, 2009; Stock, 2007; Winckelmans & A., 1993; J. Zhao & He, 2012). PSE accounts for viscous diffusion through exchange of a vortex particle strength with adjacent particles over viscosity and a cut-off function $\eta_\sigma$which approximates the kernel for the heat equation. The main idea of a PSE method is the approximate the Laplace operator in the viscous diffusion governing equation with an integral in the form of equation (27).

$$\nabla^2 f(x) \cong \frac{2}{\sigma^2}\int \big(f(y) - f(x)\big)\eta_\sigma(\vec{x} - \vec{y})dy \tag{27}$$

where η_σ is defined with equation (28).

$$\eta_\sigma = \eta\left(\frac{|\vec{x}|}{\sigma}\right)\Big/_{\sigma^3} \tag{28}$$

When written in discretized form, equation (27) is transformed in equation (29).

$$\nabla^2 f(x) \cong \frac{2}{\sigma^2}\sum_{q=1}^{N}\big(f(x^q) - f(x)\big)vol^q\eta_\sigma\big(\vec{x} - \vec{x}_q\big) \tag{29}$$

When the property f is replaced with vorticity ω, equation (30) is determined as:

$$\nabla^2\omega(x) \cong \frac{2}{\sigma^2}\sum_{q=1}^{N}\left(\omega^q - \omega(x)\right)vol^q\eta_\sigma\left(\vec{x} - \vec{x}_q\right) \tag{30}$$

Then integrating over the volume vol^p of the particle p equation (31) is determined.

$$\int_{vol^p}\nabla^2\omega(x)dx \cong \frac{2}{\sigma^2}\sum_{q=1}^{N}\int_{vol^p}\left(\omega^q - \omega(x)\right)vol^q\eta_\sigma\left(\vec{x} - \vec{x}_q\right)dx \tag{31}$$

Remembering that $\alpha_i = \int_{\Omega_i}\omega_i(x)dx$, the integral is re-written as equation (32).

$$\nabla^2\alpha^p \cong \frac{2}{\sigma^2}\sum_{q=1}^{N}(\omega^q - \omega^p)vol^q vol^p\eta_\sigma\left(\vec{x}_p - \vec{x}_q\right) \tag{32}$$

Then, inserting $\alpha^q = \omega^q vol^q$ and $\alpha^p = \omega^p vol^p$ equation (33) is achieved.

$$\nabla^2\alpha^p \cong \frac{2}{\sigma^2}\sum_{q=1}^{N}(\alpha^q vol^p - \alpha^p vol^q)\eta_\sigma\left(\vec{x}_p - \vec{x}_q\right) \tag{33}$$

Inserting equation (33) into equation (16), the viscous diffusion term i.e. the second term in the formulation leads to equation (34).

$$\left(\frac{d\vec{\alpha}^p}{dt}\right)_{Viscous\ Diff.} \cong \frac{2v}{\sigma^2}\sum_{q=1}^{N}(\alpha^q vol^p - \alpha^p vol^q)\eta_\sigma\left(\vec{x}_p - \vec{x}_q\right) \tag{34}$$

Equation (34) governs the exchange of particle strength between neighbor particles based on viscosity v, cut-off (regularization function) η_σ and radius σ. PSE scheme is conservative such as the vorticity transport equation, as the vorticity loss of a particle is equal to sum of vorticity gain of other particles. Various kernels for the cut-off function $\eta_{\sigma_{ij}}$ such as high order regularizing core or Gaussian distribution have been employed in the literature. Winckelmans (Winckelmans & A., 1993) proves that when Gaussian smoothing is utilized for η_σ, formulation leads to a second-order approximation which is consistent with the approximation of $\nabla^2 f(x)$ in equation (27). Although it has not to be same kernel function, in this study, Gaussian distribution kernel is employed for consistency with the governing equation of convection.

For non-conservation of vorticity, such an approximation given with equation (35) can be used to model the decay of 3D vortex particles by reducing the effective circulation or increasing the effective radius of the particle (Stock, 2007).

$$\Gamma = \Gamma_0 \left(1 - \exp\left(\frac{-r^2}{4vt}\right)\right) \tag{35}$$

Finally, the governing equations for a viscous vortex particles method are collected and summarized in equations (36) and (37); covering convection, vortex stretching and viscous diffusion.

$$\frac{dx}{dt} = u_\sigma(x,t) = -\sum_{i=1}^{N} \frac{q_\sigma(\vec{x} - \vec{x}_i)}{|\vec{x} - \vec{x}_i|^3} (\vec{x} - \vec{x}_i) \times \alpha_i \tag{36}$$

$$\begin{aligned} \frac{d\alpha}{dt} &= \nabla u_\sigma \cdot \alpha + v\nabla^2\alpha \\ &= \sum_{q=1}^{N} \varepsilon_{ijk} \frac{1}{\sigma^3} \alpha_i^p \alpha_k^q \left[-\frac{q(\rho)}{\rho^3} \delta_{ij} \right. \\ &\quad \left. + \frac{1}{\sigma^2}\frac{1}{\rho^2}\left(3\frac{q(\rho)}{\rho^3} - \zeta(\rho)\right)\left(x_j^p - x_j^q\right)\left(x_i^p - x_i^q\right) \right] \\ &\quad + \frac{2v}{\sigma^2} \sum_{q=1}^{N} (\alpha^q vol^p - \alpha^p vol^q) \eta_\sigma\left(\vec{x}_p - \vec{x}_q\right) \end{aligned} \tag{37}$$

where the variation of the strength of a vortex particle in time is determined with the Adams-Moulton integration scheme similar to the position change, given with equation (38).

$$\alpha_{t+1}^p = \alpha_t^p + dt\left(\frac{5}{12}\frac{d\alpha_{t+1}}{dt} + \frac{8}{12}\frac{d\alpha_t}{dt} - \frac{1}{12}\frac{d\alpha_{t-1}}{dt}\right) \tag{38}$$

4.2 Rotor Dynamics

Viscous particles are released from blade trailing edge with calculated circulation strength vector at the proper time step and as they convect and diffuse together along

the downwash, it produces induced velocity at blade aerodynamic center. Then the rotor dynamics module determines spanwise load distribution and integrates what? along the blade span to determine total force and moments at hinge locations. Combined with inertial, centrifugal and gravitational forces, blade flapping and lead-lag accelerations are calculated and integrated in time for blade dynamic response. Consequently, VVPM replaces empiric/analytic induced velocity formulations i.e. inflow model of typical comprehensive modeling approach.

One of the key contributions of this thesis is to enable comprehensive modeling with VVPM for free flight trim or maneuver analysis for unconventional rotorcraft applications. Therefore, utilization of a generic rotorcraft modeling tool is essential. In this scope, VVPM is coupled with Generic Air Vehicle Model (GAVM) (Şenipek, 2017) through replacing the inflow models of rotors. GAVM performs trim analysis or time simulation for a collection of mathematical models in terms of flight dynamics, aerodynamics, propulsion, rotational dynamics and control for each rotorcraft component. GAVM is developed with an object-oriented manner, where shared library provides simulation of multiple air vehicles simultaneously in the same domain/environment. When coupled with VVPM, this feature enables to cope with interaction between multiple rotorcrafts or swarm-like operations.

Coupling with GAVM is achieved through rotor dynamics model, where motion and position of each blade element information is exchanged with aerodynamic load variation of each blade element determined with VVPM. Rotor dynamics model is the crucial intermediate step for CFD methods to be integrated into comprehensive full helicopter dynamics. Even the most basic rotor dynamics model, such as rigid blade motion, provides insight for blade in-plane and out of plane behavior at specific flight or operating condition (Majhi & Ganguli, 2008). Combining 6 DoF flight dynamics motion, relative travel and inertial accelerations of each blade element with VVPM, provides full helicopter modeling, trim analysis and steady/unsteady maneuver simulation. Through such coupling, blade spanwise aerodynamic load distribution is determined by VVPM stage whereas centrifugal and inertial accelerations/loads that each blade experiences under full helicopter free flight

motion are determined at rotor dynamics stage. As flapping and lagging motion of each blade results in relative air flow and have direct impact on aerodynamic loads, accurate solution of blade dynamic response is essential. Additionally, accurate estimation of blade response has impact on solution convergence, robustness and computational cost in time marching steady/unsteady simulations.

Each rotor blade is divided into blade elements with known geometrical properties and mass. At each time step, blade elements are oriented at proper locations in earth reference frame and aerodynamic, centrifugal, inertial and gravitational force and moments are calculated as illustrated with Figure 4.3 and Figure 4.4. Spanwise distributions are then integrated at blade root i.e. hinge location, to determine total force and moments for flapping and lagging accelerations. Aerodynamic load distribution determined with VVPM stage is utilized in rotor dynamics stage to solve blade motion, which is then utilized at VVPM stage as the time integration continues.

The solenoidal condition for vorticity, $(\nabla \cdot \omega = 0)$ suggests that bound circulation variations stem from azimuthal and spanwise load variations, generate streamwise and spanwise vortices to be shed from the lifting surface. Accordingly, the vorticity source shed into rotor wake is calculated through Kutta-Joukowski theorem given with the vorticity formulation for each blade element.

$$\omega = -\frac{d\Gamma_{bound}}{dt} + u\nabla\Gamma_{bound} \tag{39}$$

where Γ_{bound} is the bound circulation of each blade element and u is the overall relative air velocity vector.

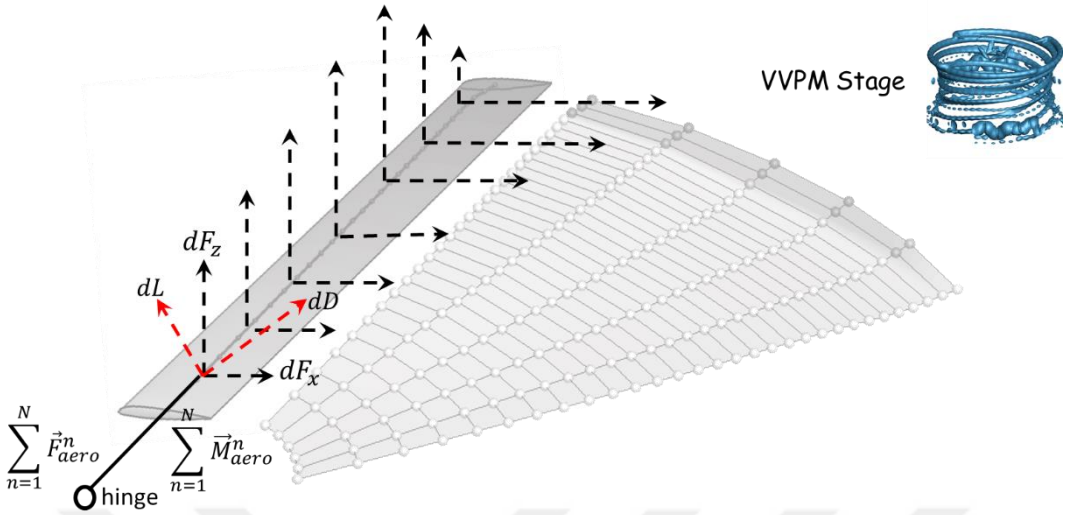

Figure 4.3 Illustration of sectional aerodynamic force and moments

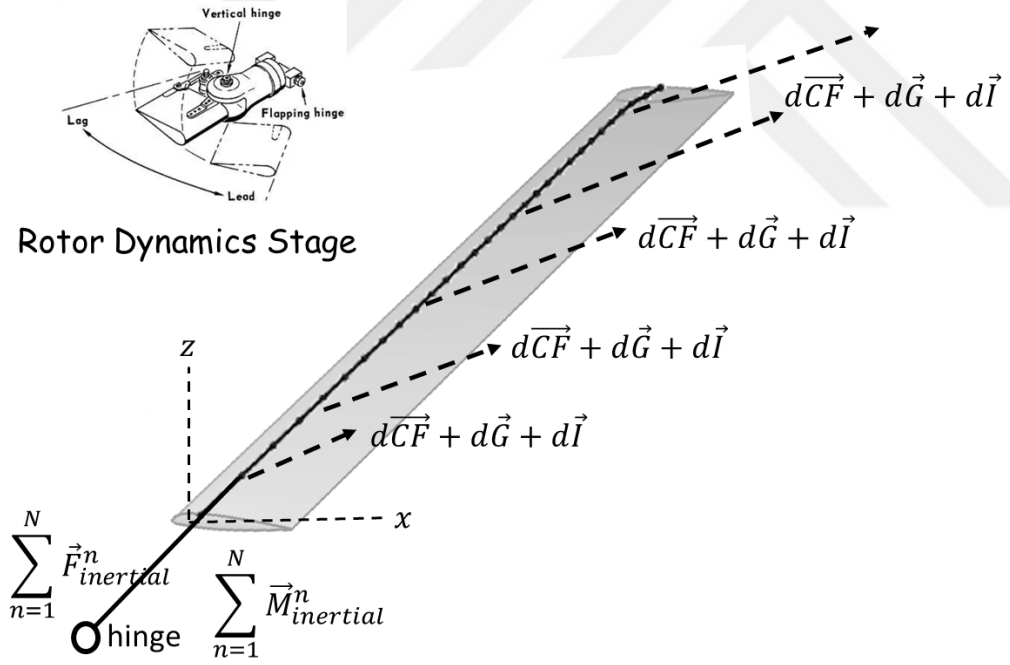

Figure 4.4 Illustration of sectional inertial force and moments

Time integration for each blade is performed to determine flap and lead-lag angles at the next time step and azimuth location. Induced velocity determined by VVPM stage at earth reference frame is transformed into blade element aerodynamic center

and reference frame at each time step through transformation matrices. Transformation matrices specific to each blade element are updated at each time step considering helicopter free flight motion, rotor hub relative motion to fuselage such as tilting mechanism of tiltrotors, blade azimuthal rotation and flapping & lagging motions around hub hinges.

Coordinate frames of interest for such a transformation are illustrated with Figure 4.5. Rotorcraft motion is defined at body reference frame oriented at center of gravity of the platform. Translational and rotational motion of the platform are then transformed into hub non-rotating reference frame considering Euler orientation of the c.g. Total air velocity vector at rotor hub is then transformed into rotating hub (shaft) frame through instantaneous azimuth angle of the reference blade. Finally, total air velocity vector each blade element experiencing is determined through transformation to blade element reference frame of each related blade segment.

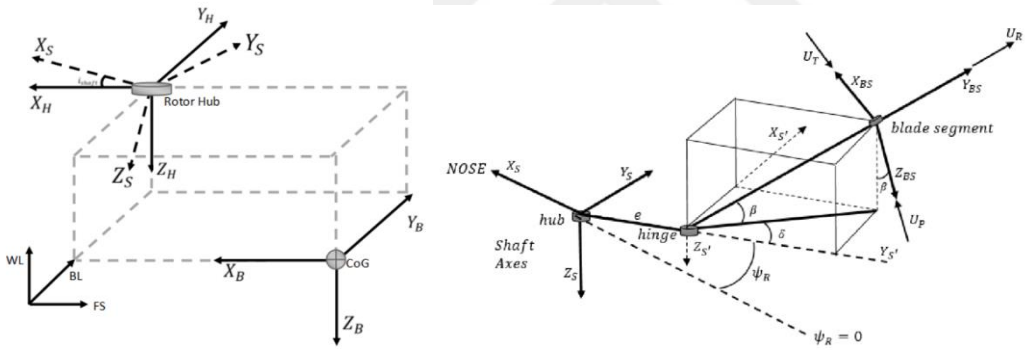

Figure 4.5 Coordinate frames (left: body and hub non rotating frames, right: hub rotating, blade and segment frames) (Şenipek, 2017)

Total transformation from vehicle carried reference frame to each blade element reference is established with equation (40).

$$\vec{V}_{BS} = R_{BS/E}\vec{V}_E = R_{BS/S'}R_{S'/S}R_{S/B}R_{\varphi}R_{\theta}R_{\phi}\vec{V}_E \qquad (40)$$

Where, R_{ϕ}, R_{θ} and R_{φ} are Euler angle transformation matrices given with equations (41), (42) and (43) , $R_{S/B}$ is transformation matrix from body reference frame to non-rotating hub reference frame given with equation (44).

$$R_{\phi} = \begin{bmatrix} cos\phi & sin\phi & 0 \\ -sin\phi & cos\phi & 0 \\ 0 & 0 & 1 \end{bmatrix} \quad (41)$$

$$R_{\theta} = \begin{bmatrix} cos\theta & 0 & -sin\theta \\ 0 & 1 & 0 \\ sin\theta & 0 & cos\theta \end{bmatrix} \quad (42)$$

$$R_{\varphi} = \begin{bmatrix} 1 & 0 & 0 \\ 0 & cos\varphi & sin\varphi \\ 0 & -sin\varphi & cos\varphi \end{bmatrix} \quad (43)$$

$$R_{S/B} = \begin{bmatrix} \cos i_{\theta} & 0 & -\sin i_{\theta} \\ \sin i_{\theta} \sin i_{\phi} & \cos i_{\phi} & \cos i_{\theta} \sin i_{\phi} \\ \sin i_{\theta} \cos i_{\phi} & -\sin i_{\phi} & \cos i_{\theta} \cos i_{\phi} \end{bmatrix} \quad (44)$$

Non-rotating to rotating shaft frame transformation is performed with instantaneous azimuth angle of the reference blade utilizing $R_{S'/S}$ matrix given with equation (45).

$$R_{S'/S} = \begin{bmatrix} sin\psi & cos\psi & 0 \\ -cos\psi & sin\psi & 0 \\ 0 & 0 & 1 \end{bmatrix} \quad (45)$$

Finally, $R_{BS/S'}$ transformation matrix given with equation (46) specific to each blade segment containing blade flapping, lead-lag and pitch angle information is utilized to determine total air velocity vector at aerodynamic center of each blade segment.

$$R_{BS/S'} = \begin{bmatrix} cos\theta & 0 & -sin\theta \\ 0 & 1 & 0 \\ sin\theta & 0 & cos\theta \end{bmatrix} \begin{bmatrix} cos\delta & sin\delta & 0 \\ -sin\delta & cos\delta & 0 \\ 0 & 0 & 1 \end{bmatrix} \begin{bmatrix} 1 & 0 & 0 \\ 0 & cos\beta & -sin\beta \\ 0 & sin\beta & cos\beta \end{bmatrix} \quad (46)$$

VVPM induced air velocity at each blade element aerodynamic center at each time step is determined at earth frame, then superimposed with rotorcraft flight velocity vector, wind velocity vector and relative airspeeds oriented rotational motion of the rotorcraft. Total air velocity vector is then utilized to calculate local effective angle of attack and Mach number for 2-D aerodynamic look-up tables. When total transformation matrix for each blade element from earth reference frame to blade

element reference frame is constituted, the only remaining unknowns are blade angles such as flap, lead-lag and pitch which represent the blade dynamics.

Those angles are determined from time integration of angle rates which are calculated through force-moment balance around related hub hinges. Aerodynamic loads, centrifugal forces, inertial accelerations arise from free flight translational and rotational motion of the rotorcraft and gravitational accelerations are calculated for each blade element, integrated up to the hinge to solve Newton's second law for each individual blade.

4.3 Trim

There exists two basic trim options, namely isolated rotor trim or wind tunnel trim and full rotorcraft free flight trim. Both trim approaches operate over the same principles. A state matrix is generated utilizing variables and outputs or targets. Derivative of the state matrix is taken to obtain the trim Jacobian which is then utilized in Newton optimization, iterating variables to reach targets. Isolated rotor trim is performed with the rotor specific targets such as thrust, torque, roll & pitch moments or total force vector and rotor specific variables such as control inputs i.e. collective & cyclic, rotational speed, shaft tilt angle etc. Free flight trim on the other hand considers 6 DoF motion of the rotorcraft configuration and is performed with platform specific targets such as flight condition or maneuver description and platform specific variables such as pilot controls, Euler angles, translational & rotational accelerations. Although essentials are same for both options, free flight trim is handled through the comprehensive mathematical model.

This chapter covers isolated rotor trim.Full rotorcraft free flight trim is mentioned at comprehensive mathematical model chapter, yet the essentials of isolated rotor trim such as individual blade – multi blade transformations and filtering mechanisms are similar. On the other hand, it is experienced that the trim Jacobian consisting of the relation between targets and variables obtained with comprehensive mathematical

model consisting of lower fidelity inflow model instead of VVPM is generally sufficient to achieve isolated rotor trim. This is evaluated to be originated from the fact that trim dynamics is much faster than induced velocity and wake dynamics as the aerodynamic loads over the blade are varying instantaneously with a control input change, whereas induced velocity and wake responses with a lag. Moreover, at each time step of the VVPM which is significantly smaller than the rotor period, the trim update is performed, resulting in a slow sweep in trim direction. Therefore, it is sufficient for the Jacobian to direct to the minimum search direction independent from the magnitude. Nevertheless, in terms of computational effort, it is always better to tune the Jacobian determined with simplified models to operate over the higher fidelity models, as re-generation of the Jacobian generally requires higher computational burden.

A trim can be defined as a rotor state where all the outputs i.e. rotor and blade responses, are periodic and not changing with time. When integrated parameters such as thrust, propulsive force, roll & pitch moments, torque etc. are considered, it is easier to decide whether a rotor is at its trim state or not, through time derivative. However, when parameters that are varying with azimuth angle are considered, such as flapping angle, lead-lag angle which are specific to each blade, as they are already time dependent, velocity or acceleration of those parameters would implicitly display trim state.

At this point, individual blade coordinate (IBC) to multi blade coordinate (MBC) transformation provides harmonic representation of blade specific parameters, so that it represents dynamic response of whole rotor system. In fact, whether it is rotor analysis or comprehensive modeling, rotor responds as all integrated together to inputs, platform motion or external excitations such as gust (Johnson, 2013b). Chasing trim state through harmonic variables assures rotor system trim and simplifies rotor motion representation. Utilization of multi-blade coordinates also provides a clear description of the TPP dynamics, which assures both integrated and periodic parameter trim when it is balanced.

Each blade has its own aerodynamic and inertial load distribution resulting in a harmonic response for a steady state or non-harmonic response for a transient operating condition. An appropriate representation of the blade motion can be performed though Fourier series and the degrees of freedom that represent the rotor response in non-rotating frame is described as multi-blade coordinates.

Considering N bladed rotor system, any dynamic property (most generalized form) can be described in MBC instead of IBC through equations (47), (48), (49) and (50).

$$Q_0 = \frac{1}{N}\sum_{m=1}^{N} Q^{(m)} \tag{47}$$

$$Q_{nc} = \frac{2}{N}\sum_{m=1}^{N} Q^{(m)} cos\ n\varphi_m \tag{48}$$

$$Q_{ns} = \frac{2}{N}\sum_{m=1}^{N} Q^{(m)} \sin n\,\varphi_m \tag{49}$$

$$Q_{N/2} = \frac{1}{N}\sum_{m=1}^{N} Q^{(m)}(-1)^m \tag{50}$$

where m stands for each of the individual blade and φ_m is the incorporated azimuth angle. When MBC is applied to flapping angles, tip path plane angles (TPP) $\beta_0, \beta_{1c}, \beta_{1s}$ and their rates $\dot{\beta}_0, \dot{\beta}_{1c}, \dot{\beta}_{1s}$ can be determined. Then the trim algorithm seeks for zero TPP rates, which represents the steady condition or rotor trim.

On the other hand, the periodic nature of the rotor system causes periodic oscillations on integrated parameters such as force and moments which are out of the IBC to MBC transformation scope. Those force and moments are generally integrated single valued targets for a rotor system both at isolated and full rotorcraft free flight trim. A moving average filter is applied on such parameters to determine mean response that is flowing to the fuselage through rotor shaft to be used in trim calculations. The

oscillatory terms are excluded in trim calculations as they are considered as vibratory loads and not altering flight dynamics of the whole rotorcraft configuration. Illustration of such filtering is depicted at Figure 4.6.

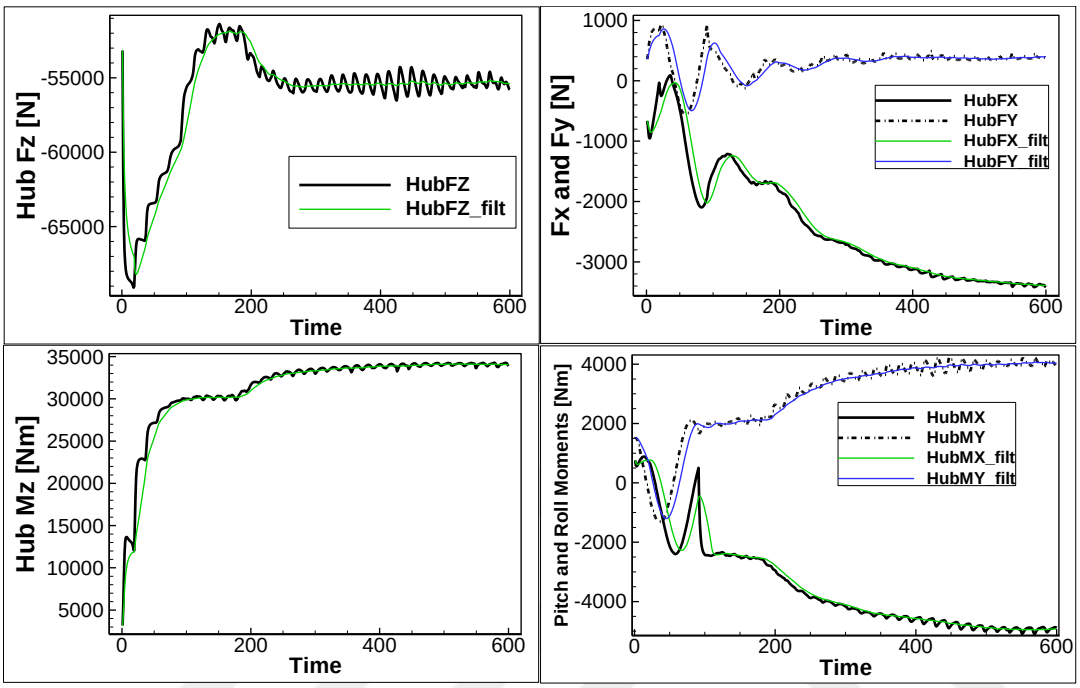

Figure 4.6 Filtering for rotor hub force and moments

After IBC to MBC transformation and filtering of the integrated parameters, the rotor system is defined as a state space model with inputs, states and outputs representations. When the rotor system is represented with a state space model, the relationship between inputs, states and outputs can easily be defined through the state matrix inverse of which would result in the Jacobian matrix. As the basic principles of state space approach are same for isolated rotor and full rotorcraft configuration, same trim algorithm is utilized for both. For more information on the state space representation, Newton algorithm and trim iteration, one can refer to comprehensive mathematical model trim chapter, Chapter 6.1.1.

4.4 Validation

The VVPM model intends to estimate rotor total integrated force and moments, inflow and wake dynamics and solution of unconventional configurations. Therefore, various validation studies with different purposes are performed with test data present in the literature and benchmark analysis tools where available. Whirl tower test data is utilized to compare rotor total thrust to torque variation throughout the control margin, commercial CFD is utilized to compare with vortices trajectory, instrumented wind tunnel test cases are utilized to compare spanwise load variations at hover and forward flight and PIV test data is utilized to compare inflow distribution along the blade span. Then co-axial wind tunnel test comparison is performed to assess capability to model unconventional configurations.

Total thrust to torque validation of the developed tool is performed with S76 main rotor tested at NASA Ames 40x80, 80x120 Wind Tunnels and Sikorsky Whirl Tower (Jepson et al., 1983; Johnson, 1980; Shinoda, 1996). Non-dimensional thrust to torque variation for the four-bladed main rotor with 205m/s tip speed, 0.393m nominal chord, swept tip and SC1095 & SC1095R8 airfoils are determined with VVPM and compared with the test data. Blades were discretized into 30 aerodynamic segments and 7.5 deg of rotor azimuth step is utilized. Comparisons are performed for varying collective angles without cyclic inputs. Total thrust and torque coefficient variations are calculated and normalized with solidity. Comparison of VVPM results with three set of test data is given at Figure 4.7. Analyses are performed at least for six revolutions at each collective set angle and convergence of thrust and torque are checked. Convergence history, wake geometry and vorticity field for a sample case (10 deg collective) are depicted with Figure 4.8. Wake geometry is illustrated per revolution up to six full revolutions and vorticity field is determined at zero deg azimuth section for fully converged solution.

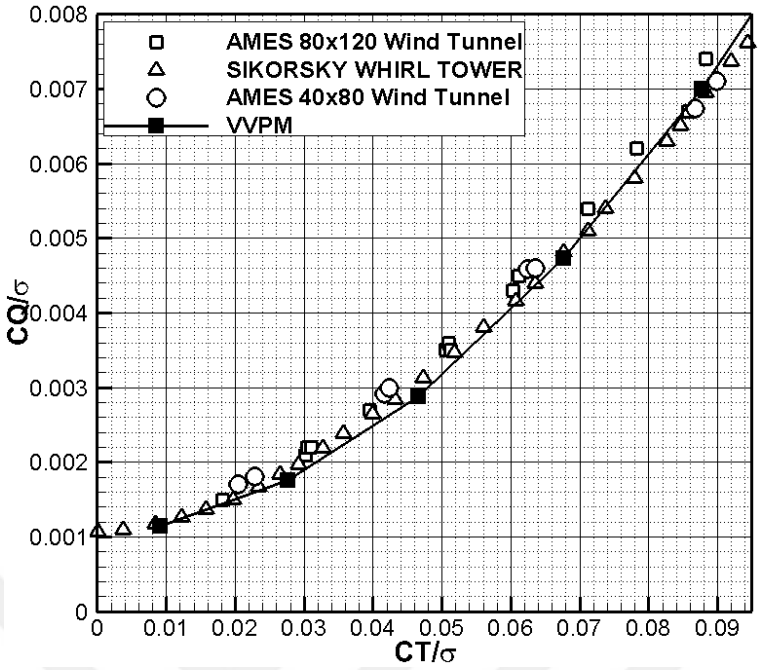

Figure 4.7 Thrust&torque test and analysis comparison for S76 main rotor

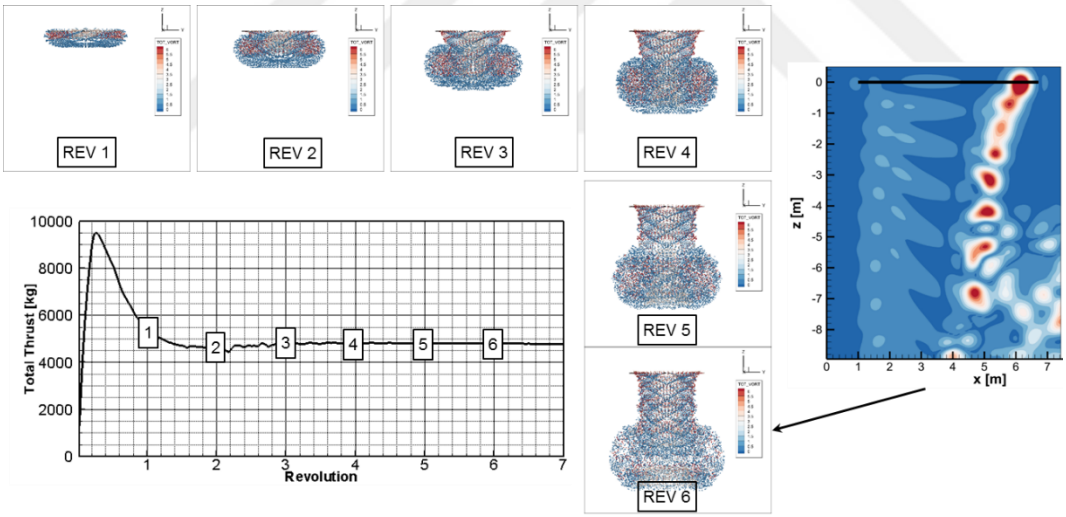

Figure 4.8 Convergence, wake evolution and vorticity field for sample case (10deg collective)

Tip vortices trajectory comparison is performed with commercial StarCCM+ flow solver for two different mesh resolution, i.e. 5% and 20% of tip chord, from Güngör's study (Güngör, 2019). Results are compared with VVPM for 48 azimuth steps corresponding to 125% tip chord in terms of vorticity contours and tip vortex

convection and results are presented in Figure 4.9. Güngör indicates that the time required for the convergence of the simulations with 128 cores for both mesh resolution is 11h 20min and 2h 20 min, excluding meshing time. The VVPM performs eight revolutions, (convergence achieved within six revolutions) in around one hour at single core. In terms of computational cost, per core execution times are 1400hrs and 280hrs with commercial CFD to 1 hour with VVPM respectively

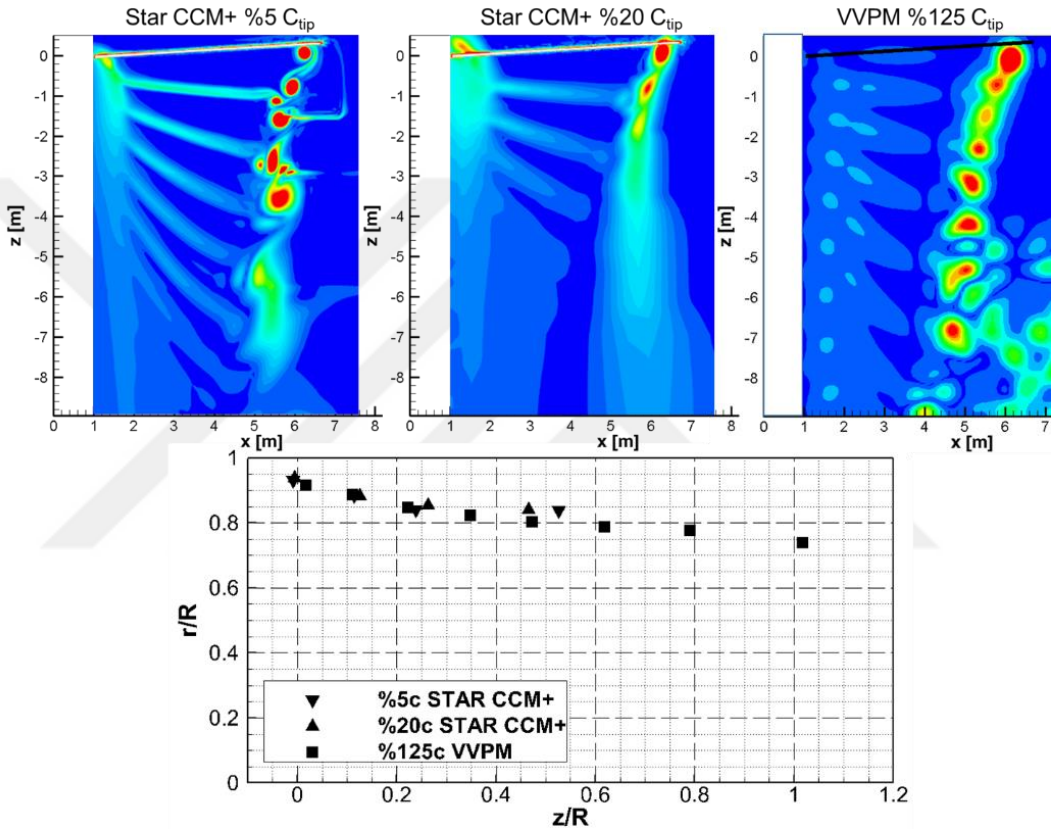

Figure 4.9 Vorticity contour and tip vortex trajectory comparison with commercial CFD

It is observed that with decrease in mesh resolution from 5% to 20% of tip chord, numerical dissipation dominates the downwash, damping the strong tip vortex within not more than 0.5 rotor revolution. On the other hand, even with a time step corresponding to 125% of tip chord which is relatively large but sufficient enough to capture total thrust and torque characteristics of a rotor, Lagrangian method

(VVPM) provides numerical dissipation free solution while still taking viscous diffusion into account.

Further comparison with test data, CFD and free-wake based commercial tools is performed with the well-known Caradonna-Tung (Caradonna et al., 1980) test case. Test model is a two bladed rotor with untwisted and constant chord blades with NACA 0012 airfoil. Rotor radius and chord are 1.143m and 0.191m as depicted with Figure 4.10.

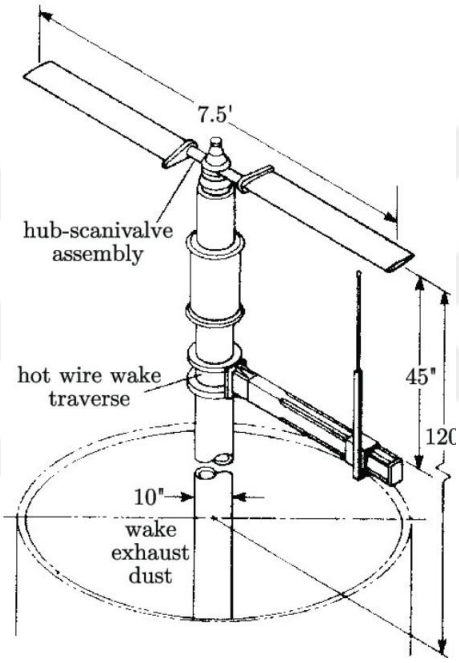

Figure 4.10 Caradonna-Tung Test Case (Caradonna et al., 1980)

Test condition:1250 rpm is analyzed, and results are compared with test data, Hybrid CFD analyses (Joulain et al., 2017) and commercial free wake codes CAMRADII and CHARM. Commercial free wake codes are operated at their default/suggested parameter configurations for wake geometry, tip vortex core dimensions, near and far wake designations of a scaled rotor. At trimmed thrust, spanwise loading and lift coefficient variations are compared at Figure 4.11 and Figure 4.12.

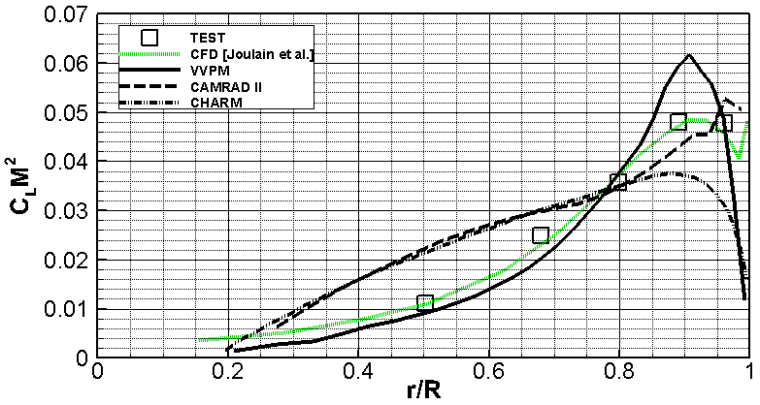

Figure 4.11 Spanwise load distribution comparison between VVPM, CAMRAD, CHARM, CFD and Test data

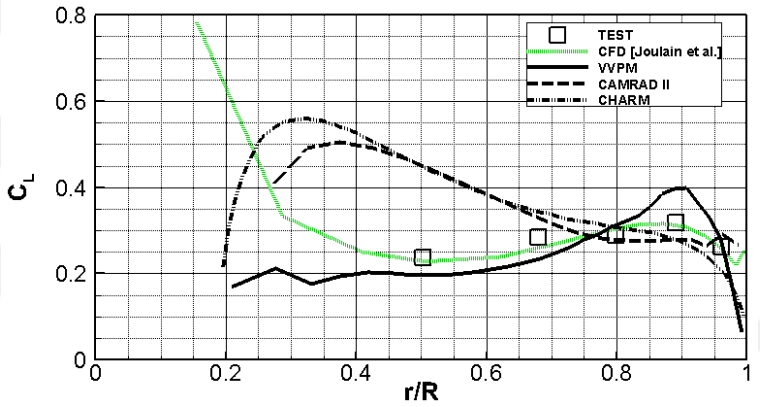

Figure 4.12 Spanwise lift coefficient comparison between VVPM, CAMRAD, CHARM, CFD and Test data

It is observed that the effect of three-dimensional flow on profile lift coefficient is significant at tip and root regions as expected. Therefore, methods using 2-D airfoil look-up approach deviates from test and 3-D CFD analyses specifically at tip and root regions. When assessed in terms of load distribution, as lift coefficient is normalized by Mach square, results overlap with test data until 95% of the span where 3-D effects become dominant. VVPM results are comparably consistent with CFD and test data, possess significant improvement over free wake-based methods in terms of spanwise load, and lift coefficient distributions.

Flow field comparisons are further continued with Ramasamy's (Ramasamy et al., 2010) PIV tests performed with untwisted blades for the high blade loading case.

Aerodynamic performance and time-average inflow measurements are compared. Model and test parameters as well as test versus VVPM aerodynamic performance comparison is presented with Figure 4.13. Correction for Reynolds effect is performed by increasing the drag coefficient by 0.014 as suggested in (Ramasamy et al., 2010)

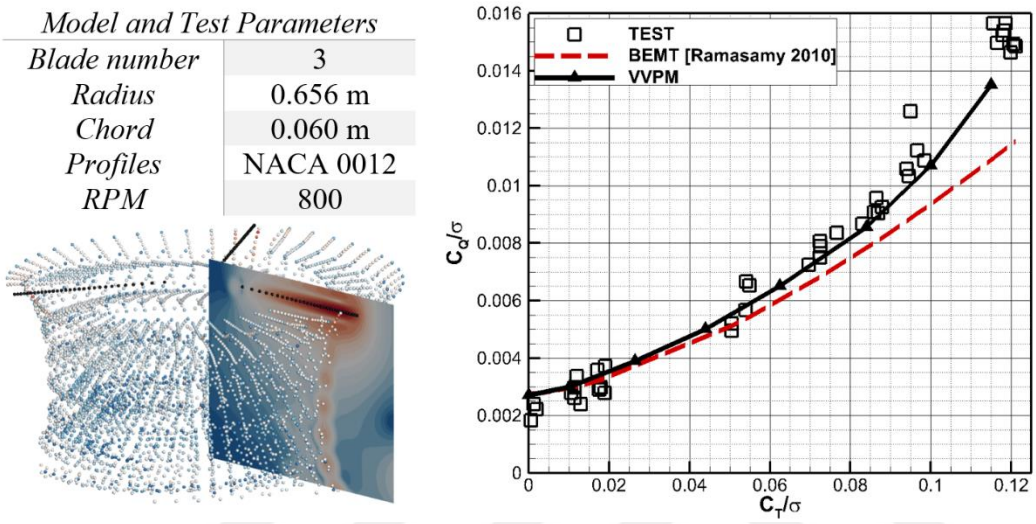

Figure 4.13 Model and test parameters (left); performance comparisons (right)

It is observed that although the airloads model is scale dependent, wake modeling and dynamics are independent from the model scale. Time averaged measured spanwise velocities at planes just above and below the rotor disc are compared with time averaged flow determined with VVPM. Time averaged or mean inflow is calculated through recording total air velocity at each spanwise location fixed in a single azimuth angle just above the rotor plane as illustrated with Figure 4.14.

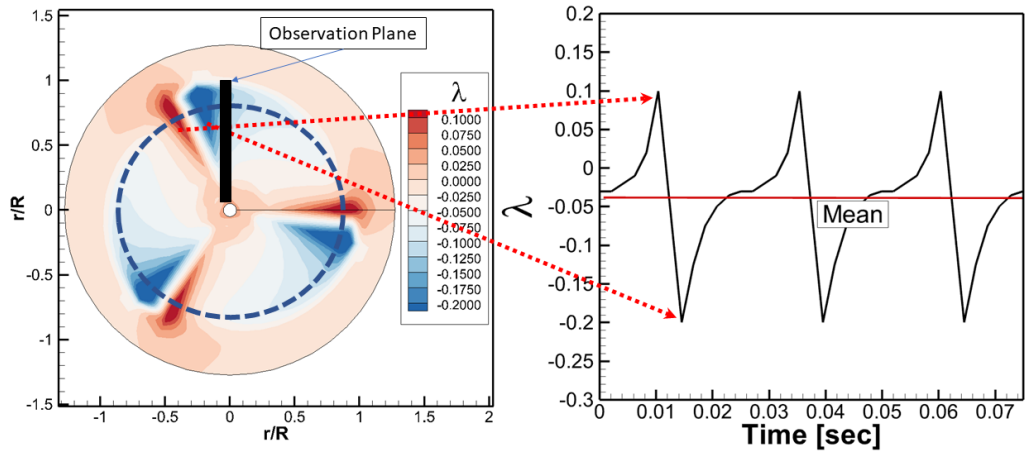

Figure 4.14 Flow variation (just above rotor plane) in time and its mean for a specific spanwise location

Recorded total air velocity is then non-dimensionalized with rotor tip speed and averaged to determine mean spanwise inflow distribution. Test comparison is presented with Figure 4.15.

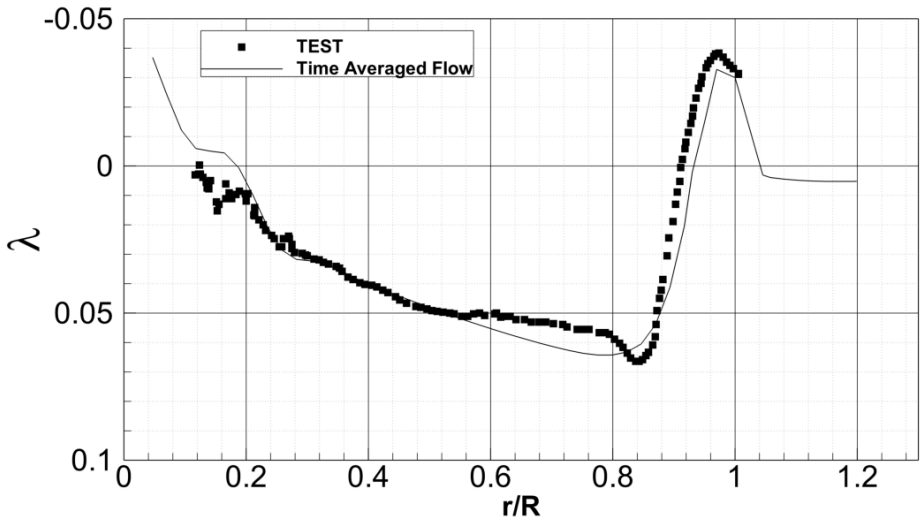

Figure 4.15 Mean inflow distribution Test (PIV) vs VVPM comparison

Forward flight modeling capability of the developed VVPM tool is explored through comparisons with S76 main rotor wind tunnel and HART-II wind tunnel test data. Full-scale S76 main rotor wind tunnel tests specified in Shinoda's work (Shinoda, 1996) are utilized to study rotor aerodynamic performance comparisons. Tests were performed with wind tunnel trim where only steady flapping exists. VVPM and

CAMRADII analyses are performed for wind speeds up to 0.25 advance ratio with the specified inputs at Table 4.2.

Table 4.2 S76 Wind Tunnel Forward Flight Trim Parameters (Shinoda, 1996)

μ	θ_0	θ_{1c}	θ_{1s}	β_0
0.01	10.3	-0.3	0.3	4.6
0.03	9.8	-1.4	0.7	5
0.06	8.3	-3.0	1.5	4.9
0.10	6.7	-2.7	2.2	5
0.15	5.9	-2	3.1	5.1
0.20	5.6	-1.6	3.8	5.1
0.25	5.8	-1.2	4.8	5.1

CAMRAD II analyses are performed with free wake option tuned specifically for the test model and comparison results are presented in Figure 4.16.

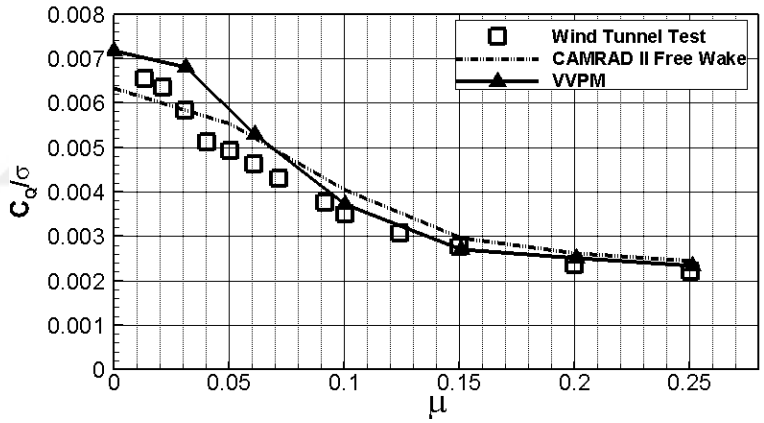

Figure 4.16 S76 Wind tunnel test versus CAMRAD II and VVPM comparison

Over 0.1 advance ratio, analyses' results overlap with wind tunnel data. Below 0.1 advance ratio, it is evaluated that, wall effect inside the wind tunnel increases the thrust levels; therefore, same trim condition is achieved with lower required power during tests. Zero longitudinal flapping eventually lead rotor to be prone to excessive blade vortex interaction as observable from Figure 4.17. The induced velocity distribution over the rotor disc reveals the blade vortex interaction-initiated fluctuations in both total thrust and torque variations over time. Blade-wake and wake-wake interactions are observable from the sample simulation illustrated with

Figure 4.17. A cut-off in terms of vorticity magnitude is employed in the illustrations to decrease the complexity in visualization of the wake structure.

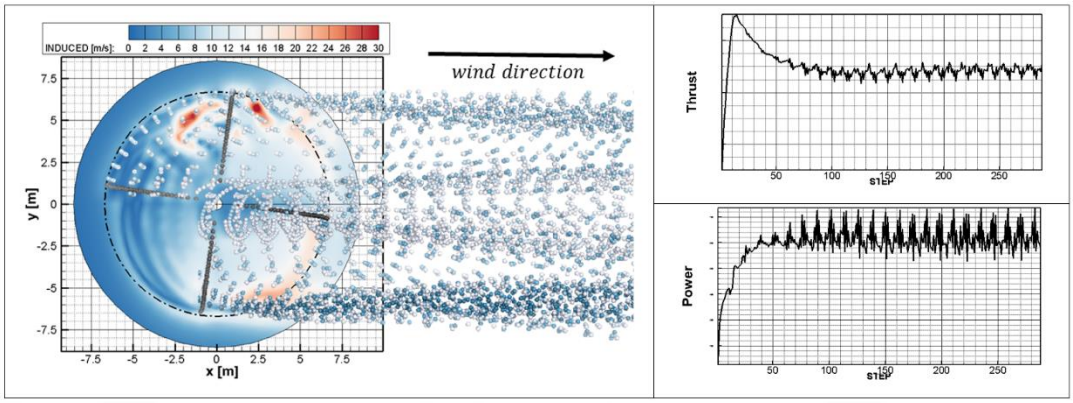

Figure 4.17 Induced velocity contour, wake structure, thrust and torque oscillations for 0.2 advance ratio

Further comparison in terms of rotor loads at forward flight is performed with HART-II wind tunnel test case (Wall, 2003). Analysis is performed for baseline rotor at 0.15 advance ratio and thrust coefficient of 0.0044, trimmed for zero hub moments with 5.3° shaft tilt. An effective shaft tilt of 4.3° is utilized in the analysis to incorporate wind tunnel wall effects on freestream at rotor location. Test model is a four bladed rigid rotor with 2-meter radius, -8° linear twist rotating at 1041 rpm. Root-cut-out is %22 and NACA23012 airfoils are employed throughout the span. Rotor normal load azimuth-wise variation specifically at section %85 span test vs analysis comparison is presented at Figure 4.18. Analysis is performed with rigid blade model, and it would be useful to re-perform with elastic blade model when implemented into the VVPM.

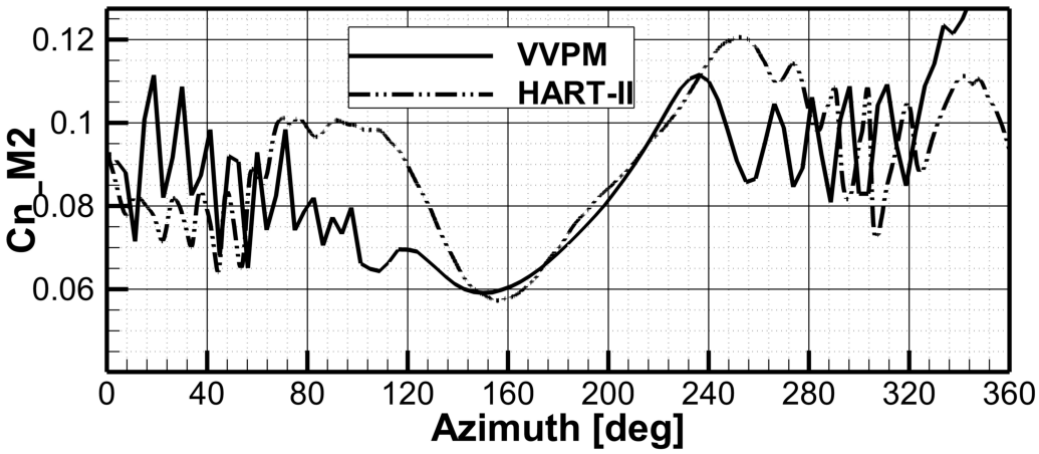

Figure 4.18 HART-II test case rotor load comparison at section r/R=0.85

Further validation study is performed with unconventional configuration, lift offset rotor and wind tunnel test data (DENG et al., 2019). In this scope, coaxial test case given in Table 4.3, is modeled for hover case and torque trim is performed for full collective range.

Table 4.3 Co-axial test model rotor parameters

Parameter	Value
Radius [m]	2
Blade Number	4
Root cut out [%]	30
Rotational Speed [rpm]	778
Separation distance[m]	0.3
Chord length [m]	0.3

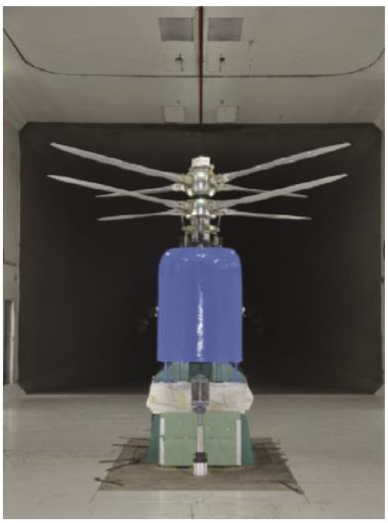

Analyses are performed with 5° azimuth steps (time steps) for 9 revolutions. Convergence is monitored for trim as illustrated with Figure 4.19.

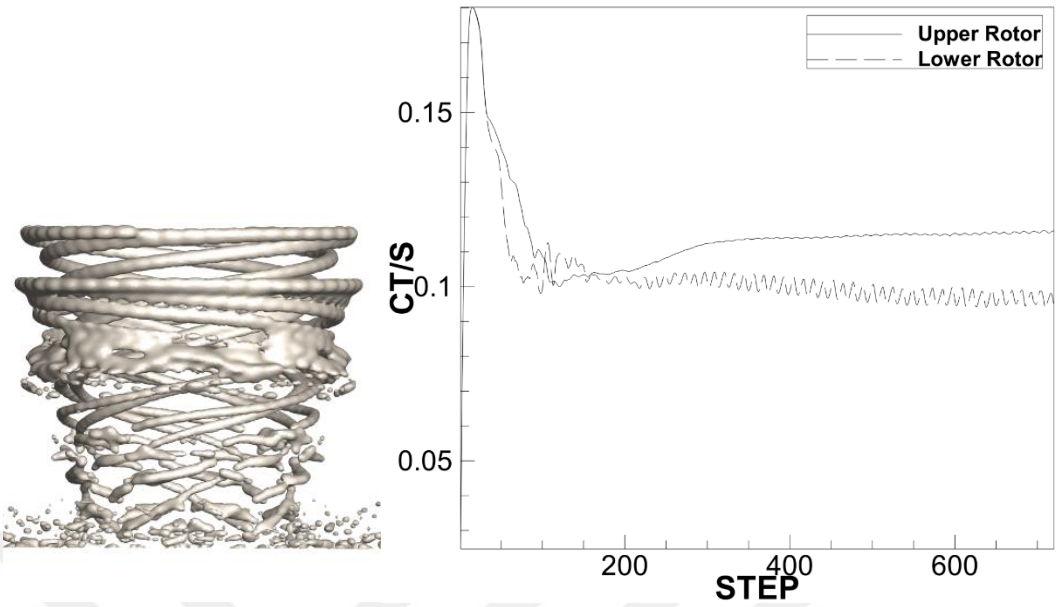

Figure 4.19 Sample co-axial rotor vorticity iso-surface and thrust convergence

Thrust levels at each torque setting is determined separately for upper and lower rotor and then compared with test data. Results are plotted over test data as depicted in Figure 4.20. It is observed that, developed VVPM tool is capable of accurately modeling co-axial rotors in terms of overall aerodynamic performance.

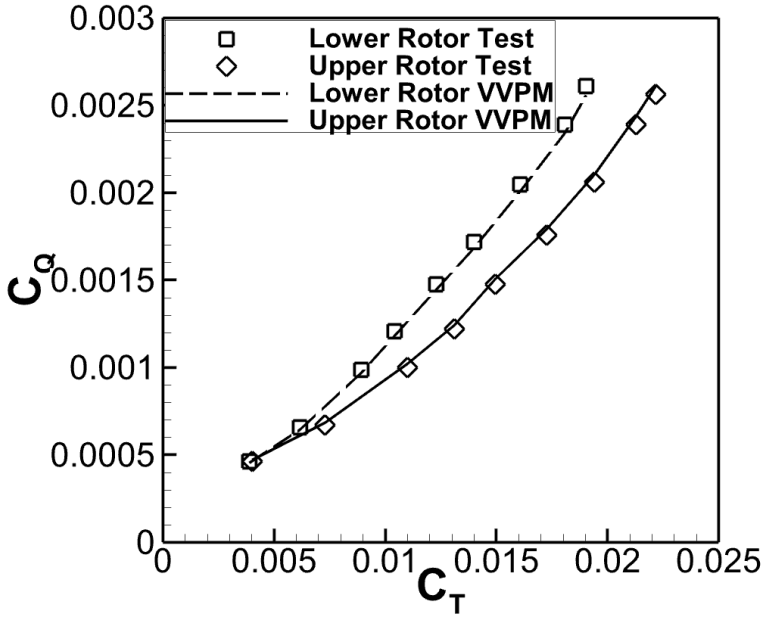

Figure 4.20 Co-axial rotor aerodynamic performance test comparison

4.5 Further Qualitative Assessment/Exploration

Having compared with test data, wake, and rotor loads estimation capabilities of VVPM for unconventional configurations are further studied with full helicopter trim option. In this scope, main rotor – tail rotor interaction, co-axial, intermeshing, and tilting proprotor configurations are modeled for hover and forward flight conditions. It is evaluated that, rotor-rotor, wake-wake and blade vortex interactions as well as dynamic behavior of rotor wakes are well-captured with unsteady fashion. Some of the results in terms of wake geometry, rotor loads and vorticity fields including iso-surfaces and streamlines are presented to illustrate the potential of VVPM for rotorcraft applications. Additionally, as VVPM is capable of calculating total air velocity vector at any location in the domain, it is very appropriate to study rotor-fuselage interaction. A sample illustration for rotor-fuselage interaction with VVPM is given in Appendix E.

4.5.1 Main Rotor – Tail Rotor Interaction

Aerodynamic interaction between main and tail for a conventional helicopter configuration can have a significant effect on tail rotor effectiveness, overall aerodynamic performance, loads, controllability, stability, and handling quality. As Fletcher (Fletcher & Brown, 2010) discusses; main-tail rotor interaction poses one of the most significant interaction phenomena, which may have a strong negative effect on total payload capability, flight loads and vibration. Furthermore, the unsteady interaction varying with flight condition might alter aerodynamic noise characteristics of the whole system through blade vortex interaction (BVI) or rotor load variation.

The interaction between main and tail rotor exhibits different characteristics according to configuration, alignment, orientation, and flight condition. Furthermore, as the author discusses in his previous study (Yücekayali & Ortakaya, 2019), distinct performance and load characteristics will be experienced depending

on position, direction of rotation of the tail rotor, sideward left and right flight conditions as well as weight and forward speed of the helicopter.

In order to assess the developed methodology in terms of solution of the main rotor - tail rotor interaction, quartering flight (strongest interaction is anticipated) simulations are performed with full rotorcraft trim, and qualitative evaluations are performed to discuss the capability and fidelity of the developed tool.

A typical 5-ton class conventional configuration helicopter with 4 bladed, CCW rotating main and 4 bladed tractor type tail rotor, is trimmed low speed quartering flight condition. Vorticity iso-surface colored with total air speed and vortex particles colored with particle strengths are illustrated in Figure 4.21.

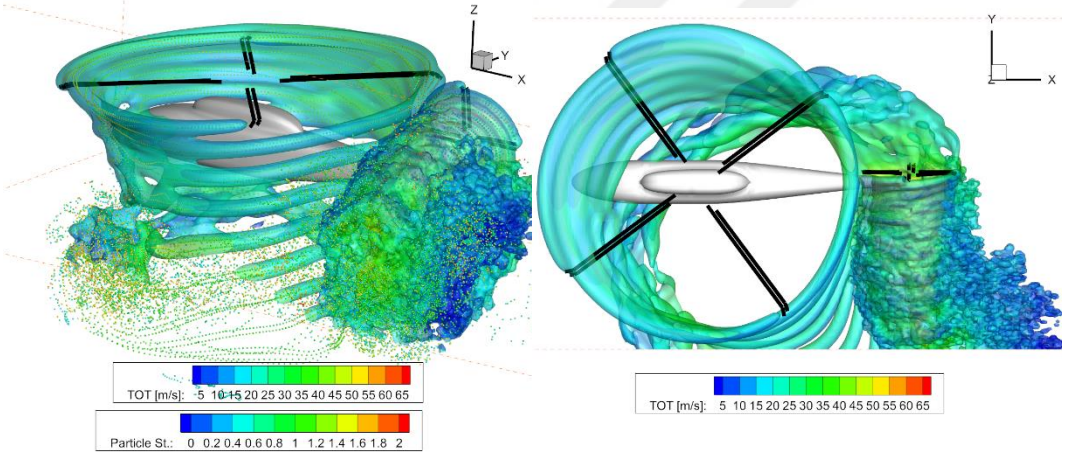

Figure 4.21 Vorticity iso-surface and particle distributions for quartering flight

Vorticity contour on a plane passing through the center of the tail rotor including vorticity iso-surfaces colored with total air speed is illustrated in Figure 4.22. Additionally, in-plane and off-plane vorticity contours are illustrated in Figure 4.23.

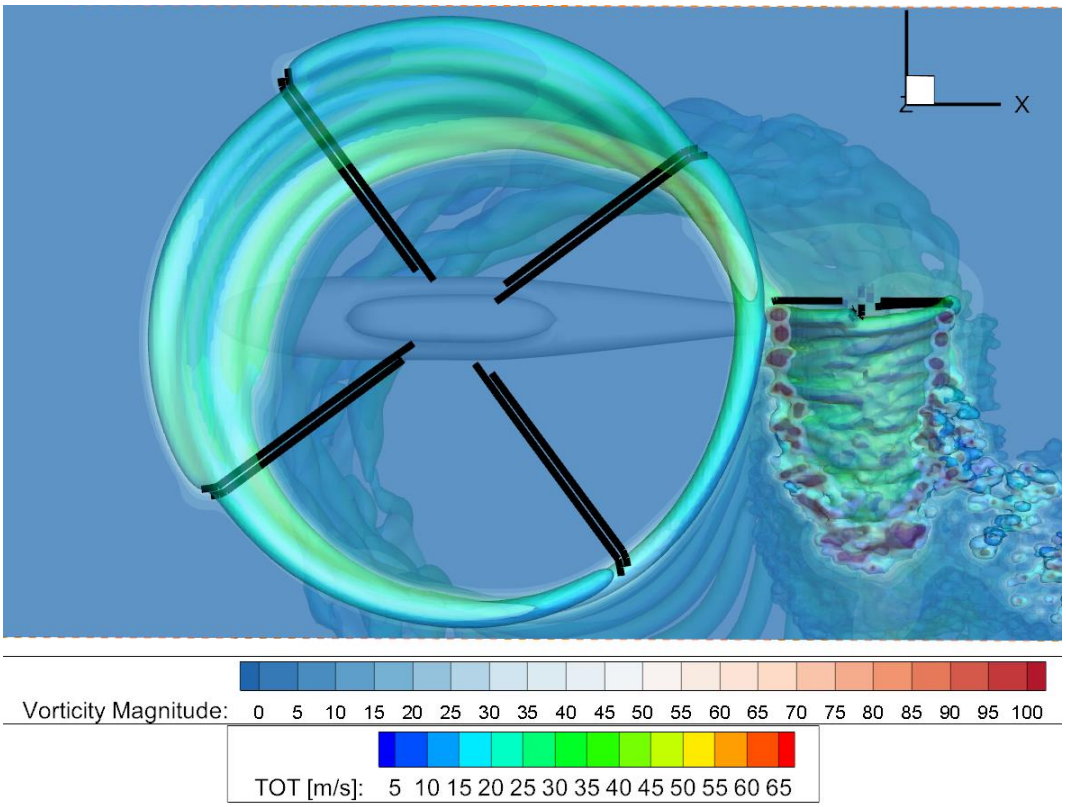

Figure 4.22 Vorticity iso surface and vorticity contour at a plane passing from the center of the tail rotor

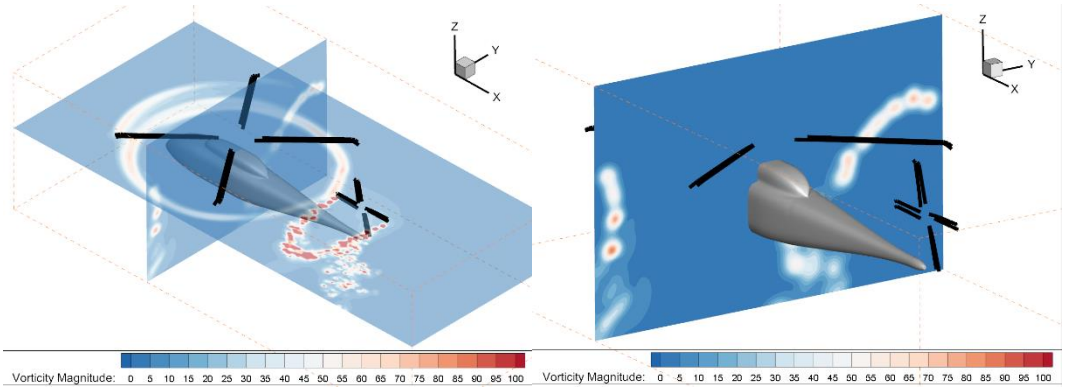

Figure 4.23 Vorticity contours at cross-planes

It is observed that, main rotor tip vortices are strongly interacting with tail rotor and Viscous Vortex Particle approach is capable of estimating main and tail rotor wake dynamics under the influence of each other. As the method inherently computes for interaction of all particles present in the domain independent from origin, in this case,

rotor blades, distance, dimension and rotation of direction, VVPM approach is evaluated as suitable to study the interaction problem.

Finally, rotor wakes are illustrated with and without vortex particles to illustrate the relation between vorticity iso-surface, tip vortices and particle density as well as strength in Figure 4.24.

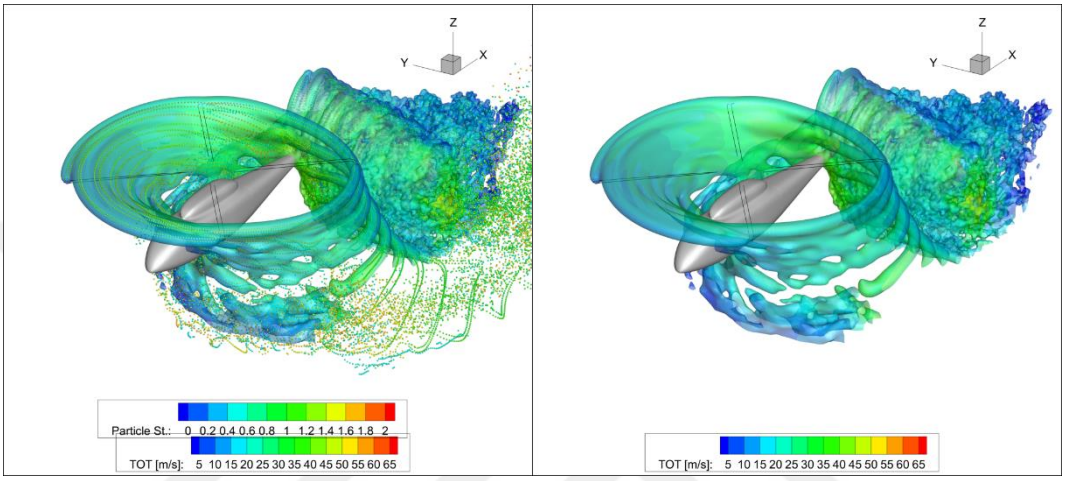

Figure 4.24 Main – tail rotor wakes with and without vortex particles

4.5.2 Co-axial Rotor Evaluation

Increasing interest in coaxial/lift offset rotors leads industry and research focus on aeromechanical modeling of such configurations. Utilization of legacy free wake methods or finite state inflow models require additional tuning parameters specific to the configuration and introduces additional challenges to provide accurate induced velocity estimations especially at different separation distances between rotors.

A review on how VVPM can contribute to evaluations of such configuration is performed by modeling a coaxial rotor with half radius separation distance between upper and lower rotors at trimmed hover and forward flight conditions. Rotor is trimmed for some arbitrary total thrust level while keeping upper and lower rotor mean torque levels equal and zero total longitudinal & lateral moments. Wake structure in terms of particle distribution is illustrated with Figure 4.25.

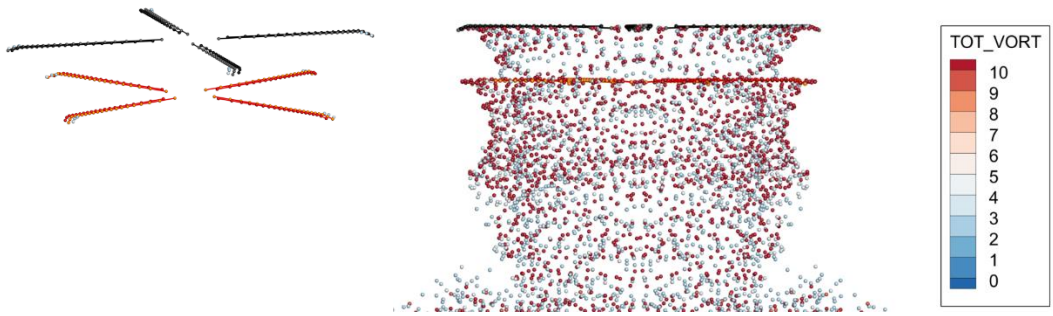

Figure 4.25 Co-axial rotor particle distribution at hover

Spanwise thrust (Fz) and effective angle of attack (AoA) distributions for blades located at 0^{th} azimuth angle is presented with Figure 4.26. It is observed that, at hover, while mean torque levels are same for both rotors, upper rotor operates in a representative ground effect condition and generates higher thrust levels throughout the span which results in a higher wake contraction. Lower rotor, on the other hand, operates like axial climb flight condition with lower normal force and effective angle of attack variation throughout blade span. It is evaluated that lower rotor is under the influence of a strong tip vortex which significantly alters spanwise distributions near tip region.

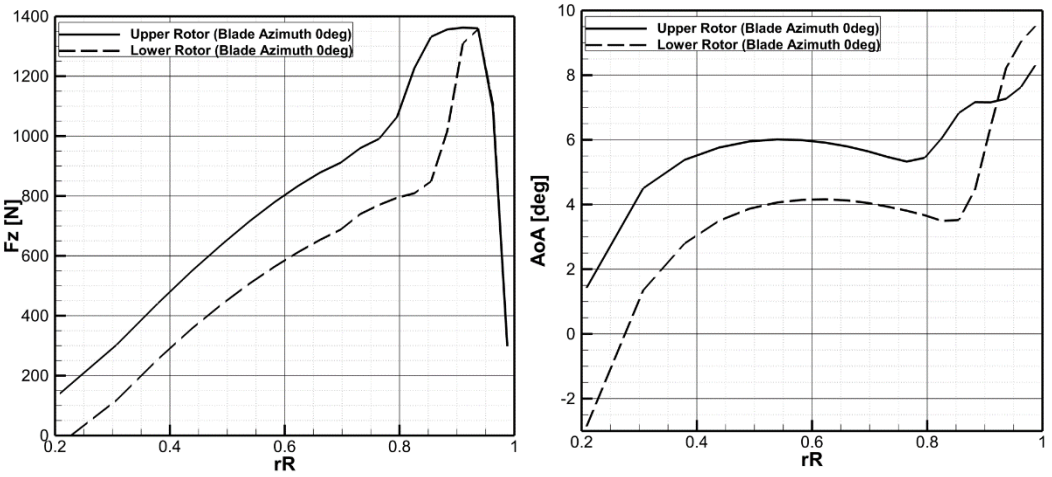

Figure 4.26 Coaxial rotor spanwise Fz and effective AoA distribution for hover

Vorticity iso surface and vorticity contour at a plane passing from the center of the rotors are illustrated with Figure 4.27. Vorticity iso-surface exhibits the wake

structure for contra rotating rotors interacting with each other at hovering condition, whereas the vorticity contour at cross-plane displays tip vortices trajectories and their roll-up at an arbitrary wake age.

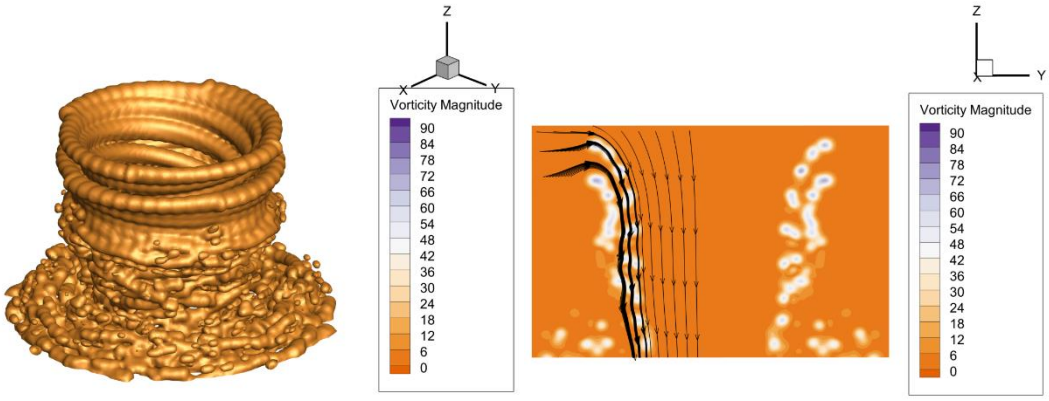

Figure 4.27 Coaxial rotor vorticity iso-surface and contour at a slice x=0

Forward flight simulation is performed at an intermediate forward speed i.e. 80 knots. Wake evolution in terms of particle distribution with rotor revolution is presented with Figure 4.28.

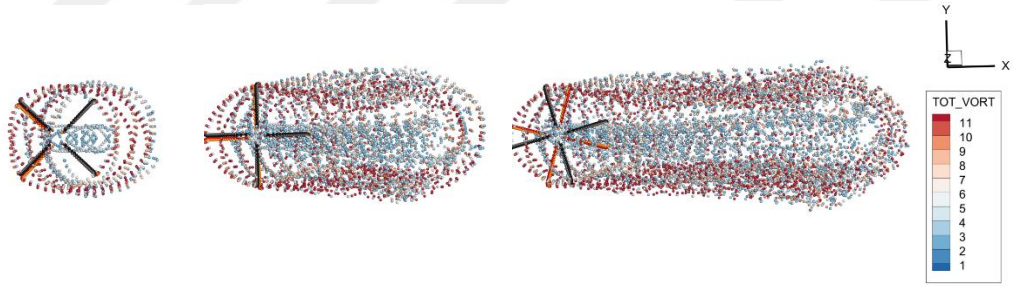

Figure 4.28 Coaxial rotor wake evolution at 80 knots forward speed

Vorticity contours at planes passing from center of the rotors at both directions as well as streamlines for 80 knots level forward flight are plotted at Figure 4.29. Trajectories of tip vortices and the super vortex rolled-up from disc edge vortices of upper and lower rotors are observable. Vorticity iso-surface exhibits the complex wake geometry of contra-rotating rotors interacting with each other.

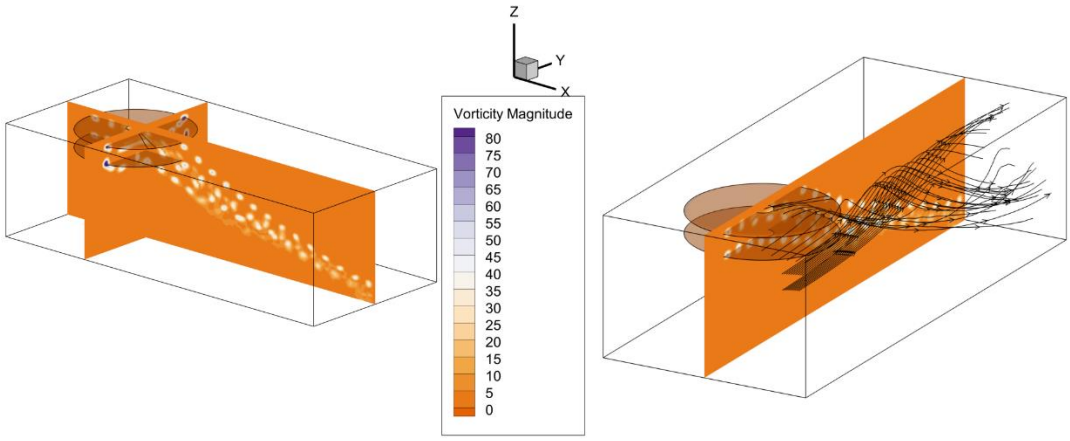

Figure 4.29 Vorticity contours at cross-planes and streamlines at 80 knots forward speed

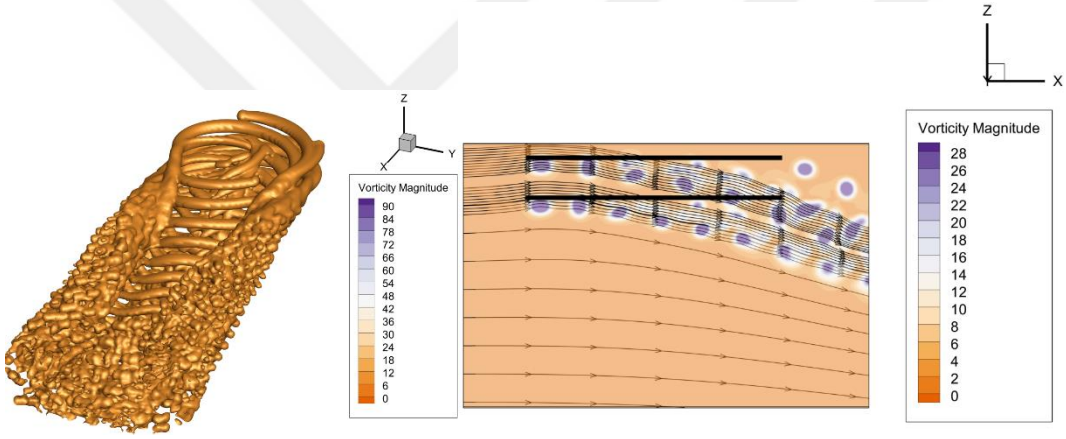

Figure 4.30 Vorticity iso-surface and contour at cross-plane with streamlines at 80 knots forward speed

It is observed that wake is highly skewed, upper and lower rotors are operating in similar conditions and generating mirrored rotor loads as illustrated at Figure 4.31.

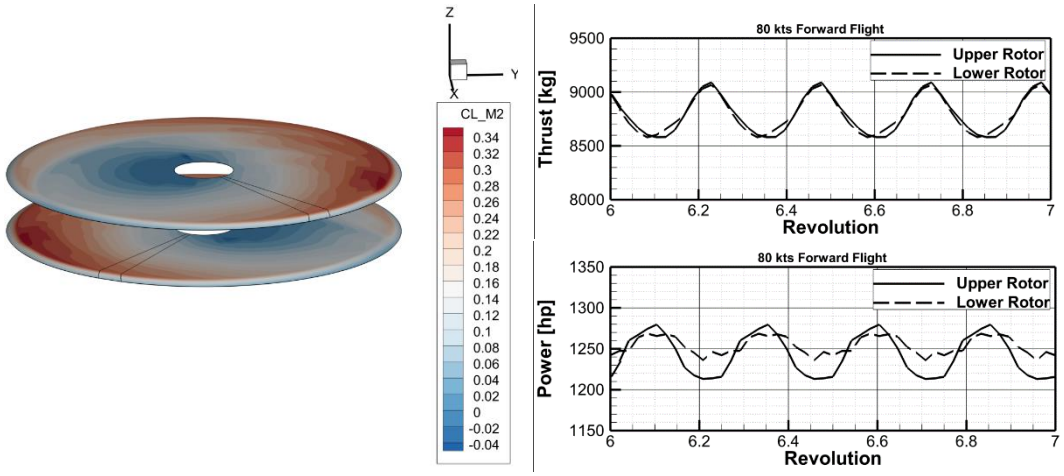

Figure 4.31 Coaxial upper and lower rotor loads distributed over the discs and variation with rotor revolution at 80 knots forward speed

4.5.3 Intermeshing

Intermeshing configuration introduces additional challenge to model unsteady and complex from blade-vortex & blade-wake interactions specifically at the overlapping region. VVPM performance on such configuration is assessed qualitatively through modeling the same rotor geometry with the co-axial case for an intermeshing configuration and performing hover and forward flight analyses. Rotor is trimmed for some arbitrary total thrust level while keeping rotor1 and rotor2 mean torque levels equal. Non-dimensional airloads distribution over the rotor disc and vorticity iso-surface for hovering flight condition is given in Figure 4.32. Vorticity contours in x-z and y-z planes are presented in Figure 4.33. Strong interaction between two rotors is observed. When airloads disc distribution is investigated, it is observed that the highest drag force i.e. torque or power contribution, is generated at around 0° and 180° azimuths where two tip vortices are inter-crossing each other.

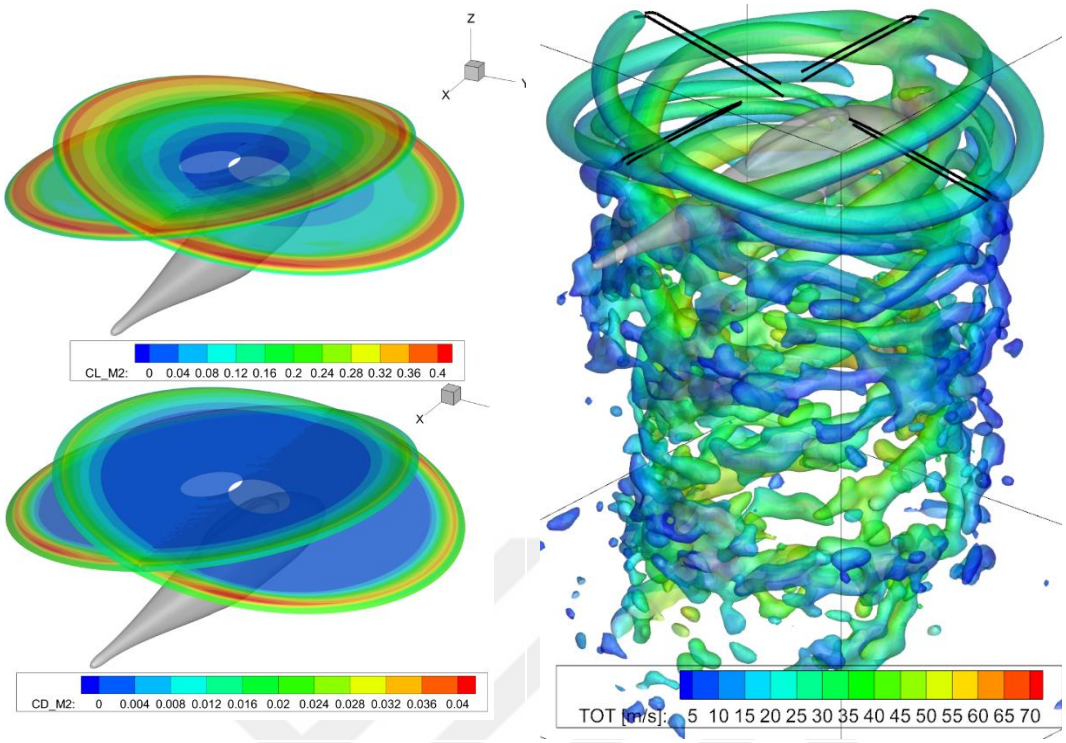

Figure 4.32 Non-dimensional airloads distribution and vorticity iso-surfaces for an intermeshing rotor at hover flight condition

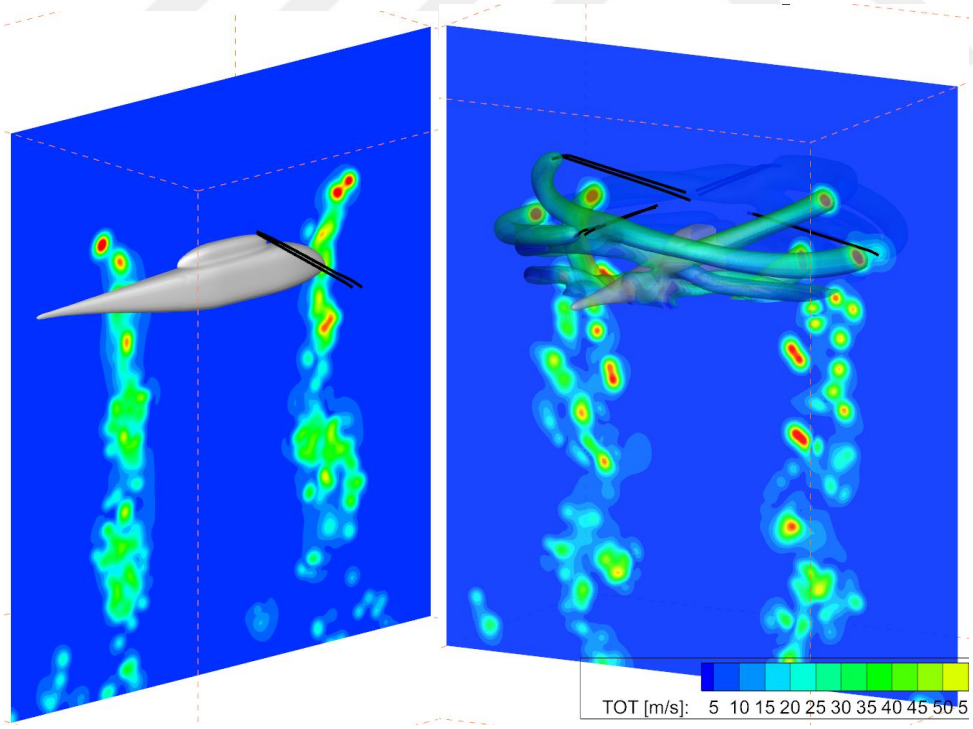

Figure 4.33 Vorticity contour over x-z and y-z contours at hover condition

Similar trim analysis is performed for a moderate forward flight condition (50 knots) and wake evolution in terms of vorticity iso-surfaces are illustrated with Figure 4.34 and Figure 4.35.

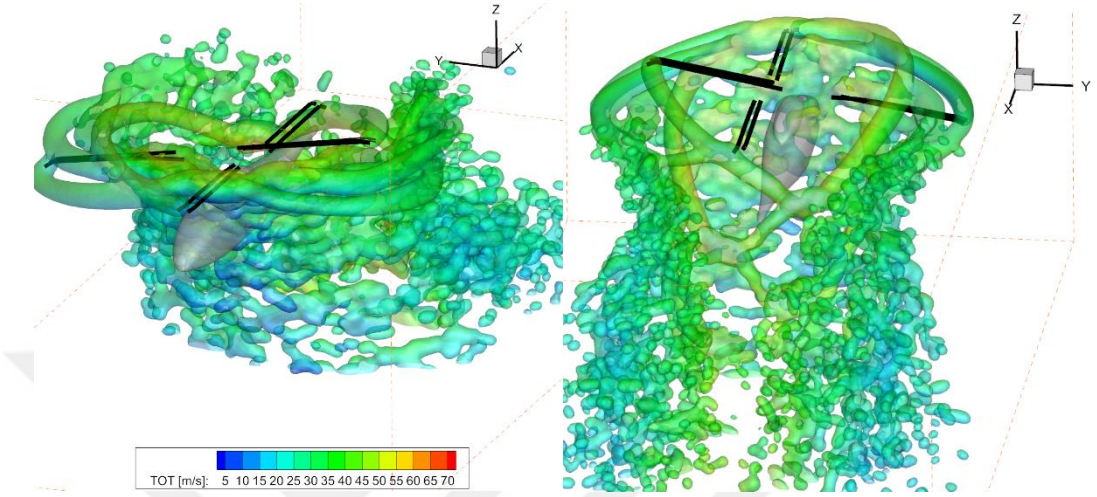

Figure 4.34 Vorticity iso-surface colored with total air speed in 50 knots forward flight condition

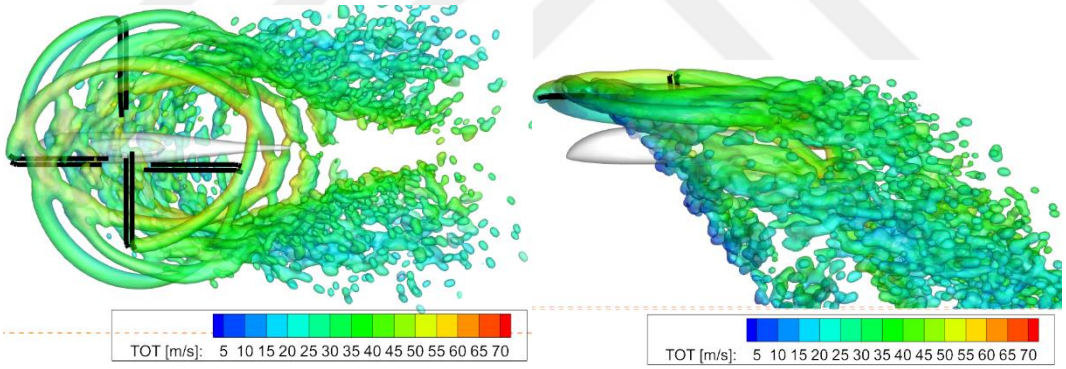

Figure 4.35 Vorticity iso-surface colored with total air speed in 50 knots forward flight condition

Vortex particle distributions per each revolution at forward flight is presented in Figure 4.36, Figure 4.37 and Figure 4.38.

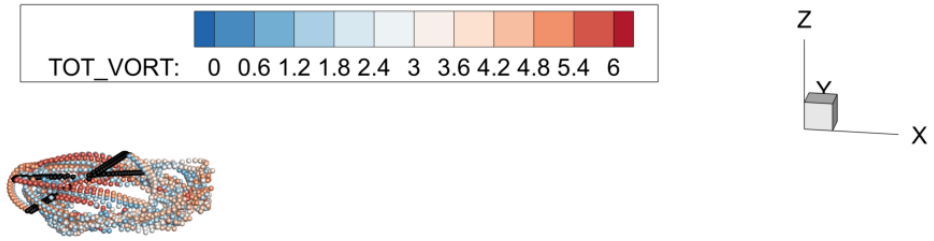

Figure 4.36 Intermeshing rotor particle distribution in forward flight 1st rev.

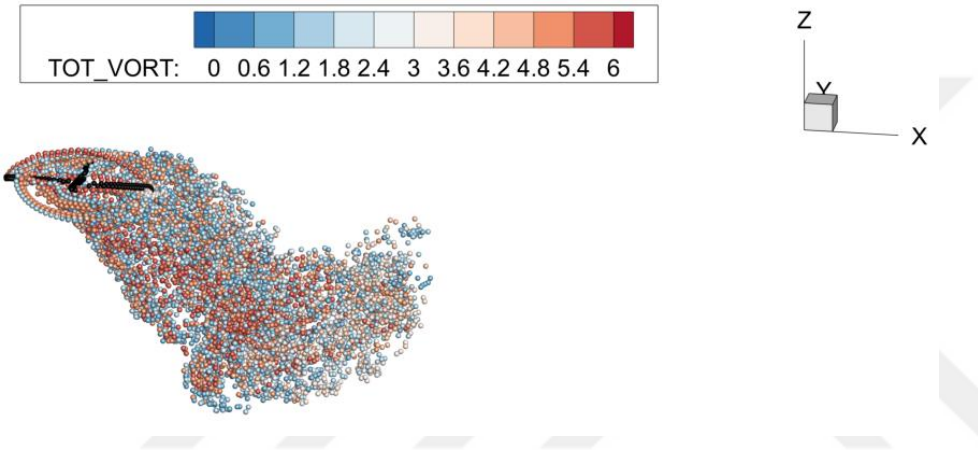

Figure 4.37 Intermeshing rotor particle distribution in forward flight 2nd rev.

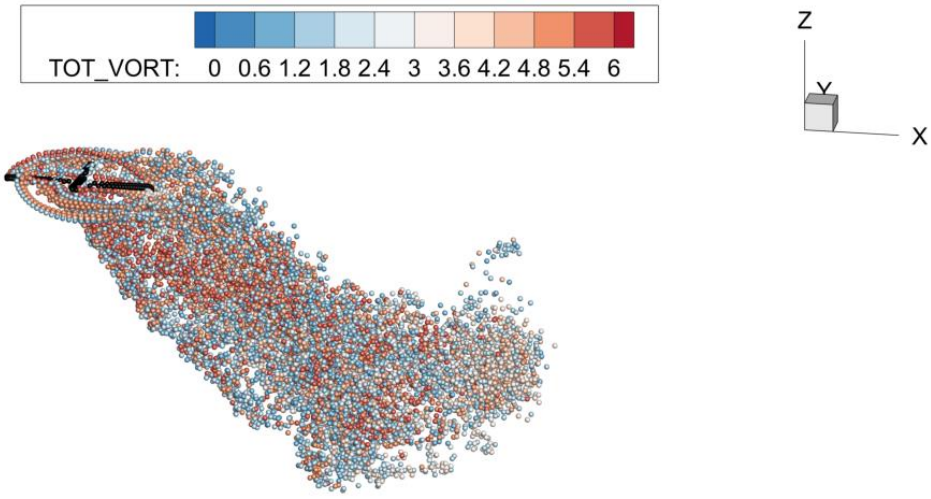

Figure 4.38 Intermeshing rotor particle distribution in forward flight 3rd rev.

4.5.4 Tilting Prop-rotor

Transition modeling for tiltrotors are essential, yet challenging, because of the unsteady characteristics and complex aerodynamic interaction of a tilting wake structure. In this scope, a three bladed proprotor transition flight is simulated with VVPM and wake structure is presented for qualitative assessment in Figure 4.39, Figure 4.40 and Figure 4.41. The asset in the tilting prop-rotor analysis achieved with VVPM is the ability to implement combination of varying flight speeds, nacelle tilt and control angles into the simulation without a necessity of any tune or empirical parameter unlike legacy vortex-wake based comprehensive modeling approach. Dynamic trim or pre-defined control angles can be set for the prop-rotor during the transition within the so-called transition corridor which is specific to aircraft design (Miller & Narkiewicz, 2006).

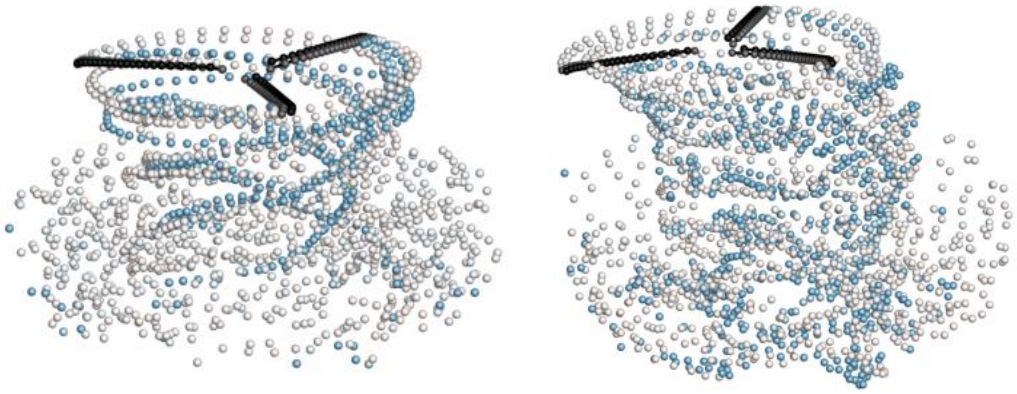

Figure 4.39 Tilting prop-rotor simulation

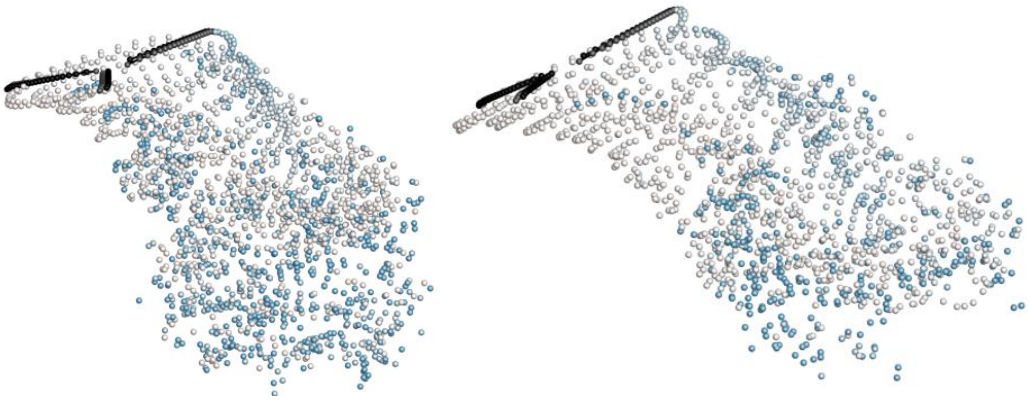

Figure 4.40 Tilting prop-rotor simulation

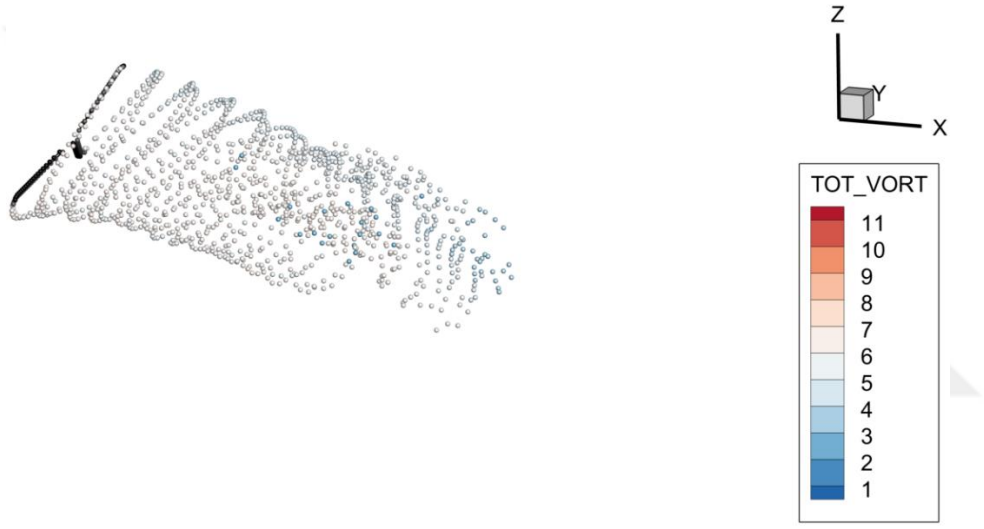

Figure 4.41 Tilting prop-rotor simulation

4.6 Verification Check

A conventional helicopter is trimmed with two approaches: First, moving in the domain where the medium is still, and the helicopter is traveling at 100 knots level forward flight. Second, the helicopter is floating and trimmed under 100 knots headwind. In terms of flight dynamics, these two conditions represent the same operating environment and the same aeromechanical response is expected for both. The wake evolution and geometry for both analysis is compared in Figure 4.42 to Figure 4.45.

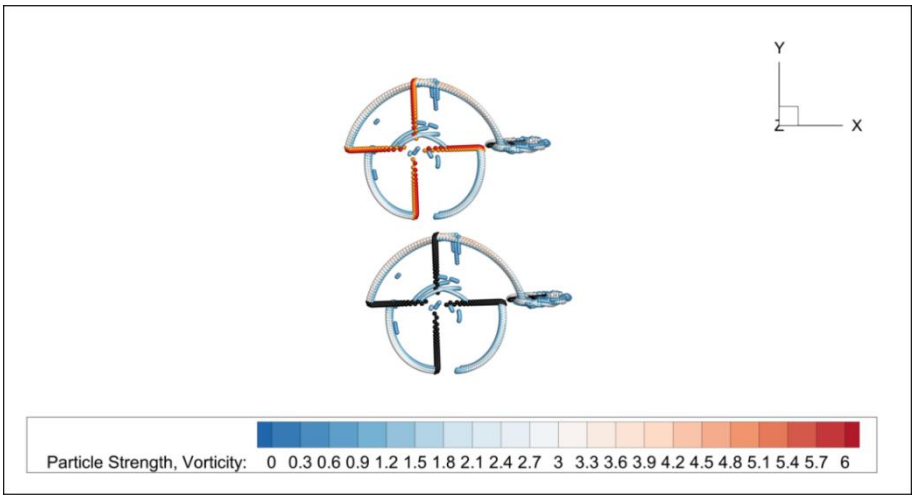

Figure 4.42 Wakes for moving and floating configuration, initial cond.

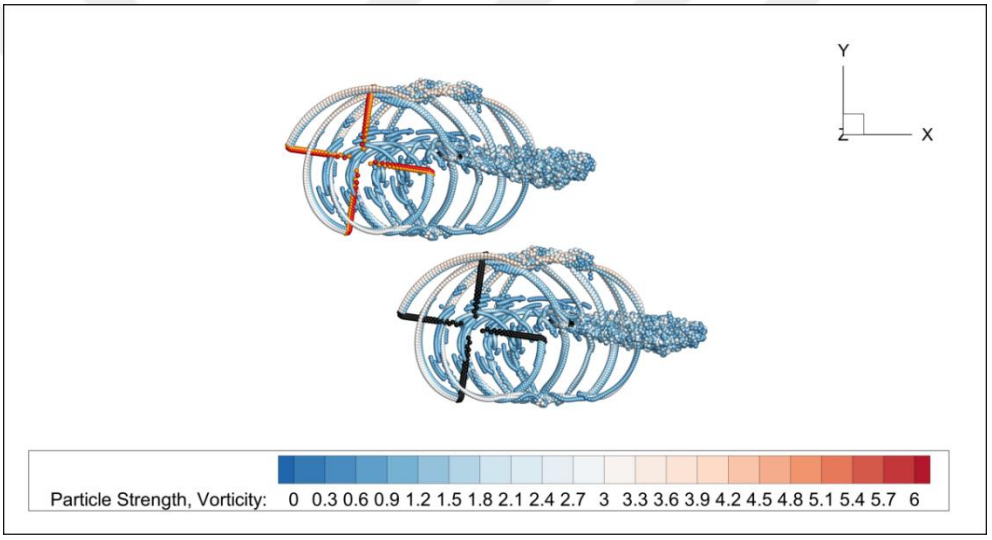

Figure 4.43 Wakes for moving and floating configuration, 1st main rotor rev.

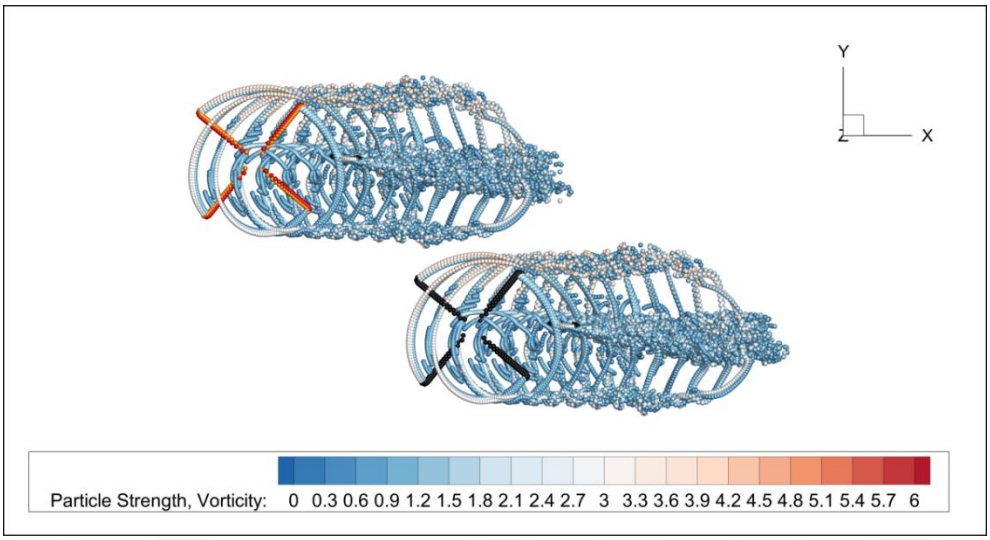

Figure 4.44 Wakes for moving and floating configuration, 2nd main rotor rev.

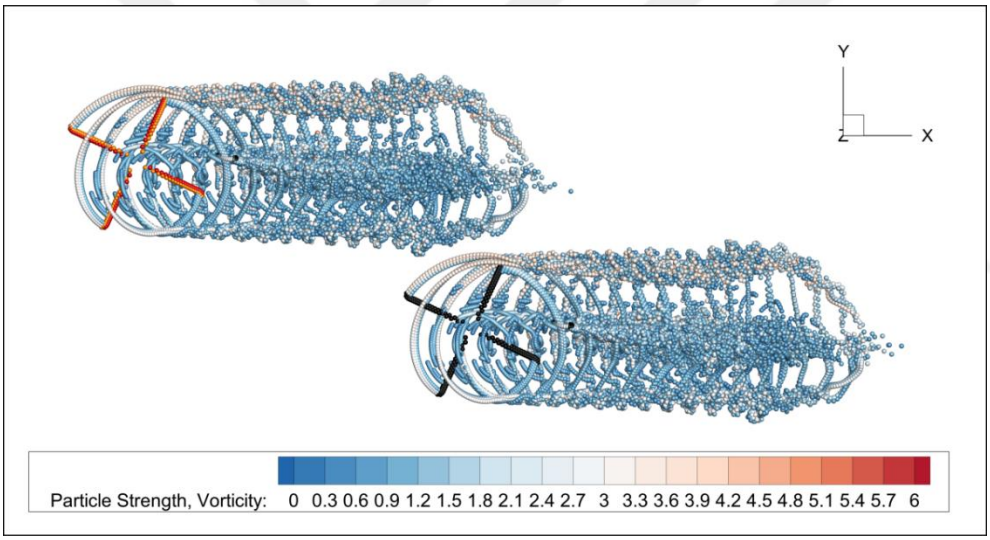

Figure 4.45 Wakes for moving and floating configuration, 3rd main rotor rev.

It is observed that, in terms of qualitative assessment, wake evolutions are exactly symmetric.

In terms of quantitative assessment performance parameters such as power, Euler angles and control angles, all the variables converged to exactly the same trim condition. Thrust and torque coefficient variation with simulation step for moving and floating main rotors are presented in Figure 4.46. It is observed that, total thrust and torque variations of main rotor in both analyses are perfectly aligned.

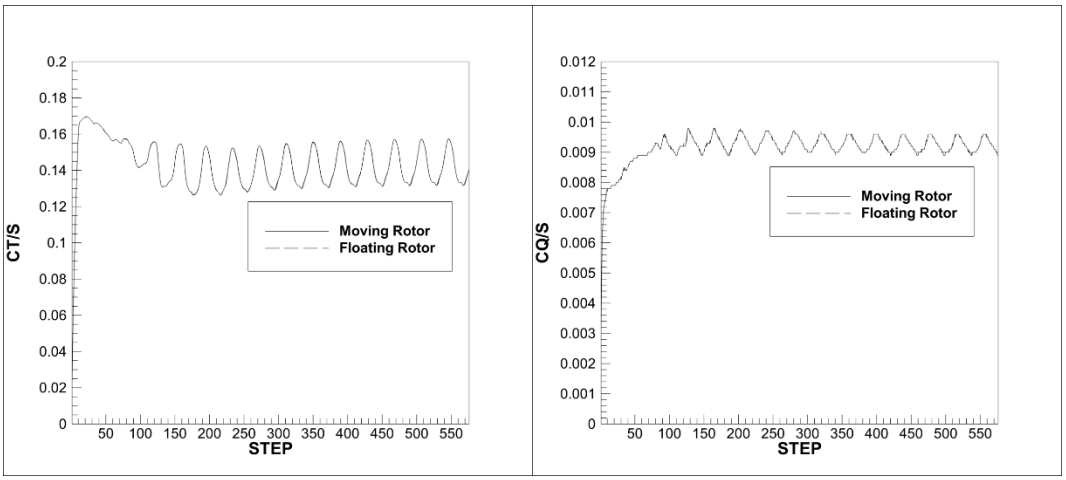

Figure 4.46 Thrust and torque variation of moving and floating main rotors

Similar comparison is performed for the tail rotors of both analyses in Figure 4.47. It is observed that, thrust variations of both moving and floating tail rotors are exactly aligned, however, there is a 10% difference in the torque oscillations.

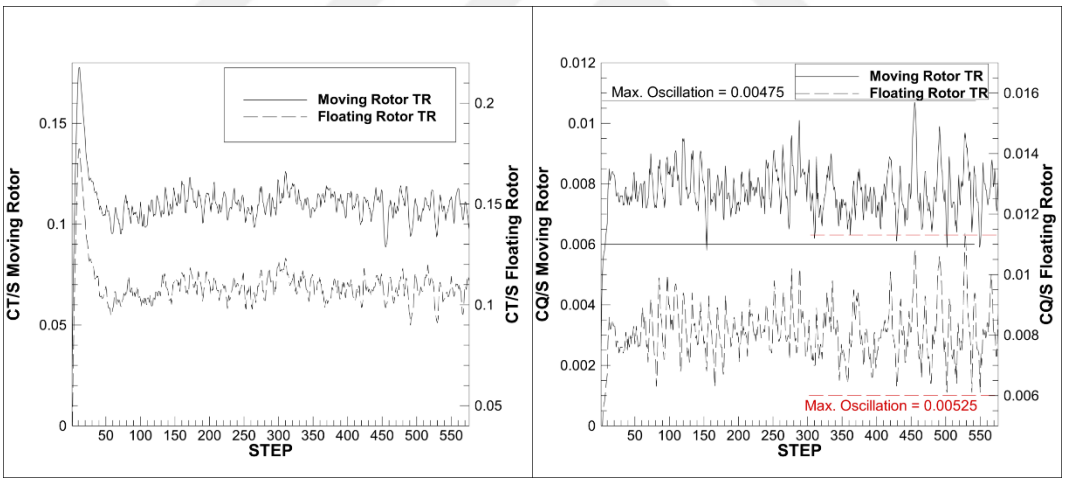

Figure 4.47 Thrust and torque variation of moving and floating tail rotors

The reason of the difference in the tail rotor torque oscillations is explained through going back to the fundamental equations. The equation (51), diffusion of the vorticity formulation is re-given for completeness.

$$\frac{\partial \omega}{\partial t} + u \cdot (\nabla \omega) = \frac{d\omega}{dt} = v\nabla^2\omega + \nabla u \cdot \omega \qquad (51)$$

The second term in the diffusion equation represent the vortex stretching, is absent in case of moving rotor and still air, whereas the vortex stretching exists in case of the floating rotor and the air is flowing as headwind. The vortex stretching is responsible from vorticity diffusion and gets significant in far wake. Therefore, generally the effect of vortex stretching on the source rotor is negligible as it alters wake dynamics at far wake, especially in high speed forward flight conditions, where rotor wake rapidly moves away from the rotor. However, if another rotor is placed in the rotor wake or far wake of the first rotor where the vortex stretching is significant, such as a tail rotor in this case, as the wake dynamics of the main rotor vary, tail rotor operating characteristics vary. This is evaluated to be the reason of the difference in oscillating loads of a moving rotor and floating rotor.

CHAPTER 5

AEROACOUSTICS MODEL

Whether it is a civil or military operation; likewise, a conventional helicopter configuration or a new VTOL concept, in real life rotorcrafts operate and maneuver in complex dynamics including of unsteady, non-periodic, transient effects with aerodynamic interactions and interferences; therefore generated aerodynamic noise is potentially significantly different from the estimation of simplified models with simplified loads and flight dynamics (Bres et al., 2004). Therefore, an aeroacoustics solver coupled with VVPM, generating the required high fidelity and resolution aeromechanical data as well as coupled with a rotorcraft comprehensive model, provides the utmost accurate noise representation of a full rotorcraft configuration in flight or maneuvering conditions. Acoustic wave propagation on a ground surface 150m below for a sample quartering trimmed flight condition of a conventional helicopter determined with the model developed in this study is illustrated with Figure 5.1.

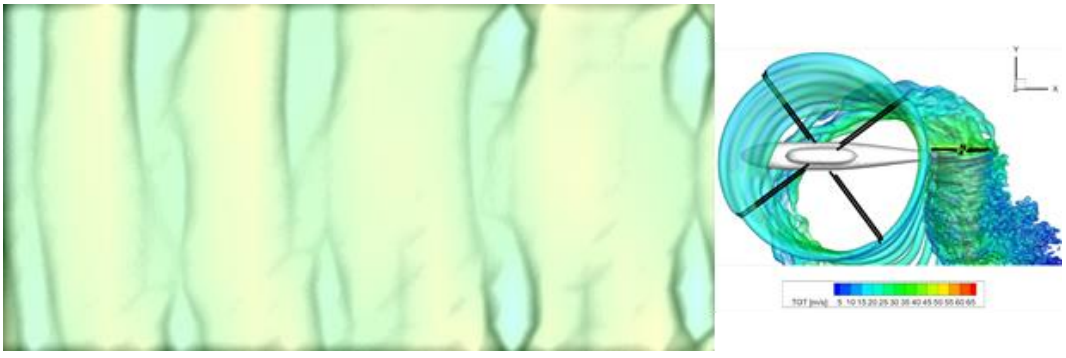

Figure 5.1 Acoustic wave propagation on ground surface (height:150m) for a quartering conventional helicopter configuration

The aeroacoustics model developed in this scope, takes rotorcraft aeromechanical solution, performs pre-process calculations to transform concentrated blade loads into unsteady pressure distribution, utilizes Farassat 1A integral solution of Ffowcs-

Williams Hawking's and performs sound pressure level calculations, frequency analysis and weighted sound level computations at any observer location.

First, theory, fundamentals, and governing equations for an acoustics solution of a moving body with pressure variation on the surface is discussed. Then, the aeroacoustics solver utilized in this study is introduced. The two interface algorithms; concentrated loads to pressure distribution and wake resolution & loads increase algorithms are described. Validation of the acoustics solver with HART-II wind tunnel test data is performed and summarized. Finally, developed VVPM coupled acoustics model (VVPAM) is further qualitatively explored for flyover simulation and blade-vortex interaction (BVI) evaluations.

5.1 Fundamentals and Governing Equations

Like most of the rotorcraft acoustic solvers in the literature, integral formulation of Ffowcs Williams – Hawking's (FWH) equation is utilized to propagate acoustic pressure fluctuations at observer locations for further sound level evaluations. Aeroacoustics is governed by fundamental fluid dynamics laws and FWH equation is essentially the exact re-arrangement of mass conservation equation and Navier-Stokes equations into form of an inhomogeneous wave equation. Solution of FWH equation requires knowledge of primary field variables such as density ρ, momentum ρu_i and pressure p over the source surface. Having such information generated for the domain of interest, i.e. in our case, thousands of meters perhaps, requires impractical computational resource especially when integral formulations are available for FWH. Considering that the burden arises from the domain size much larger than aerodynamic problems as well as potential dispersion and artificial dissipation issues of numerical methods, integral formulation of FWH coupled with a rotor CFD or comprehensive solver is practical both in accuracy and feasibility. Implementation of integral formulation of FWH equation provides two surface and one volume source terms which are incorporated with monopole source as thickness

noise, dipole source as loading noise and quadrupole source as broadband noise components of aerodynamically generated total noise signature.

Derivation of FWH equation is similar to derivation of Lighthill's famous acoustic analogy, which is determined by re-writing the Navier-Stokes equations. Derivation is summarized in Appendix B, only the final form of Lighthill's acoustic analogy is given here with equation (52) for consistency (Hirschberg & Rienstra, 2004).

$$\frac{1}{c_o^2}\frac{\partial^2 p'}{\partial t^2} - \frac{\partial^2 p'}{\partial^2 x_i'} = \frac{\partial^2}{\partial x_i \partial x_j}\left(\rho v_i v_j - \sigma_{ij}\right) - \frac{\partial f_i}{\partial x_i} + \frac{\partial^2}{\partial t^2}\left(\frac{p'}{c_o^2} - \rho'\right) \qquad (52)$$

where p and ρ are pressure and density, c_o is the speed of sound, f_i is the external force field. σ_{ij} is defined with equation (53).

$$\sigma_{ij} = p\delta_{ij} - P_{ij} \qquad (53)$$

where P_{ij} is the compressive stress tensor.

Derivation of FWH equation starts with continuity and conservation of momentum laws of fluid dynamics given with equations (54) and (55).

$$\frac{\partial \rho}{\partial t} + \frac{\partial}{\partial x_i}(\rho u_i) = 0 \qquad (54)$$

$$\frac{\partial}{\partial t}(\rho u_i) + \frac{\partial}{\partial x_j}\left(\rho u_i u_j + P_{ij}\right) = 0 \qquad (55)$$

where P_{ij} is the compressive stress tensor defined by Lighthill's acoustic analogy.

The generalization for the FWH is done by setting a moving surface $S(\vec{x}, t) = 0$ enclosing the acoustic sources. $S > 0$ represent the domain out of the source volume whereas $S < 0$ is the volume left inside the encapsulating moving and permeable surface. The discontinuity at $S = 0$ represents the mass or momentum injection as the source of noise. In order to have a generalized formulation, generalization theory is utilized given with equations (56) and (57) for any variable q

$$\frac{\bar{\partial} q}{\partial x_i} = \frac{\partial q}{\partial x_i} + \Delta q \frac{\partial S}{\partial x_i} \frac{\partial H(S)}{\partial S} \tag{56}$$

Δq is the jump because of artificial discontinuity and

$$\frac{\partial H(S)}{\partial S} = \delta(S) \tag{57}$$

where H is the Heaviside function. Utilization of generalized derivative, given with equation (56), on the equations (54) and (55) leads to generalized continuity and momentum equations with artificial discontinuity given as equations (58) and (59) (Brentner & Farassat, 2003).

$$\begin{aligned} &\frac{\bar{\partial} \rho}{\partial t} + \frac{\bar{\partial}}{\partial x_i}(\rho u_i) \\ &\qquad = \frac{\partial \rho}{\partial t} + (\rho - \rho_o)\frac{\partial S}{\partial t}\delta(S) + \frac{\partial}{\partial x_i}(\rho u_i) + (\rho u_i)\frac{\partial S}{\partial x_i}\delta(S) \end{aligned} \tag{58}$$

$$\begin{aligned} &\frac{\bar{\partial}}{\partial t}(\rho u_i) + \frac{\bar{\partial}}{\partial x_j}\left(\rho u_i u_j + P_{ij}\right) \\ &\qquad = \frac{\partial}{\partial t}(\rho u_i) + \rho u_i \frac{\partial S}{\partial t}\delta(S) + \frac{\partial}{\partial x_i}\left(\rho u_i u_j + P_{ij}\right) \\ &\qquad + \left(\rho u_i u_j + \Delta P_{ij}\right)\frac{\partial S}{\partial x_i}\delta(S) \end{aligned} \tag{59}$$

Implementing the definitions given with equations (62) and (63);

$$\frac{\partial S}{\partial t} = -v_j \frac{\partial S}{\partial x_j} \tag{60}$$

$$\frac{\partial S}{\partial x_j} = n_j, \quad u_j n_j = u_n, \quad v_j n_j = v_n \tag{61}$$

Generalized continuity and momentum equations are determined as equations (62) and (63).

$$\frac{\bar{\partial} \rho}{\partial t} + \frac{\bar{\partial}}{\partial x_i}(\rho u_i) = [\rho_o v_n + \rho(u_n - v_n)]\delta(S) \tag{62}$$

$$\frac{\bar{\partial}}{\partial t}(\rho u_i) + \frac{\bar{\partial}}{\partial x_j}\left(\rho u_i u_j + P_{ij}\right) = \left[\rho u_i (u_n - v_n) + \Delta P_{ij}\hat{n}_j\right]\delta(S) \qquad (63)$$

The definitions of the variables in the constituting equations are; u_n is the fluid velocity normal the to source surface S, $\hat{n}_j$ the surface normal i.e. unit vector outward the source surface S and v_n is the normal velocity of the moving surface S.

Like Lighthill's acoustic analogy, FWH equation is determined through taking time derivative of mass conservation law given with equation (62) and subtracting the divergence of the momentum law given with equation (63). FWH equation written in the light of Lighthill's acoustic analogy is given by (Brentner & Farassat, 2003) equation (64).

$$\begin{aligned}\left(\frac{1}{c_o^2}\frac{\bar{\partial}^2}{\partial t^2} - \frac{\bar{\partial}^2}{\partial x_i \partial x_i}\right) p'(\vec{x}, t) \\ = \frac{\partial}{\partial t}\{[\rho_o v_n + \rho(u_n - v_n)\delta(S)]\} \\ - \frac{\partial}{\partial x_i}\left\{\left[\Delta P_{ij}\hat{n}_j + \rho u_i (u_n - v_n)\right]\delta(S)\right\} \\ + \frac{\partial^2}{\partial x_i \partial x_j}\left[T_{ij} H(S)\right]\end{aligned} \qquad (64)$$

where; T_{ij} is the Lighthill stress tensor given with equation (65).

$$T_{ij} = \rho u_i u_j + P_{ij} - c^2 \rho' \qquad (65)$$

Further simplification of FWH is made by setting the source surface $S = 0$ coincides with the solid surface, i.e. blade surfaces in this case, so that the normal velocity of the source surface becomes same with the normal velocity of the fluid passing through the source surface $u_n = v_n$. By doing so, the most common, generalized partial differential for of the FWH equation given with equation (66) is determined (Brentner & Farassat, 2003; Hirschberg & Rienstra, 2004; Özyörük et al., 2017).

$$\left(\frac{1}{c_o^2}\frac{\bar{\partial}^2}{\partial t^2}-\frac{\bar{\partial}^2}{\partial x_i \partial x_i}\right)p'(\vec{x},t) = \frac{\partial}{\partial t}\{[\rho_o v_n \delta(S)]\}-\frac{\partial}{\partial x_i}\{[\Delta P_{ij}\hat{n}_j]\delta(S)\} + \frac{\partial^2}{\partial x_i \partial x_j}[T_{ij}H(S)] \quad (66)$$

First term on the right represents the acceleration of the acoustic sources because of the displacement of the integral surface and corresponds to monopole source. Second term on the right represents the momentum source acting on the fluid shear force variation on the integral surface including pressure distribution and incorporated with dipole sources. Third, and the last term on the right represents turbulent fluctuations at the external region of the source surface and is incorporated with the quadrupole sources.

Monopole and dipole sources incorporated with thickness and loading noise components and comprises rotational noise, related to linear aerodynamic theory, constitutes most of the noticeable noise signature from a distance from the source. Quadrupole sources are incorporated with the broadband noise. Thickness noise is due to acceleration and displacement of the fluid flow by the rotor blades whereas the loading noise represents the harmonic non-impulsive and impulsive blade-vortex interaction (BVI) noises. Broadband noise on the other hand, is incorporated with turbulent flow near blade surface, and due to blade self-noise, with random pressure fluctuations, attached or de-attached boundary layers, tip vortex formation, laminar vortex shedding and trailing edge.

The quadrupole term is generally neglected when noise signature of multiple rotor configuration on ground surface which is around hundreds of meters in distance is of interest. Considering the atmospheric absorption characteristics which damps the higher frequencies and the harmonic and impulsive noise components which generally dominates the overall noise signature, neglecting the quadrupole term is considered as a fair assumption. Besides, solution of the quadrupole term requires flow filed information at utmost resolution to catch the broadband effect, which

seems to be impracticable for rotorcraft applications (Brentner & Farassat, 2003). Finally, when occurs, blade-vortex interaction noise dominates overall noise spectra and is the major noise source at medium to high flight speeds with level or approach trajectories (Prieur & Splettstoesser, 1999). Therefore, BVI noise is the key aspect to be avoided in order to improve the public annoyance, which can be assessed with the implementation of the second term of the FWH equation. For these reasons, quadrupole terms are neglected throughout this dissertation.

Although generalized mass conservation and momentum equations are written with mixed aeroacoustics variables such as $\rho' \; and \; p'$, the FWH equation is written in the form of pressure as the chosen aeroacoustics variable by using the relation $p' = c_o^2 \rho'$. Utilization of pressure as the aeroacoustics variable of choice results in mass injection or entropy fluctuations incorporated with monopole sources. However on the other hand if the density is used, the same terms appear in quadrupole formulation. This basically drives the decision to utilize pressure as the choice of the aeroacoustics variable as the motion of the integral surface can be incorporated with monopole kind of source. On the other hand, density should be used for if fluid-structure interaction is considered and the motion of the integral surface introduces turbulence to the flow (Hirschberg & Rienstra, 2004).

Finally, for numerical solution and implementation, the FWH equation given with equation (66) is transformed into integral formulation. Literature (Brentner & Farassat, 2003; Hirschberg & Rienstra, 2004) provides useful guides for derivation of the integral formulation of FWH equation. Neglecting the quadrupole terms and splitting thickness and loading noise components, Farassat 1A integral formulation is achieved as equations (67) and (68).

$$p'_T(\vec{x},t) = \frac{1}{4\pi}\int_{f=0}\left[\frac{\rho_o(\dot{v}_n + v_{\dot{n}})}{r[1-M_r]^2}\right]dS + \frac{1}{4\pi}\int_{f=0}\left[\frac{\rho_o v_n\left(r\dot{M}_r + c_o M_r - c_o M^2\right)}{r^2[1-M_r]^3}\right]dS \tag{67}$$

$$p_L'(\vec{x},t) = \frac{1}{4\pi c_o}\int_{f=0}\left[\frac{\dot{l}_r}{r[1-M_r]^2}\right]dS + \frac{1}{4\pi}\int_{f=0}\left[\frac{l_r - l_M}{r^2[1-M_r]^2}\right]dS + \frac{1}{4\pi c_o}\int_{f=0}\left[\frac{l_r\left(r\dot{M}_r + c_o M_r - c_o M^2\right)}{r^2[1-M_r]^3}\right]dS \quad (68)$$

$(\vec{x},t)$ in the formulation is the observer location and observer time, v_n is the source surface normal velocity, r is the slant vector from observer to source, and M_r is the Mach number in the emission direction. Mach number in the emission direction can be computed through equation (69). On the source surface, which is the blade surface in this case, the fluid velocity in the normal direction is zero. The loading terms l_r and l_M are therefore defined as $l_r = \vec{l}\cdot\left(\frac{\vec{r}}{|\vec{r}|}\right)$ and $l_M = \vec{l}\cdot\vec{M}$ where l is the stress vector over the surface and determined with equation (70).

$$M_r = \frac{1}{c_o}\vec{V}\cdot\left(\frac{\vec{r}}{|\vec{r}|}\right) \quad (69)$$

$$\vec{l} = \left[(p-p_o)\delta_{ij} - \tau_{ij}\right]n_j \quad (70)$$

Contribution of viscous forces, τ_{ij} is much smaller than the pressure, therefore is ignored (Özyörük et al., 2017).

5.2 Aeroacoustics Solver

The rotor noise prediction solver utilized in this study had been developed within the industry-academy co-operation program by Prof. Özyörük from Middle East Technical University (Özyörük et al., 2017), funded by Turkish Aerospace Industries. The developed tool integrates the FWH equation in time with retarded and advanced time options. Surface integrals carried out with high order quadrature can operate both on structured and unstructured meshes. Parallel computation capability had been tested decomposing either mesh or observer times. Solver had been developed to be coupled with CFD methods, therefore it has the capability to process quadrupole sources. Yet, as discussed at chapter "5.1 Fundamentals and

Governing Equations", broadband noise is out of the scope of this study, therefore only thickness and loading noise will be considered. For further information on quadrupole terms, reader is advised to the development paper (Özyörük et al., 2017).

The author has already published previous studies using the aeroacoustics solver with commercial rotorcraft codes. In his study (Yücekayali, Şenipek, Ortakaya, et al., 2019) author utilized CHARM, commercial Comprehensive Hierarchical Aeromechanics Rotorcraft Model, to provide required aeromechanical data to validate acoustic analysis results with HART-II wind tunnel case and compare acoustic pressure time variation with a benchmark tool, PSU-WOPWOP. Comparison with test data and commercial tools revealed that, the aeroacoustics solver estimates rotor noise successfully. In another study, (Atalay, Yücekayalı, et al., 2019) the aeroacoustics solver is again coupled with CHARM to study main rotor and tail rotor interactional noise for a conventional configuration helicopter at various flight conditions. Effect of tail rotor direction of rotation and orientation on tail rotor loads, vibration and noise is studied. In his recent study (Yucekayali et al., 2019), which is an outcome of this thesis, the author proposed the pressure distribution methodology from concentrated rotor loads which is the methodology developed and improved with this dissertation and will be discussed at chapter "5.4 Aerodynamics-Aeroacoustics Models Interface". Validation results of the aeroacoustics solver utilized in this study with commercial rotorcraft modeling tools is summarized at Appendix C.

The aeroacoustics solver calculates pressure fluctuation contribution from each mesh cell with a specified surface pressure and propagates sound waves up to any observer location of interest. Solver requires blade kinematic motion i.e. position at each time step, operating environment details such as wind vector, ambient pressure, temperature etc., flight condition as flight vector, rotational speed and pressure values at the center of each surface cell at each time step. Illustration of the method implemented in the aeroacoustics solver and related integral formulation is given with Figure 5.2 and equations (71) (72).

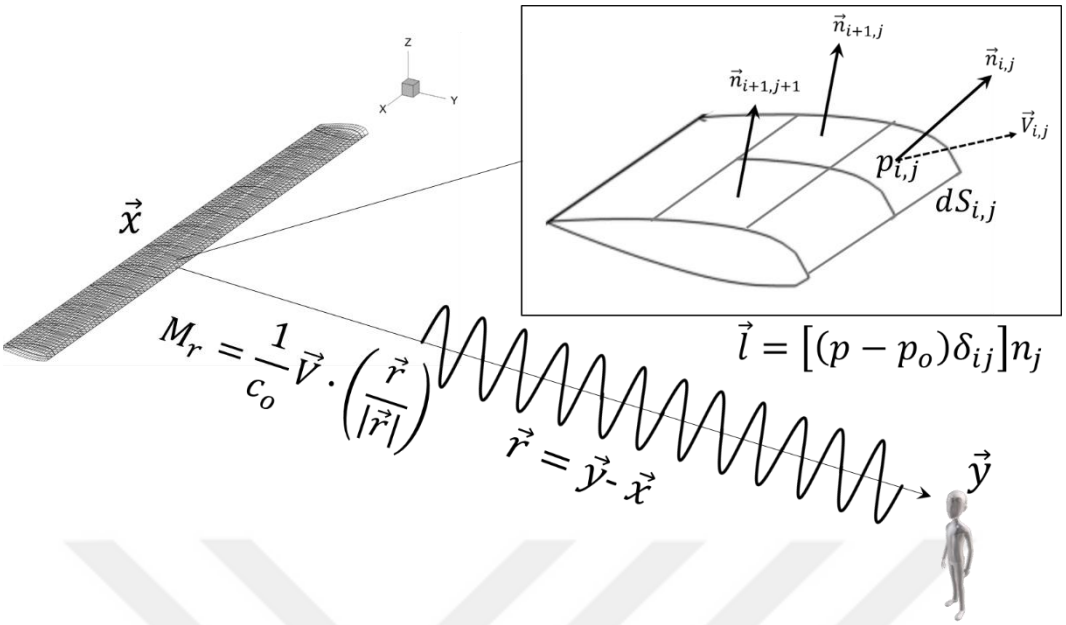

Figure 5.2 Illustration of the integral solution for FWH

$$p'_T(\vec{x},t) = \frac{1}{4\pi}\int_{f=0}\left[\frac{\rho_o(\dot{v}_n + v_{\dot{n}})}{r[1-M_r]^2}\right]dS + \frac{1}{4\pi}\int_{f=0}\left[\frac{\rho_o v_n\left(r\dot{M}_r + c_o M_r - c_o M^2\right)}{r^2[1-M_r]^3}\right]dS \tag{71}$$

$$p'_L(\vec{x},t) = \frac{1}{4\pi c_o}\int_{f=0}\left[\frac{\dot{l}_r}{r[1-M_r]^2}\right]dS + \frac{1}{4\pi}\int_{f=0}\left[\frac{l_r - l_M}{r^2[1-M_r]^2}\right]dS + \frac{1}{4\pi c_o}\int_{f=0}\left[\frac{l_r\left(r\dot{M}_r + c_o M_r - c_o M^2\right)}{r^2[1-M_r]^3}\right]dS \tag{72}$$

The solution of integral formulation of FWH is performed through numerical algorithm and amongst the other, retarded time and forward time integration schemes are used in nearly all the rotorcraft noise codes in the literature (Brentner & Farassat, 2003).

In retarded time algorithms integral solution is performed at source surface at the emission or retarded time. This requires root finding at observer location backward

in time to find the time at when noise is emitted from the source as at the time when observer notifies the sound wave, the source had already moved. Unless the motion of the source is very simple, which is not in case of a maneuvering rotorcraft or even of a steady flight condition of a multi-rotor with blades are flapping, lead-lagging and rotating in different directions, calculating of the retarded time might not be practical. Therefore, the root finding for each panel of rotor blade is required to be performed over equation (73) to determine the time of emission at observer location.

$$t - \tau - \frac{r(\tau)}{c} = 0 \tag{73}$$

where c is speed of sound, τ emission time, t observer time and $r(\tau)$ is the vector from panel center to observer location at emission time. $r(\tau)$ is constant at root-finding, therefore, it is important to keep in mind that retarded time formulation requires fixed observer location and observer time during the integral solution.

In forward time integration scheme on the other hand, source time is the primary concern, and in such a solution, the observer time is not followed and sound waves arrive to the observer location with uneven time steps proportional to the acoustic ray or path they travel from. In this approach, the overall observer acoustic signal is found from the summation of the acoustic signal radiated from each source element of control surface during the same source time. In forward time integration scheme, the observer is not required to be fixed during the integration and the equally spaced sequence of emission time results in unequally spaced observer times which requires interpolation and re-sampling for further acoustic calculations.

For maneuvering rotorcrafts, generally long-time simulations are required especially if the maneuver is unsteady, resulting in non-harmonic loadings. Moreover, for multi-rotor configurations or even for a conventional helicopter configuration, there exists more than one rotor at different rotational speeds. In order to have a complete acoustic analysis for such a configuration, aeromechanical data for at least one revolution of the slowest rotor is essential, which on the contrary might require more than one revolution for interaction dominated cases. For the time interval that slowest

rotor performs one full revolution, the faster or fastest rotors on the platform perform multiple rotations resulting in large aeromechanical data. Finally, for special conditions such as blade-vortex interaction dominated flight regimes, high resolution aeromechanical data is must-have in order to resolve BVI noise characteristics (Yucekayali et al., 2019). Depending on those facts, a forward time integration scheme is selected and utilized throughout this study as it is more efficient in case of large number of operations which is a natural outcome of complex rotorcraft motions, high resolution aeromechanical data of multiple rotor configurations. This outcome and decision are also supported by Mishra's (Mishra et al., 2016) and Bres's (Bres et al., 2004) works present in the literature.

5.3 High Resolution Wake for Acoustic Simulations

The performance of VVPM to provide foundation to rotorcraft aeroacoustics through generation of high resolution and accuracy, time dependent blade aerodynamic loads and motion data is assessed. Such high-resolution aeromechanics data requires significant computation time. Therefore, a variable time step calculation capability is developed and implemented, which provides the capability to vary solution time step i.e. azimuth step for rotor of interest during analysis to increase data resolution.

At validation chapter for the VVPM most of the time solution time step was set to time interval of 5 to 7.5 degrees rotor revolution. It is observed that such time step is enough to assess rotor total aerodynamic performance. However, on the other hand, when the time scale and the frequency spectra of interest is considered, accurate acoustic analysis require higher resolution aeromechanical loads and kinematics data. In this a scope an add-on to the VVPM is developed which varies the step size of the simulation after convergence of rotor loads and wake dynamics. Then with the decreased step size, at least one more full revolution is performed while recording all the required aeromechanical data for further acoustic calculations. Illustration of wake resolution increase algorithm is depicted in Figure 5.3 and Figure 5.4.

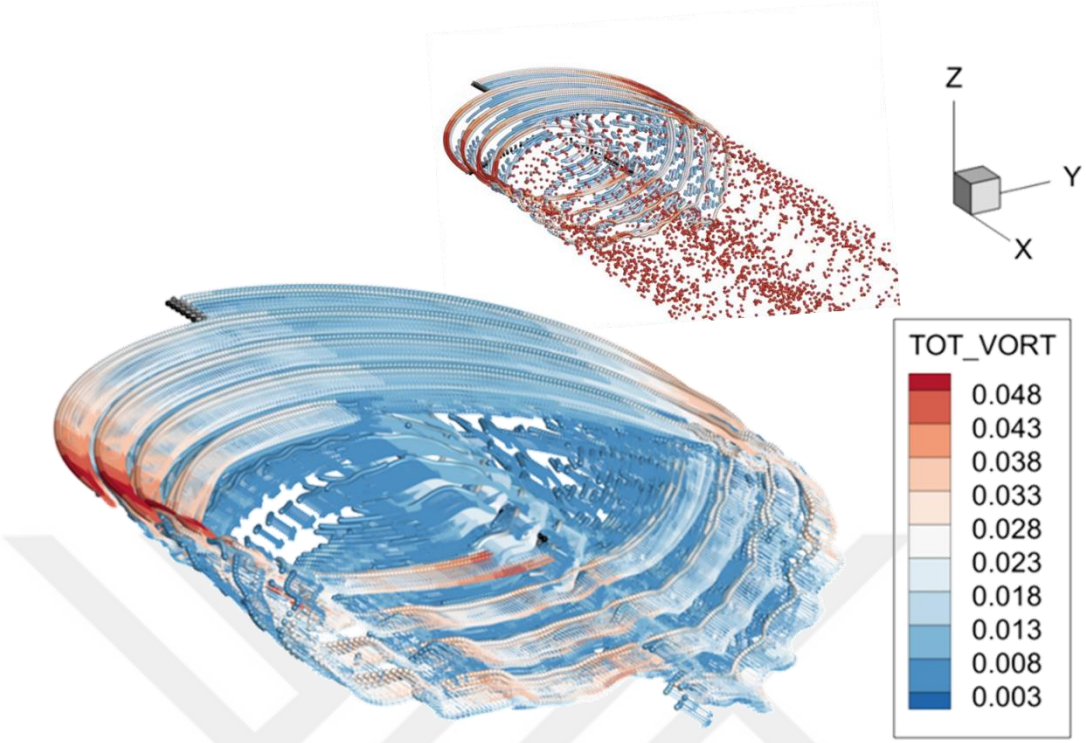

Figure 5.3 Increased wake and airloads resolution for aeroacoustics data

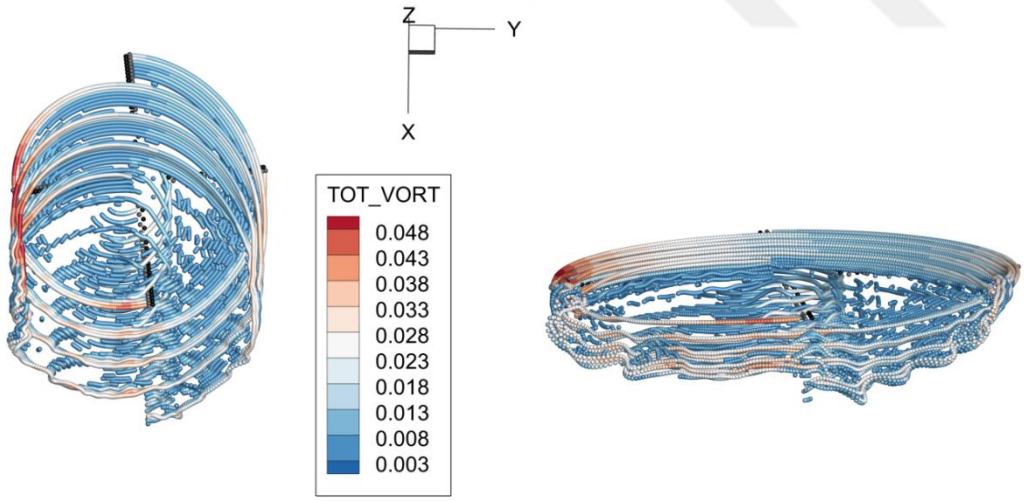

Figure 5.4 Increased wake and airloads resolution for aeroacoustics data

Although 1-2 degrees azimuth steps are generally sufficient for typical acoustic analysis, in order to accurately resolve noise characteristics of special conditions

such as blade-vortex interaction dominated flight regimes time steps small as 0.5 degrees azimuth intervals is essential (Bres et al., 2004).

VVPM simulations are performed with 20 & 40 spanwise blade sections and 360, 480 and 1440 (1, 0.75- and 0.25-degree azimuth steps) azimuth steps for sensitivity assessment as depicted in Figure 5.5. Analysis case is the HART-II test case (Wall, 2003) where BVI is dominant.

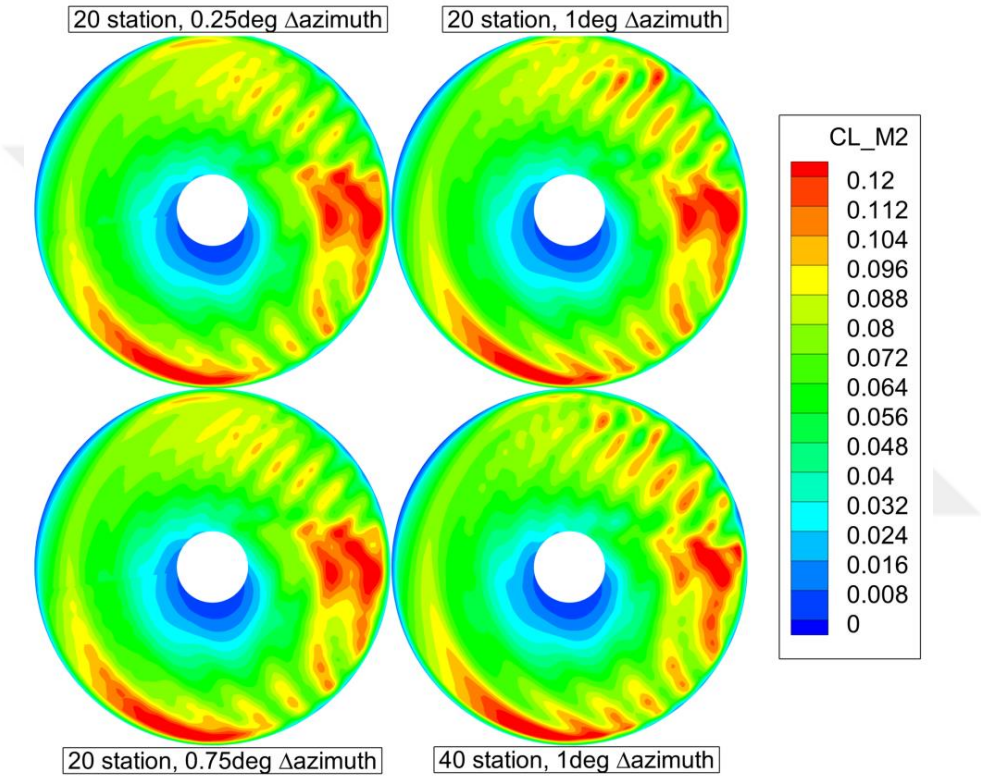

Figure 5.5 Sensitivity analysis for different spanwise & azimuth-wise resolutions.

It is observed that, solution methodology is robust and credible as increasing the solution resolution i.e. decreasing the azimuth steps has not a significant effect on rotor load distribution. Besides, with time step of 1 degree's azimuth intervals exhibits all the blade-vortex interaction wave fronts and is convenient to utilize in acoustic analyses.

5.4 Aerodynamics-Aeroacoustics Models Interface

Acoustic signature of a rotorcraft is a combined overall response of the coupled and complex aeromechanical environment that rotors/propellers operate in. This multi-disciplinary nature requires a comprehensive modeling to accurately estimate the dynamic and aerodynamic response of the platform. As the main input of an acoustic analysis is such aeromechanical data, for an accurate prediction of overall noise characteristics of a configuration, a comprehensive analysis approach is essential. Note that an acoustic analysis requires blade surface pressure distribution and variation in time. Although there are numerous comprehensive modeling codes in the literature alongside the one developed in this study, generally blade surface pressure distribution is not the concern of the comprehensive codes except limited number of concentrated loads distributed over the chord line. Besides the acoustic solver utilized in this study is primarily developed for CFD data covering blade surface pressure.

As Brentner discusses, calculating blade surface pressure is a difficult problem originating the difficulty in the determination of wake dynamics, shed & trailed vortices and their convention and determination of rotorcraft airloads within the complex aeromechanical environment during a steady or unsteady maneuvering flight regime (Brentner & Farassat, 2003).

Development of the VVPM approach and coupling with a rotorcraft mathematical model provided such comprehensive modeling capability with high fidelity, resolution, and accuracy airloads data. Yet, the blade loads are determined as spanwise distributed concentrated force and moments. Therefore, in this study, a methodology is proposed to distribute concentrated airloads into chordwise and spanwise pressure distribution. The proposed methodology is described in the following paragraphs.

First, particle induced, blade induced, and free stream velocities are combined to determine local total velocity vector, Mach number and effective angle of attack for each blade element as illustrated with Figure 5.6.

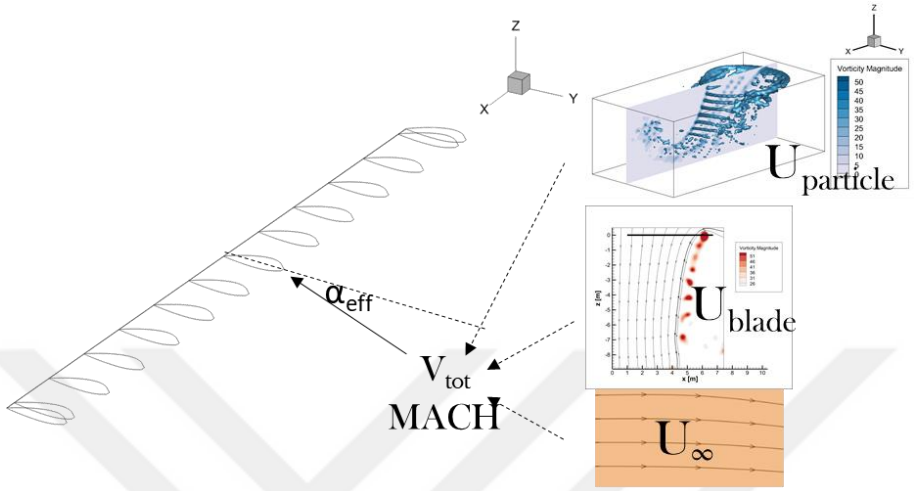

Figure 5.6 Total velocity vector and effective angle of attack illustration for blade sections

In parallel, blade sections & incorporated airfoil geometries are utilized to generate a structured cartesian surface mesh over the blade geometry as depicted with Figure 5.7.

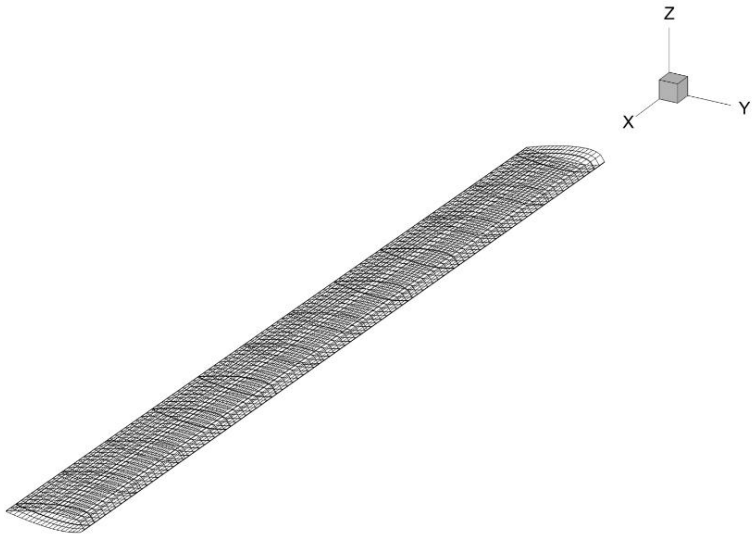

Figure 5.7 Blade surface geometry and surface mesh

Airfoil pressure database stored in terms of non-dimensional surface distance and pressure coefficient as illustrated with Figure 5.8 is then utilized with the effective angle of attack and local Mach number to determine chordwise pressure distribution at each blade section as illustrated with Figure 5.9.

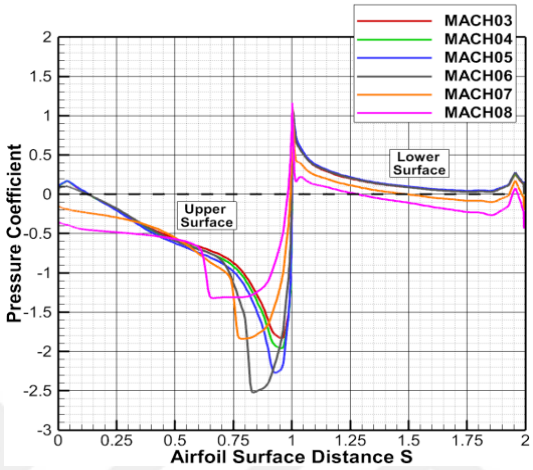

Figure 5.8 Airfoil surface pressure distribution stored as pressure database

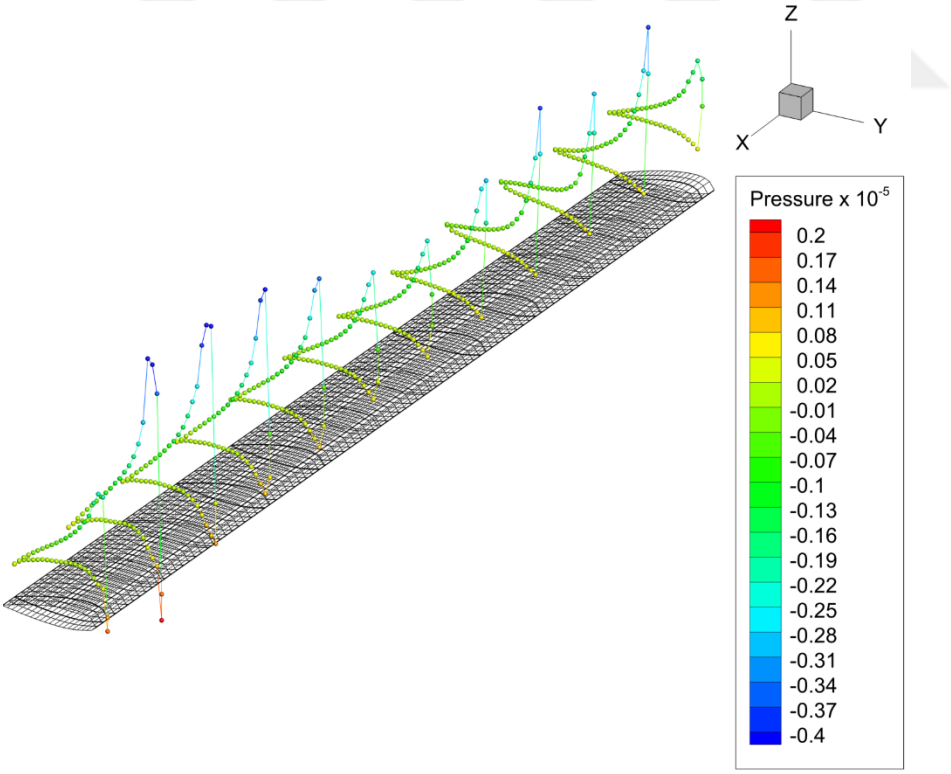

Figure 5.9 Chordwise pressure distribution at each blade section

Chordwise pressure coefficient distribution at each blade section interpolated from the pressure database is dimensionalized with local dynamic pressure. The 2-D pressure information at each blade section is then utilized to distribute pressure over the 3-D blade geometry/mesh as shown in Figure 5.10 at each azimuth location.

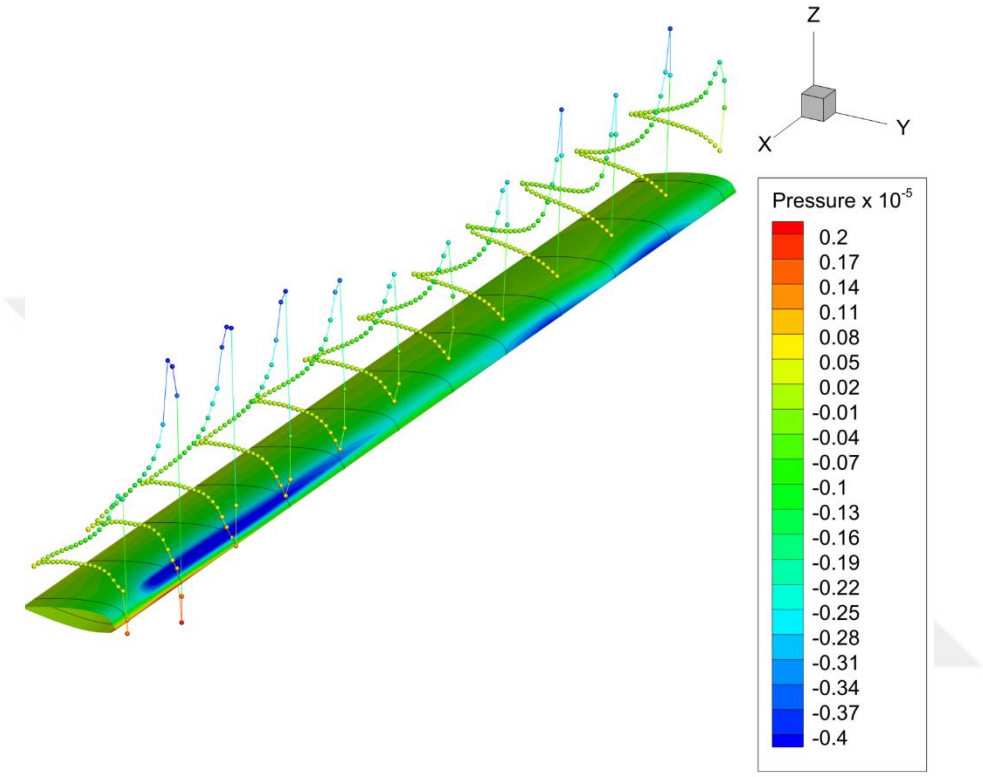

Figure 5.10 Pressure distributed over the blade geometry

Linear, cubic and polynomial interpolation algorithms have been implemented which exhibits similar performance at smooth and steady flight conditions. However, some aeromechanical phenomena such as Blade-Vortex interaction results in significant and sudden spanwise load variations in case of which cubic and polynomial interpolation approaches fail to capture the pressure peaks and alteration over the blade geometry. Linear interpolation is evaluated to be the best alternative to distribute pressure over the blade geometry from an arbitrary number of 2-D blade sections, yet, it requires a minimum number of input resolution i.e. blade section and azimuth step to successfully capture sudden load variations such as BVI induced peaks. Typically, it is observed that 20 spanwise blade sections distributed along 100

spanwise cells and 360 azimuth steps (1-degree steps) is enough to capture aerodynamic interactions.

Similarly, a sensitivity study is performed for chordwise cell resolution. In this scope, rotor blade is represented by 20 (20 upper, 20 lower, total 40), 40 (40 upper, 40 lower, total 80), and 60 (60 upper, 60 lower, total 120), chordwise cells, geometry and related pressure distributions are presented in Figure 5.11 to Figure 5.13. It is observed that, at least 40 chordwise elements is required to have an accurate geometric representation though 20 chordwise elements do not cause resolution loss.

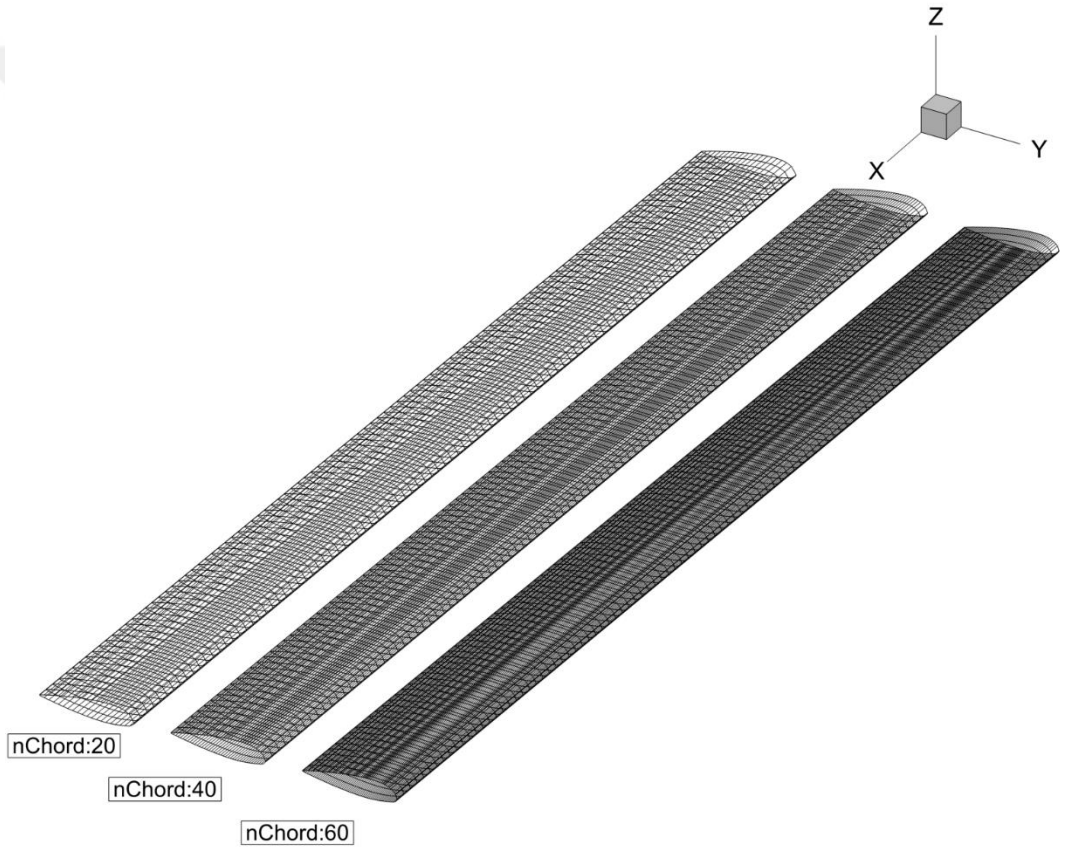

Figure 5.11 Blade geometric representation with different number of chordwise elements

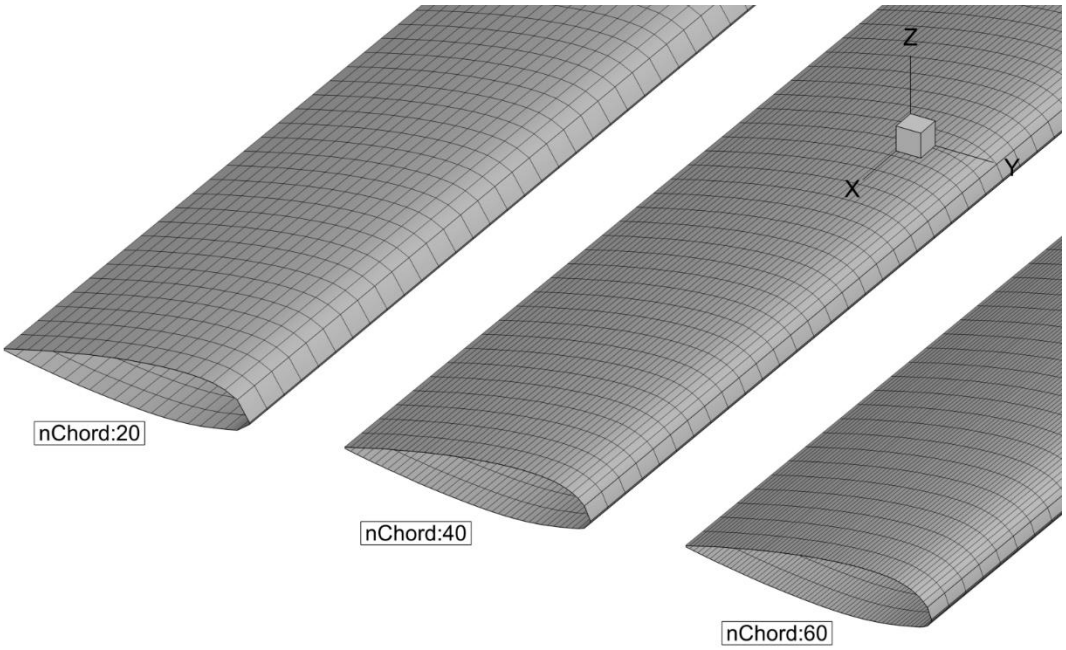

Figure 5.12 Blade geometric representation with different number of chordwise elements

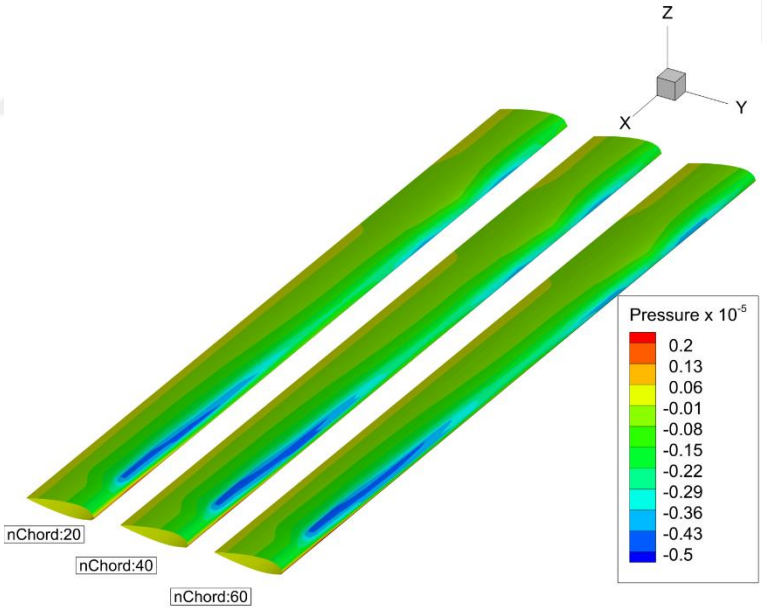

Figure 5.13 Comparison of distributed pressure over the blade geometry at different number of chordwise elements

Finally, rotor total thrust variation over one revolution determined with the VVPM rotor and determined from integration of the distributed pressure are compared in

Figure 5.14. It is observed that, accuracy loss of the proposed pressure distribution methodology is negligible in both 2-D (chordwise) and 3-D projections (spanwise).

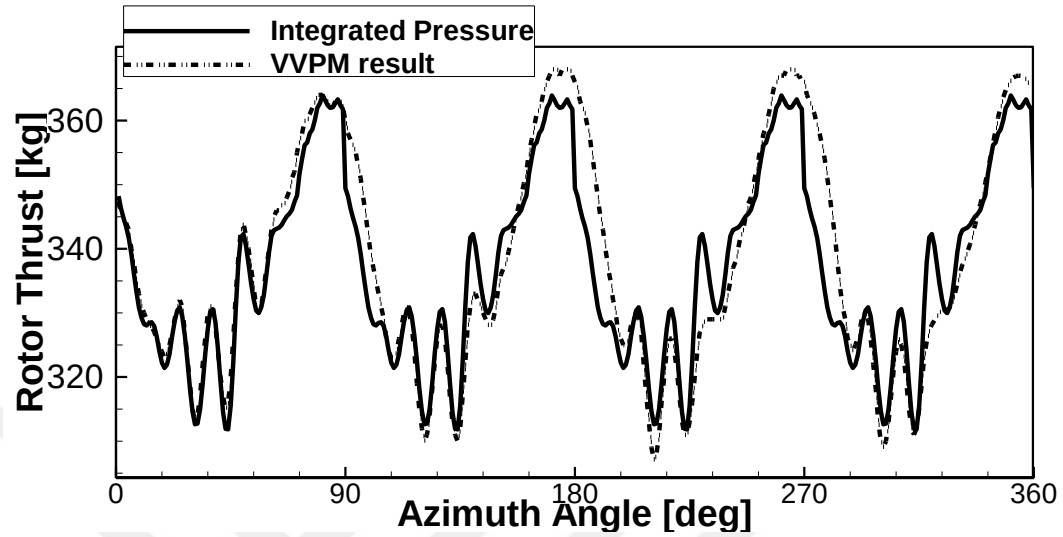

Figure 5.14 Rotor total thrust variation comparison determined with VVPM and Pressure integration over the blade surface

After computing the spanwise and chordwise pressure distributions over the real blade geometry at each desired azimuth location as illustrated with Figure 5.15, aeroacoustics solver computes for the acoustic pressure propagation at any desired observer location.

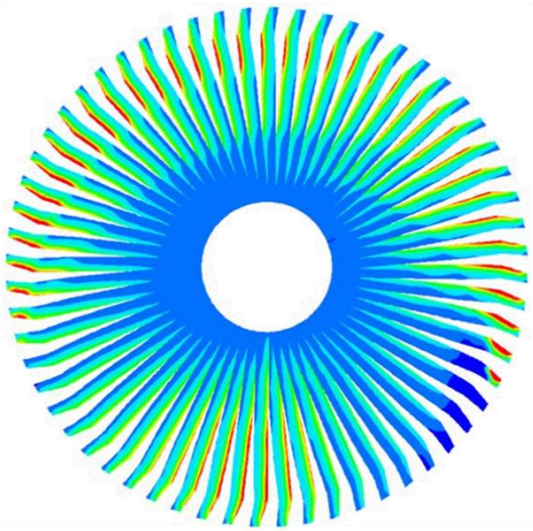

Figure 5.15 Blade pressure distribution at each azimuth location

In conclusion, the analysis and process steps for the VVPM coupled aeroacoustics model (VVPAM) is as follows:

1. *Rotorcraft trim analysis* ……..…….

   Trim analysis is performed with comprehensive rotorcraft model either with dynamic inflow model then utilize VVPM solution or directly with VVPM solution.

2. *Wake refinement* ……..

   Converged VVPM analysis is further continued with decreased time steps to generate high resolution aeromechanical (aerodynamics and kinematics) data.

3. *Pressure distribution*……..….

   High resolution airloads data is utilized to project concentrated airloads over blade geometry as pressure distribution through pressure database.

4. *Aeroacoustics analysis*……..
   Perform acoustic calculations separately for each rotor at any desired observer location.
5. *Superimpose*……

   Interpolate or superimpose multiple rotor acoustic solution to determine equally spaced, discretized, and total acoustic pressure variation at observer location.

6. *Post-Process*……
   Perform post-process computations to transform acoustic pressure into sound pressure level, perform FFT analysis to study frequency spectrum, determine sound exposure level or crease SPL acoustic contours as output.

5.5 Validation

Comprehensive modeling is an essential tool for rotorcraft aeromechanics, which studies not only rotor aerodynamic performance, efficiency, loads, vibration but also rotor aeroacoustics. For validation purposes of the developed VVPAM tool, variable time step option is utilized to provide aeromechanical data for HART-II test case to acoustic solver (TACO) and acoustic pressure variation is generated at an observer location below rotor disc at advancing side i.e. Microphone 11 at Wall's terminology (Wall, 2003). HART-II test case is a scaled version of BO-105 helicopter main rotor with rectangular blade planform, 2-meter radius and -8° linear twist. Analysis condition belongs to BL case having 0.15 advance ratio with 4.5° effective shaft tilt angle, i.e. shaft angle of attack (α_s). Model parameters are summarized in Table 5.1

Table 5.1 HART-II test case model

Parameters	**Values**
Rotor radius	2m
RPM	1041 rpm
Blade Twist	-8° linear
Precone	2.5°
Root-cut-out	22%
Number of blades	4
Airfoil	NACA23012, constant
Planform	Rectangular

After convergence is achieved with 7.5 degrees azimuth steps, one additional rotor revolution is performed to generate required loads data for acoustic analysis at 1 degree's azimuth step. Wake geometry and evolution for variable time step analysis of HART-II test case is depicted with Figure 5.16.

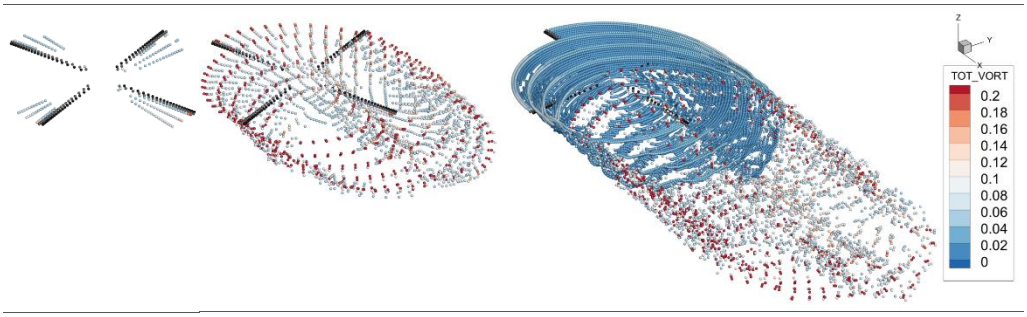

Figure 5.16 Variable step wake evolution, starts with 7.5 azimuth steps, ends with 1-degree azimuth steps

Aerodynamic load distribution over the rotor disc is determined with the increased resolution aeromechanical data. Then test versus analysis comparison is performed for a section at 86% spanwise location. Both are depicted in Figure 5.17. Analysis is performed for zero rolling and pitching moments. Blade is assumed rigid and wind tunnel wall effects are ignored.

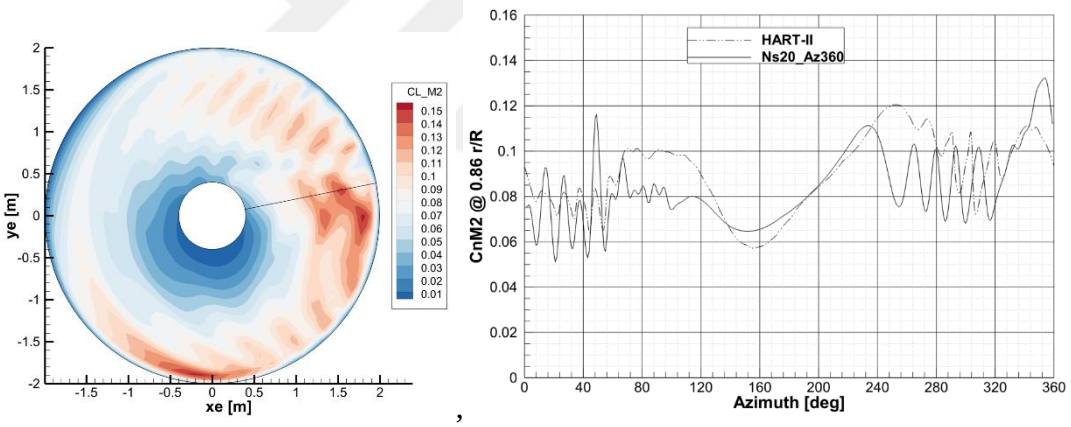

Figure 5.17 Load distribution on disc and test vs analysis comparison at a section at r/R=0.86

Acoustic solution is determined with the aeroacoustics solver (TACO) at the specified observer location and acoustic pressure variation is compared with test data in Figure 5.18. It is observed that both positive and negative pressure pulses arise from blade-vortex interactions are well captured which displays suitably of VVPM for rotorcraft aeroacoustics analysis purposes.

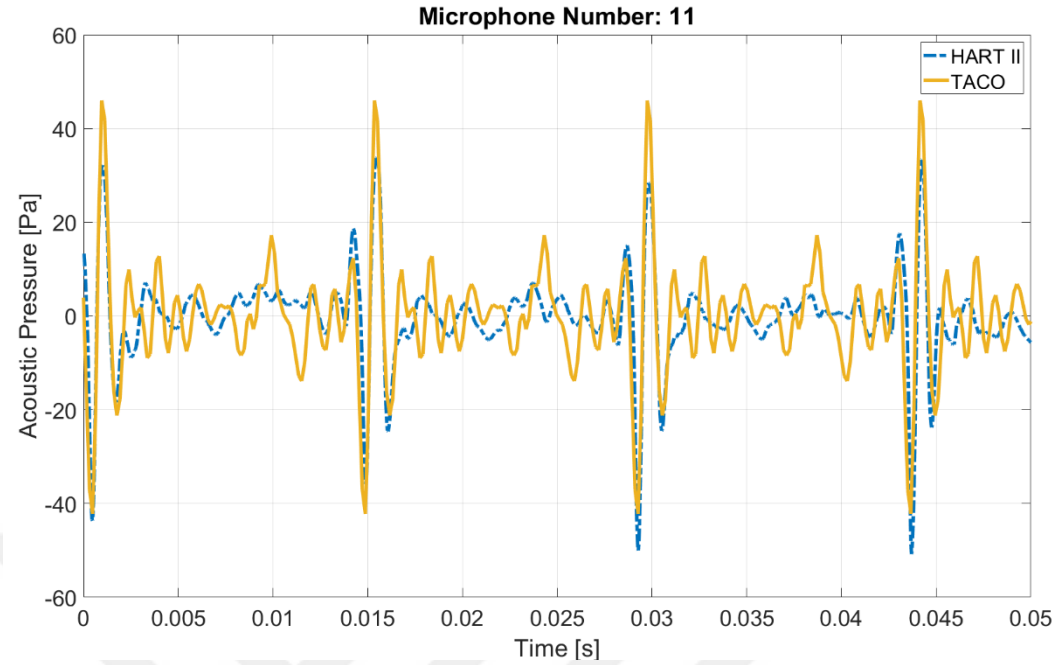

Figure 5.18 Acoustic pressure time variation, test vs analysis comparison

SPL contours at the plane 2 meters below the rotor disc are compared in Figure 5.19.

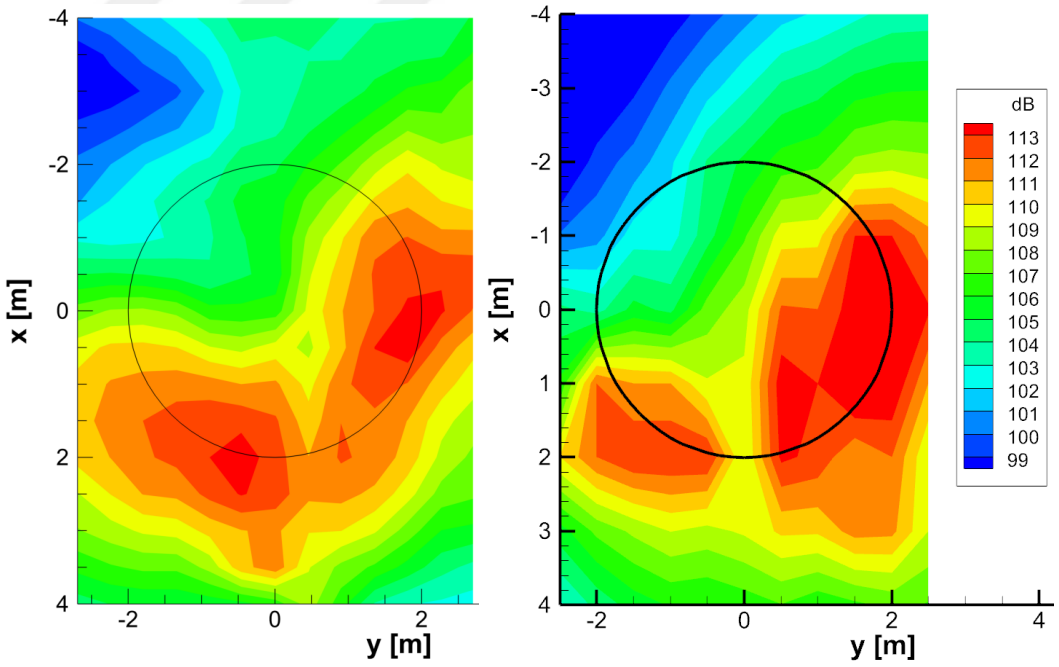

Figure 5.19 SPL contour at a plane below rotor disc, test (left) vs analysis (right) comparison

Further investigation on the acoustic response is done through splitting total noise into thickness and loading noise components and performing a frequency analysis (FFT) to assess the frequency spectrum of the specified noise contributions. Having a rotational speed of 1041 rpm and 4 blades, the principal frequency of the rotor is expected to be at 70 Hz. When the thickness noise frequency spectrum given in Figure 5.20 (left), a single peak at exactly 70 Hz is observed as expected. This is a natural outcome of the fact that the thickness noise is incorporated with blade kinematics at rotor rotational harmonic. When the loading noise frequency spectrum is given in Figure 5.20 (right), multiple noise peaks at 1,2,3, … N /per rotor harmonics as expected.

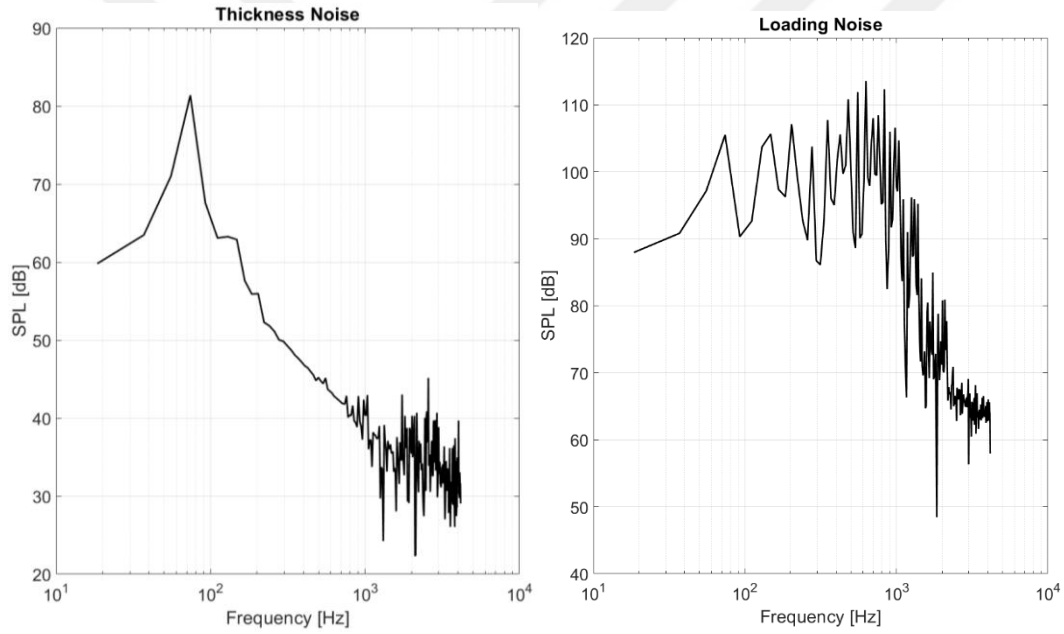

Figure 5.20 Thickness and loading noise frequency spectrum for HART-II case

Further assessment is performed through a similar frequency spectrum analysis is HART-II test data and comparison with total noise frequency response of the analysis as given in Figure 5.21.

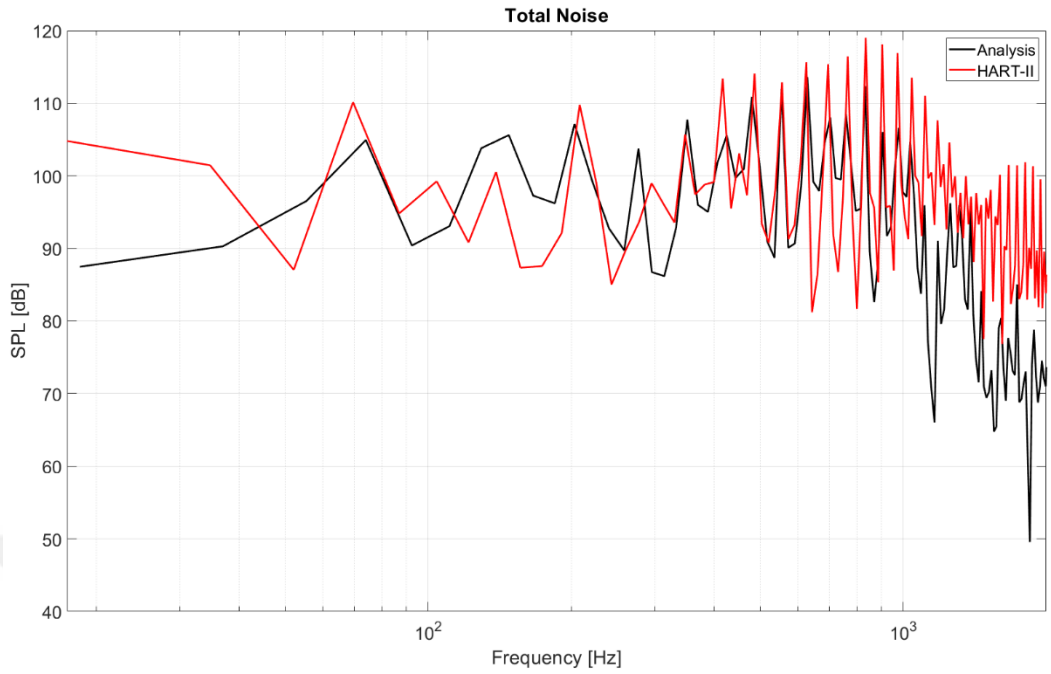

Figure 5.21 Frequency spectrum comparison of analysis with HART-II test data

5.6 Further Exploration of VVPAM

Additional further qualitative analyses are performed to evaluate capability, fidelity, accuracy, and resolution characteristics of the developed VVPAM tool. In this scope, acoustic contour time variation (unsteady) on ground surface for a trimmed level flight and a conventional full helicopter BVI noise investigation at an approach flight condition are performed.

5.6.1 Acoustic Contour at Ground for a Level Flight Condition

VVPAM capability is further assessed in terms of calculating acoustic wave propagation at ground surface. A conventional configuration helicopter is trimmed at level flight condition and sound pressure level contour variation with time is determined on ground surface. As illustrated with Figure 5.22 and Figure 5.23, total acoustic waves of a full rotorcraft configuration are propagating on ground surface.

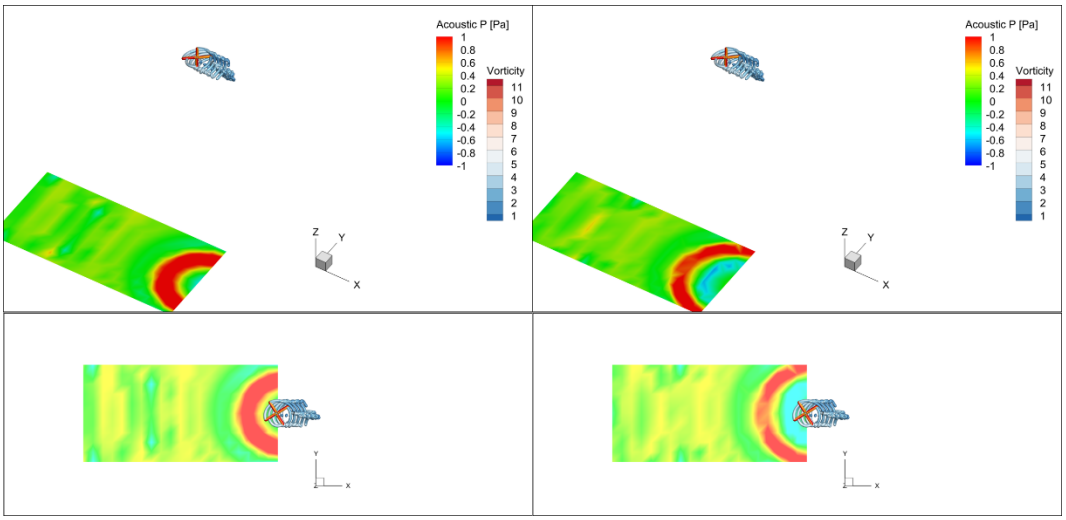

Figure 5.22 Acoustic wave propagation on a ground surface below 150m

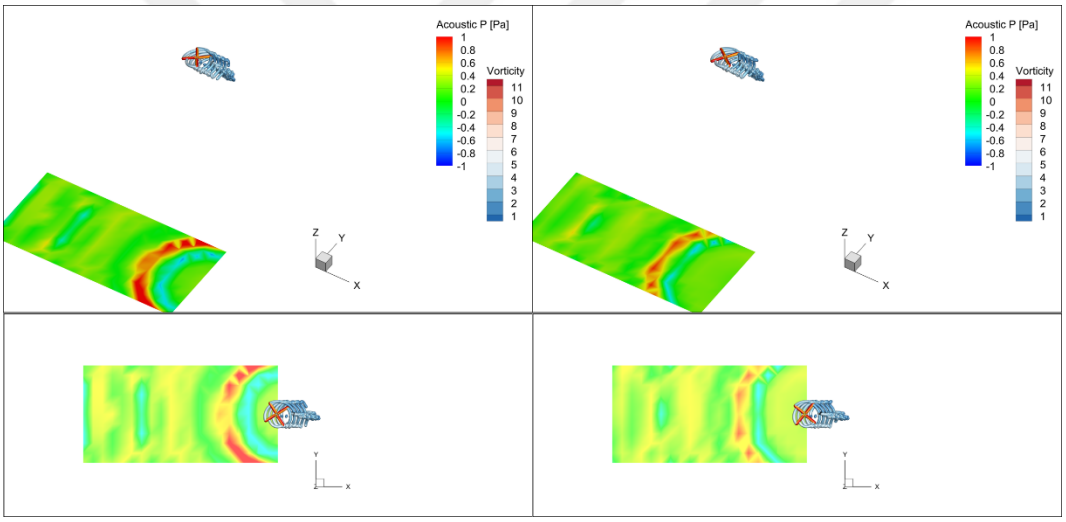

Figure 5.23 Acoustic wave propagation on a ground surface below 150m

5.6.2 Full Helicopter BVI Noise Study

The developed VVPAM approach is further tested with assessment of one of the most important phenomena in rotorcraft noise; the blade-vortex interaction (BVI) noise. When the vortices of the previous blades interact with the upcoming blades, the famous slapping noise is experienced, which dominates the overall noise levels of the whole rotorcraft. BVI produces a periodic, low frequency and distinct noise

peaks and can be considered as one of the most annoying characteristics of rotorcraft noise.

BVI noise can be decreased with advanced blade design, as the early attempts for reduction were concentrating the blade tip shape and the vortex generation as Prieur discusses (Prieur & Splettstoesser, 1999) back in the 1990's. On the other hand, BVI is a physical aeromechanical outcome of rotating blades and can be eliminated entirely. However, designating clearly, abetment of BVI dominated flight regimes can be achieved if those flight regimes are identified beforehand which is basically the essence of this dissertation.

In order to evaluate and identify BVI flight regimes and noise outcome of the related interactions which is specific to each rotorcraft configuration, an accurate representation of the rotor/blade dynamic response and wake dynamics is essential for a full rotorcraft free flight trim analysis. The VVPAM approach developed in this study has proved itself in terms of accurate and high-fidelity wake simulations, aerodynamic performance and loads calculations and aerodynamic noise analysis of rotor/propellers including BVI noise.

In this chapter, the developed VVPAM is further assessed at full helicopter BVI dominated flight regime in terms of trim analysis, wake and noise simulations in order to evaluate the accuracy and fidelity of the VVPAM and to develop a better understanding for a BVI regime, the interaction between the vortices and blades and the slapping noise.

In this scope, a conventional helicopter is trimmed in an approach flight condition which is anticipated to be a BVI regime. Analysis is performed at 100 knots air speed with 6 degrees descent condition as illustrated in Figure 5.24. The observer is located 100 meters ahead and 150 meters below helicopter c.g. Acoustic analysis is performed for one full revolution of main rotor and blade vortex interaction locations incorporated with the acoustic response is investigated.

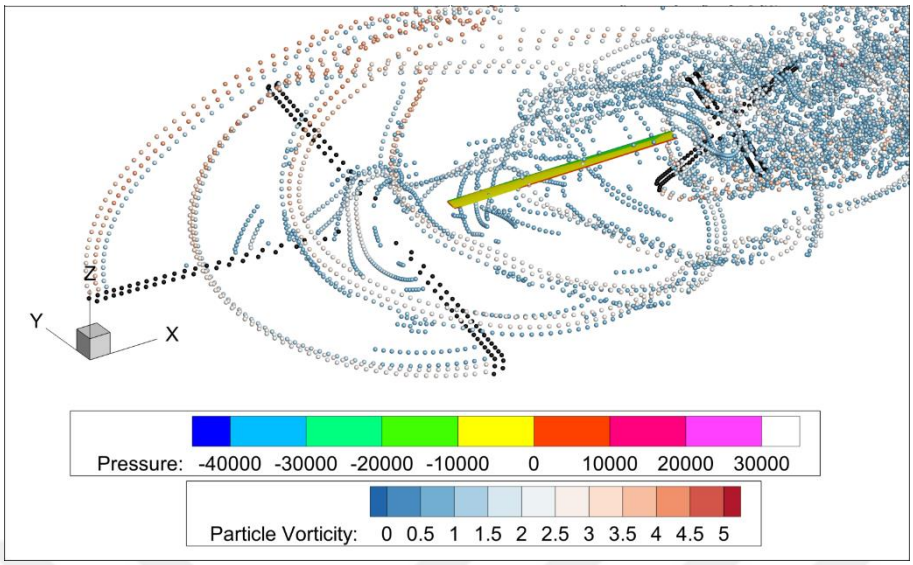

Figure 5.24 BVI condition full helicopter trim

Thickness noise (monopole) and loading noise (dipole) pressure response corresponding to the BVI condition acoustic analysis are given in Figure 5.25.

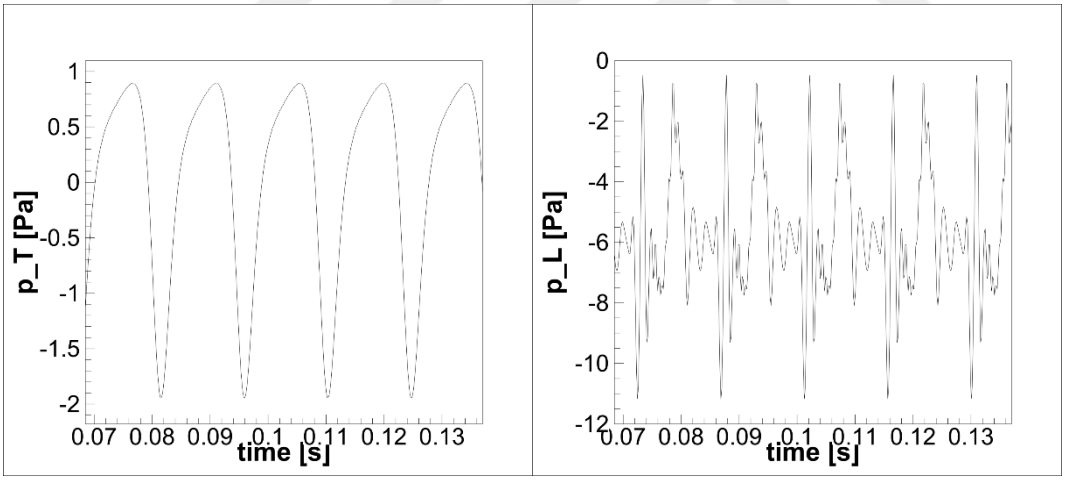

Figure 5.25 Main rotor thickness and loading noise, acoustic pressure response

Total acoustic pressure response of the BVI condition, in other words superposition of the pressure fluctuations of thickness and loading noise is given in Figure 5.26.

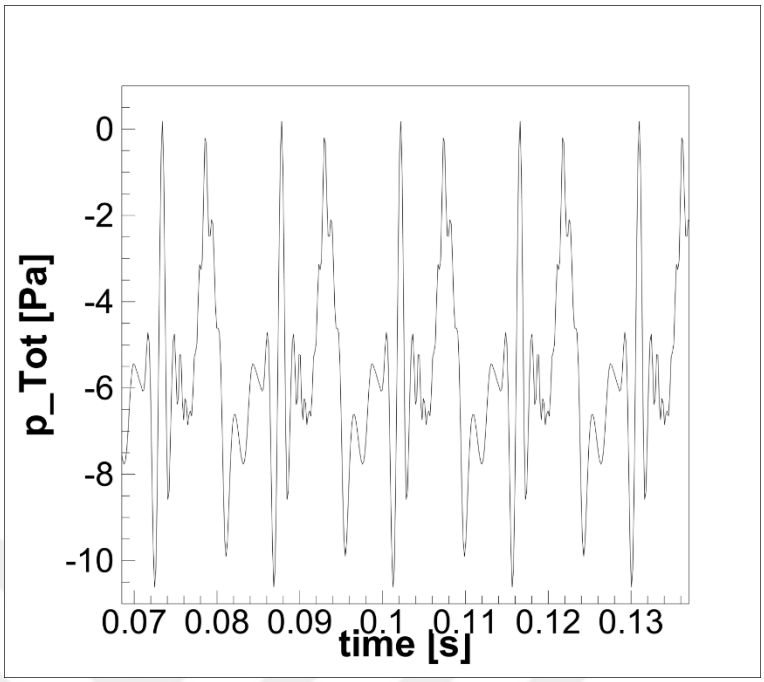

Figure 5.26 Main rotor total acoustic pressure response

When the acoustic pressure variation within a revolution of the main rotor is considered, it is observed, that there exist various pressure peaks all originated from blade-vortex interactions at different azimuth locations. In order to decompose the pressure peaks and incorporate with blade-vortex interaction instances, the wake interaction history of a single blade is studied, and it is observed at least five strong vortex interactions take place in a single rotation. Then, the acoustic response time is synchronized with the rotor solution, and the five vortex interactions are correlated with the pressure peaks in the acoustic signal. The observed BVI instances are one at advancing side, one at 180° azimuth, two around retreating side and one at around 350° azimuth. All the five identified blade-vortex interaction instances are marked on the acoustic pressure response given with Figure 5.27 are illustrated in Figure 5.28, Figure 5.29, Figure 5.30, Figure 5.31 and Figure 5.32.

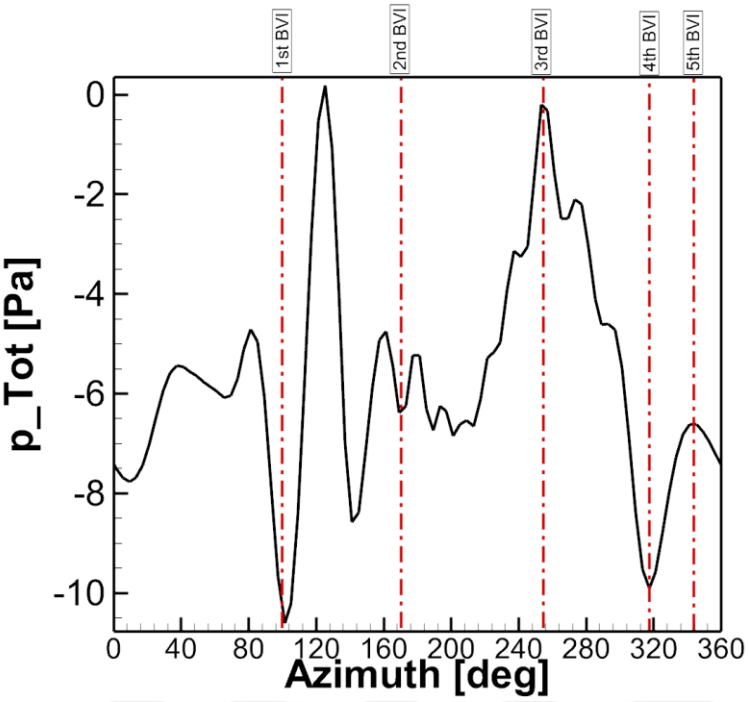

Figure 5.27 Acoustic pressure response for a single blade for one full revolution and identified BVI instances

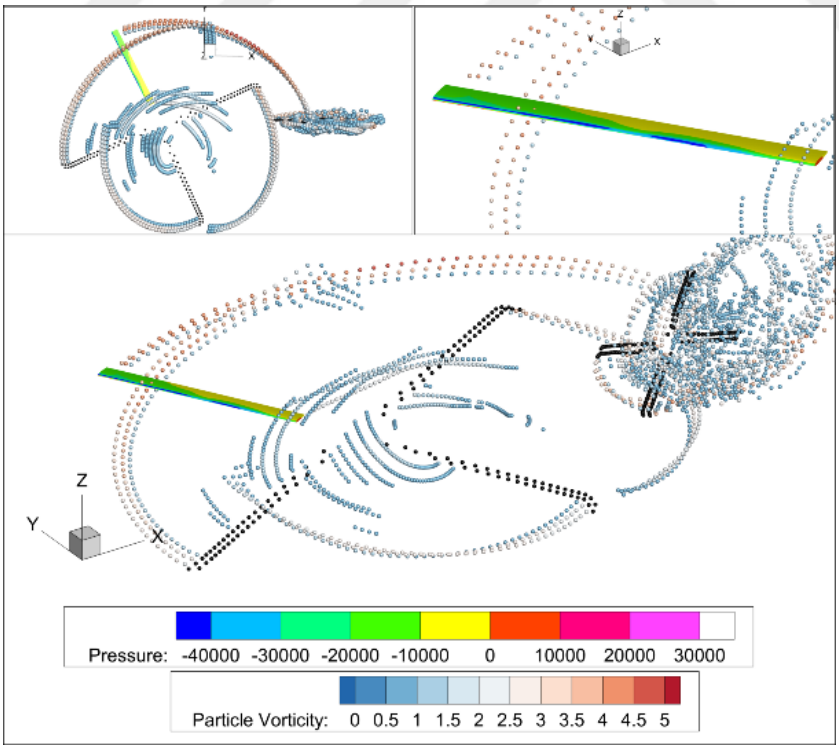

Figure 5.28 1st BVI instance, advancing side

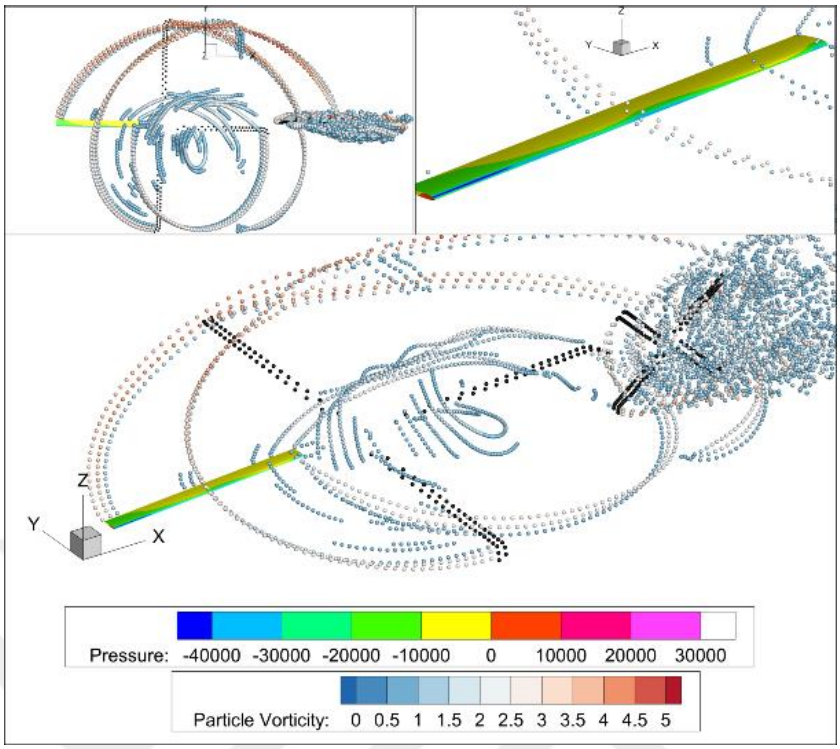

Figure 5.29 2nd BVI instance, around 180° azimuth

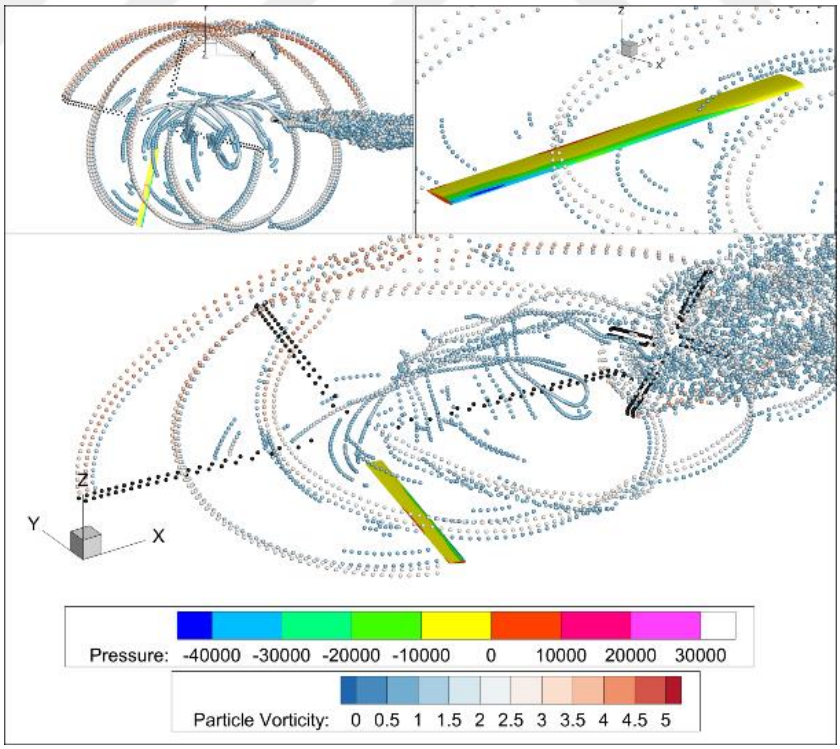

Figure 5.30 3rd BVI instance, around retreating side

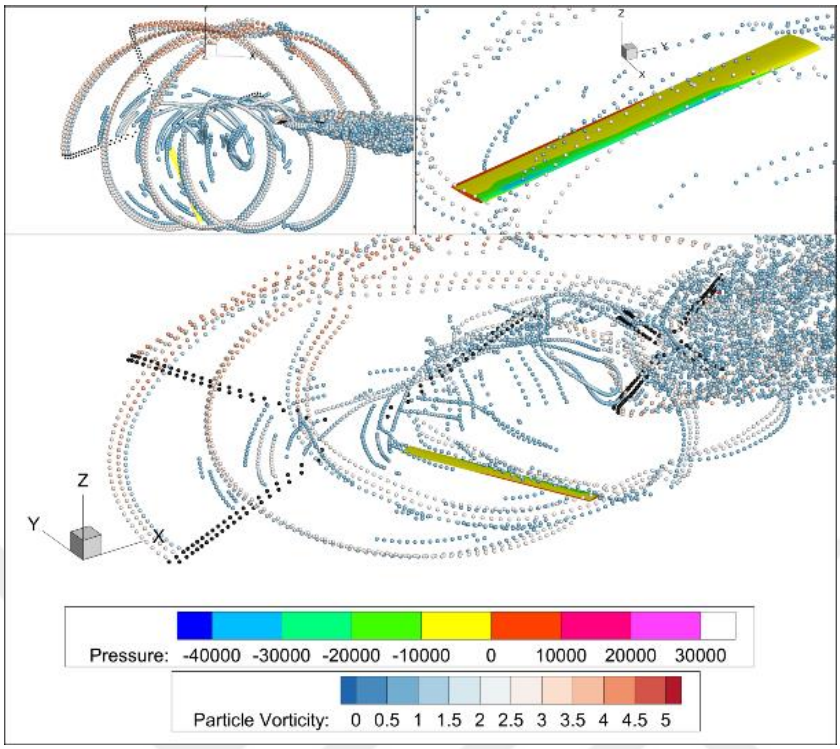

Figure 5.31 4th BVI instance, around retreating side

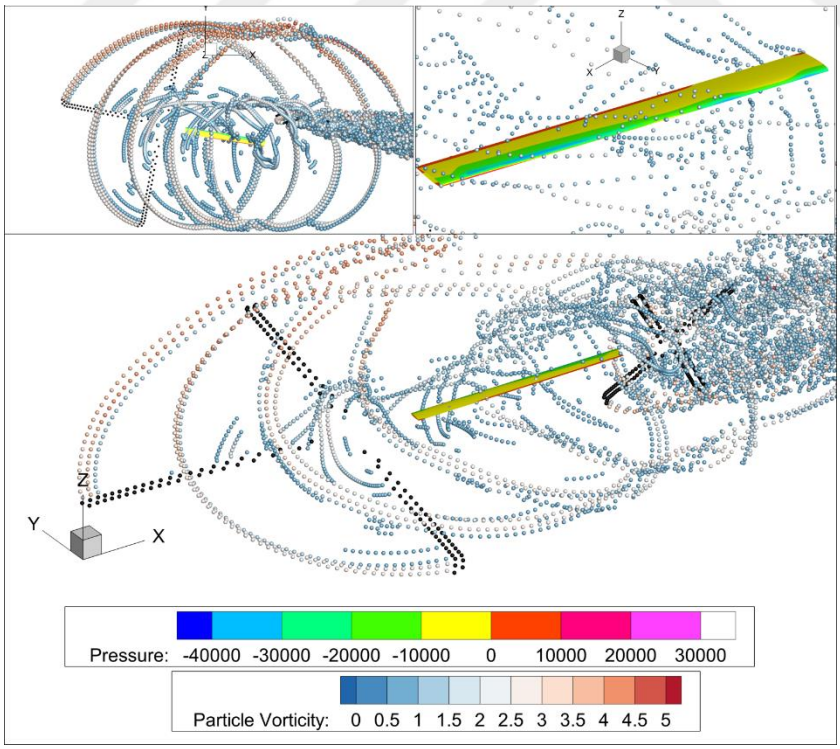

Figure 5.32 5th BVI instance, around 350° azimuth

CHAPTER 6

SIMULATION MODEL

Simulation model covers rotorcraft non-linear mathematical model, noise model (a surrogate model) and terrain model coupled together to generate real time flight dynamics simulation of the platform while providing acoustic calculations at ground surface or multiple observers. A SAS is implemented over the mathematical model to stabilize the instable non-linear system though when the model predictive control is active, the SAS is not required. Flight dynamics behavior for a circular trajectory and related acoustic spheres are illustrated with Figure 6.1.

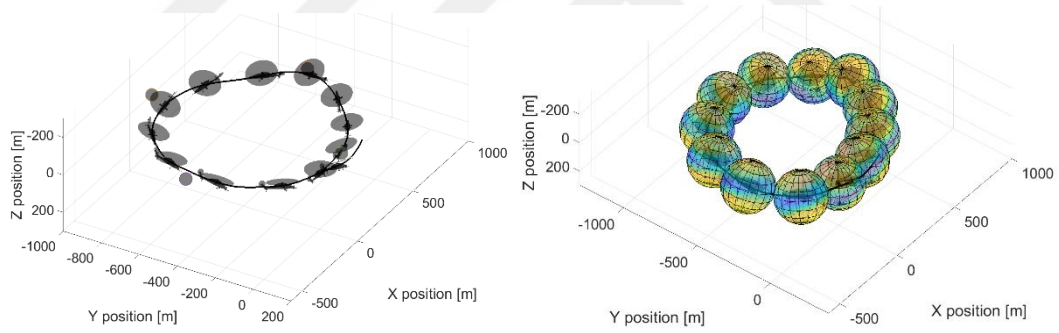

Figure 6.1 Rotorcraft comprehensive model equipped with acoustic sphere

Noise model is composed of pre-determined acoustic sphere database generated for varying flight path angle (covering descent, climb and sideslip conditions), take-off weight and flight speeds. Terrain model is a surface mesh representing the ground surface, where for each node acoustic calculations are performed to generate SPL contour and feedback to objective function is provided.

6.1 Comprehensive Mathematical Model

The multidisciplinary nature of a rotorcraft requires calculation of performance, trim, rotor blade motion, airloads, and structural loads as well as flight dynamics combined and coupled for estimation of aeromechanical behavior. Best representation of a rotorcraft is done through comprehensive modeling which requires a balance between fidelity and practicability yet a high level of technology (Johnson, 2013a). As estimation of acoustic response of a rotorcraft requires combination of all such disciplines, a comprehensive modeling approach is of interest in this study. In this scope, a non-linear mathematical model covering a wide range of rotorcraft problems, capable to calculate rotor aerodynamic performance and loads is utilized to provide flight dynamics response of the prediction model and plant.

The nonlinear and generic rotorcraft mathematical model utilized in this study was developed under the master's study in METU at 2017 (Şenipek, 2017). Since then, the mathematical model is utilized, modified and improved within various studies such as coupling with CFD for improved actuator surface development, (Yücekayali et al., 2018), coupling with aeroacoustics solver for noise modeling (Yucekayali et al., 2019), coupling with a model predictive control approach for rotorcraft agility assessment (Şenipek et al., 2019; Yücekayali, Şenipek, & Ortakaya, 2019) and for trajectory optimization purposes (Yücekayali et al., 2017) or even utilized for fixed-wing propeller aircraft aeroacoustics impact (Şenipek et al., 2017).

The mathematical model is compiled as a .dll library over which optimal control developments are performed in this dissertation. Additionally, the mathematical model is modified to be coupled with the VVPM to generate a comprehensive modeling framework with higher fidelity and accuracy.

The modular structure of the utilized mathematical model enables to elaborate desired rotorcraft components at higher detail while to simplify the rest providing a useful flexibility in modeling. Combined with the object-oriented nature, mathematical model provides an environment to populate rotor configurations and

compound them with main body of the rotorcraft enabling simulation of multi-copter or the booming electric VTOL configurations. All aerodynamic and inertial force and moment contributions from rotors, propellers, fuselage, empennage, and wings are determined at their related locations then transformed and transferred to aircraft total center of gravity. Combining all force and moments at aircraft center of gravity, enables one to solve the equations of motion for translational and rotational accelerations. The trim algorithm computes for overall equilibrium whereas the simulation model numerically integrates the equations for time response of the system. Then relative motion of each component transformed back to incorporated reference frames to further compute individual dynamic response.

Illustration of modular structure of the mathematical model is depicted in Figure 6.2. “Main Frame” is the base model and acts as a collocation module, taking pilot and controller inputs, distributing boundary conditions, inputs, relative motion and air velocity to each component and collecting response of each rotorcraft component. Then performs time integration or co-operates with trim module for simulation or trim analysis.

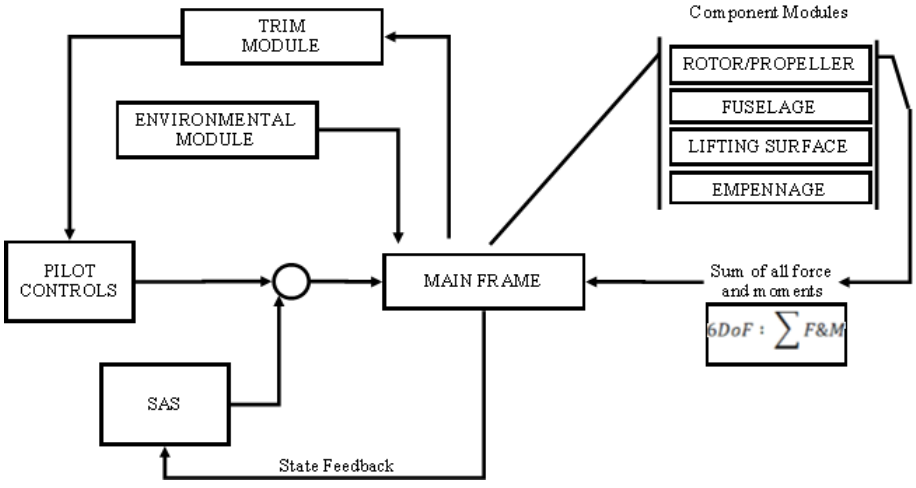

Figure 6.2 Illustration of modular structure

Environmental module determines air properties at the operating environment and provides required dynamic parameters during simulation. The atmospheric states such as pressure, temperature and humidity can be either defined as desired or

calculated through standard atmospheric properties. The speed of sound and absorption related parameters are then determined accordingly and utilized in aerodynamics and aeroacoustics calculations.

Components modules are the physical rotorcraft components such as rotors, propellers, wings, fuselage, horizontal and vertical tail as well as engine that cluster together to represent rotorcraft configuration. Typical components of a conventional configuration are illustrated with Figure 6.3.

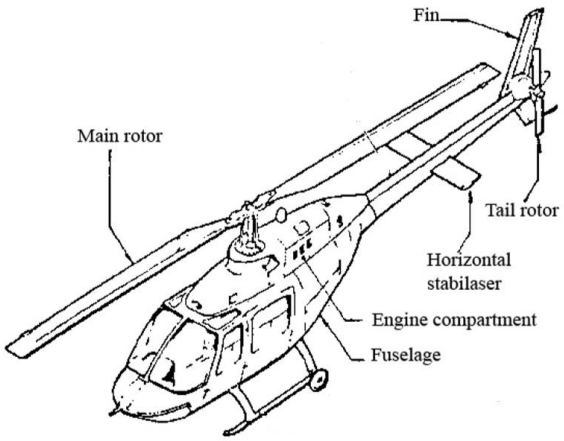

Figure 6.3 Main components of a typical rotorcraft – conventional configuration (Şenipek, 2017)

Rotor/propeller module is the foremost component for a rotorcraft mathematical model. As being the main force and moment source of a rotorcraft, the accuracy and fidelity of the mathematical model depends on the accuracy and fidelity of the rotor model. Most of the computation effort is spent in this component where inflow distributions, blade dynamic behavior, wake geometry and total aerodynamic force and moments are predicted according to the desired detail. A typical blade element method is implemented for rotor analysis where inflow dynamics can be either determined through dynamic inflow model (Peters et al., 1987; Peters & He, 1989, 1995) or VVPM approach. Utilization of inflow models is basically sufficient for trim analysis or overall performance analysis of a rotorcraft Rajmohan (Rajmohan et al., 2011), whereas the utilization of VVPM in rotor modeling provides time accurate

simulation of the rotor which is essential for maneuvering flight conditions. Rotor dynamics is resolved like the methodology presented in chapter 4.2. The rotor dynamics model provides 2nd order coupled flapping and lagging dynamics. Effect of blade inertial parameters and hub parameters such as blade weight, inertia, hinge-offset, root-cut-out, dampers, springs and delte-3 angle are included in the model. Rotor component includes rigid blade with non-uniform chord, sweep, twist distributions and two dimensional viscous, compressible airfoil aerodynamic databases. Empirical/analytical models are integrated to represent tip effects, blade sweep, stall due to rotation and yawed flow.

Empennage is another important component class for rotorcrafts as accurate modeling provides accurate controllability, static and dynamic stability assessments. The empennage component cover horizontal tail and vertical tail provides lift, drag and moment to overall platform, if exists, related to airspeed, flight path angle, angle of attack and Euler angles of the platform. If dynamic inflow model is selected for the analysis, the downwash effect on the empennage can be calculated with wake skew angle and a tube within where the downwash speed changes with the distance to center of the hub. If VVPM is selected for the analysis, the induced velocity is inherently calculated through contribution of each vortex particle in the domain.

Fuselage model implemented through an aerodynamic database consisting of 6 DoF force and moments either in wind axis or body axis, is responsible for calculations of aerodynamic force and moments, rotorcraft total gravitational force vector and total inertial moments.

All the rotorcraft components are collocated under a base object, which collects all force and moments from each component, solves equations of motion for whole system, keeps the operating condition information, translational and rotational motion and acceleration, and communicates with the “integrator” object on behalf of the whole platform. The “integrator” object performs time integration, solves the state space equations, and performs trim calculations. The class diagram and dynamic system inputs/outputs and integrator objects are illustrated in Figure 6.4.

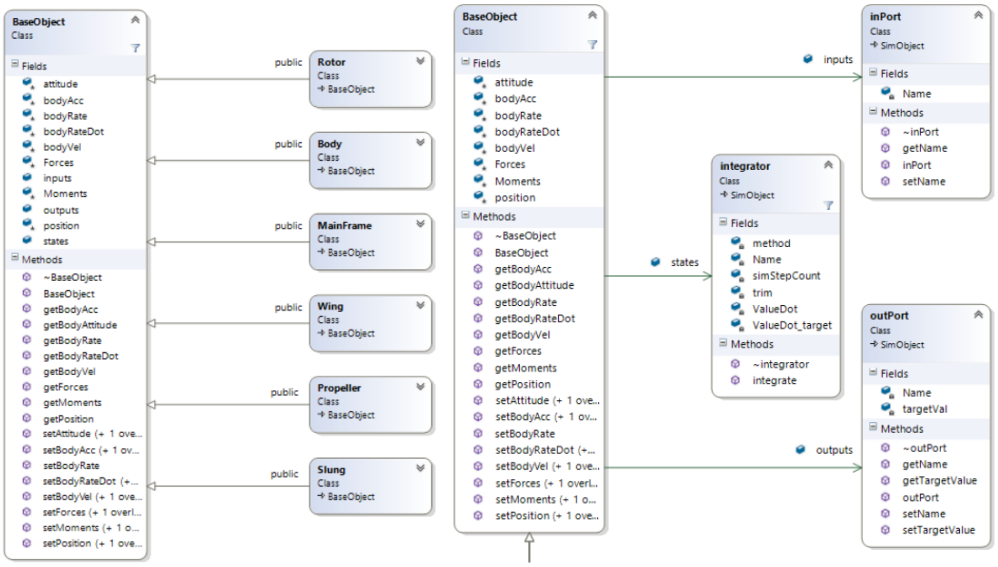

Figure 6.4 Left: Class diagram of BaseObject Class and its child objects, Right: Dynamic system inputs, integrator and output classes (Şenipek, 2017)

There as six essential class objects to build up a rotorcraft namely: rotor, body, main frame, wing, propeller and slung. Each class has its own specific functions and models and operates under the base object. The base object manages all the components, through setting the initial condition, boundary condition, convergence criteria and calculation methods specific to each component and collects the outputs.

6.1.1 Trim

Isolated rotor trim was mentioned at chapter 4.3. This chapter covers full rotorcraft free flight trim, though both has similar basis. Trim for a free flight condition can be defined as a 6 DoF dynamic equilibrium around c.g. of the platform, providing permanence of the state and state derivatives in the absence of external excitations such as additional control inputs, gust or instability.

To determine a trim state, all force and moments generated through each rotorcraft component such as rotors, propeller, fuselage, empennage, and wings are collected at center of gravity of the configuration which are then utilized to solve equations of motion. Trim and simulation operate over the same procedure. Following the

solution of the flight dynamics equations, translational and rotational acceleration are iterated to achieve target values for trim whereas integrated in time for simulation.

Newton's unconstrained optimization algorithm is utilized to determine trim state of a rotorcraft. First, the relation between inputs, rotorcraft states and outputs are correlated through state space representation of the system. Then perturbing the state derivatives and outputs with states and inputs, sensitivity matrix or the Jacobian is determined. Then the relation between model and variables of the trim state is correlated through the J with equation (74).

$$\begin{bmatrix} {dx}/{dt} \\ y \end{bmatrix}_{model} = \underbrace{\begin{bmatrix} {\partial \dot{x}}/{\partial x} & {\partial \dot{x}}/{\partial y} \\ {\partial y}/{\partial x} & {\partial y}/{\partial u} \end{bmatrix}}_{JACOBIAN\ (J)} \begin{bmatrix} x \\ u \end{bmatrix}_{variable} \tag{74}$$

Then the error between the target states and reference states can be defined as;

$$E(\tilde{x}) = \begin{bmatrix} {dx}/{dt} \\ y \end{bmatrix}_{model} - \begin{bmatrix} {dx}/{dt} \\ y \end{bmatrix}_{desired} \tag{75}$$

Or utilizing equation (74) with equation (75) the error array is defined as;

$$E(\tilde{x}) = \underbrace{\begin{bmatrix} {\partial \dot{x}}/{\partial x} & {\partial \dot{x}}/{\partial y} \\ {\partial y}/{\partial x} & {\partial y}/{\partial u} \end{bmatrix}}_{JACOBIAN\ (J)} \begin{bmatrix} x \\ u \end{bmatrix}_{variable} - \begin{bmatrix} {dx}/{dt} \\ y \end{bmatrix}_{desired} \tag{76}$$

The trim algorithm, i.e. Newton algorithm tries to minimize the error between model response and desired i.e. reference states and outputs. In other words, the unconstrained optimization algorithm seeks a feasible set of $\begin{bmatrix} x \\ u \end{bmatrix}_{variable}$ that results in $E(\tilde{x}) = 0$. The search is performed with an iterative process, where at each iteration a $\Delta \begin{bmatrix} x \\ u \end{bmatrix}_{variable}$ is estimated and superimposed on the previous value with a relaxation. The delta state and inputs determined through equation (77) is

$$\Delta \begin{bmatrix} x \\ u \end{bmatrix}_{variable} = -J^{-1} E(\tilde{x}) \tag{77}$$

$$\begin{bmatrix} x \\ u \end{bmatrix}_{variable}^{k+1} = \begin{bmatrix} x \\ u \end{bmatrix}_{variable}^{k} + R\Delta \begin{bmatrix} x \\ u \end{bmatrix}_{variable}^{k} \quad (78)$$

where R is the relaxation array, except complex trim cases, unity is observed as sufficient.

Two fidelity levels are set for full rotorcraft free flight trim approaches. One is with utilization dynamic inflow models, which provides harmonic load variation, interaction free inflow dynamics with simplified distribution over the rotor disk, therefore fast and straightforward for trim purposes. Second is with utilization of VVPM for rotor/propellers, providing higher fidelity aerodynamic loads, including rotor-rotor, rotor-wake interactions, requires longer analysis time for loads and wake dynamics to converge. The best approach for having a trimmed free flight condition with VVPM providing utmost complexity and fidelity is to first determine a trim condition with dynamic inflow model then switch to VVPM and use that trim state as initial condition and target. Such approach is illustrated for hover flight condition of a typical conventional configuration helicopter in Figure 6.5. The initial trim condition is set as input for the VVPM full helicopter analysis for at least 200 time steps in order to have the rotor wake to initiate and evolve to some aspect, then the trim algorithm switches to VVPM trim where around 400 time steps are sufficient to reach trimmed flight condition. It can be observed that within the initialization stage i.e. first 200-time steps, rotor dynamics coupled with the VVPM starts to determine TPP dynamic response then the convergence accelerates with the trim switch. The rotor loads transferred to the fuselage through rotor shaft are filtered with a moving average filter as depicted in Figure 6.6 as described at chapter 4.3 as the mean loads are the concern for a trim condition where the higher N/per harmonics are considered as the vibratory loads that have negligible effect on rotorcraft flight dynamics.

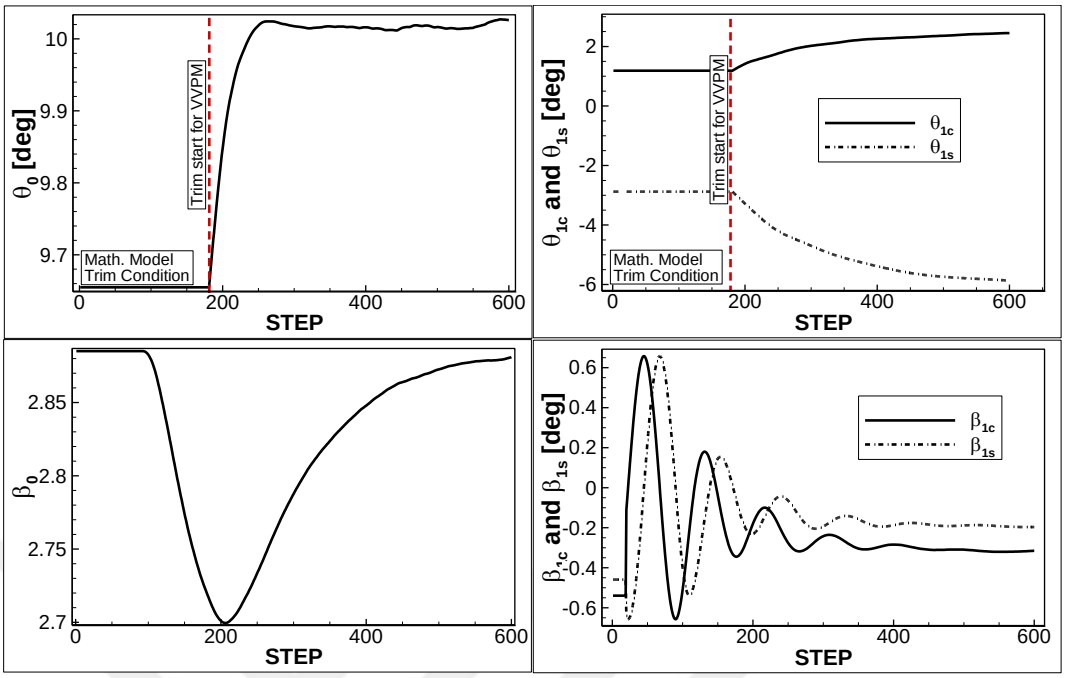

Figure 6.5 Trim switch from dynamic inflow to VVPM at hover

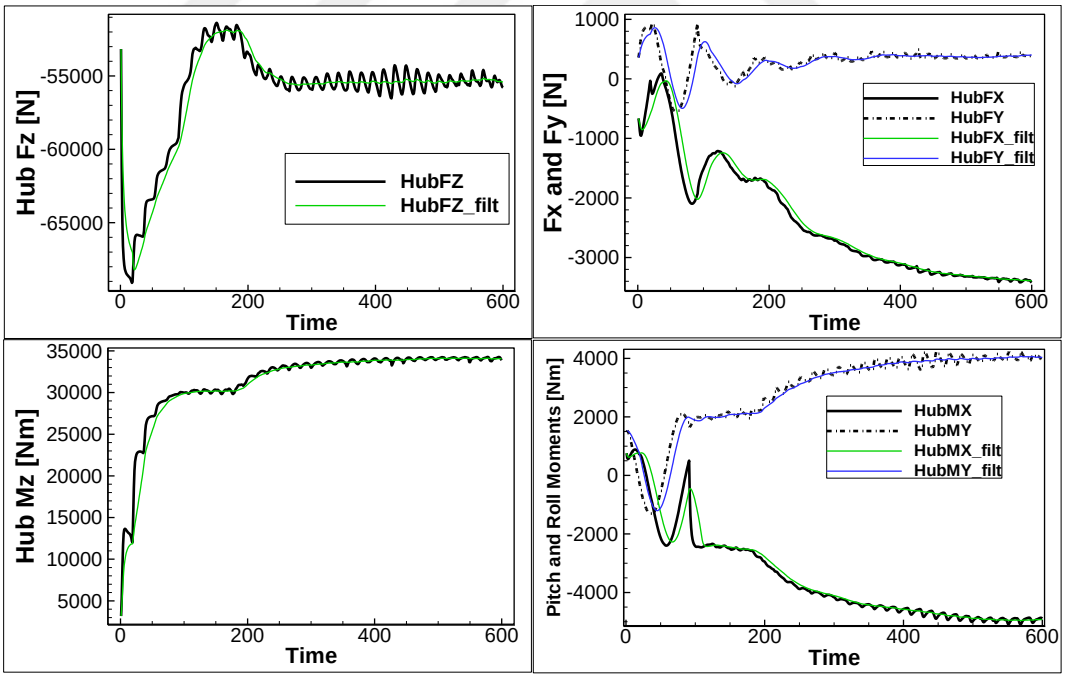

Figure 6.6 Filtered rotor loads for utilization in trim iteration

Eventually, with the trim approach developed in this study, any free flight trim condition for any rotorcraft configuration can be determined with initialization using

dynamic inflow models then switching to VVPM. Consequently, a trim analysis such as the one illustrated with Figure 6.7, including all the aeromechanical interactions and wake, inflow and blade dynamics can be achieved.

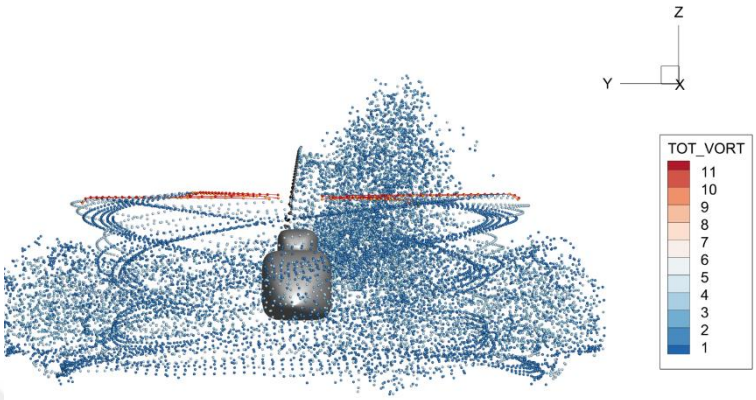

Figure 6.7 Conventional configuration helicopter hover trim

6.1.2 SAS

Having a coupled comprehensive model with varying fidelity approaches at each rotorcraft component, generally results in a non-linear, unstable mathematical model. Most of such non-linearity is a physical outcome of complex aeromechanical environment that a rotorcraft operates in.

Therefore, a closed-loop stabilization (SAS) is implemented over the non-linear mathematical model in order to damp excessive and disruptive rates of the platform. Linear quadratic regulator (LQR) approach which is generally a well-suited solution for stabilization of coupled multiple-input-multiple-output (MIMO) rotorcraft problems, is implemented to build a SAS loop over the non-linear mathematical model operating on p,q and r channels.

SAS is required to be generated and tuned specifically to the rotorcraft configuration. The sample helicopter model utilized in this study is a typical 5-tons class helicopter with 4 bladed 6-meter radius main and 4 bladed 2-meter radius tail rotors. Tip speed for both rotors are 205 m/s. Chord lengths are 0.4 and 0.2 meters, respectively.

SAS on and off dynamic response of the reference problem from 70 knots level flight i.e. a typical forward speed, condition without any external input for 20 seconds are studied and illustrated with Figure 6.8 and Figure 6.9.

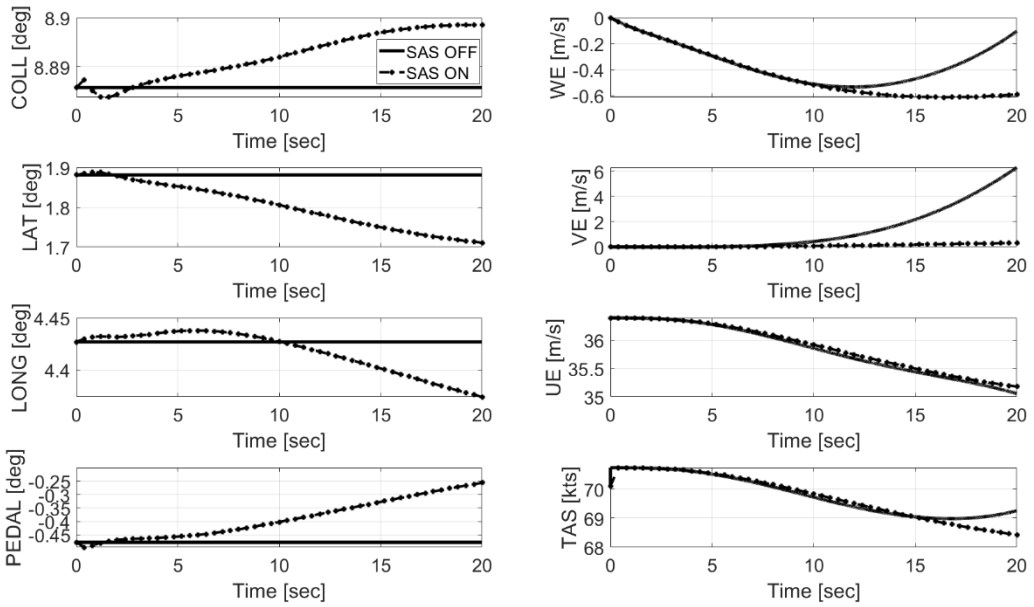

Figure 6.8 SAS on and off simulation, control angles

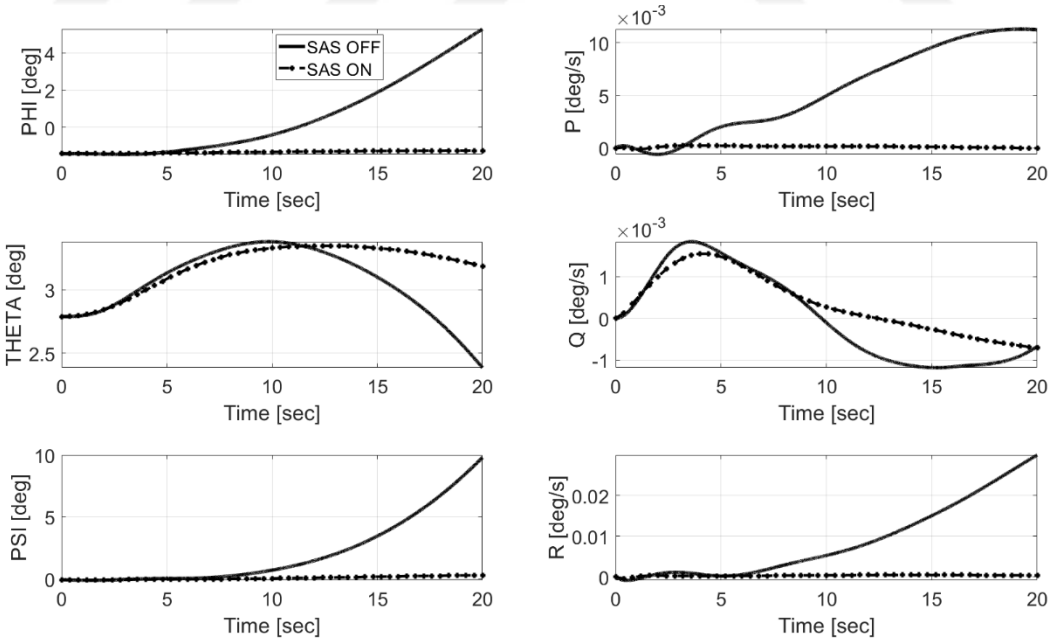

Figure 6.9 SAS on and off simulation, Euler angles

It is observed that LQR is capable of significantly stabilizing the unstable system. SAS is further tested with external pulse longitudinal cyclic and pedal inputs (three seconds) responses presented through from Figure 6.10 to Figure 6.13.

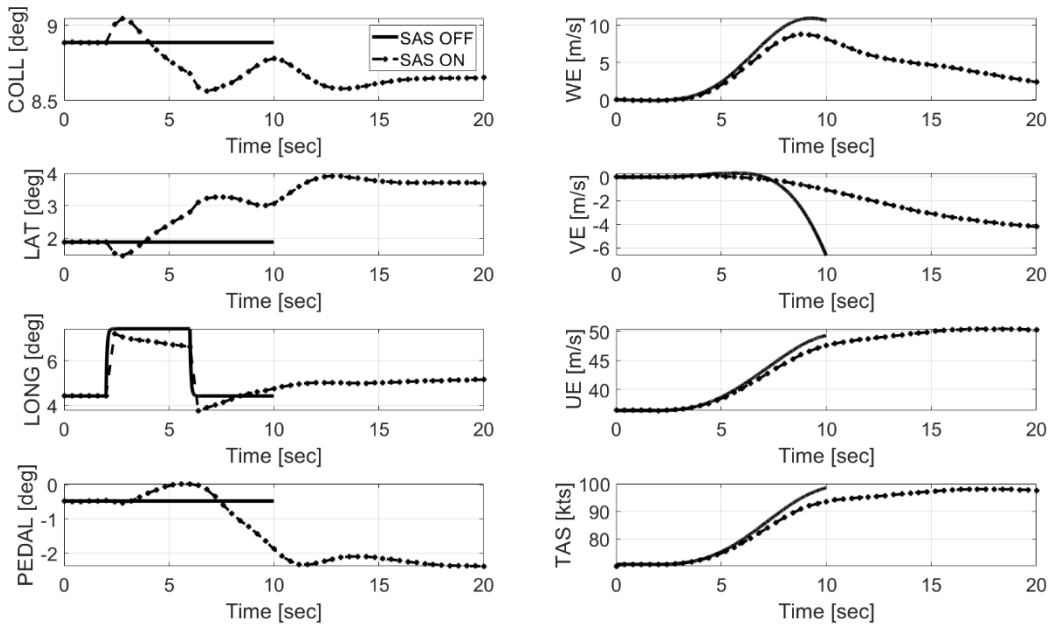

Figure 6.10 SAS on and off simulations for longitudinal cyclic step input

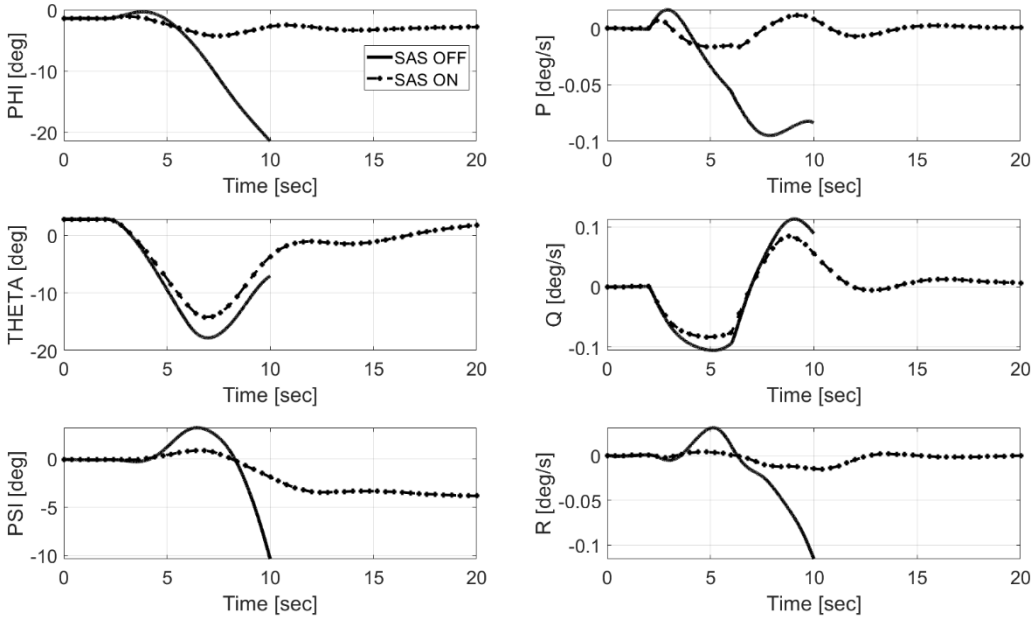

Figure 6.11 SAS on and off simulations for longitudinal cyclic step input

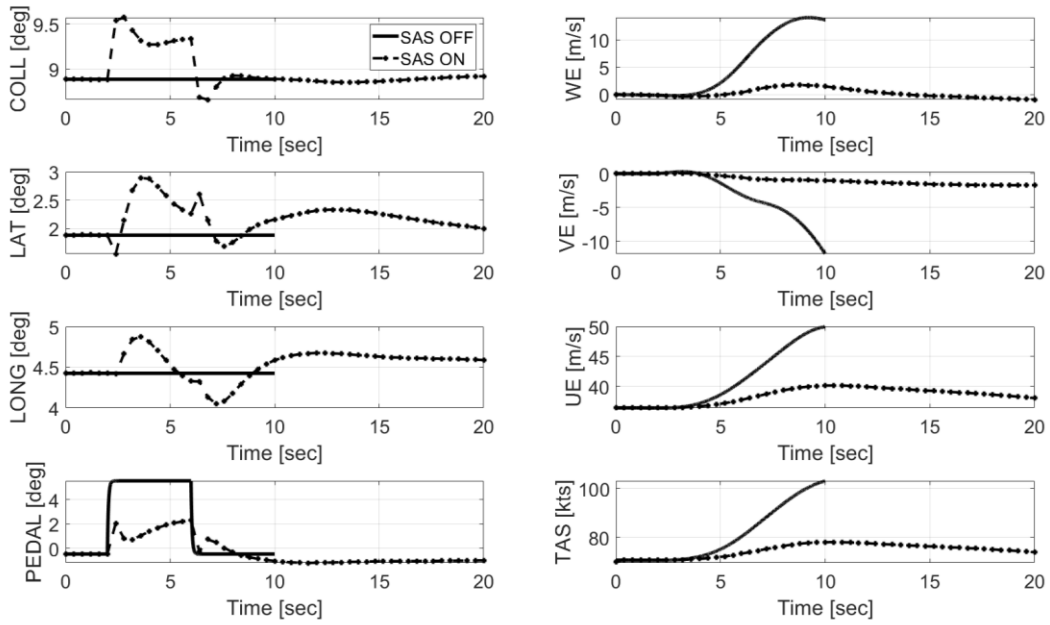

Figure 6.12 SAS on and off simulations for pedal step input

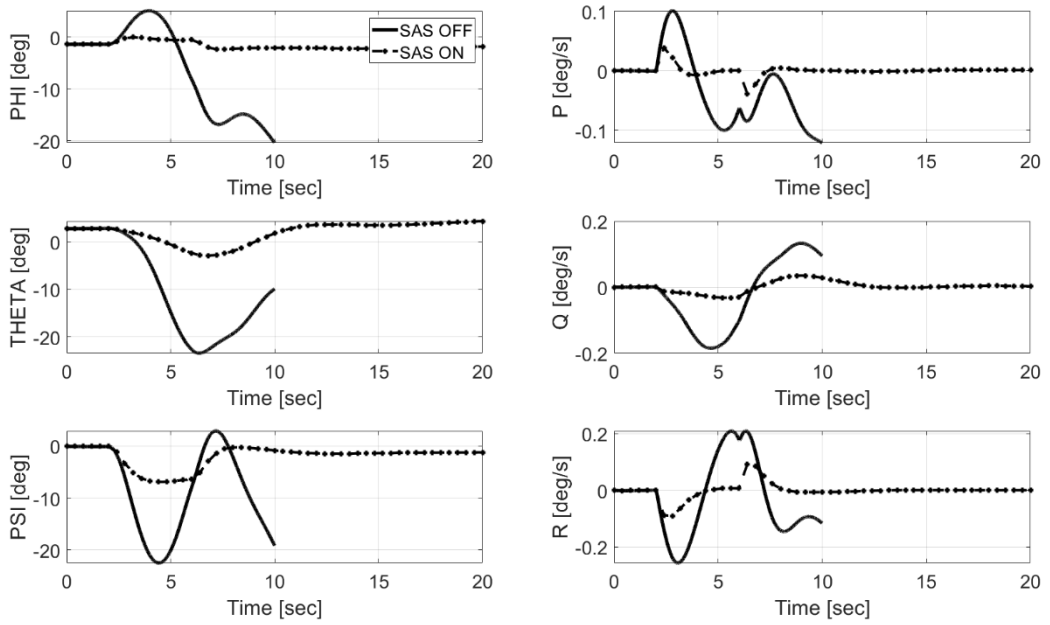

Figure 6.13 SAS on and off simulations for pedal step input

Finally, a collective step input is given at hover flight condition and dynamic response of the system with SAS on and off are studied as depicted in Figure 6.14 and Figure 6.15.

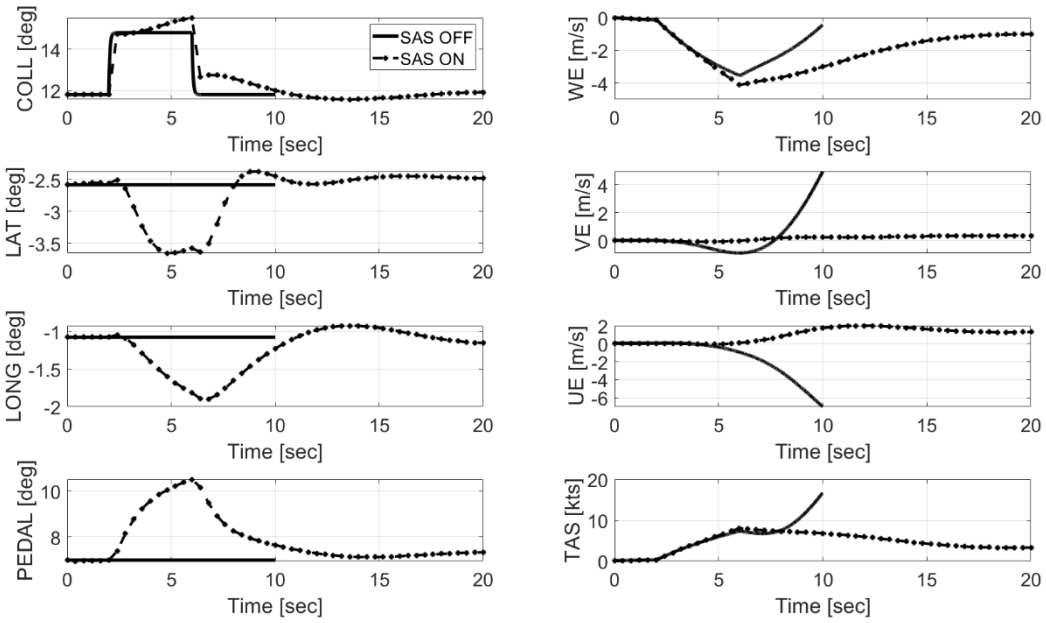

Figure 6.14 SAS on and off simulations for collective step input

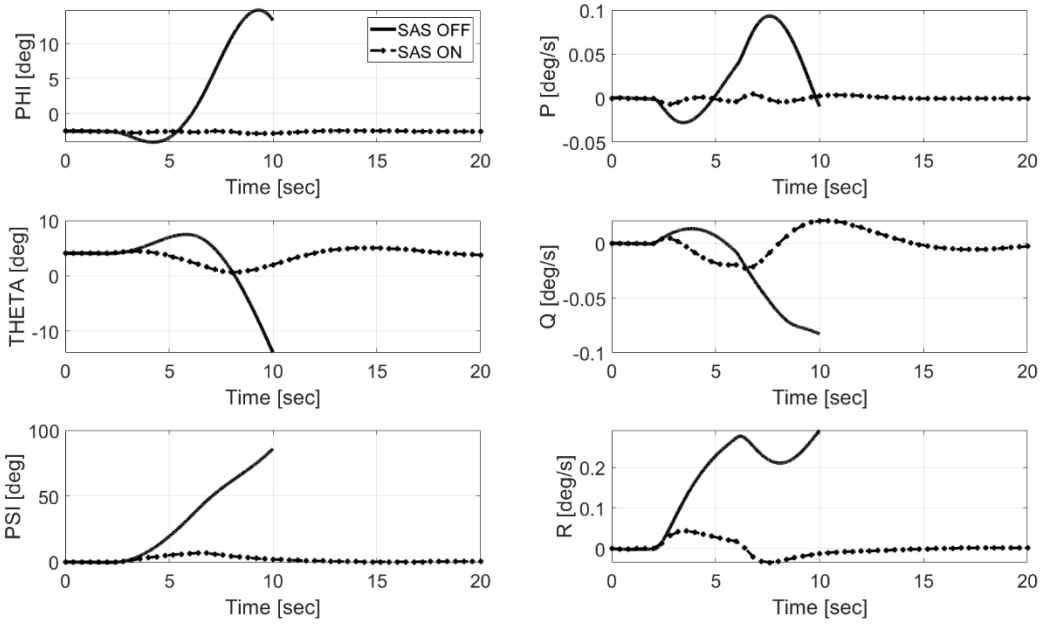

Figure 6.15 SAS on and off simulations for collective step input

It is observed that LQR is capable of significantly stabilizing the system through zeroing the $p, q\ and\ r$ rates of the platform for all channels and forward speeds.

A model predictive control SAS is also studied, application and sample results are given in Appendix D

6.2 Noise Model / Surrogate Model

A typical acoustic analysis for rotorcrafts consists of time variation of blade pressure distribution, kinematic motion, and operating environment information. Then acoustic pressure waves generated by each blade are integrated up to the observer location (Bernardini et al., 2015). Generally, the aeromechanical solution of the rotor is performed with a comprehensive modeling tool or CFD and the acoustic integration is performed by the solution of Ffowcs-Williams-Hawking equation in integral form. Such approach requires time varying high-resolution aeromechanical data and acoustic solution makes it enormously expensive for trajectory optimization purposes.

To provide a real time simulation model in terms of acoustic calculations, a sphere approach that estimates instantaneous noise signature on ground is developed and implemented. Utilization of a sphere approach requires previously performed rotor aeromechanical and acoustic solution at observers at equal distances from rotor hub i.e. located on a surface, to be stored in a database. Then, as the author discusses (Yücekayali & Ortakaya, 2015b), the frequency content of an acoustic signature on the stored sphere can be projected through slant vector from surface up to the observer while taking atmospheric absorption and spreading losses into account. Unlike the general approach in the literature (Hartjes & Visser, 2019; Morris et al., 2015; WANG et al., 2018; Yücekayali & Ortakaya, 2015b), a whole sphere grid instead of a hemisphere grid is implemented in this study. The main reason for this is the fact that the observers do not always lie on the lower half of the horizon. On the contrary, at high roll and pitch angles that might be encountered over the optimized trajectory or at low altitude flight profiles and when the observers at high ground or at the large distances even with slight Euler angles, the slant vector of observers of interest orient at the upper half of the horizon or i.e upper half of the

sphere. Therefore, full sphere grids as illustrated with Figure 6.16 and Figure 6.17 are generated and implemented into the acoustic database in this study. Additionally, instead of a single sound pressure level, whole frequency spectrum is stored in the database as accurate formulation of losses through the atmosphere at observer locations require frequency content of a sound level (Yücekayali & Ortakaya, 2015b).

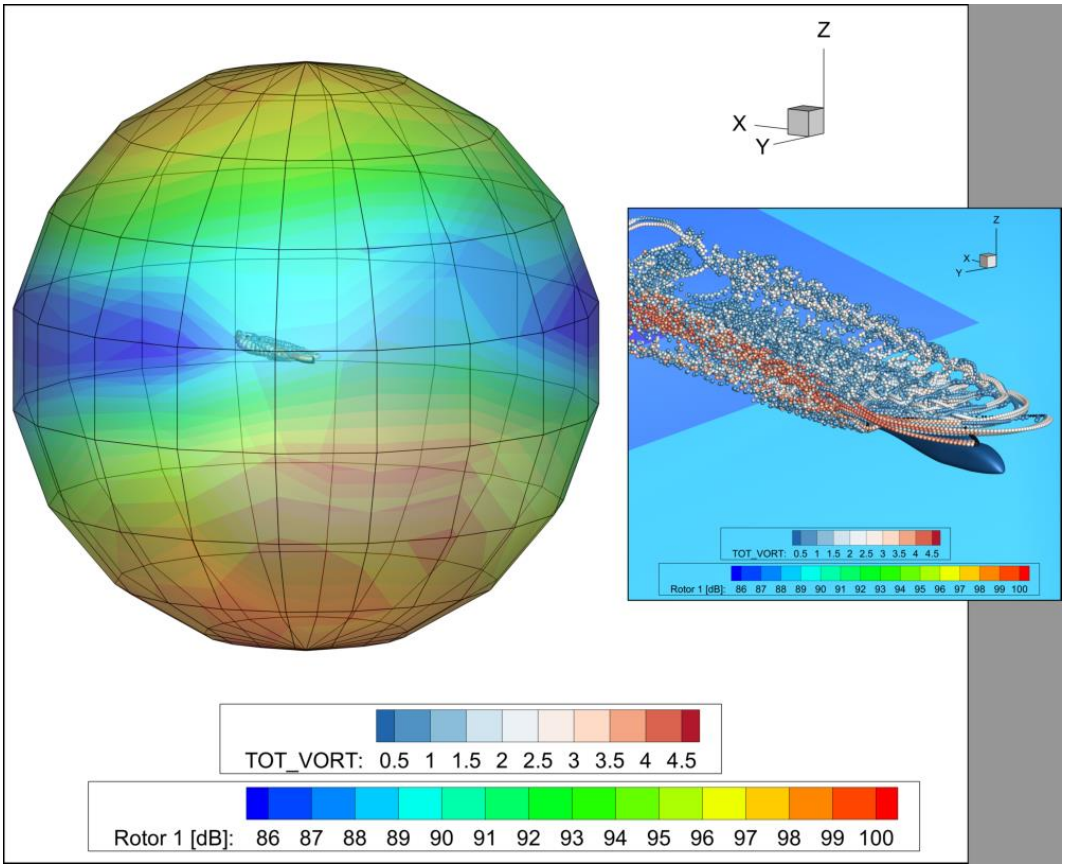

Figure 6.16 Acoustic sphere noise contour for a typical flight

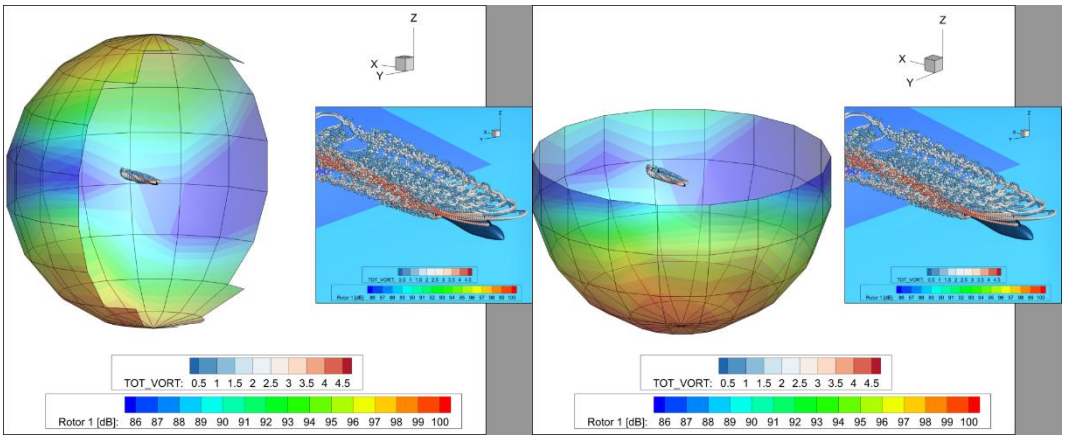

Figure 6.17Acoustic sphere cut into half for a typical flight condition

As illustrated with the author before (Hartjes & Visser, 2019; Yücekayali & Ortakaya, 2015b) computation of noise level at a single observer location independent from distance can be performed at 100 Hz. Moreover, the fidelity of the result depends on the fidelity of the solution from which sphere is generated and stored. As a matter of fact, the acoustic sphere can be generated through flight tests which provides test fidelity without computational effort penalty. In this study on the other hand, in order to have utmost analysis fidelity and detail in the stored sphere database, VVPM coupled acoustic solver (VVPAM) is utilized. The comprehensive mathematical model using VVPM provides unsteady aerodynamic loads, rotorcraft and blade kinematic motion then acoustic solver performs acoustic solution at 180 observers located on a sphere with radius of 150m, large enough to assume rotorcraft as a point noise source (Putnam, 1975).

Acoustic pressure time variation given with Figure 6.18 for a typical solution, at each observer location on the spherical grid determined with VVPAM is transformed into SPL through equations (79) and (80).

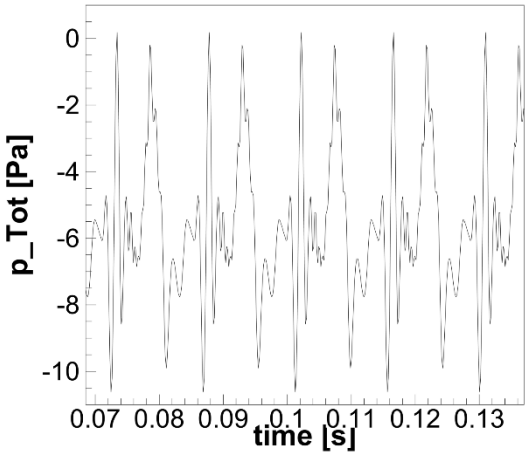

Figure 6.18 Typical acoustic pressure time variation at an observer location

$$SPL(\vec{x})^i = 20log\left[\frac{p'_{rms}(\vec{x})^i}{p'_{ref}}\right] \tag{79}$$

$$p'_{rms}(\vec{x})^i = \left[\frac{1}{t_2 - t_1}\int_{t_1}^{t_2}\left(p'\left(\vec{x}^i, t\right)^2 dt\right)\right]^{1/2} \tag{80}$$

Where superscript" ^{i} "represents ith observer on the sphere surface and $\vec{x}$ is the incorporated coordinates. p'_{ref} is taken as $20\mu Pa$ as classical. The time interval for root mean square (rms) $t_2 - t_1$ is generally taken as an interval covering sufficient number of acoustic signals.

Once the spheres are generated and stored, sound pressure level (SPL) can be projected from the sphere surface up to the observer location through equation (81).

$$L(r) = L(r_h) + \Delta L_{spreading} + \Delta L_{absorption} \tag{81}$$

$L(r)$ is the SPL at a desired location outside the acoustic sphere, $L(r_h)$ is the SPL at the surface of the sphere, $\Delta L_{spreading}$ is total SPL losses due to spherical spreading and $\Delta L_{absorption}$ is total SPL losses due to atmospheric absorption. Spherical spreading loss in driven by the distance between the observer location and the source, in this case the sphere surface and is determined with equation (82)

$$\Delta L_{spreading} = -20\log\left(\frac{r}{r_h}\right) \quad (82)$$

r is the slant distance to the observer location and r_h is taken as the sphere radius.

Atmospheric absorption on the other hand represents the propagation loss affected by ambient condition such as operating altitude, temperature and humidity. The absorption model utilized in this study is discussed by Putnam (Putnam, 1975) and implemented in (Yücekayali & Ortakaya, 2015b). The total absorption is determined assuming homogenous and quiescent medium through two contributors: "Classical Absorption" and "Molecular Absorption" as given with equation (83)

$$\Delta L_{abroption} = L_c + L_{mol} \quad (83)$$

Classical absorption, L_c is incorporated with transformation of acoustical energy into heat energy and is significant at high frequencies. Molecular absorption, L_{mol}, on the other hand, is incorporated with molecular collisions and is determined with correlation formulations proposed by Putnam (Putnam, 1975). Classical absorption is determined with equation (84).

$$L_c = 1.58x10^{-13}\left[\frac{1.365T}{T+107}\right]\frac{f^2}{P} \quad (84)$$

Where T is ambient temperature in Kelvin, P is ambient pressure [Pa] and f is the frequency of the sound pressure. Molecular absorption on the other hand, is determined with the correlation formulation given with equation (85).

$$L_{mol} = L_{mol_max}F\left\{\frac{h_a}{h_{mol_max}}\right\} \quad (85)$$

Where, F is a table look-up variable and function of ratio between absolute humidity and the humidity where the maximum molecular absorption takes place i.e. h_{mol_max}. L_{mol_max} is the maximum molecular absorption given with equation (86).

$$L_{mol_max} = 10^{[logf+8.4299x10^{-3}T-2.755624]} \quad (86)$$

Absolute humidity h_a in equation (85) is determined through the logarithm and fitting formulation given with equation (87).

$$h_a = 10^{[\log(RH) - B]} \tag{87}$$

Where RH is the relative humidity, B is the polynomial fit function calculated through equation (88).

$$\begin{gathered} B = b_0 + b_1 T + b_2 T^2 + b_3 T^3 \\ b_0 = 1.328924 \qquad b_1 = -3.1797x10^{-2}[1/C°] \\ b_2 = 2.1737x10^{-4}[1/C°]^2 \quad b_3 = -1.7496x10^{-6}[1/C°]^3 \end{gathered} \tag{88}$$

The humidity where maximum molecular absorption occurs is calculated with equation (89).

$$h_{mol_max} = \sqrt{\left(\frac{f}{1010}\right)} \tag{89}$$

Considering the methodology utilized in this study, absorption is employed as a function of the frequency content, ambient temperature, pressure and humidity. Stored frequency content is then utilized to project whole spectrum to observer location while taking atmospheric absorption and spreading losses into account. The methodology is illustrated with Figure 6.19. Spreading and attenuation losses can be observed at observer location separately. Spreading losses act whole frequency spectrum whereas atmospheric attenuation is more effective at higher frequency band. Having projected frequency spectrum at observer location enables to determine A-weighted sound pressure level as desired.

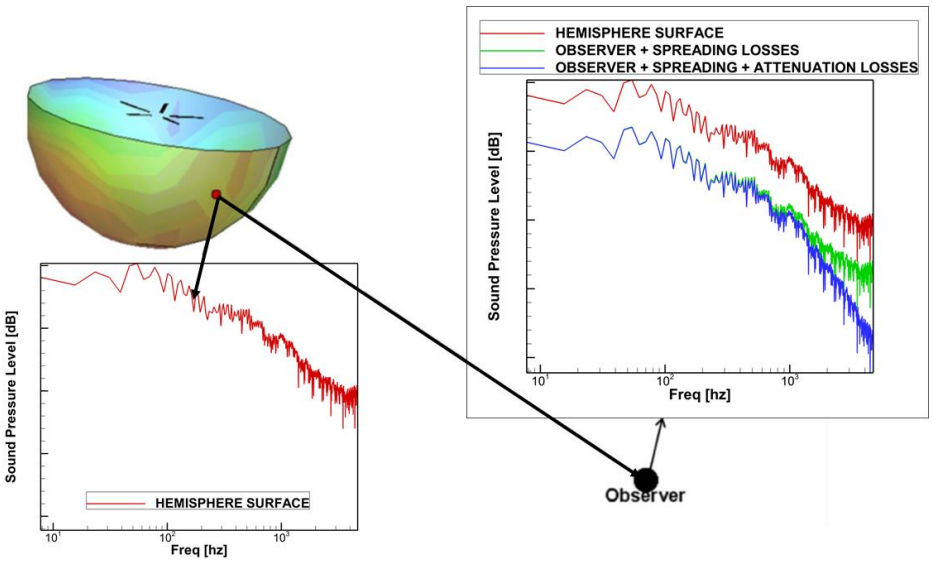

Figure 6.19 Projection of frequency spectrum from sphere surface to observer location

Projection approach from sphere surface to an observer location can further be expanded by increasing the number of observer and transform into a grid of computation over the pre-defined terrain so that instantaneous SPL contour is computed at each acoustic computation step as illustrated with Figure 6.20.

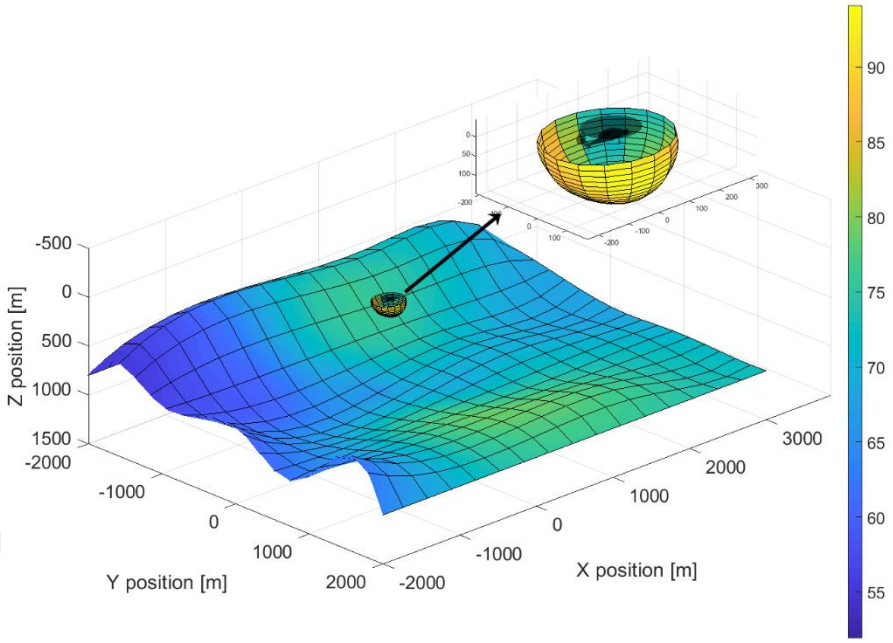

Figure 6.20 Instantaneous SPL contour on ground (terrain) surface

The acoustic contribution to the total objective function is incorporated with average sound exposure level (SEL) which is the average of variable sound energy level with an arbitrary duration mapped into overall duration. The SEL value at each observer location (or grid point in this case) is determined over a summation formula as a function of exposure time and area given with (90).

$$SEL_{av} = 10log_{10}\sum_{n}^{N}\left(10^{SPL_{dB,n}/10}\Delta t/N\right)\Delta A/A_0 \qquad (90)$$

where SPL_{dB} is sound pressure level in decibels at a time n, ΔA is the observer area, normalized with a reference area so that average sound exposure level is not only averaged with time but also with space. A sample averaged SEL calculation is performed for the hovering full helicopter (main and tail rotors) illustrated with Figure 6.20. The instantaneous noise contour on ground is utilized to determine SEL distribution through equation (90) so that the duration effect of exposure is considered. SPL contour distribution starting from t=0 seconds to t=100 seconds are illustrated from Figure 6.21 to Figure 6.24.

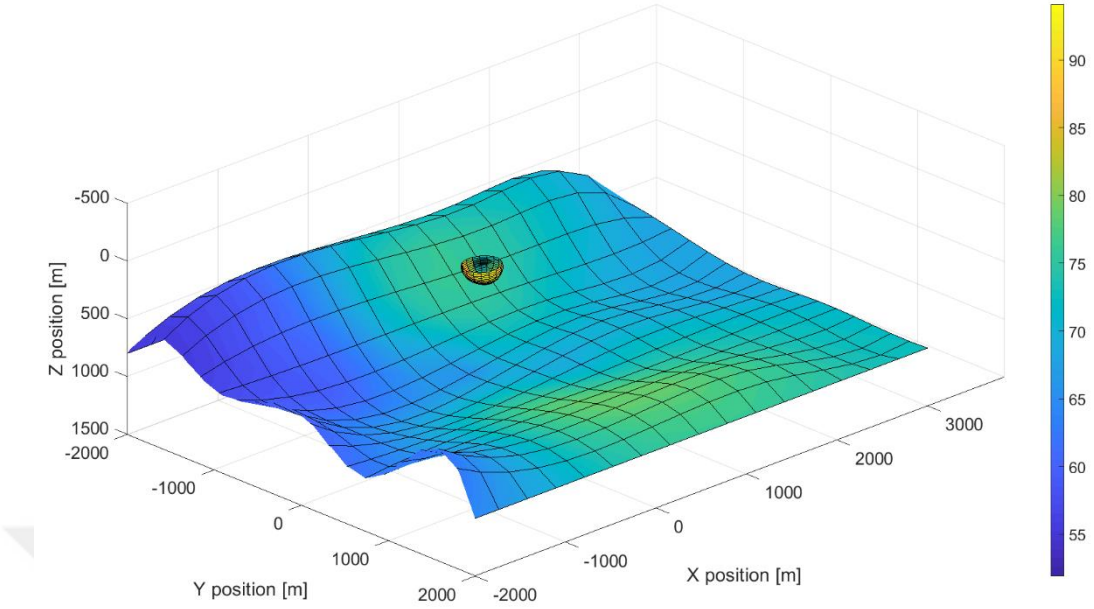

Figure 6.21 SEL contour at t=0 seconds for hovering helicopter

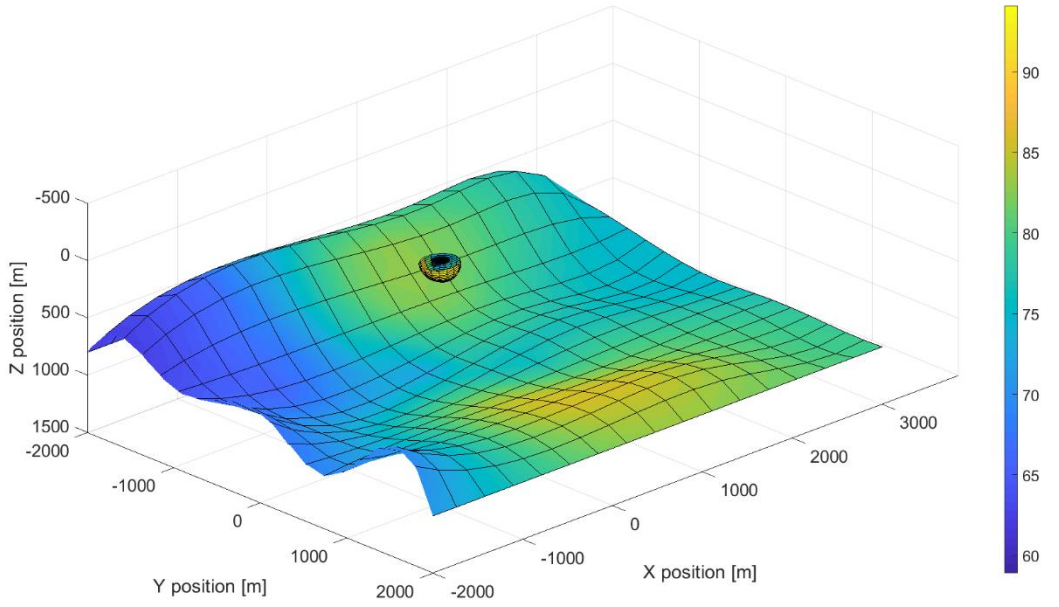

Figure 6.22 SEL contour at t=25 seconds for hovering helicopter

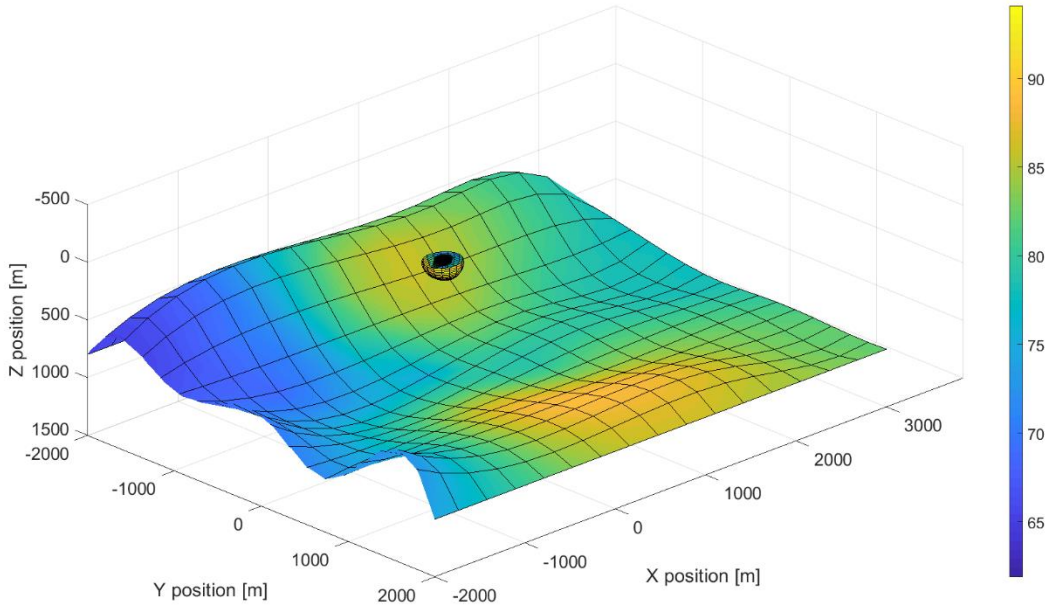

Figure 6.23 SEL contour at t=50 seconds for hovering helicopter

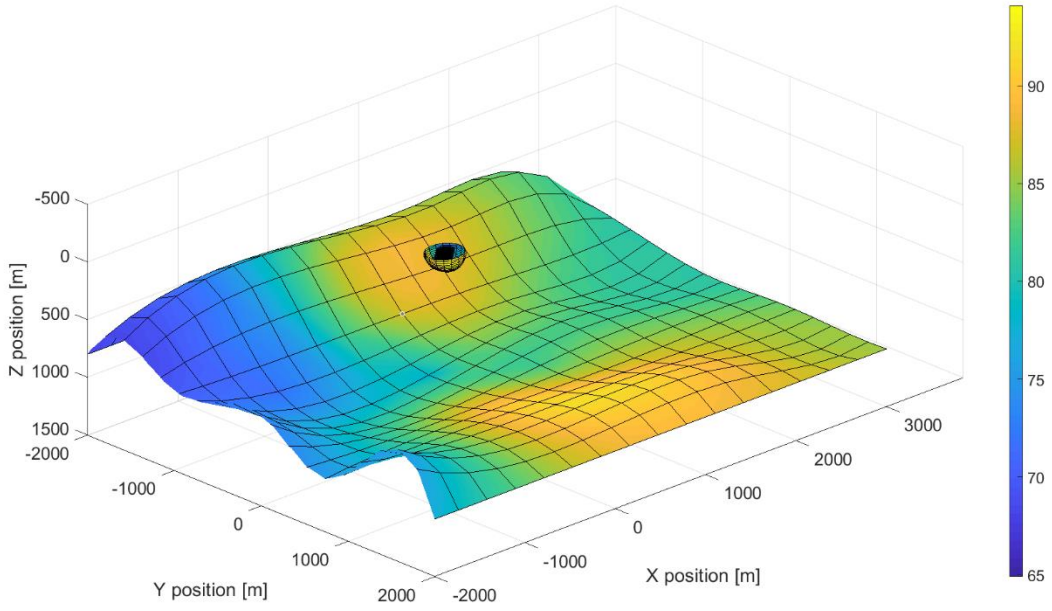

Figure 6.24 SEL contour at t=100 seconds for hovering helicopter

As observed, the sound exposure level (SEL) increases with time therefore introduces “time exposed” as an additional cost to the overall objective function.

6.2.1 Multiple Rotor Acoustics

Depending on the fact that acoustic pressure fluctuations are in the order of 10^2 Pa and when compared to atmospheric pressure in the order of 10^5 Pa, acoustic solutions are linearizable and it is feasible to superimpose acoustic waves (in time domain of course). Therefore, as long as the acoustic response of rotors/propellers are determined with a methodology at a fidelity and accuracy high enough to capture aeromechanical and related aeroacoustics response including blade-vortex interaction, blade-wake and wake-wake interactions, it is practical to determine noise signature separately and superimpose later on. The main assumption in this approach is to assume that acoustic filed does not give feedback or effect back to the rotor aeromechanical behavior. This is evaluated as a fair assumption as typically gage pressure values over a rotor blade is around 10^4 whereas the acoustic pressure waves are in the order of 10^1.

One of the key aspects in multiple rotor solutions is that, as each rotor has a different rotational speed, blade number, direction of rotation and orientation, the acoustic signature at the same observer is constituted at different sampling rate or frequency. At this point, utilization of forward time integration scheme displays its advantage over retarded time integration scheme. At retarded time integration scheme, the acoustic fluctuations at observer location is determined with equally spaced time intervals with an additional root-finding algorithm. Then in case of a multiple rotor solution, the acoustic signals at the observer location generated by each rotor is re-sampled and interpolated to generate equally spaced one single acoustic signal for further assessments. On the other hand, at forward time integration scheme, the acoustic fluctuations at the observer location are determined in source time, where pressure wave generated in equally spaced time intervals yet arrive to observer in an unequally space time intervals. Then the re-sampling and interpolation is performed for multiple rotor case like retarded time integration scheme, which eliminates the need for root-finding algorithm introducing additional computational cost and numerical error.

For multiple rotor acoustic signature, after the acoustic response for each rotor is calculated at the observer location, a proper frequency or re-sampling rate is essential in order not to damp any harmonics in the signal. The most convenient way is to select re-sampling rate according to the fastest rotor i.e. the rotor with highest rotational speed.

A sample conventional configuration helicopter acoustic signature for a flyover condition is studied. Helicopter starts a course 150 m away from the observer location at 150m height and flies over the observer at 100 knot level flight condition. 4 bladed main-rotor with a rotational speed of 285 rpm and 4 bladed tail-rotor with rotational speed of 960 rpm acoustic signals are resampled at 60 hz as illustrated in from Figure 6.25 to Figure 6.28.

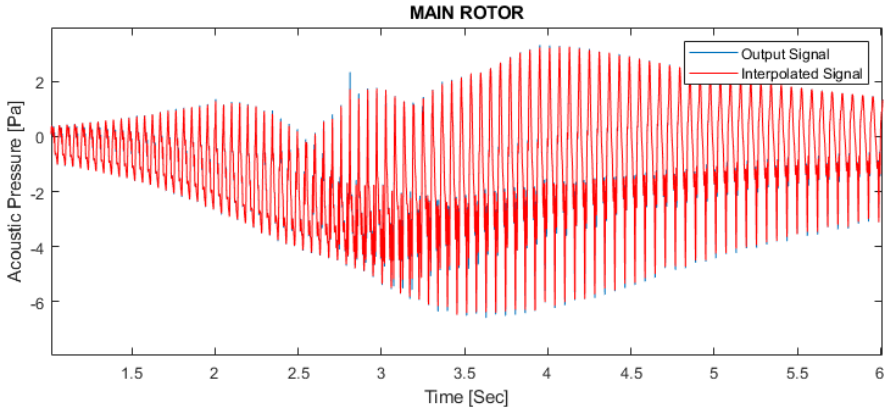

Figure 6.25 Main rotor acoustic analysis output signal and re-sampled signal

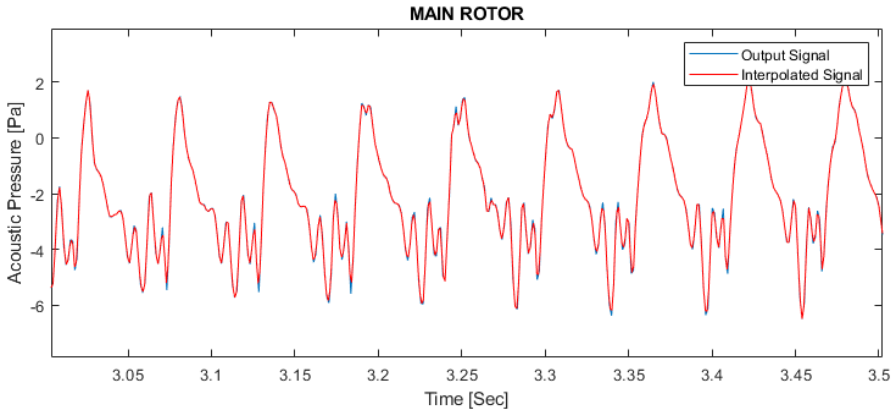

Figure 6.26 Main rotor acoustic analysis output signal and re-sampled signal

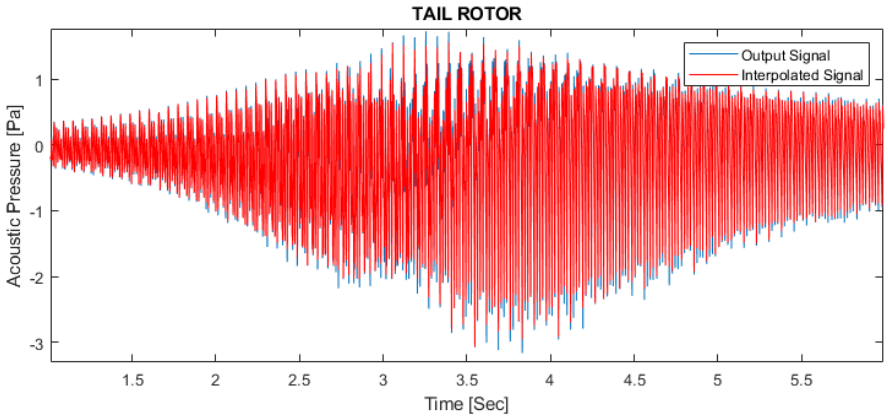

Figure 6.27 Tail rotor acoustic analysis output signal and re-sampled signal

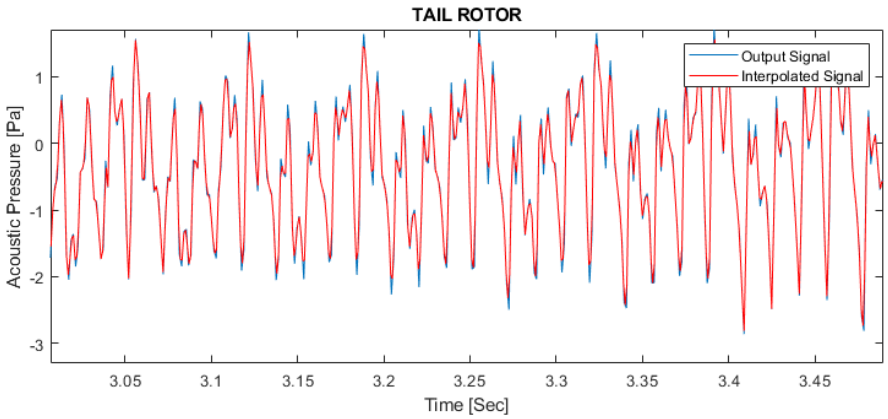

Figure 6.28 Tail rotor acoustic analysis output signal and re-sampled signal

It is observed that when interpolated (re-sampled) at a different frequency then the original signal, a negligible accuracy loss is introduced.

Now both acoustic pressure signals from main and tail rotor are at the same sampling rate and time synchronized. Direct superposition of both signals produces total noise signature of the conventional configuration helicopter at flyover condition as depicted in Figure 6.29 and Figure 6.30.

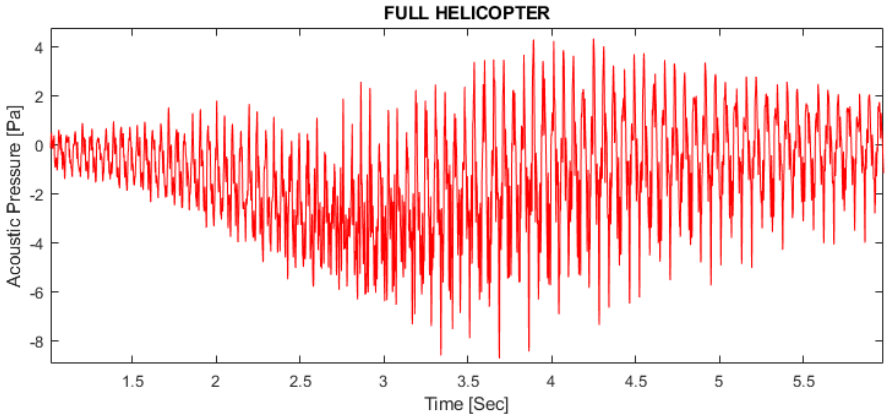

Figure 6.29 Full helicopter acoustic signature at flyover condition

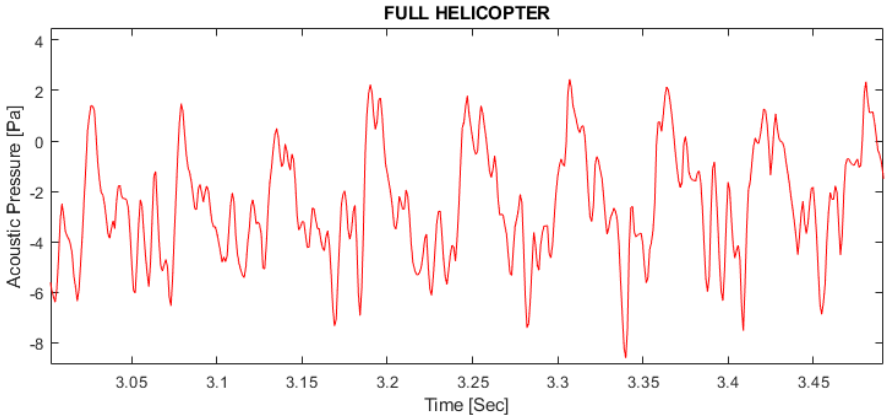

Figure 6.30 Full helicopter acoustic signature at flyover condition

Moreover, even though a forward time integration scheme is utilized, the output of the multiple rotor post-process is an equally spaced, structured acoustic signal which is ready for further acoustic evaluations. In this scope, SPL contours over acoustic sphere for main rotor only, tail rotor only and full rotorcraft are determined are compared in Figure 6.31 and Figure 6.32.

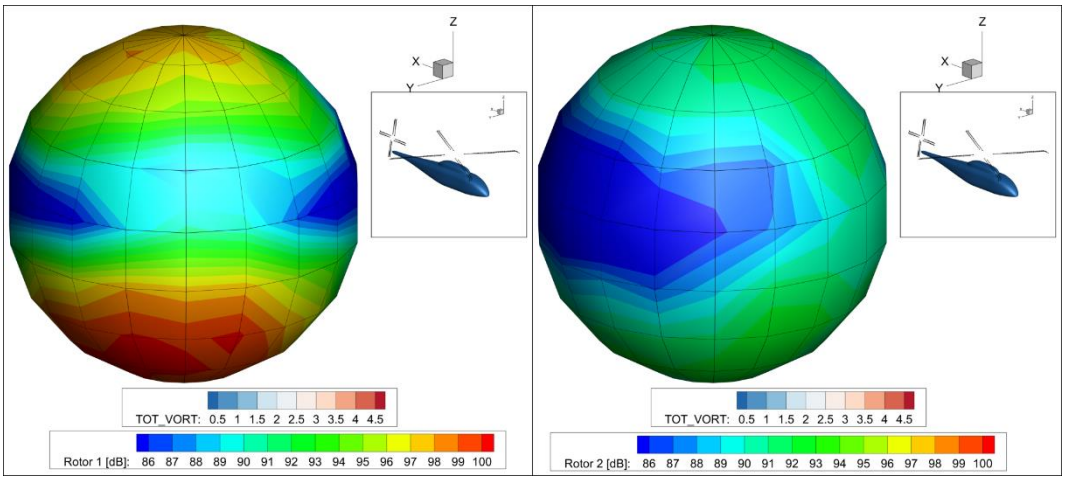

Figure 6.31 Main rotor only and tail rotor only acoustic spheres at level flight

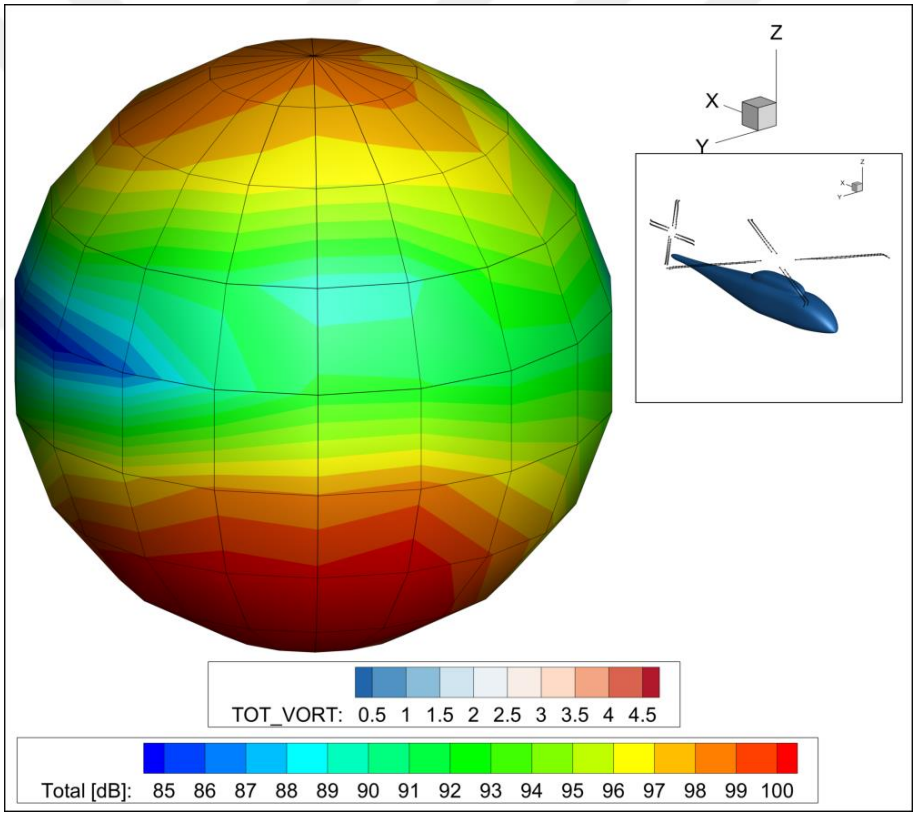

Figure 6.32 Full rotorcraft acoustic sphere at level flight

6.2.2 Sphere Database

The aerodynamically generated noise of a rotor is affected by operating condition such as altitude, temperature and humidity and flight condition such as thrust, torque, propulsive force, pitch and roll moments, flight speed, tip path plane orientation etc. Considering all the variables effecting noise signature of a rotor, for a rotorcraft where at least two or more rotors are operating simultaneously, the number of dependent parameters increases linearly, and utilization of a database becomes unfeasible. However, with a comprehensive point of view, there exists only a unique trim condition with specific flight dynamics states for a single steady flight condition defined with total weight of the platform, flight speed and flight path angle. Although, during a maneuver or transition from one steady flight to another flight condition all those trim states dynamically vary, whenever a trimmed unaccelerated flight condition is achieved, the states such as thrust, torque, propulsive force, tip path plane angle i.e. all the variables that can effect noise signature, are unique and can be estimated and calculated beforehand. Therefore, keeping the point of view of acoustic response at rotorcraft level, dependent variables for a database can be reduced to thrust level, flight speed and flight path angle which is also in parallel with general perception of literature (Bernardini et al., 2015; Tsuchiya et al., 2009).

As VVPM has proved itself in terms of its capability of solving blade-blade and rotor-rotor interactions, Blade-Vortex Interaction (BVI) noises are inherently included in the sphere database. There are basically two drawbacks of a sphere approach. First, the intermediate acoustic states are interpolated from most similar flight conditions resulting on accuracy loss. Second, sphere approach provides a quasi-steady acoustic solution which fails to estimate unsteady or maneuvering noise signature. Both drawbacks are intended to be minimized with continuous expansion of the acoustic database at varying dependent rotorcraft flight states/variables.

The dependent states/parameters selected for sphere database generation are blade loading, air speed, angle of attack and sideslip (Behr & Reindel, 2008). The blade loading is a comprehensive parameter covering total weight of the platform and

operating condition such as altitude and temperature. Air speed covers flight speed and advance ratio. Angle of attack and sideslip of the platform covers tip path plane angle orientation, climb and descent states of the operating rotors.

An illustration for the generated acoustic sphere database is given in Figure 6.33 and Figure 6.34.

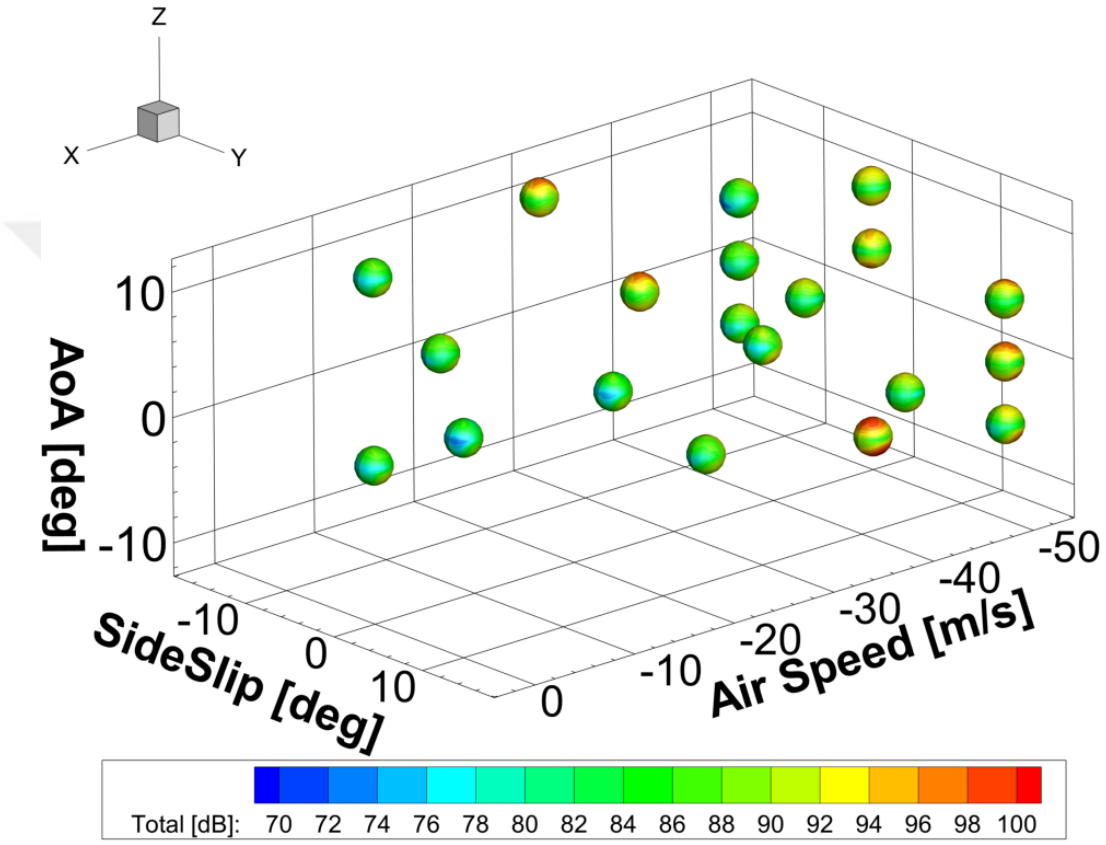

Figure 6.33 Acoustic sphere database illustration for constant C_T/σ

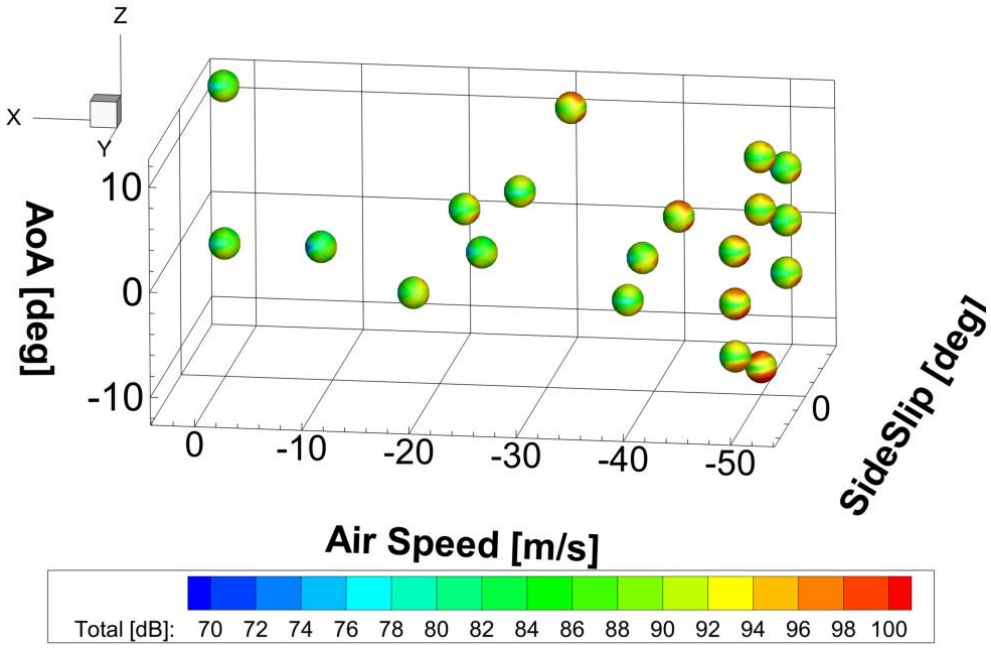

Figure 6.34 Acoustic sphere database illustration for constant C_T/σ

6.2.3 Verification

Two verification studies are performed for the acoustic sphere approach. One is SPL comparison at an observer location outside of the sphere with direct acoustic simulation and acoustic sphere approach. Other is comparison of acoustic sphere determined through interpolation from other spheres and direct calculation from the acoustic solver.

For a level trimmed flight condition, SPL level at an observer location 2x the radius of the acoustic sphere as illustrated with Figure 6.35, is determined both with sphere approach and direct acoustic simulation and results are compared. It is observed that, acoustic sphere approach performs the SPL projection from sphere surface to observer location covering the spherical losses to determine noise impact at the observer location significantly accurate and fast. The performance of sphere approach in terms of accuracy and computational cost is compared with acoustic simulation in Table 6.1.

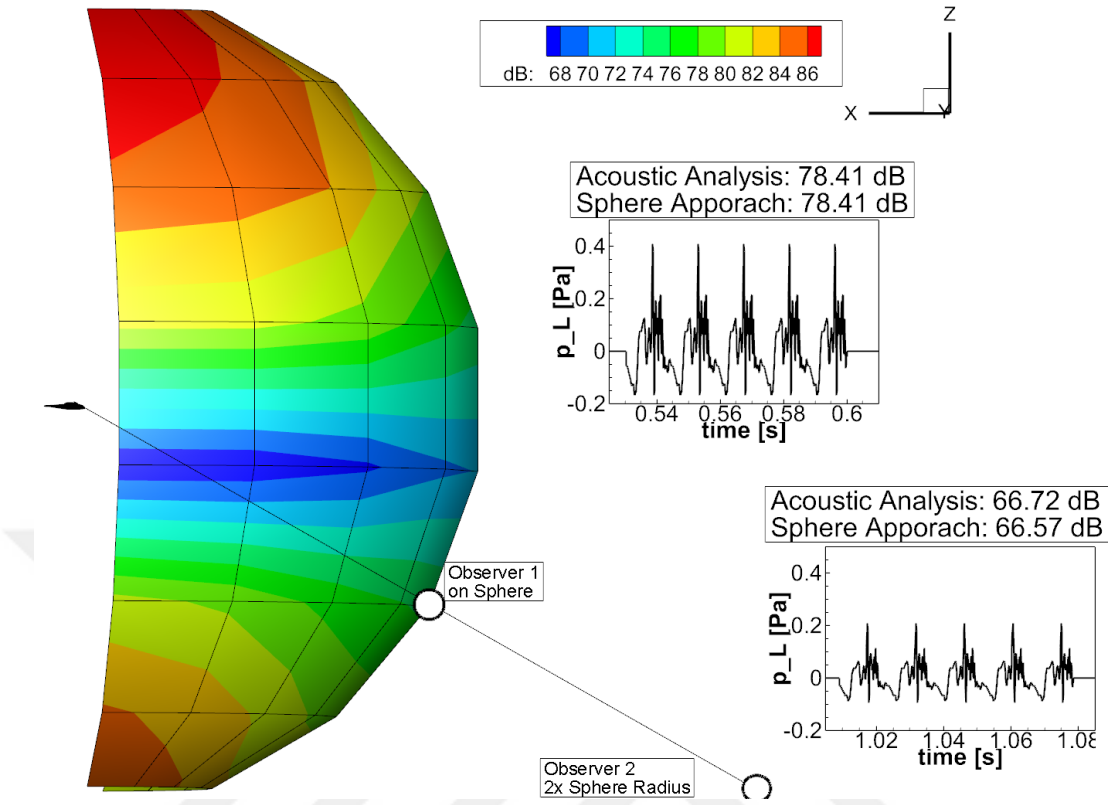

Figure 6.35 Comparison sphere approach with direct acoustic simulation

Table 6.1 Performance comparison of sphere approach and acoustic simulation

Approach	**Calculated SPL**	**Computation Time**
Acoustic Sphere	66.57 dB	0.004 seconds
Acoustic Simulation	66.72 dB	15 seconds

Verification of the acoustic sphere database i.e. noise model, is further performed through determining an intermediate acoustic sphere through the noise model and comparing it with the acoustic sphere specifically generated for the incorporated flight regime. In other words, in order to verify that interpolation between acoustic spheres are performed correctly and without significant resolution loss, acoustic sphere for a six degrees steady descending flight condition is determined from the noise model and compared with acoustic sphere of direct analysis result depicted in Figure 6.36.

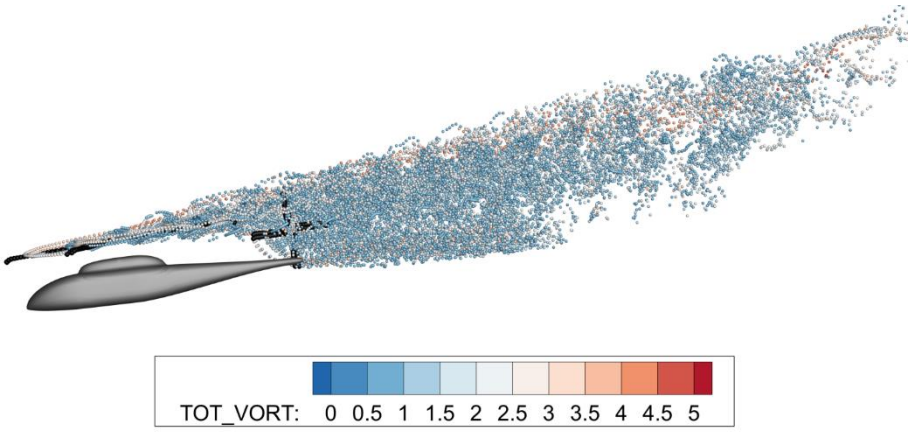

Figure 6.36 6 degrees approach/descending flight condition

The interpolated acoustic sphere and the acoustic sphere specifically calculated for the 6 degrees approach condition are compared in Figure 6.37. No accuracy loss is observed, and it is assessed that the database system and interpolation routines are correctly implemented.

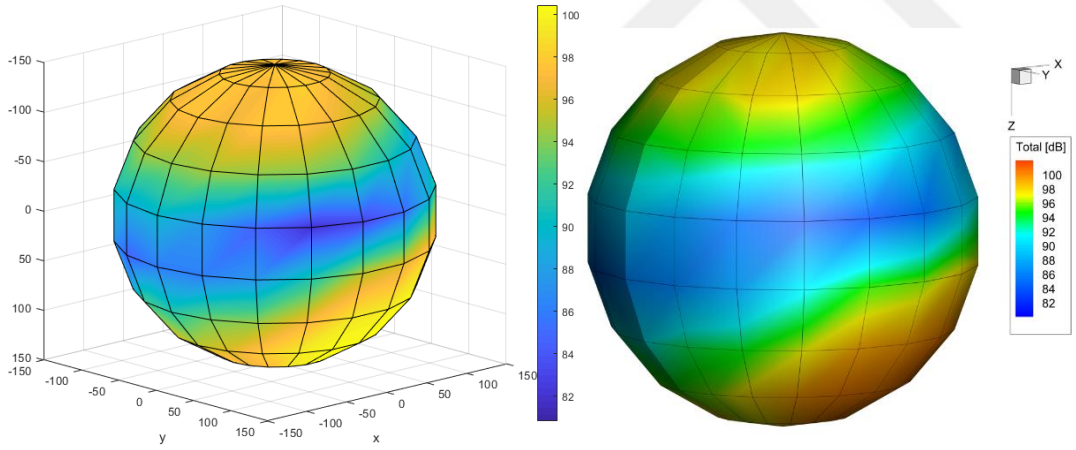

Figure 6.37 Interpolated acoustic sphere (left), direct calculated acoustic sphere (right)

6.3 Terrain Model

Terrain model represents the ground surface including elevations, obstacles, community land and settlements; provides information of noise sensitive regions to implement into the optimization cost function. The terrain is represented with a

surface mesh, generally with a cartesian mesh, then each node represents an observer location i.e. microphone location. The acoustic model determines noise response of the rotorcraft at each observer (node) location through sphere model as illustrated with Figure 6.38 or direct solution i.e. VVPAM.

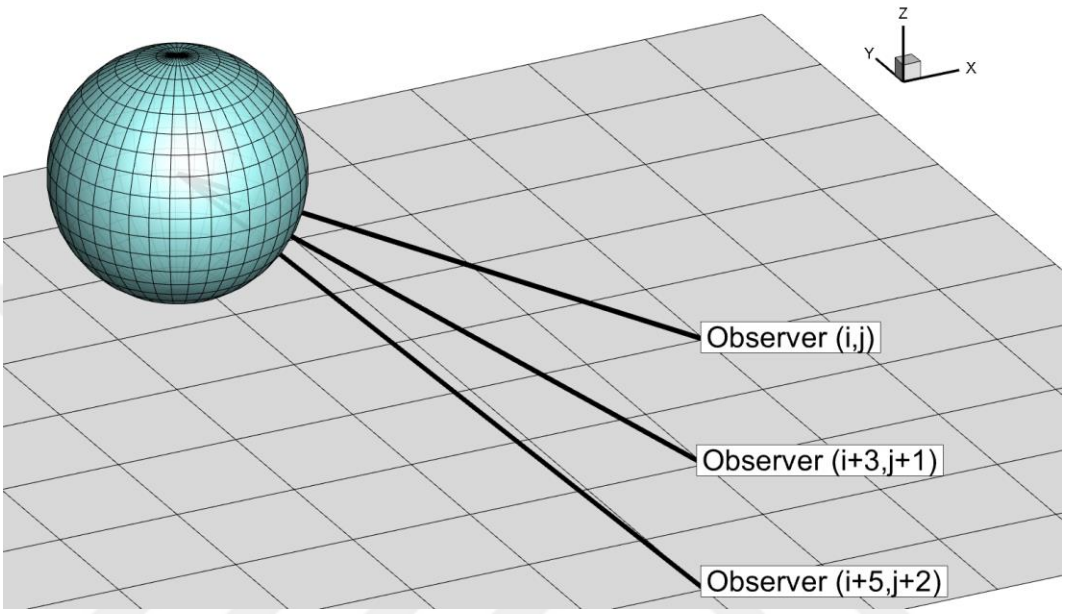

Figure 6.38 Terrain mesh and observer (node) illustration

Three dimensional maps/views of any part of the world is easily can be attained nowadays. In order to utilize as a terrain model and generate a SPL contour though, a grid/mesh is required to be generated. Fortunately, growing engineering applications lead CAD geometry for cities or terrain, like every other thing, to be reached easily. An example is provided with Figure 6.39 for Prague map and 3-D CAD.

Figure 6.39 Representative map and 3-D cad model for Prague

Having the three-dimensional model of a city or terrain provides all the required information for the utilization as a terrain model in the simulations. Although such import can easily be made, the main concern of this study is providing the generalized framework, therefore an arbitrarily generated terrain model is utilized with a representative noise sensitive area. The default terrain model utilized in the development and calculations is presented in Figure 6.40. Total noise level and frequency content/spectrum at each node is calculated and SPL contours are determined through post-process algorithms. In case a surface or a node falls between the rotorcraft and the node of calculation, it is assumed that sound waves do not penetrate through the obstacles. This leads the optimization to benefit from landforms, through utilization of terrain to conceal noise sensitive regions if possible, at normal flight operation. The default terrain is symbolized with a cartesian mesh of 20x20 representing 4x4km area with elevations up to 500m. A noise sensitive region is oriented at north-east corner (in North-East-Down reference frame positive X and positive Y direction) and included in the optimization function throughout the study.

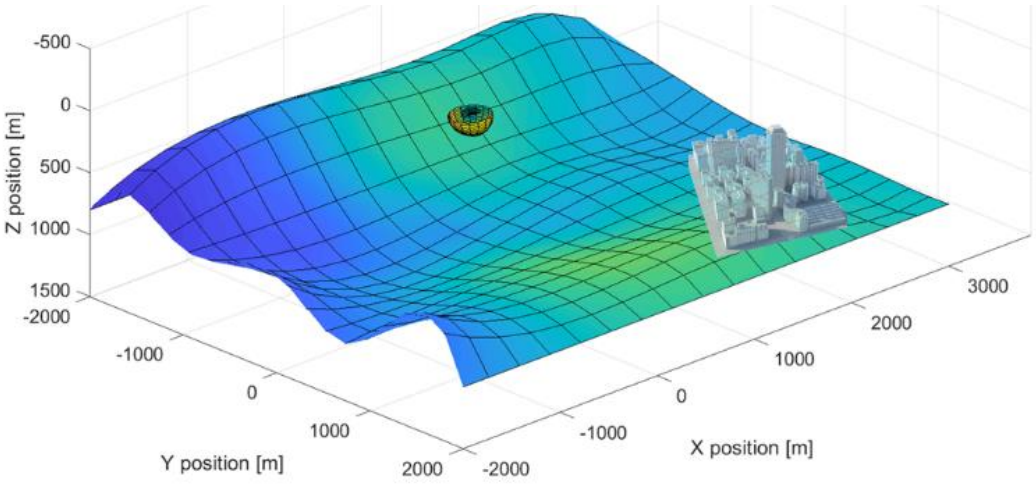

Figure 6.40 Default terrain model

6.4 Simulation Model

Simulation model is a real time computable non-linear and coupled flight dynamics model for any type of rotorcraft configuration, equipped with acoustic sphere database and terrain model providing instantaneous acoustic signature on ground surface or multiple observer locations. A model predictive control algorithm provides optimal control inputs to the plant to track simultaneously generated optimized trajectory. MPC updates control inputs at every control horizon time interval. The simulation model is equipped with an acoustic sphere noise model which performs acoustic calculations such as noise levels at desired observer locations and SPL contour at the terrain surface at every acoustic horizon time interval. As illustrated with Figure 6.41, simulation starts from a trimmed flight condition at each prediction horizon time interval, MPC collects instantaneous rotorcraft states and performs an optimization stage to generate the trajectory to be tracked and control inputs to track the trajectory. Independent from the MPC, acoustic noise model continuously performs calculations. Therefore, whether a MPC is active or not, as long as the simulation continues with over trimmed condition without any disturbances or specific pilot control inputs given externally, model simulates the flight dynamics, aeromechanics and acoustic calculations.

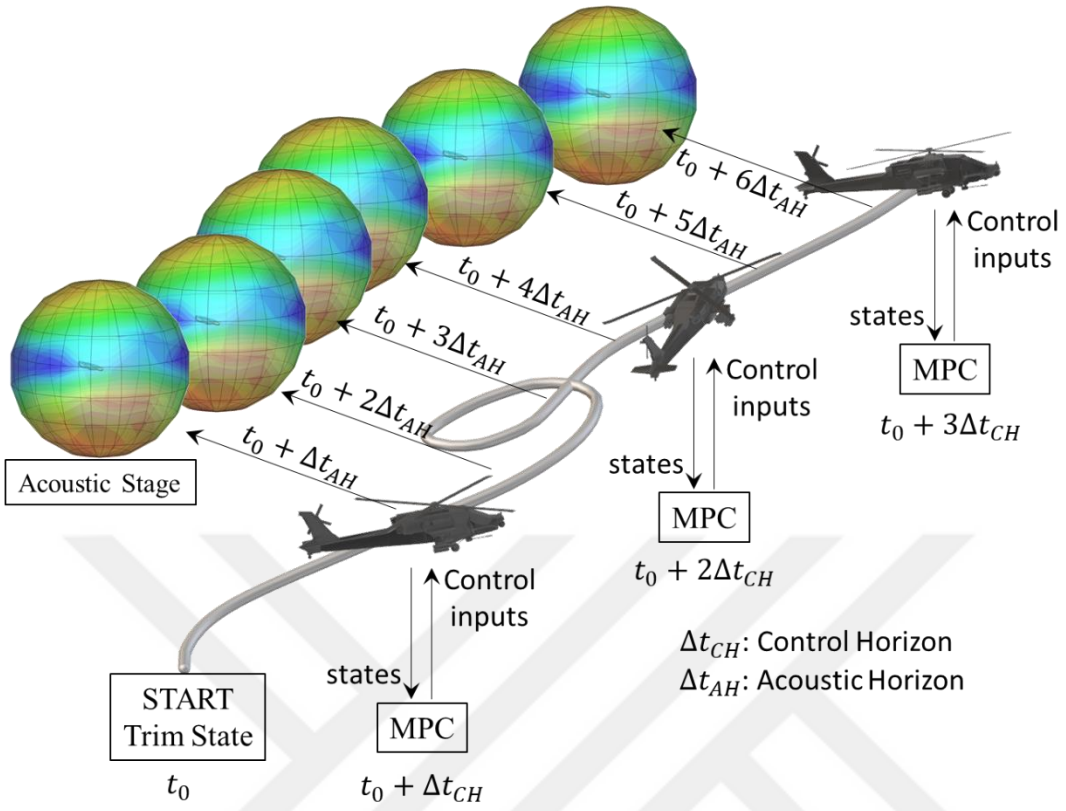

Figure 6.41 Illustration for the simulation model

The simulation model developed in Simulink environment is illustrated in Figure 6.42. “CONTROLS” consists of rotorcraft control inputs, i.e. collective, cyclic, and pedal for a conventional configuration, and are updated after each control horizon intervals by the MPC algorithm. A low pass filter operates over the produced control inputs to representing the actuator dynamics. An LQR SAS stabilizes and damps the excess rotational velocities, p, q, r but not necessarily be active for all simulations.

The main structure is built over the “rotorcraft model” function, which performs force moment calculations and integrates the plant model in time with simulation frequency. Pilot controls and SAS corrections were continuously fed into the “rotorcraft model” where an update to control inputs is performed at each control horizon time interval. The MPC is introduced to the system through “Control Optimization” sub-system. This sub-system is conditionally enabled through a “modulo” function which produces the enabling signal at each prediction horizon

time interval such that the MPC sub-system does not operate unless the simulation counter displays the proper time. This approach enables to perform a control optimization once in every prediction horizon frequency. Similarly, the acoustic module is introduced to the simulation model through “acoustic contour” sub-system. This sub-system is likewise a conditionally enabled system where the module function produces the enabling signal at every acoustic horizon time intervals. As development environment utilized a mathematical model library, it is possible to study multiple rotorcrafts and perform trajectory optimization simultaneously. A sample, multiple rotorcraft trajectory optimization and track simulation is given in Appendix F.

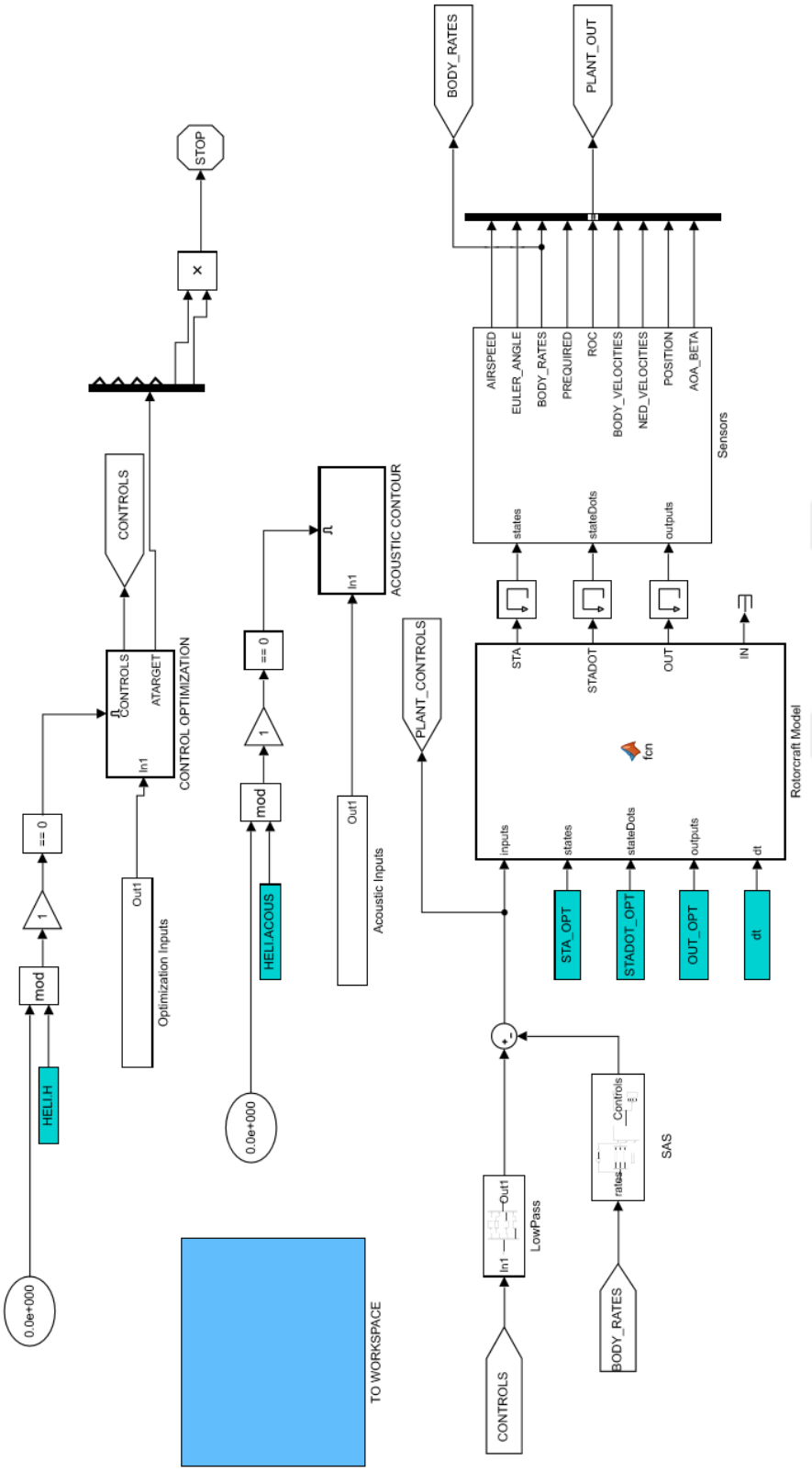

Figure 6.42 Simulation Model Visual in Simulink Environment

6.5 Development Environment

The overall trajectory optimization framework is developed in MATLAB environment, where sub-systems are developed in other languages and implemented as dynamic link libraries ".dll"s into the simulation environment. MATLAB is responsible from the data links and simulation infrastructure.

The rotorcraft mathematical model had been developed in C++ language with an object-oriented manner. The mathematical model operates independently, reads inputs, performs all calculations such as force and moment balance, equation of motion, trim etc., and time integration for simulation purposes. The information exchange between the MATLAB and the mathematical model is performed through ports. At each time step, pilot control inputs are sent to the mathematical model, where all calculations are performed and one time step integration is performed and all the outputs are sent back to the MATLAB workspace for further utilization in control and optimization algorithms. This approach provides memory management, simplicity, and robustness as well as data security and computational speed. It is observed that similar mathematical model when written in MATLAB operates 500-600 times slower. The simulation model utilized in this study operates real time with 500 hz frequency.

VVPM is developed as an external and separate tool in Fortran language with object oriented and modular structure. VVPM is initially developed as an isolated rotor model, after completion of validation and verification activities, it is re-written in C++ language within the mathematical model environment. Therefore, VVPM and the mathematical model are tightly coupled.

The acoustic solver is developed in Fortran language and utilized as an executable. MATLAB operates the mathematical model, where the aeromechanical solution is determined as desired, then MATLAB prepares the blade pressure and kinematics data, executes aeroacoustics analysis, performs post-processes for either acoustic signal, SPL contour or sphere database.

The noise model utilized within the simulation model is a database interpolation algorithm which is developed in MATLAB and uses built-in three-dimensional interpolation algorithms. The atmospheric absorption, spherical losses and projection of SPL are calculated within MATLAB Simulink in real time coupled with the simulation model.

The optimization algorithm utilized in model predictive stage is developed in MATLAB, implemented into the Simulink simulation model. Either developed optimization algorithm or built-in “fmincon” algorithm is available upon selection of the user.

CHAPTER 7

TRAJECTORY OPTIMIZATION AND TRACK

Trajectory optimization and track constitutes the optimal control basis flight profile optimization framework. Combining the simulation model with model predictive control environment enables one to generate optimal trajectories and optimal control setting to track the generated trajectory simultaneously. In simulation model scope, the mathematical model governs the flight dynamics solution of the rotorcraft of interest, noise model determines instantaneous SPL contour on the ground surface on interest and terrain model provides the required landform information of interest including urban areas, noise sensitive regions and empty fields. Linked with the MPC, the methodology developed in this study provides an trajectory optimization environment which provides optimal flight profile compliant with mission requirements and manipulates noise contour on ground in favor of community annoyance as illustrated in Figure 7.1.

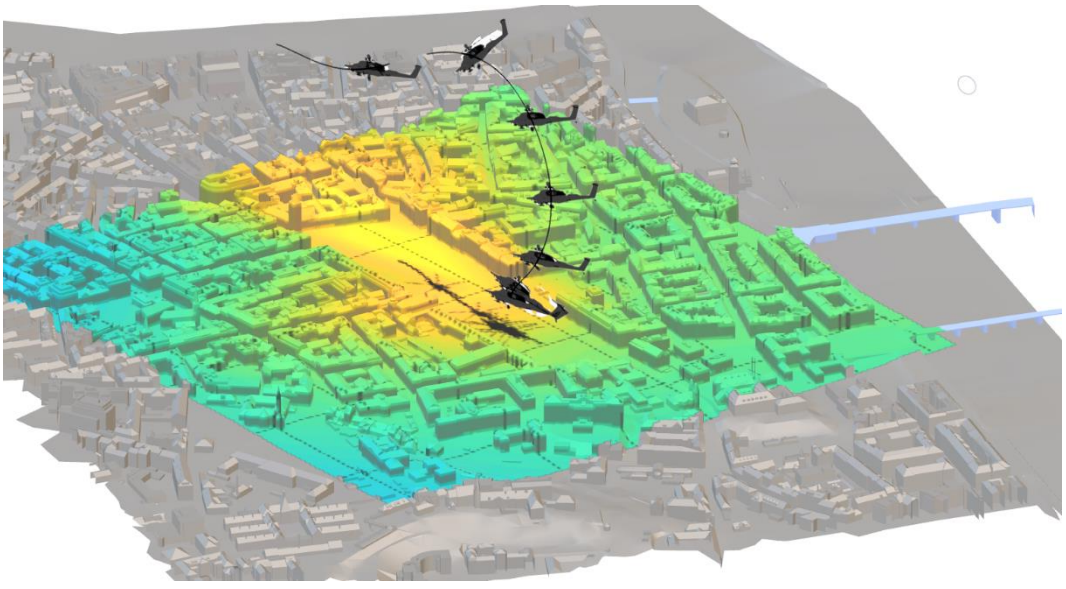

Figure 7.1 A sample output for the noise impact on ground during take-off (rotorcraft geometry is up scaled for illustration)

A modular overall objective function is developed covering individual cost functions from aeroacoustics, performance, safety, comfort, and mission/waypoint requirements. Through varying the weightings of each cost function, the overall objective is manipulated according to the needs. An initial implementation of the MPC framework to test military maneuvers with mission/waypoint concerns only is illustrated with Figure 7.2.

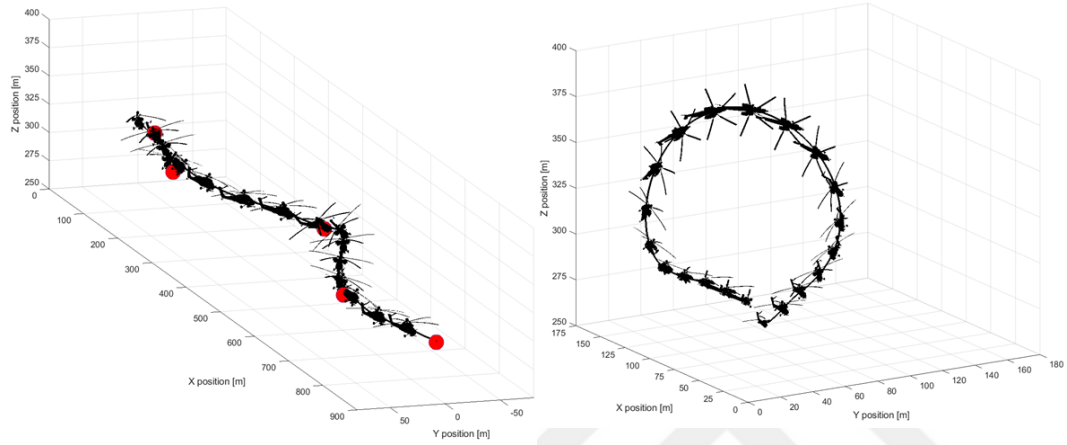

Figure 7.2 Sample Slalom and teardrop maneuvers with model predictive control (Yücekayali, Şenipek, & Ortakaya, 2019)

This chapter presents the MPC basis, the objective function covering contributions from acoustics, performance, safety & comfort, avoid regions and mission/waypoint costs, optimization algorithm and trajectory optimization framework.

7.1 Method – MPC

Model predictive control (MPC) defines the control methodology which utilizes a reference model to predict the future states of the plant and generates a sequence of inputs by incorporating an objective function with an optimizer. MPC requires a model describing the relation between the inputs and the states of the plant. There is a trade-off between the prediction model fidelity and the desired accuracy, efficiency, and computational cost. This model is operated by the optimization algorithm to minimize a cost function while meeting related bounds and constraints.

The optimized control set is then directed to the plant to observe the anticipated dynamic response of the plant.

Reference tracking is the general application of MPC where the error between instantaneous or future behavior of the system, i.e. system states, with desired states is direct inputs of the optimization algorithm. In this study on the other hand, classical MPC understanding is slightly modified so that trajectory generation and control optimization for track are performed simultaneously. The objective cost is not directly a function of helicopter states but a function of upper level performance indicators such as noise, performance, safety, comfort, and waypoint concerns, so that states are included indirectly in the optimization.

An illustration of the model predictive control scheme is depicted with Figure 7.3. At each control horizon time interval, a model predictive stage is combined with an optimization algorithm which perturbs the control setting and estimates system future behavior as well as variation of the cost function for s specified duration. Then the optimum control setting is calculated which minimizes the objective cost function and kept constant until the next optimization stage.

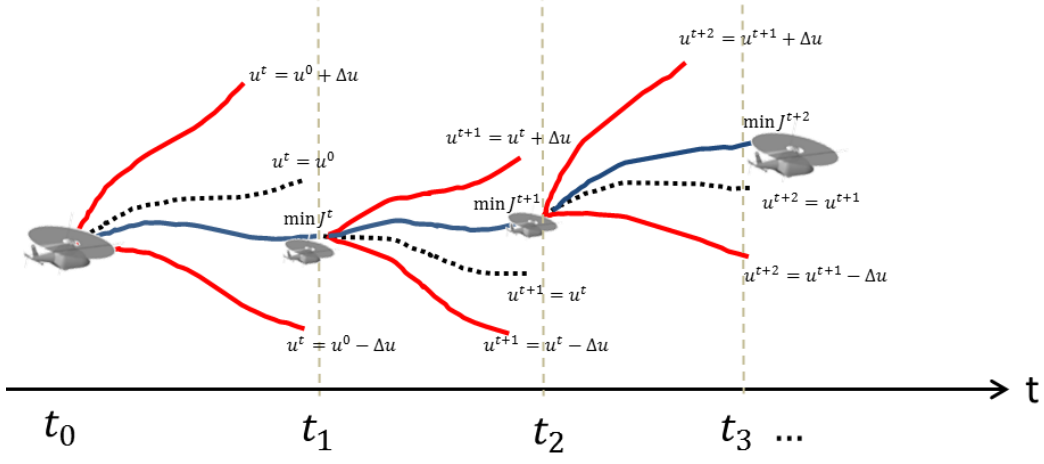

Figure 7.3 Illustration of MPC scheme

At each prediction stage, trajectory is optimized for a prediction horizon time interval, yet only fed into the plant for control horizon time interval. On the other hand, acoustic calculations are performed at every acoustic horizon time interval

independent of the MPC. The illustration of control horizon, prediction horizon and acoustic horizon is given in Figure 7.4.

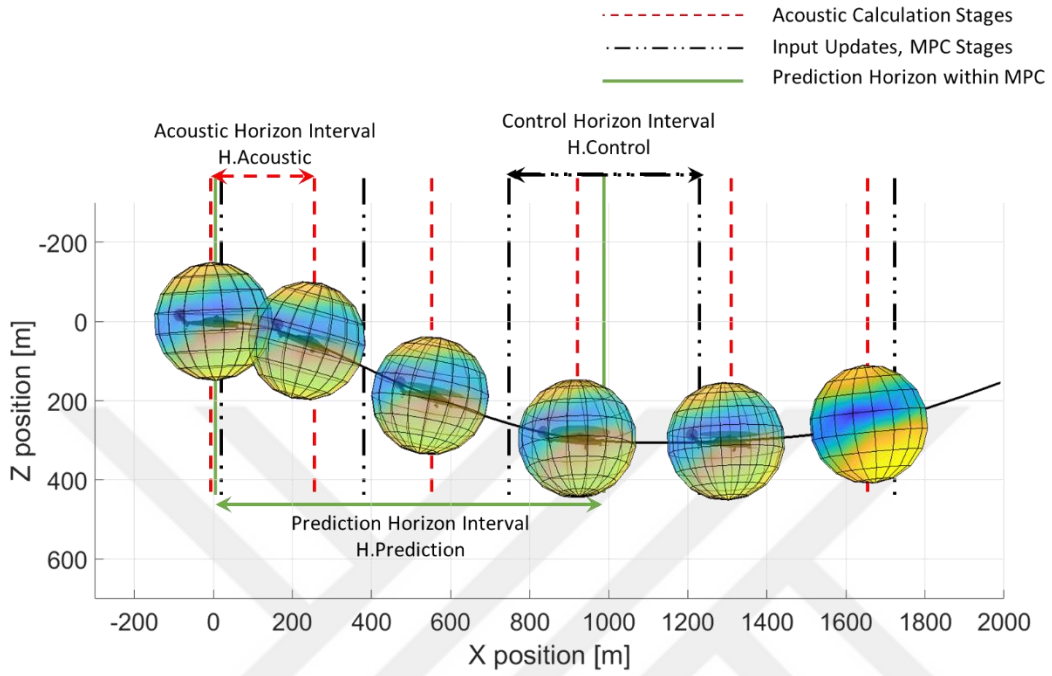

Figure 7.4 Prediction horizon, control horizon and acoustic horizon illustration

The methodology proposed with this study is a comprehensive optimization framework covering different disciplines and/or topics such as flight dynamics, acoustics and simulation. The basic flow chart of the trajectory optimization and track framework is illustrated in Figure 7.5. The model predictive control stage considers specific constraints and a comprehensive objective function, utilizes a surrogate model of the plant and a terrain model to perform future prediction of the system and optimize the trajectory and the related control input to track the generated trajectory simultaneously. The control setting generated for a prediction horizon period of time is sent to the plant where it is utilized for a control horizon period of time and the dynamic response of the plant is feedback to the next model predictive optimization stage.

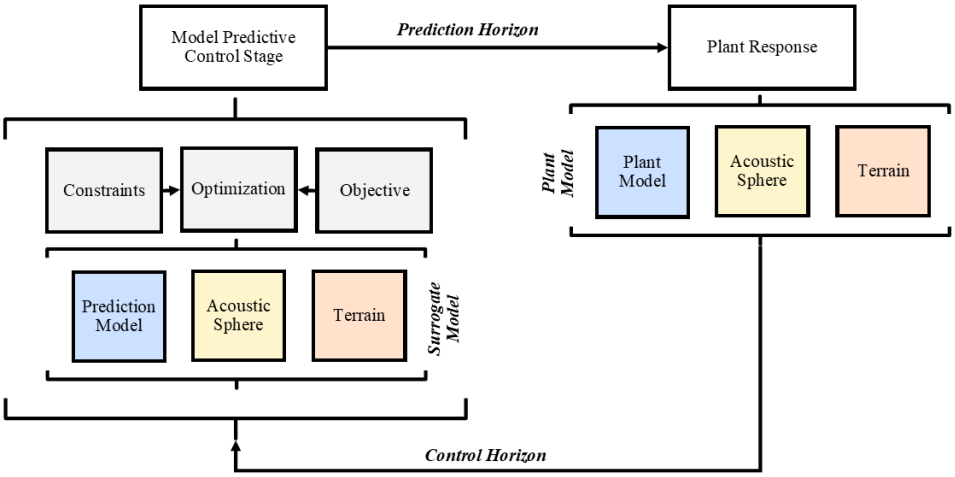

Figure 7.5 Flow chart of trajectory optimization and track framework

The approach uses local search for local minima as at the start of the trajectory optimization for the next horizon period instantaneous helicopter states, operating and ambient conditions are collected, local minimum for the cost function is searched within a constrained domain for inputs to achieve pilot-like smooth behavior.

When the simulation model presented in Figure 6.42 is considered, the MPC corresponds to the marked portion of the Simulink model illustrated in Figure 7.6.

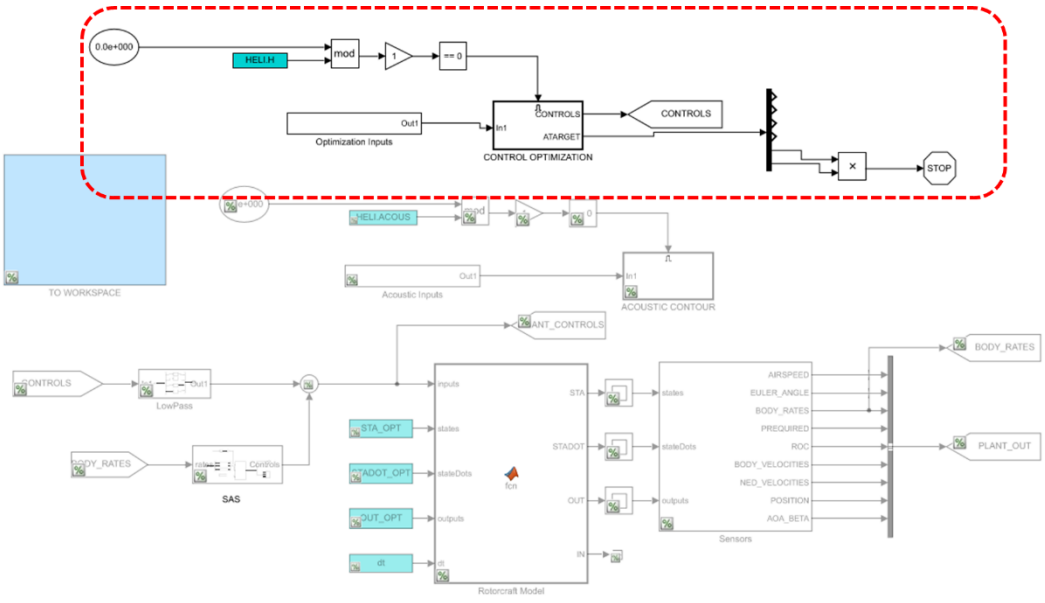

Figure 7.6 MPC structure in the simulation model

The “Control Optimization” sub-system covers the optimization environment producing the control input setting for the prediction horizon time interval. At the prediction stage, a prediction model like the plant model is developed in Simulink environment as depicted in Figure 7.7. The “Rotorcraft Model” is either the exact non-linear copy or a linearized representation of the plant. The same SAS is implemented in the case of non-linear MPC. Same acoustic model with same acoustic horizon is implemented in the prediction model.

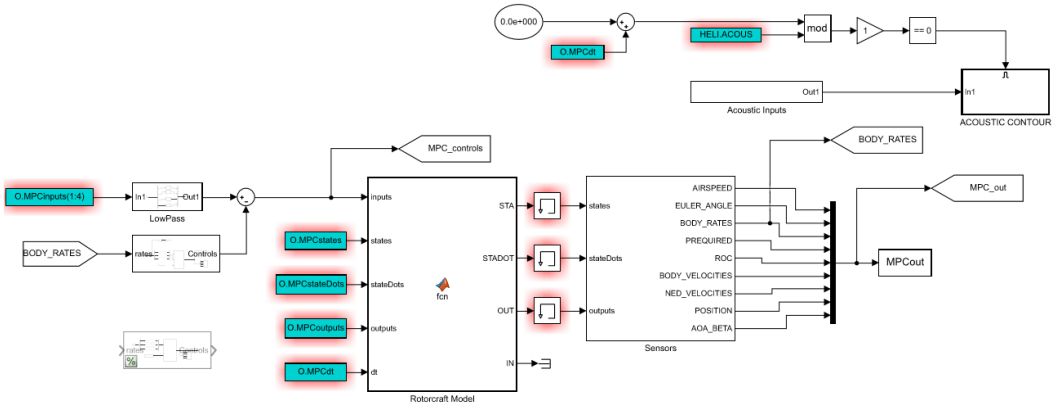

Figure 7.7 Prediction model Simulink flow diagram

7.2 Objective Function

The overall objective function is determined with contributions from each sub-objective that are the concerns of this study. The objective function is developed as a modular and easily editable. Each sub cost function from each discipline has a weighting coefficient multiplied with, which introduces the importance order. This weighting coefficients can be either decided manually or with an additional optimization stage according to the success of the generated trajectory.

The overall cost function is constituted as an array of all sub cost functions introduced from acoustics, performance, safety & comfort, avoid regions and mission & waypoints aspects. The overall cost function is defined with equation (91).

$$J_{Overall} = [J_{acous}\, J_{Fuel}\, J_{Safety}\, J_{Trim}\, J_{Comfort}\, J_{Avoid}\, J_{Position}\, J_{Direction}] \quad (91)$$

Then the overall control cost is constituted with an array including all the control variables of the platform. For a conventional helicopter, the control cost is defined with equation (92).

$$u = [\theta_0\ \theta_{1c}\ \theta_{1s}\ \theta_p] \quad (92)$$

On the other hand, for multi rotor configurations or unconventional configurations, the control array can expand. Therefore, it is better to define a generalized control cost array as given with equation (93).

$$u = [\theta_1\ \cdots\ \theta_n] \quad (93)$$

Then the overall objective function can be constructed through multiplication of cost arrays and their transposes with weighting matrices as given in equation (94).

$$F = J_{Overall}\, QQ\, {J_{Overall}}^T + u\, RR\, u^T \quad (94)$$

where, the weighting matrix QQ defined as equation (95) consists of eight weights coefficients for each of the objective costs and introduces the importance order.

$$QQ = \begin{bmatrix} Q_1 & & \\ & \ddots & \\ & & Q_8 \end{bmatrix} \quad (95)$$

Similarly, weighting matrix RR defined as equation (96) consists of n number of weight coefficients where n is the number of control variables specific to a rotorcraft configuration.

$$RR = \begin{bmatrix} R_1 & & \\ & \ddots & \\ & & R_n \end{bmatrix} \quad (96)$$

7.2.1 Acoustic

The acoustic cost is defined as combination of instantaneous noise levels at noise sensitive regions and time averaged SEL which introduces additional penalty for duration and area of exposure. The acoustic state of a rotorcraft is sensitive to

external disturbances such as control inputs, change in accelerations, Euler angles, flight speeds and flight path angles. Consequently, sudden increase in noise levels at observer locations can be experienced especially around BVI dominated flight regimes. Therefore, the maximum permitted noise level is introduced as an additional penalty with a margin i.e. bumper to the acoustic cost instead of implementing as a constraint. By doing so, a smooth trajectory with feedforward sense can be generated without violating the limit. This is done by introducing a bumper to the maximum permitted noise level around 5dB and an additional penalty to the acoustic cost is introduced inversely proportional with the instantaneous margin to the bumper limit as illustrated with Figure 7.8.

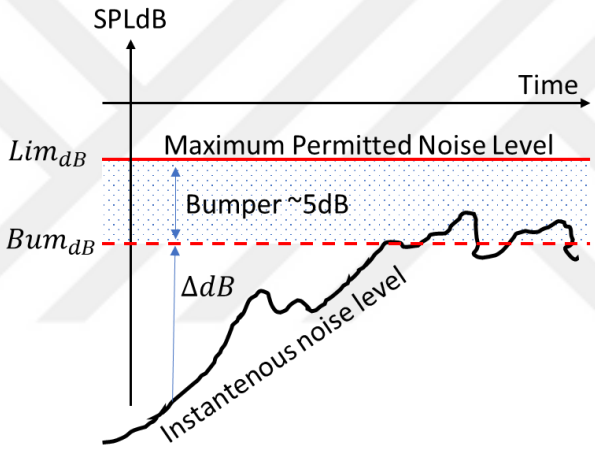

Figure 7.8 Illustration for maximum permitted noise level, bumper limit and instantaneous noise level during simulation.

The acoustic cost is defined with equation (97).

$$J_{acous} = \sum_{m=1}^{Nobs} a_m \left\{ SPLdB_m + SELdB_m + {}^{1}/_{\Delta dB_m{}^{n}} \right\} \qquad (97)$$

where $SPLdB_m$ is instantaneous noise level, $SELdB_m$ is sound exposure and ${}^{1}/_{\Delta dB_m{}^{n}}$ is the margin the max. permitted noise level for observer m. $Nobs$ is the total observer number and a_m ensures the importance order of the observers. $SPLdB_m$ component tries to minimize instantaneous noise levels at all time.

However, coupled with other objectives such as performance, safety, comfort, and mission requirements, $SPLdB_m$ can increase significantly during the simulation. $SELdB_m$ on the other hand introduces the time average content, therefore even though instantaneous noise levels increase and violate bumper limit, time averaged noise levels can still stay minimum as sudden increases in SPL for short durations can be unimportant when overall flight profile is considered. $1/{\Delta dB_m}^n$ component ensures the noise levels always stay under the maximum permitted noise level independent from duration and it dominates the overall objective as the margin to bumper region gets smaller.

7.2.2 Performance

Power requirement of a rotorcraft at a flight regime is an integrated parameter representing the operating state for overall platform and is an essential stage for industry to utilize in flight performance analyses such as cruise speed, endurance and range calculations, and OEMs to utilize in mission planning such as estimation of required fuel quantity. As observed from Figure 7.9, a typical cruise performance chart for a conventional helicopter (Federal Aviation Administration (FAA), 2019), power required as so instantaneous fuel consumption depends on operating condition such as altitude, temperature, weight and air speed. Moreover, rotorcraft power requirement depends on the complex aeromechanical environment that it operates within, on flight regime or maneuver, center of gravity (c.g.) configuration and even mission equipment which continuously varies throughout the mission. Consequently, for accurate estimation of instantaneous power required and fuel consumption, a comprehensive mathematical model reflecting all the dependent variables effect the flight dynamics is essential. The comprehensive mathematical model utilized in this study was already validated with flight tests present in the literature for various helicopters (Şenipek, 2017). Moreover, whenever desired, the dynamic inflow model can be replaced with VVPM for utmost fidelity and accuracy as discussed in this study. Eventually, the rotorcraft mathematical model is capable

of calculating power required variations significantly accurate. In this scope, at prediction stage during trajectory optimization, power required variation and fuel consumption is calculated accurately and introduced as a cost to the overall objective.

Implementing total fuel and instantaneous fuel consumption into the optimization objective as an additional penalty enables green, i.e. low emission and consumption trajectories while considering all other objectives. The fuel cost is introduced with equation (98).

$$J_{Fuel}^{t} = \int_{t_0}^{t} SFC + P_{required} + \frac{d_{remaining}}{V_{average}} \tag{98}$$

where, SFC: is the specific fuel consumption and when integrated from start i.e. t_0 to the time of calculation gives total fuel consumption so far and $P_{required}$ is the instantaneous required power. $d_{remaining}$ is the remaining distance to waypoints and $V_{average}$ is the average flight speed. Implementing such penalty to the overall cost, results in short paths with efficient flight speeds and avoidance of rotorcraft states at the end of the mission i.e. terminal states, at high accelerations, high climb rates and large control inputs. Additionally, with the last term in fuel cost, a feedforward sense is introduced as an additional penalty which avoids slowdowns near waypoints or terminal condition.

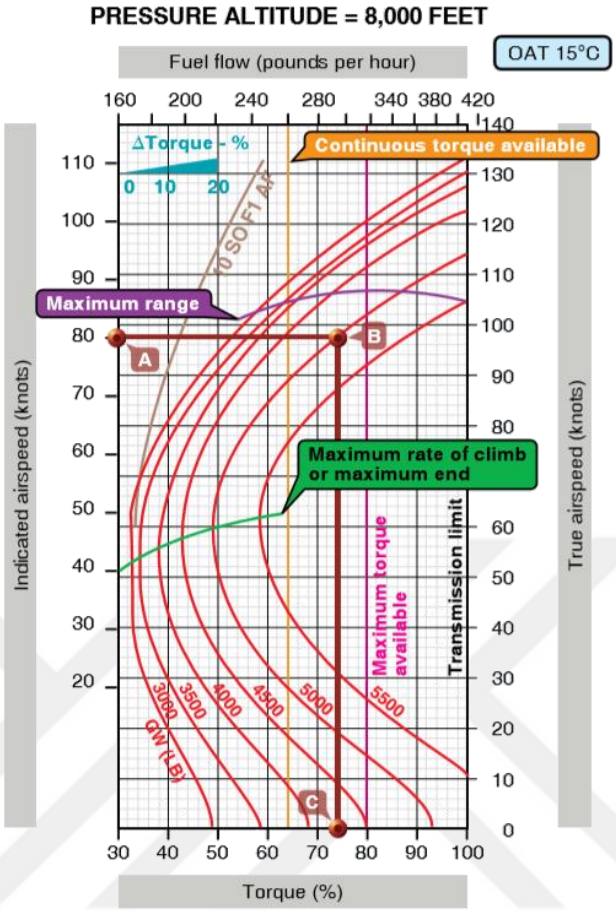

Figure 7.9 Typical performance cruise chart for conventional helicopter (Federal Aviation Administration (FAA), 2019)

7.2.3 Safety & Comfort

Safety and comfort are assured with tracking of translational and rotational speeds, accelerations, Euler angles, margins remaining to the platform specific limits such as never exceed speed (V_{NE}), power available or transmission limit, roll and pitch angle limits, control limits and control input rates.

Safety parameters are implemented as additional cost to the overall objective, J_{Safety}, ensuring rotorcraft operates in its control margin therefore can response to unforeseen circumstances in terms of control authority. Dynamic limits according to rotorcraft instantaneous states can be applied by penalization through translational

velocities, u, v, w, translational accelerations a_x, a_y, a_z, Euler angles, ϕ, θ, ψ and rotational speeds p, q, r of the platform/configuration. Those dynamic limits can be pre-defined specific to platform at each flight speed or can be generated during simulation through the difference between instantaneous values and trim values at the related flight condition. Moreover, the deviation from the trim state can be implemented as an additional cost to the objective function, J_{Trim}, providing a smoother trajectory by penalizing harsh maneuvers and sudden control inputs.

Comfort, on the other hand, is implemented as additional cost, $J_{comfort}$, to the objective function through control input rates, $\dot{\theta}_0, \dot{\theta}_{1c}, \dot{\theta}_{1s}, \dot{\theta}_p$, (collective, cyclic and pedal inputs), translational velocities, u, v, w, translational accelerations a_x, a_y, a_z, Euler angles, ϕ, θ, ψ and rotational speeds p, q, r. Additionally, considering the comfort is correlated with vibrational characteristics, it is evaluated that degradation of comfort can be experienced at flight conditions with high level of power required, high forward speed, high altitude, and temperature. Additional penalties can be implemented at increased power requirements or airspeed, whereas currently not considered at this study.

While expanding the safety and comfort cost function, it is experienced that, flight envelope protection schemes or algorithms can easily be developed with a model predictive control approach as the predictive stage already provides a future dynamic behavior insight of the plant which can be penalized according to margins left to the configuration specific limits.

7.2.4 Avoid regions

Implementing avoid regions into the cost function rather than as constraints to optimization, results in a well-behaved trajectory generation and tracking performance. However, considering within the cost function brings a trade-off between other objectives and the avoid regions. As the avoid regions are hard boundaries that shall never be crossed, a trade-off cannot be made. Therefore, a

spherical bumper region, covering the avoid region is introduced, through which the rotorcraft is allowed to pass with an additional penalty if the optimization decides as more beneficial while considering all other circumstances and objectives. Whether the avoid region is an obstacle, or a dynamic obstacle, the bumper is attached to it with the same kind of motion. The additional penalty inside the bumper region is related with the instantaneous distance vector with an increased multiplier version of the cost function outside of the bumper region. The definition of the bumper region (grey), avoid region (red) and distance vectors are illustrated in Figure 7.10.

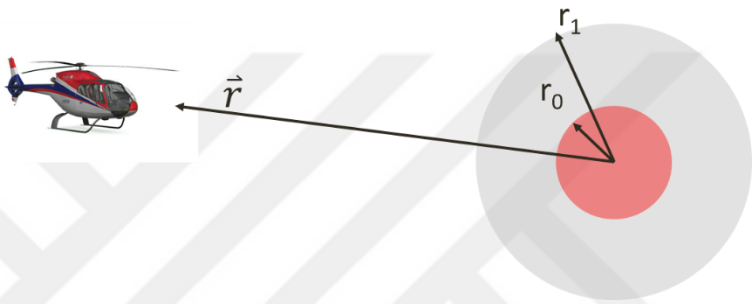

Figure 7.10 Definition of bumper region

The contribution to overall objective, i.e. the cost of the avoid regions are determined with the summation formulation given with equation (99).

$$J_{avoid} = \sum_{m=1}^{N} \begin{cases} {}^{1}/_{|\vec{r}|} \ when \ |\vec{r}| > r_1 \\ \left({}^{1}/_{|\vec{r}|}\right)^{n} \ when \ r_1 > |\vec{r}| > r_0 \\ \infty \ when \ r_0 > |\vec{r}| \end{cases} \tag{99}$$

A sample trajectory optimization with and without bumper considered in the objective function is performed and results are presented with Figure 7.11, Figure 7.12 and Figure 7.13. The solid line represents the optimal trajectory with bumper region, whereas the dotted path represents the optimal trajectory without bumper region. Both simulations are performed other everything are same. When no bumper region is introduced, the optimization cannot cope with the trade-off between approaching to avoid region and path length as passing through the avoid region is prohibited and creates extremely large additional penalty. When bumper region is

introduced, optimization function generates the sense of approach distance and makes the trade-off between getting closer to the avoid region and other penalty contributors. In other words, avoid region acts like a potential, smoothly increasing the penalty with decreasing distance.

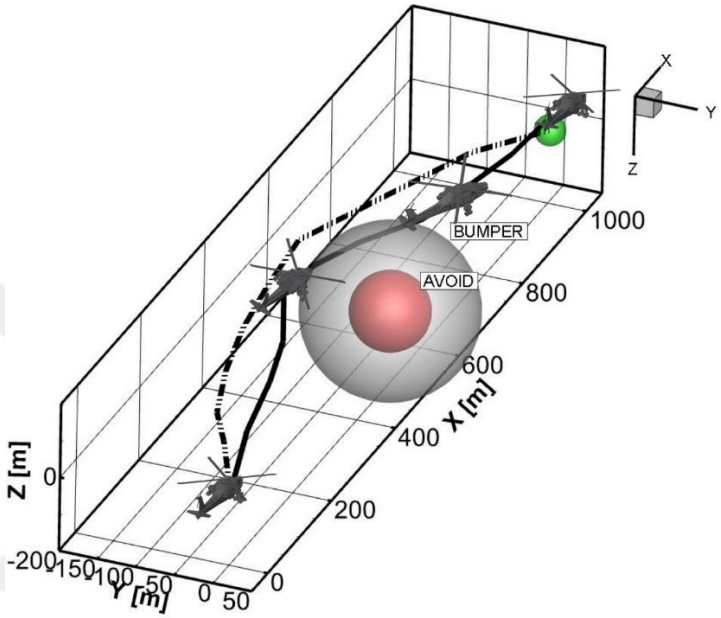

Figure 7.11 A sample trajectory optimization with bumper region (solid line : with bumper region, dotted line : without bumper region)

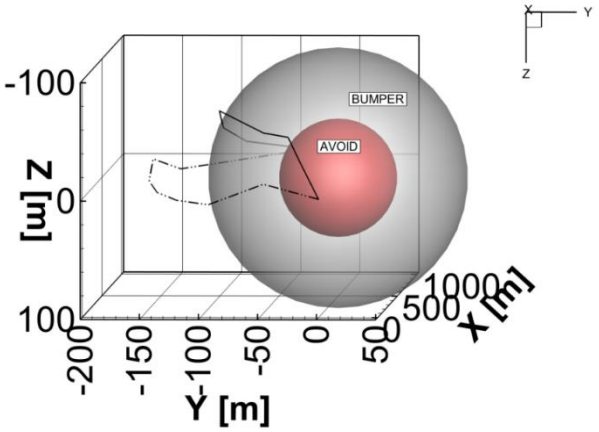

Figure 7.12 A sample trajectory optimization with bumper region (solid line : with bumper region, dotted line : without bumper region)

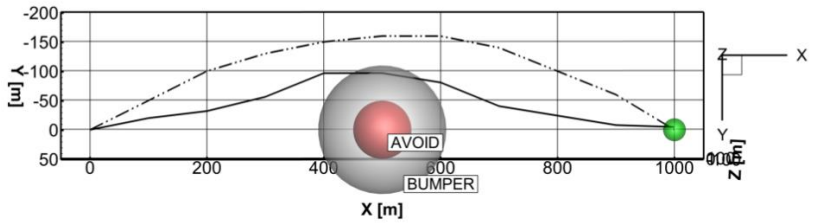

Figure 7.13 A sample trajectory optimization with bumper region (solid line : with bumper region, dotted line : without bumper region)

7.2.5 Mission & Waypoints

The essence of this study is to generate noise minimal trajectory and track for a rotorcraft while accomplishing the nominal or usual mission. Therefore, a mission planner and way point tracker algorithm operate throughout the simulations, providing mission requirements, mission waypoints to be passed and overall planning of the fight trajectory. Mission planner is always aware of all waypoints, holds the queue information of the waypoints and gets involved in the trajectory optimization process so that passage from all the waypoints are assured. Mission planner contributes to trajectory optimization and track through two cost functions to overall objective.

First is the position cost, $J_{position}$, composed of relative distances to all waypoints except the ones already accomplished. Position cost is fed by the instantaneous distances to each waypoint as illustrated in Figure 7.14 throughout the simulation, therefore always aware of other waypoints to be passed introducing a feedforward characteristics.

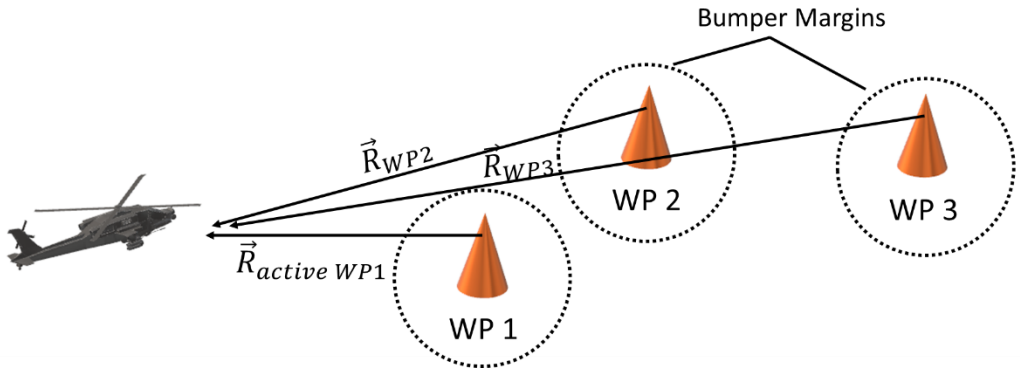

Figure 7.14 Illustration for position cost of objective

A contribution from each waypoint is collocated within the position cost proportional to inverse of the instantaneous distance through equation (100).

$$J_{position} = \sum_{m=Active\ WP}^{WPn} a^m \frac{1}{|\vec{r}^m|} \tag{100}$$

where WPn is the total waypoint number, a^m is weighting factor determined by the mission planner at each optimization stage, $\vec{r}^m$ is the relative distance vector from rotorcraft to each waypoint calculated before and during the optimization. Inverse of the instantaneous distance to each waypoint is multiplied with a weighting factor in order to sort the waypoint in an order to pass which is already defined before the simulation.

The second cost function is the direction cost function, $J_{direction}$, which brings penalty proportional to the angle between flight path vector and position vector of the active waypoint. Optimization algorithm tries to align flight path vector with the position vector of the active waypoint i.e. vector from rotorcraft to the waypoint as illustrated with Figure 7.15, through the direction cost function given with equation (101).

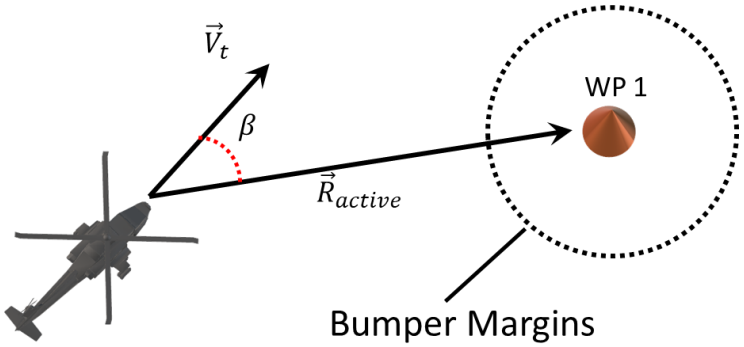

Figure 7.15 Illustration for direction cost function

$$J_{direction} = |1 - \cos(\beta)| = \left|1 - \frac{\vec{V}}{|\vec{V}|} \cdot \frac{\vec{R}_{active\,WP}}{|\vec{R}_{active\,WP}|}\right| \tag{101}$$

Both cost functions are managed by a mission planner algorithm which sorts the waypoints, incorporates the bumper margins, and decides active waypoint through a waypoint switching algorithm. Two switch conditions are implemented within the mission planner, one utilizing the bumper margins, other utilizing a waypoint switch line located at each waypoint and oriented perpendicular to the position vector from rotorcraft to incorporated waypoint. First switch decision is made through monitoring rotorcraft position along the prediction horizon during the MPC optimization stage. If at any instant within the horizon, rotorcraft passes through the active waypoint's bumper margin, the algorithm switches to the next waypoint by defining it as the active waypoint and excluding the existing from the mission queue. The second switch decision is made through defining an imaginary waypoint switching line that is oriented at the waypoint and perpendicular to the position vector from rotorcraft to the active waypoint calculated at beginning of the prediction stage. If at any instant the rotorcraft crosses the waypoint switching line, the algorithm switches to the next waypoint by defining it as the active waypoint and excluding the existing from the mission queue. Note that in three-dimensional space, the switching line corresponds to a perpendicular plane. Mission planner operates at the beginning of the MPC stage to decide the active waypoint and throughout the prediction stage to continuously monitor waypoints and perform switching whenever required. Additionally, mission planner decides weighting factors for the position

cost function giving highest weight to the waypoint first in the queue and lowest to the last in the queue. If a waypoint is already passed or switched, then it is removed from the queue by the mission planner. The illustration for switching conditions and the decision flowchart is presented in Figure 7.16 and Figure 7.17.

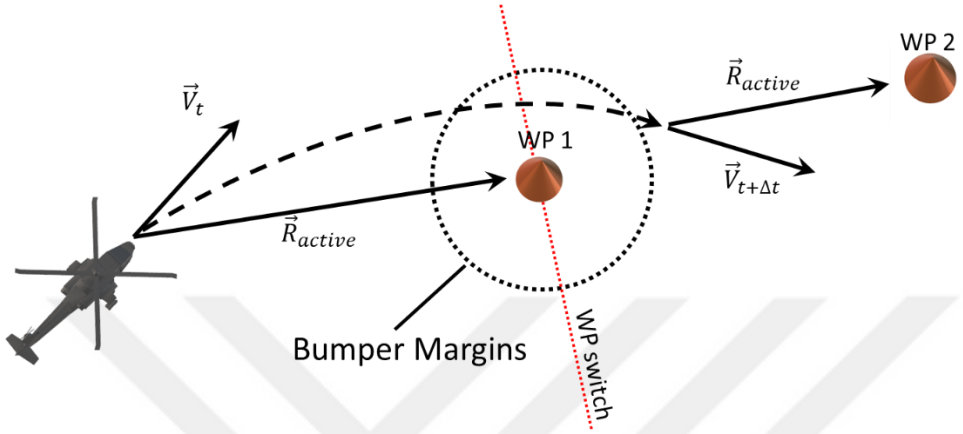

Figure 7.16 Illustration of waypoint switching conditions

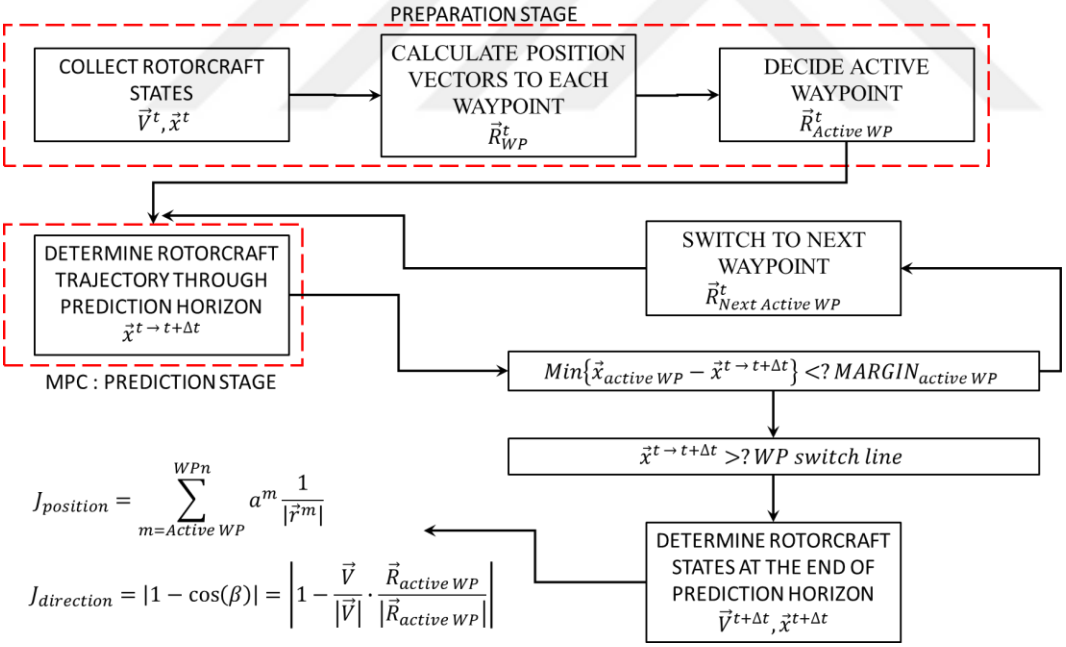

Figure 7.17 Flow chart for waypoint switching decision

7.3 Constraints

Having a detailed overall objective function still does not eliminate the need of constraints for optimization function. These constraints are generally incorporated with platform specific limitations that shall not be violated throughout the simulation. Additionally, helicopter maneuverability may be restricted in terms of passenger or pilot comfort aspects through constraints on translational and rotational accelerations, attitude limitations. Further constraints may be required when operating around airports, helipads, and urban areas if there exists confined civil airspace or flight corridors.

Therefore, constraints are generally required as the coupled non-linearity of the mathematical model results in exceedances in channels/states that are not primarily damped within a mission. Penalization through cost function sometimes is not sufficient to ensure rotorcraft operates within its controllable flight envelope. For this reason, constraints, if decided to be included, are required to be generated as platform specific or mission specific considering the operating environment and assignment such as transport, ambulance, surveillance, touristic etc.

Platform specific constraints such as never exceed speed, roll & pitch attitude limitation, wind-azimuth envelope, altitude limits, power available or transmission limits, control limits or rates shall be defined before simulation. Those limitations cannot be violated at any instant for safety issues. Otherwise, helicopter dynamic response/maneuverability can be restricted in terms of comfort aspects.

Mission specific constraints cover the operating civil airspace, flight corridors, avoid zones, maximum and/or minimum speed and altitude limitations, assigned flight corridors during approach, take-off, or flyover are required to be defined before the simulation. Whereas there can be dynamic constraints such as existence of other aircrafts in the domain of interest. Generally, civil airspace especially around urban areas is divided into zones to be avoided or flight corridors defined for specific type of aircrafts as depicted with Figure 7.18 and Figure 7.19.

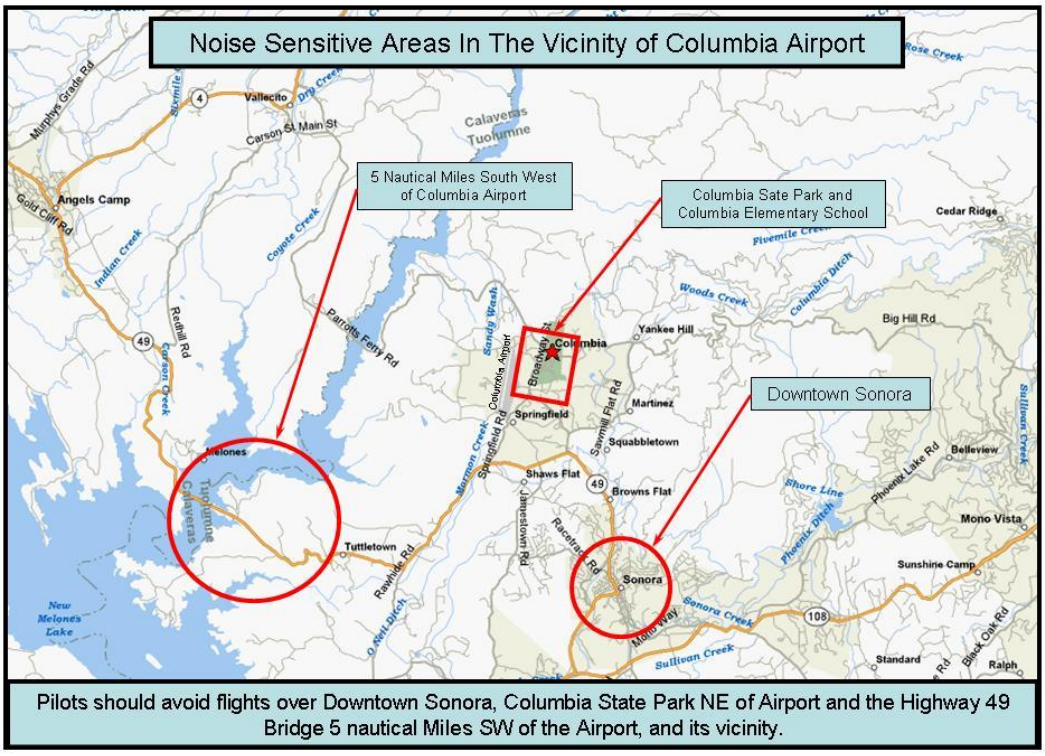

Figure 7.18 Avoid regions in the vicinity of Columbia Airport (*Noise Sensitive Areas*, n.d.)

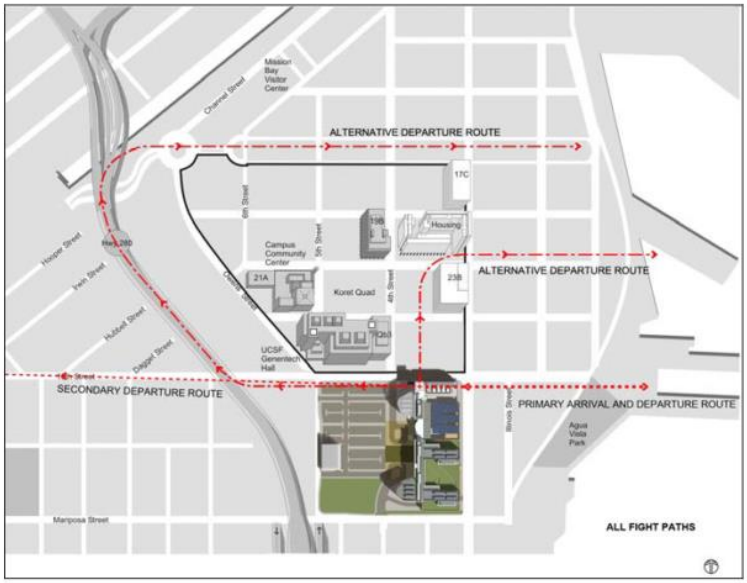

Figure 7.19 An example for dedicated flight corridors and routes (Behr & Reindel, 2008)

7.4 Optimization Algorithm

The quality of the optimized trajectory and control input to track the generated trajectory depends on the accuracy of the flight dynamics representation and numerical optimizer. The complexity of the objective function requires determination of gradient and Hessian in order to estimate the feasible search direction therefore the optimization algorithm considering the motivation of this study shall be fast, simple, consistent, and practical.

The author previously utilized the CONMIN optimizer (Tamer et al., 2011) for helicopter rotor blade design for minimum power required which is a gradient based method utilizing feasible search direction and obtains the gradients numerically. Such gradient methods cannot always provide a global optimum solution, however, considering the motivation of this study, a local search, local minimum optimization scheme is beneficial which enables pilot like behavior while implementing comfort, safety, acoustic and performance objectives. Besides, having such a complex and multi-disciplinary objective function generally does not exhibits an achievable global optimum as one or more objectives might require impractical flight conditions. Therefore, a trade-off between the objectives is required to be made over an initial state, i.e. local search, up to a nearby state with better total cost. Consequently, a gradient based, computationally efficient, constraint and multivariable optimization approach is required. The best option is the utilization of the built-in optimization functions within the development environment. Nevertheless, an unconstraint Newton optimization algorithm is developed in order to improve to computational efficiency. Both the implemented optimization algorithm and the selections and settings of the MATLAB's built-in "fmincon" optimization algorithms are summarized in this chapter.

The implemented optimization algorithm is basically Newton's optimization approach for unconstrainted problems. It calculates the gradient numerically and approximates the Hessian matrix. Independent from the definition of the cost function, the objective of the optimization algorithm is to minimize the cost which

is basically a function of pilot control input set. As u is the input vector with four elements ($u \in R^4$) consisting of collective, longitudinal cyclic, lateral cyclic and pedal controls the formulation for the optimization algorithm is performed with u vector only for convenience. If an objective function is defined such as equation (102),

$$minimize\ J(u) \tag{102}$$

Then the first order necessary optimality condition in this case is then written as;

$$\nabla J(u) = 0 \tag{103}$$

The iterative solution formulation of the optimality condition represented by the Newton method, i.e. the Newton equations is then written as;

$$u_{t,k+1} = u_{t,k} - \frac{\overbrace{\nabla f(u_{t,k})}^{p_k}}{\nabla^2 f(u_{t,k})} \tag{104}$$

Re-arranging equation (104), equation (105) is determined as;

$$\left(\nabla^2 f(u_{t,k})\right) p_k + \nabla f(u_{t,k}) = 0 \tag{105}$$

p_k is the descent or search direction, the subscript "$_k$" represents the iteration number and "$_t$" is the index of the time interval for which the optimal control is being calculated. The duration of the time interval corresponds to the finite horizon decision. The calculated optimal control at time t is directed to the plant for the state response i.e. x_{t+1} and kept constant until the next optimization stage, i.e. $t + 1$. Solving the Newton equations for descent direction,p_k, transforms the optimization problem into a minimization problem of the quadratic function of p. Therefore instead solving the original problem, minimizing the quadratic function of p by finding a solution for $\nabla p = 0$, by then determining solution of the original problem by utilizing the descent direction, p and a step length α, optimization is achieved on u_t as follows;

$$solve\ for\ \nabla p_k = 0 \tag{106}$$

The calculation of derivatives is computationally expensive as s simulation is being performed for each perturbation in the control input to estimate future behavior of the plant. Alternatively, the Hessian matrix is defined and implemented into equation (105) to determine a quadratic representation;

$$\nabla^2 = B \tag{107}$$

$$B_k p = -\nabla f(u_{t,k})\ obtain\ p_k \tag{108}$$

where B is the Hessian matrix and calculated recursively with the update formula of Broyden, Fletcher, Goldfort and Shanno (BFGS);

$$B_{k+1} = B_k - \frac{(B_k s_k)(B_k s_k)^T}{s_k^T B_k s_k} + \frac{y_k y_k^T}{y_k^T s_k} \tag{109}$$

where

$$s_k = x_{k+1} - x_k \tag{110}$$

And

$$y_k = \nabla f(x_{k+1}) - \nabla f(x_k) \tag{111}$$

Therefore, re-calculation of the Jacobian of the objective function with respect to the control inputs is enough to estimate the Hessian matrix. Then the control input setting is updated with the descent direction and step length with equation (112).

$$u_{t,k+1} = u_{t,k} + \alpha_k p_k \tag{112}$$

Implemented algorithm approximates the Hessian and utilizes an unconstrained optimization approach therefore generally provides faster computation. However, MATLAB built-in function “fmincon” (The MathWorks, 2012) utilizes a sequential quadratic programming (SQP) and implements constraints over non-linear optimization algorithms and utilizes a center difference derivative method, therefore provides a more comprehensive optimization framework. For those reasons, “fmincon” optimization function is utilized as a default approach whereas the Newton optimization algorithm is always available on demand. The configuration parameters for the “fmincon” function as utilized is summarized in Table 7.1.

Table 7.1 Configuration parameters for “fmincon” (The MathWorks, 2012)

Field	Selected Configuration	Explanation
Optimization Algorithm	SQP – Sequential Quadratic Programming	Computationally Efficient and imposes upper and lower bounds for variables i.e. control inputs in this case
Gradient Calculation methodology	Finite Difference: central differencing	Provides second order differencing
Max.Function evaluations	3	Number of Jacobian updates
Max. Iterations	100	Max. total number of iterations
Bounds	Active	Upper and lower bounds to variables
Scale Problem	True	Normalizes all constraints and objective function therefore no weighting is required

7.5 Trajectory Optimization

At each predictive stage, MPC algorithm estimates future dynamics of the system for optimization purpose and selects the control input with the co called best prediction response. A trade-off between computational cost, trajectory smoothness and accuracy are performed through trial and error, and 10 seconds prediction horizon combined with 2 seconds control horizon is decided as a rule of thumb for trajectory optimization and track purposes. In this scope, at every 2 seconds, the model predictive stage (MPS) performs 10 seconds future simulations to decide the best alternative. Then the control input providing the best future dynamics is utilized for only 2 seconds, after which another 10 seconds optimization stage (MPS) steps in as illustrated in Figure 7.20, Figure 7.21 and Figure 7.22.

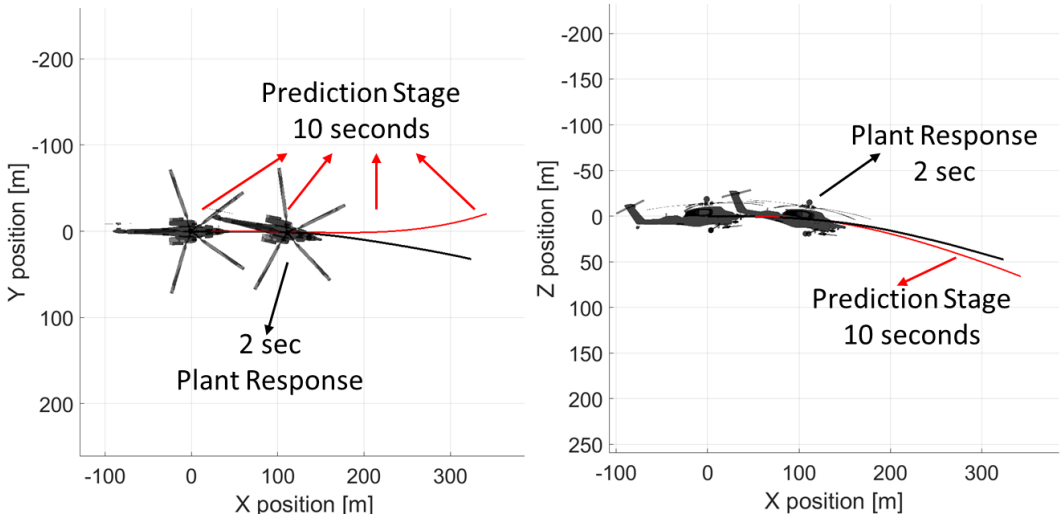

Figure 7.20 Illustration for prediction stage response and plant response

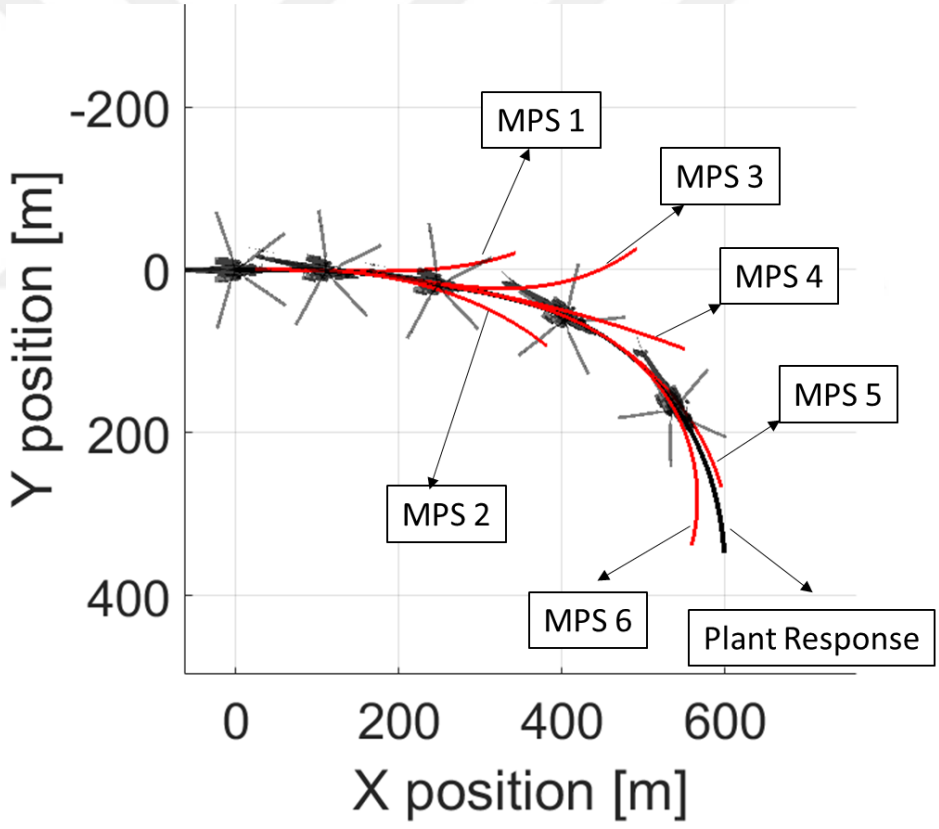

Figure 7.21 Illustration for prediction stage response and plant response

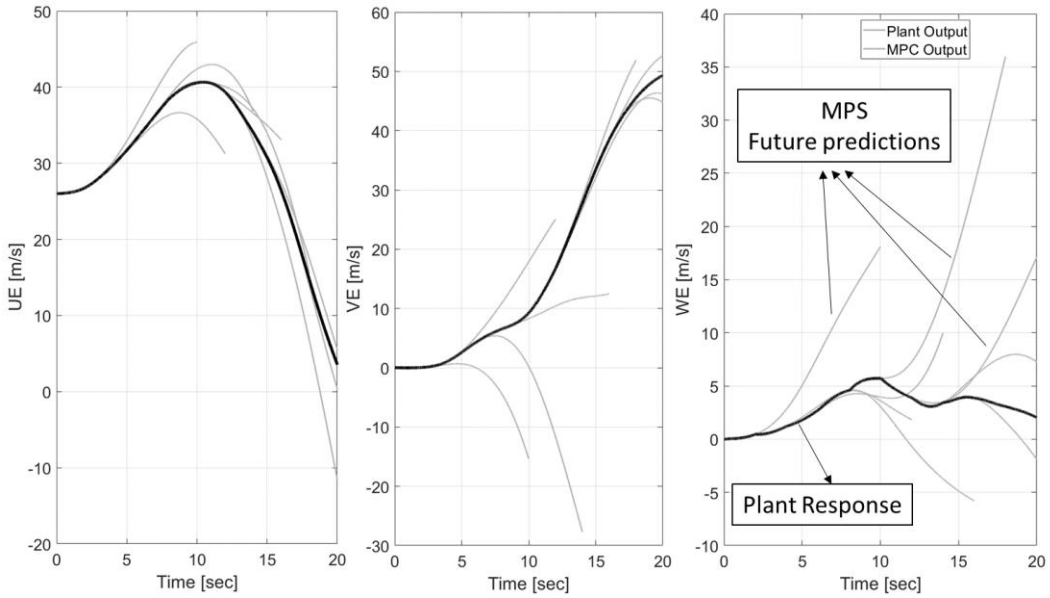

Figure 7.22 NED speeds, MPS future predictions and Plant response

7.6 Prediction & Control Horizons

The durations picked for prediction and control horizons has a direct effect on characteristics of the generated trajectory and track performance. The general sense in the literature is to select the prediction horizon according to the dynamic system of interest (Atalay, Şenipek, et al., 2019; Worthmann, 2012). In this scope, trajectories with varying prediction to control horizon ratios are generated and compared to pick the best combination. 8, 10 and 14 seconds prediction are combined with 2 seconds control horizons, leading ratios of 4, 5 and 7. Trajectory generation and track for a slalom course is studied with mission waypoint tracking concern only, i.e. excluding all sub-objective functions through zeroing relater terms in the weighting matrices except terms of $J_{position}$ and $J_{direction}$ given with equations (100) and (101). The slalom course is defined with four waypoints and the helicopter is trimmed at 50 knots level flight initially. 50 meters of bumper radius is defined for the waypoints and as all cost contributions from performance, safety and comfort are

excluded, the helicopter is allowed to accelerate and actuate freely. Trajectory generation and track performances for varying ratios are presented in Figure 7.23, Figure 7.24 and Figure 7.25 in terms of path lines, Euler angles, rates and controls.

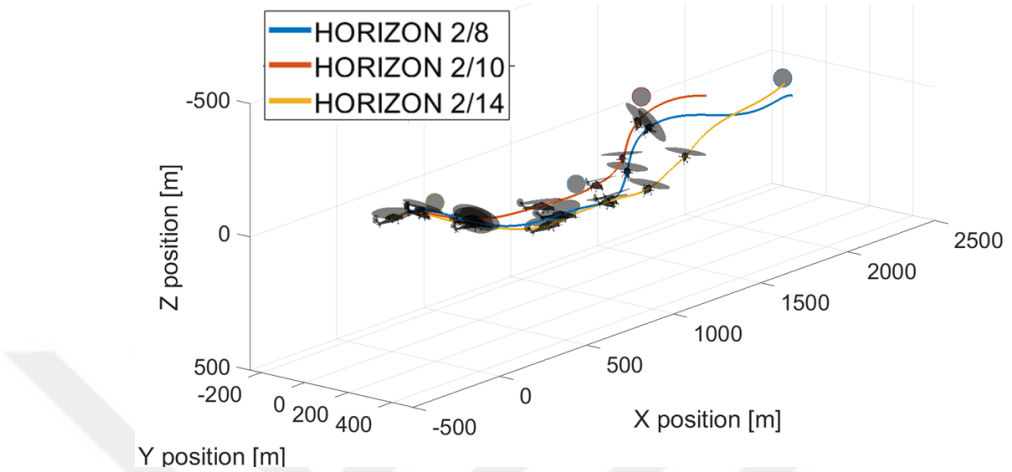

Figure 7.23 Comparison of different prediction to control horizon ratios

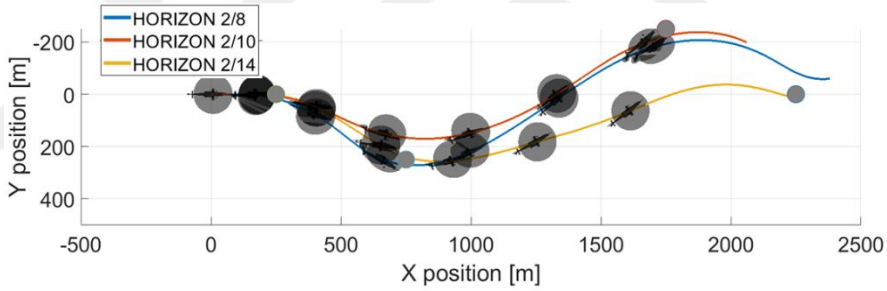

Figure 7.24 Comparison of different prediction to control horizon ratios

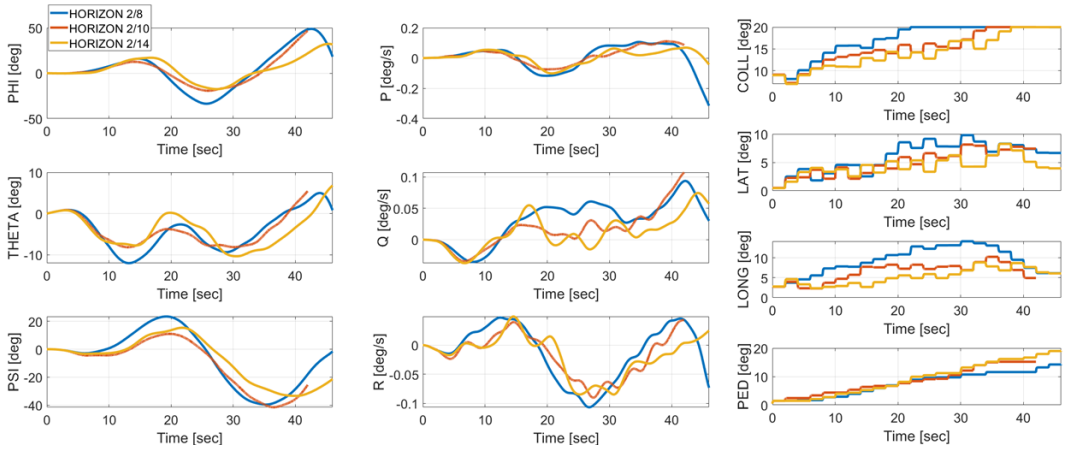

Figure 7.25 Comparison of different prediction to control horizon ratios

When results are examined, it is observed that the prediction to control horizon ratio has a strong effect on the generated trajectory and track performance. It is observed that the highest prediction horizon results in a smoother trajectory through introducing a feedforward mechanism which on the other hand decreases waypoint tracking performance yet with an improved terminal accuracy. Smallest ratio on the other hand, having the shortest horizon for future dynamic states of the platform, provides best waypoint track performance however with largest control inputs, Euler angles and rates. The intermediate prediction to control horizon ratio provides a balanced trajectory generation and track characteristics in terms of waypoint tracking performance, terminal accuracy, required input magnitude and plant dynamic response such as body rates and angles. Velocity components in Earth reference frame for model predictive stage and plant response are presented for varying prediction horizons in Figure 7.26.

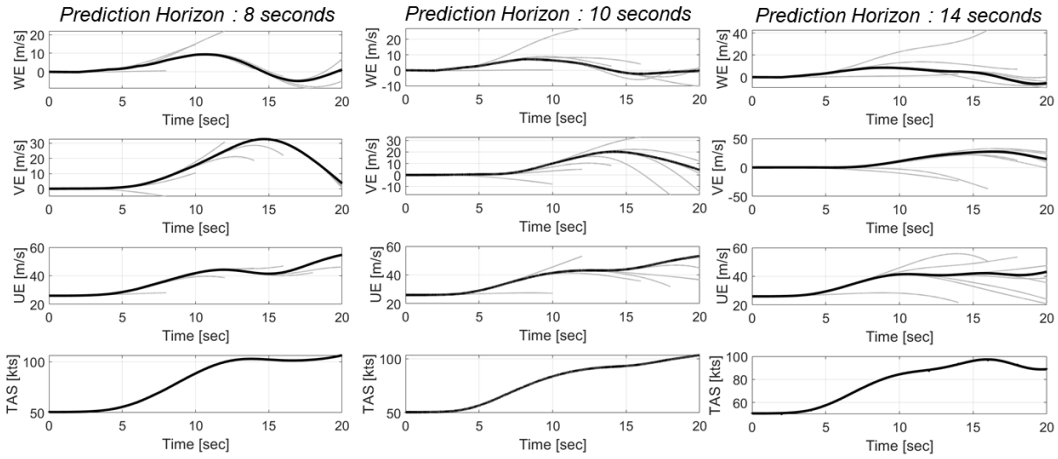

Figure 7.26 Comparison of different prediction to control horizon ratios

Finally, as only the waypoint track objective is included in the overall cost function excluding acoustics, performance, safety and comfort contributions, any constraint to keep the trim state or damp the rotation and acceleration rates are absent resulting in a uncontrolled flight regimes and Euler angles. Standing upon the conclusion of the prediction to control horizon ratio study, 10 seconds to 2 seconds horizon durations is evaluated as the best-balanced alternative and is utilized throughout this study.

CHAPTER 8

RESULTS

Various evaluations with different test purposes are performed on the developed comprehensive modeling, aeroacoustics analysis and trajectory optimization & track approaches. Each evaluation is performed to test, evaluate, and demonstrate a different capability of the overall developed methodology.

This chapter covers the results determined for the simulations listed below:

- A conventional full helicopter configuration is trimmed with comprehensive VVPM, at various forward speeds and hover, trim parameters and acoustic characteristics are studied.
- A flyover acoustic simulation with a conventional helicopter configuration is performed, transient noise impact at an observer location on ground is studied. This study is performed to assess capability and performance of the developed tool for evaluation of a rotorcraft in terms of civil certification requirements.
- A theoretical multi-rotor with combination of co-axial, pro-rotor, propeller and wings design is performed. Trim analysis with comprehensive VVPM is performed to demonstrate the capability to model complex and unconventional configurations, solve for aerodynamic performance, interactions and flight dynamics response. Additionally, acoustic analysis is performed for hovering flight condition to demonstrate to assess noise characteristics of complex & unconventional configurations such as a multi-rotor.
- Trajectory optimization samples are performed for a jump take-off and acceleration mission and a 360° turn mission. Although acoustic response is calculated throughout the simulations, these simulations are performed with

only mission concerns to assess trajectory optimization and track performance.

- Green trajectory optimization samples are performed for an acceleration and flyover mission and a horseshoe turn and climb mission. These simulations are performed to demonstrate the trajectory optimization and track capability with acoustic, performance, safety, comfort, and mission/waypoint concerns.

8.1 Full Helicopter Trim Acoustic Analysis

Full rotorcraft trim analysis for a conventional configuration helicopter is performed for hover, and level flight with moderate forward speed, and high forward speed conditions with VVPM coupled comprehensive model as depicted in Figure 8.1 and Figure 8.2. Then VVPAM is utilized for further noise analysis and acoustic sphere.

Analysis model given in Figure 8.1 is a typical 5-ton class conventional helicopter configuration with 4 bladed main and tail rotors. ROBIN fuselage is utilized as a generic fuselage model with scaled aerodynamic database with flat plate area of a typical 5-ton class helicopter. S76 main rotor with anhedral blade tips is utilized as main rotor and tail rotor is sized to always provide required anti-torque in all flight conditions.

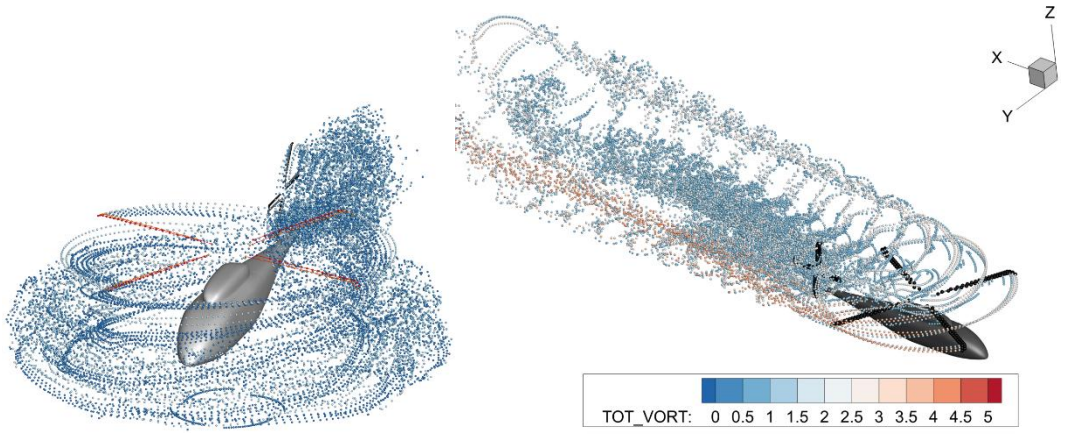

Figure 8.1 Conventional helicopter analysis model

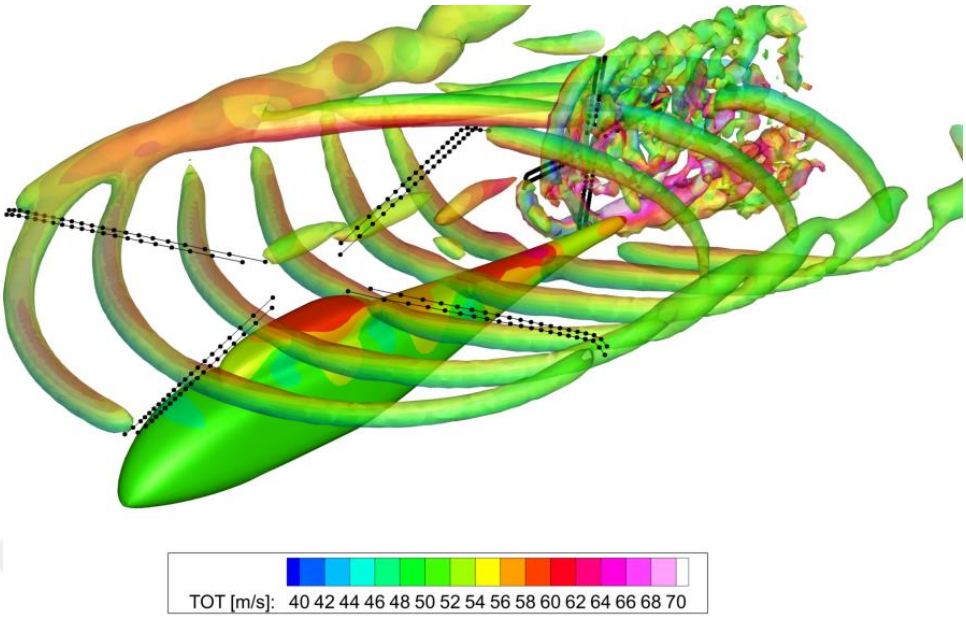

Figure 8.2 Conventional helicopter level flight trim q-criterion iso-surface

Main and tail rotor parameters for the analysis model are presented in Table 8.1.

Table 8.1 Conventional helicopter analysis model

Main Rotor		**Tail Rotor**	
Parameter	Value	Parameter	Value
Radius [m]	6.71	Radius [m]	2
Blade Number	4	Blade Number	4
Root cut out [%]	22	Root cut out [%]	30
Tip Speed [m/s]	205	Tip Speed [m/s]	205
Chord Length [m]	0.39	Chord Length [m]	0.20
Tip shape	Swept Anhedral Tapered	Tip shape	Swept Tapered

Full rotorcraft trim analysis for all three flight conditions (hover, moderate and high speed level forward flight) are performed and the results in terms of hub force & moments, control inputs and power & Euler angles convergence histories are presented in Figure 8.3, Figure 8.5 and Figure 8.7. Acoustic analysis results, in terms of total SPL contour on the acoustic sphere, in-plane and out-of-plane acoustic pressure variations specifically to thickness and loading noise components, are presented in Figure 8.4, Figure 8.6 and Figure 8.8.

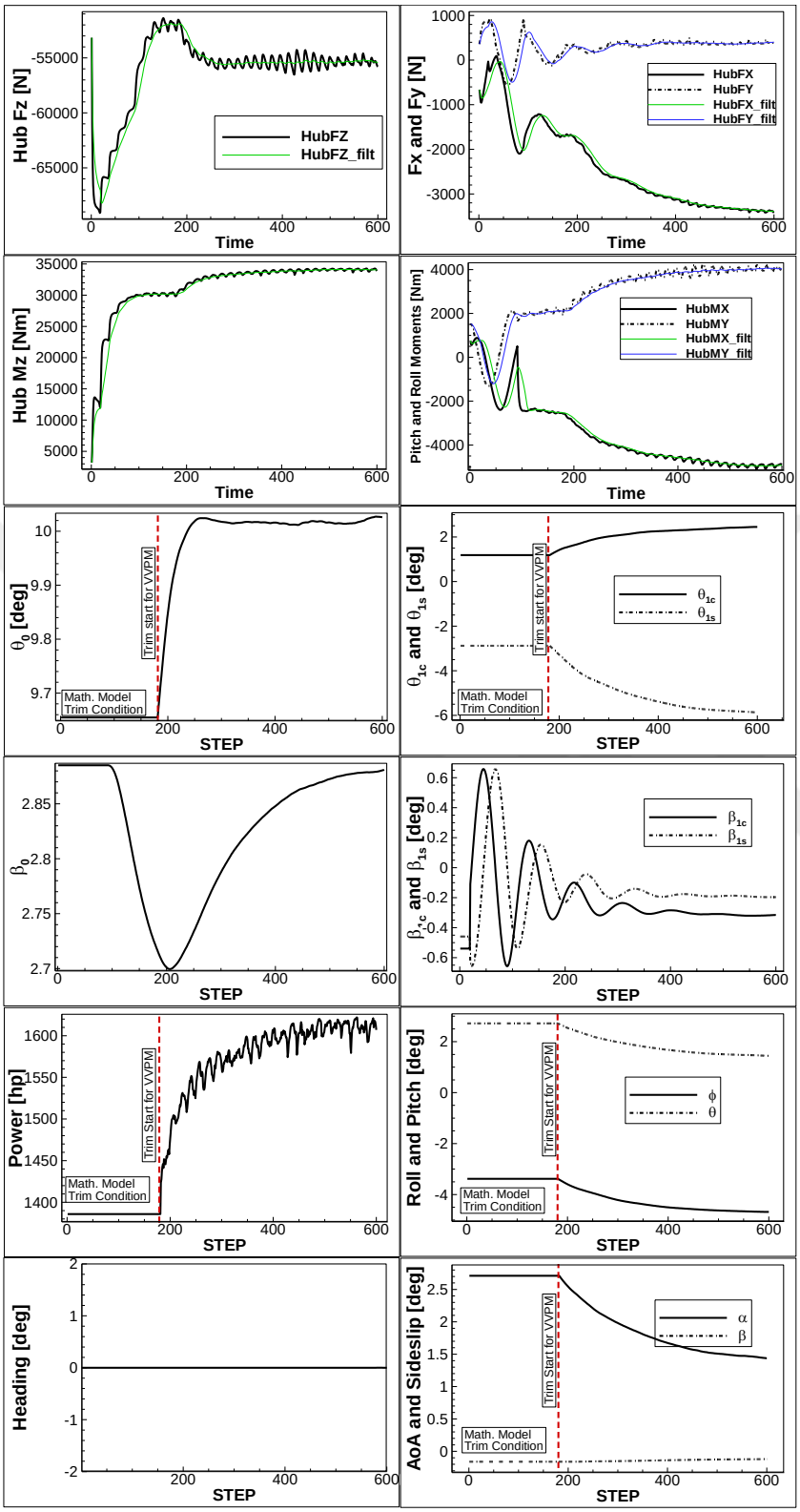

Figure 8.3 Hover trim variables & inputs convergence history

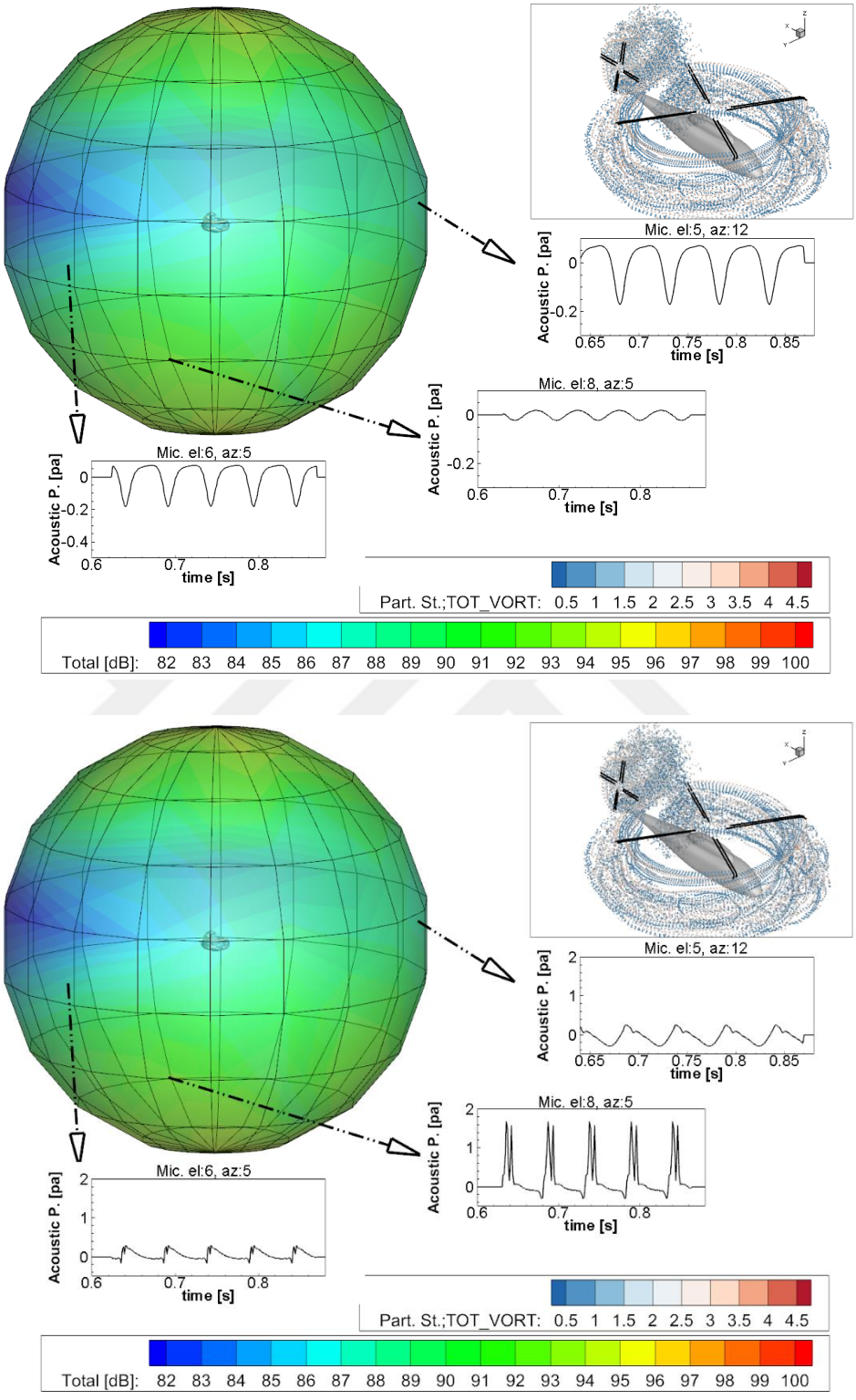

Figure 8.4 Hover trim total SPL contour, in plane & out of plane acoustic pressure variation of thickness (upper) and loading (lower) noise components

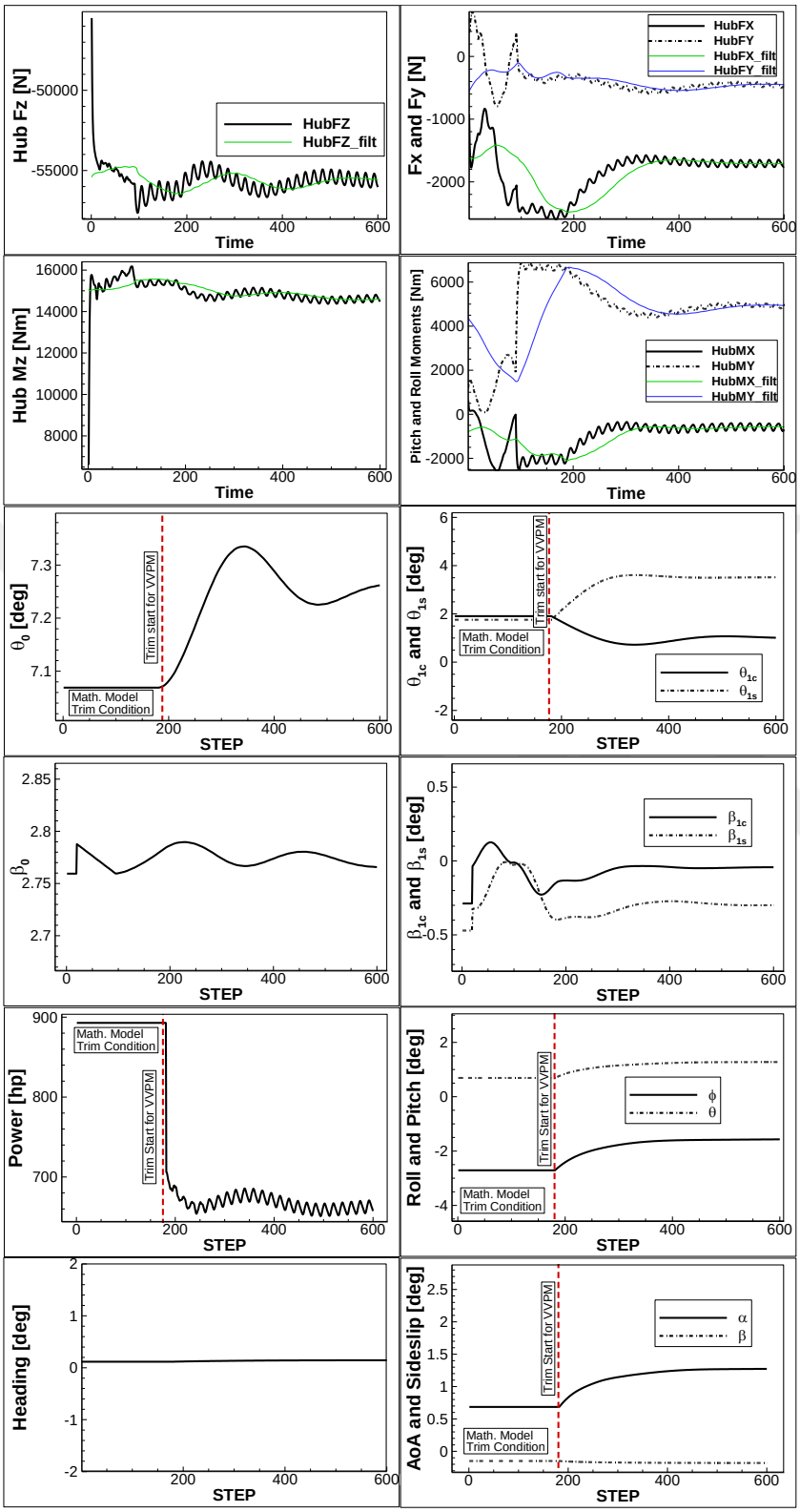

Figure 8.5 Moderate speed trim variables & inputs convergence history

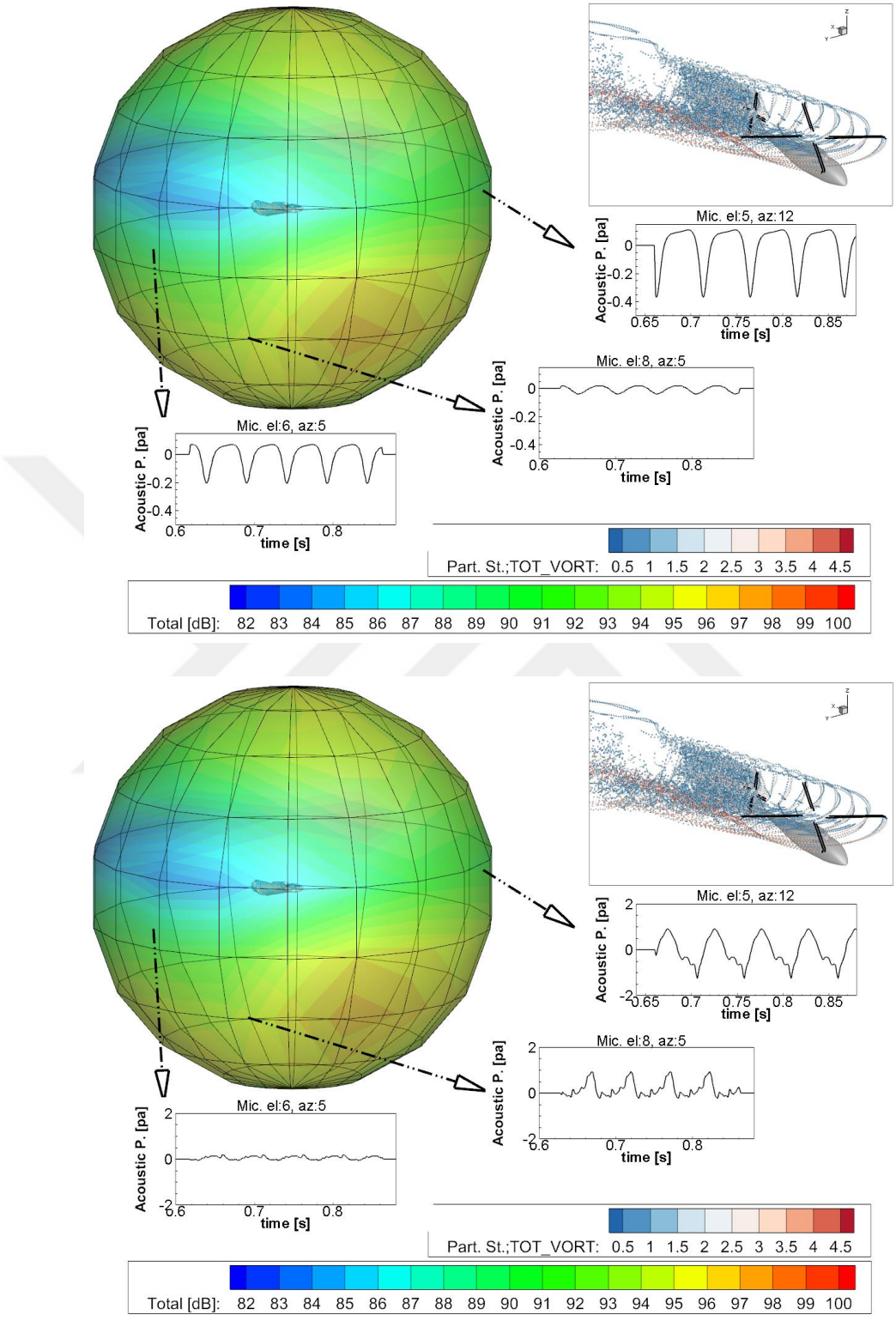

Figure 8.6 Moderate speed trim total SPL contour, in plane & out of plane acoustic pressure variation of thickness (upper) and loading (lower) noise components

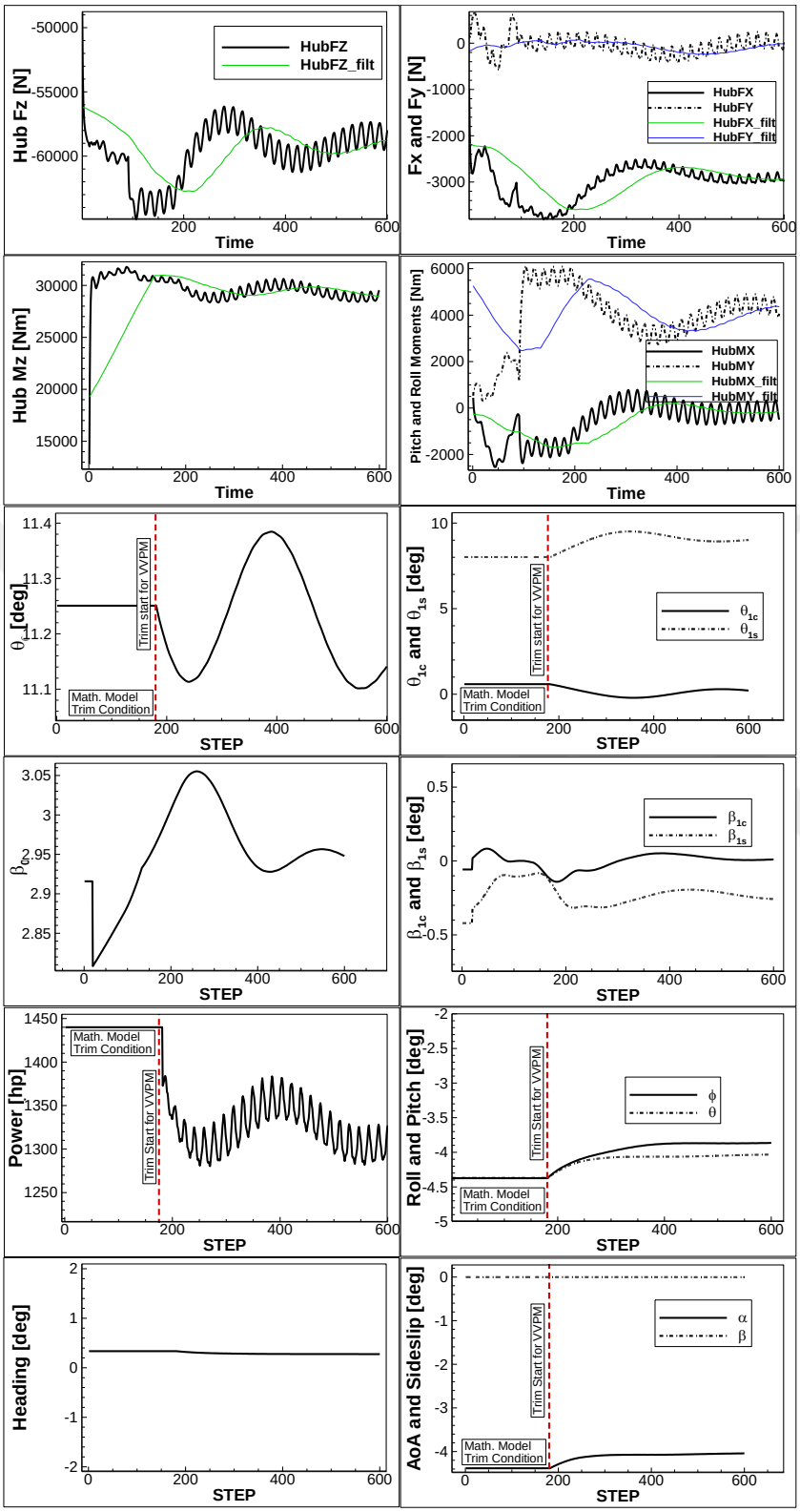

Figure 8.7 High speed trim variables & inputs convergence history

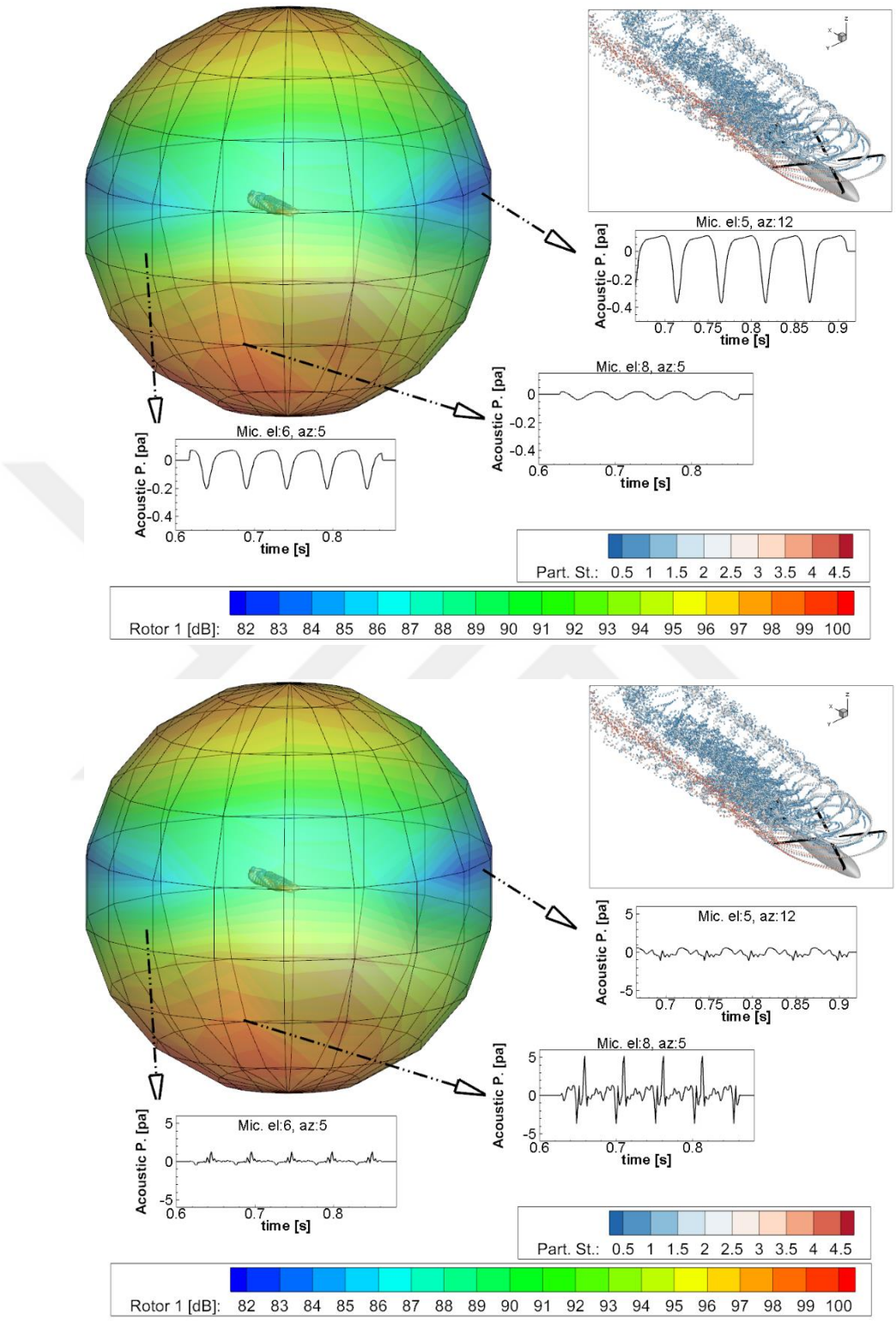

Figure 8.8 High speed trim total SPL contour, in plane & out of plane acoustic pressure variation of thickness (upper) and loading (lower) noise components

This chapter reveals the full rotorcraft trim simulation and aeroacoustics analysis capability of the developed methodology. Analysis results provide an assessment of directivity characteristics of different noise components. It is observed that acoustic pressure fluctuations due to thickness noise is larger in rotor in-plane whereas decreasing in elevation directions. On the contrary, acoustic pressure fluctuations are smaller in rotor in-plane and increase with elevation angle. It is observed that, as the flight speed increases, the overall noise levels also increase. At hovering flight condition, the overall SPL contour in azimuth direction stays almost symmetric although the fact that tail rotor noise contribution disturbs the symmetricity. The trim conditions, acoustic sphere SPL contours, directivity characteristics and thickness & loading noise emitting directions are all determined as expected.

8.2 Flyover Acoustic Simulation

Acoustic certification has become one of the most dominant design drivers in the rotorcraft industry. Although, currently, the only means of compliance for civil certification in terms of noise is test, where simulation of the certification-imposed test conditions are essential.

In this scope, the capability developed with this thesis is tested for flyover condition which is one of the three flight profiles that civil certification require compliance. For the previously mentioned conventional helicopter analysis model, 100 KTAS level flight simulation is performed with viscous vortex particle coupled acoustic solver and instantaneous SPL contours are determined at ground surface. The flyover flight profile for noise certification of the helicopter is illustrated in Figure 8.9. The transient acoustic analysis at a mesh surface representing the ground is performed for 100x50 grid with dimensions of 300m to 150m. Although when the noise frequency is considered, the mesh grid shall be much denser, this study is performed for capability demonstration.

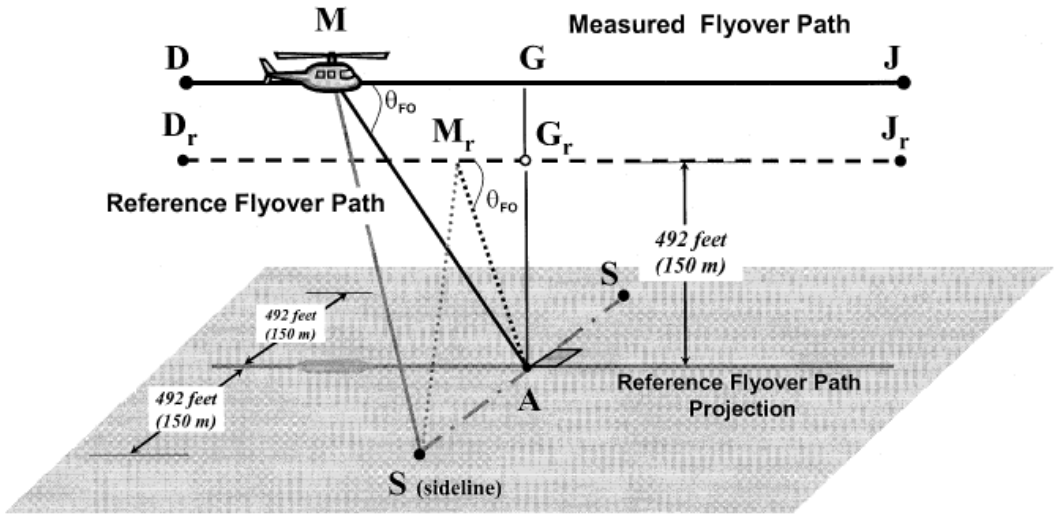

Figure H2.
Comparison of Measured and Reference Flyover Profiles

Figure 8.9 Flyover flight profile for noise certification of helicopters

Instantaneous SPL contours are presented at 6 different simulation times are depicted in Figure 8.10, Figure 8.11 and Figure 8.12.

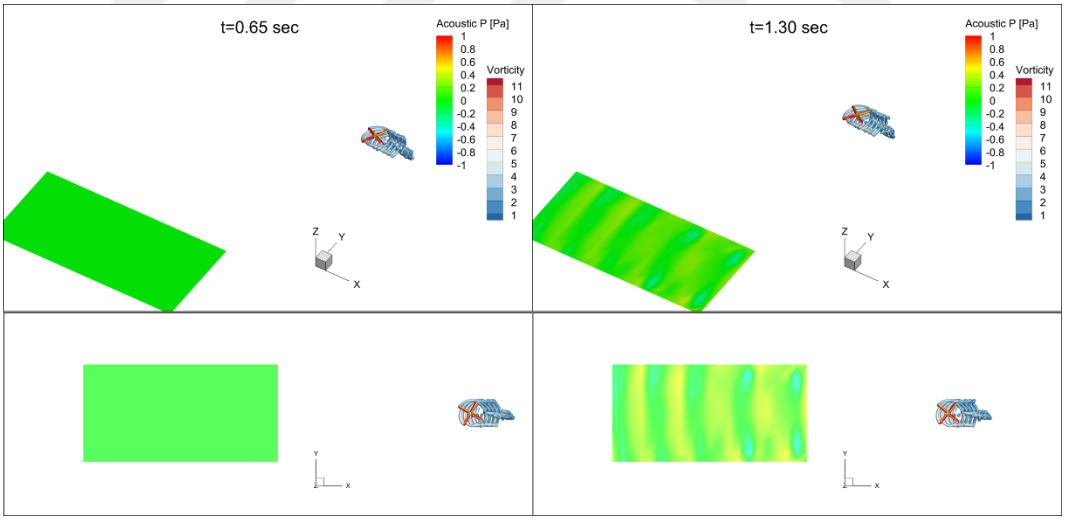

Figure 8.10 Instantaneous acoustic pressure contour for flyover simulation

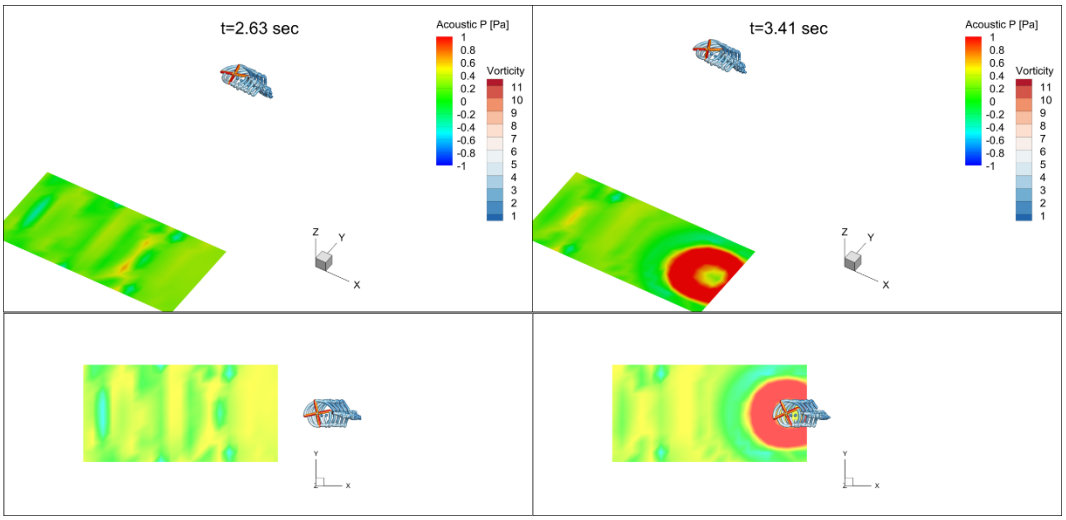

Figure 8.11 Instantaneous acoustic pressure contour for flyover simulation

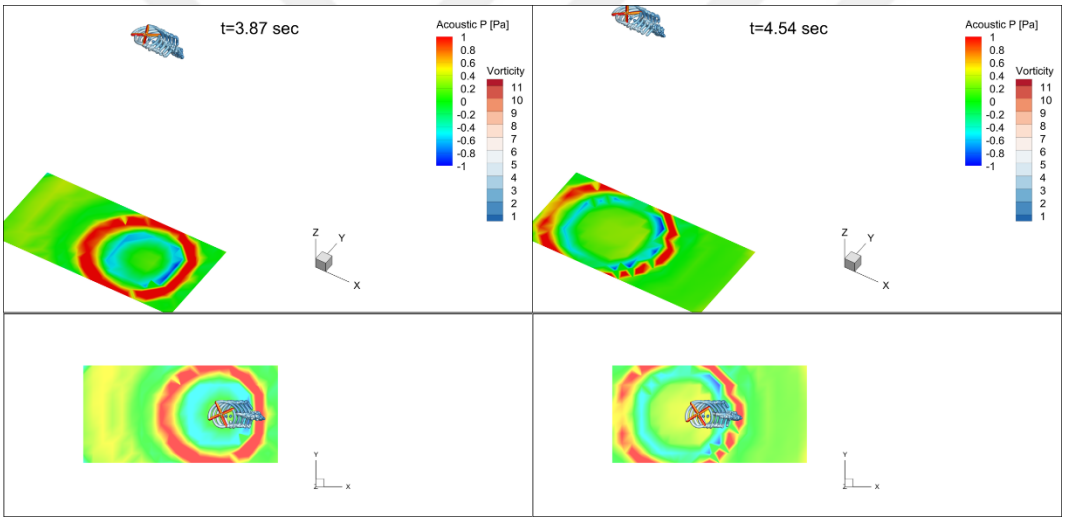

Figure 8.12 Instantaneous acoustic pressure contour for flyover simulation

The acoustic waves propagation on the ground surface can be clearly identified which leads a better understanding and assessment of rotorcraft noise impact on community. Moreover, Doppler shift in the direction of flight and tail rotor interference/contribution on overall acoustic signature can be visualized.

SPL variation with time for the center microphone specified in certification tests, i.e. point A in Figure 8.9 is determined with 1/rev windowing and presented in Figure 8.13. The red solid line represents the instance of overhead. It is observed that 10 dB

down time interval can be identified and further EPNLdB calculations can be performed for certification compliance. This reveals that the simulation capability developed in this study provides an environment for analysis of certification-imposed test conditions.

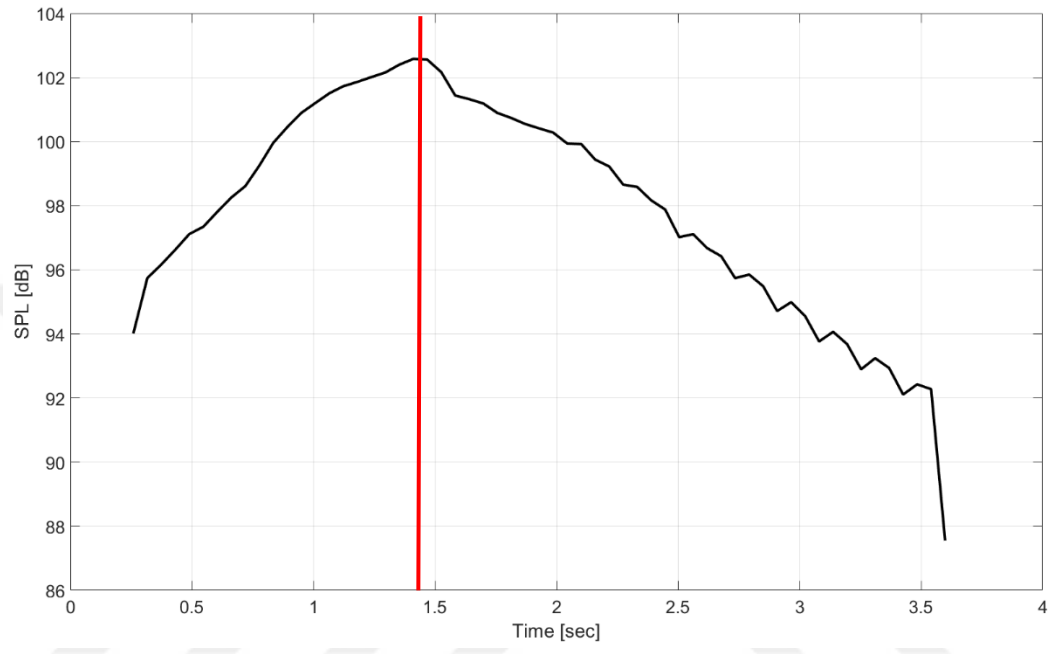

Figure 8.13 SPL variation for flyover

Thickness and loading noise acoustic pressure variations for the specified condition and microphone for the flyover condition are presented in Figure 8.14 and Figure 8.15. Thickness noise acoustic pressure gets minimum as the rotorcraft is at overhead as expected considering the in-plane directivity characteristic of thickness noise (Brentner & Farassat, 2003). Loading noise acoustic pressure on the other hand, reaches its peak value as the rotorcraft is at the overhead of the microphone as expected, considering the forward and downward directivity characteristics of the loading noise component (Brentner & Farassat, 2003).

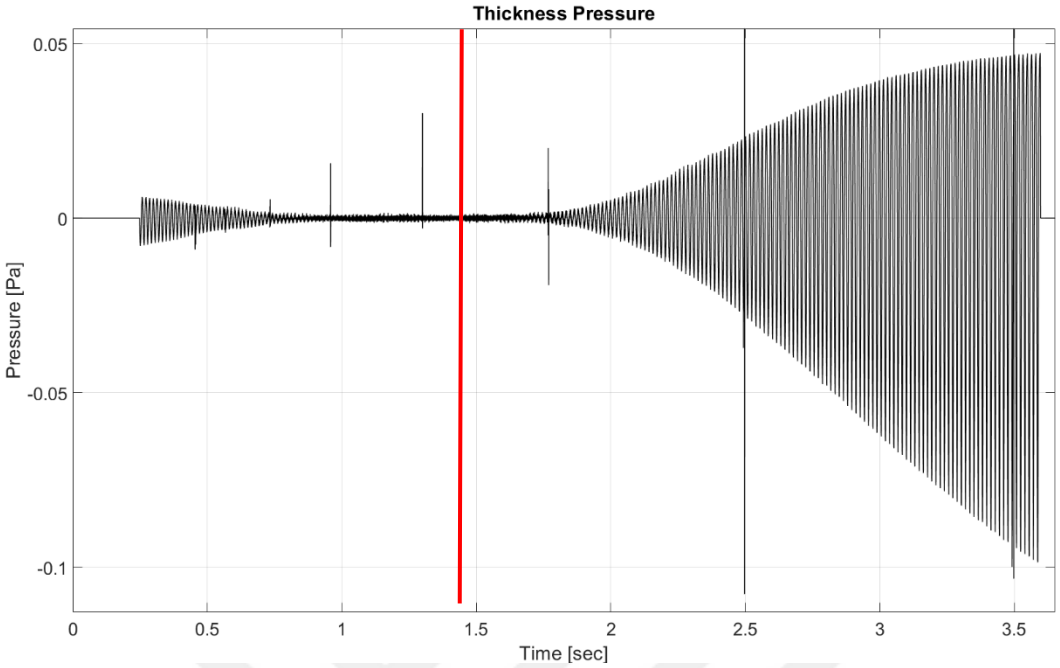

Figure 8.14 Thickness noise acoustic pressure variation for flyover case

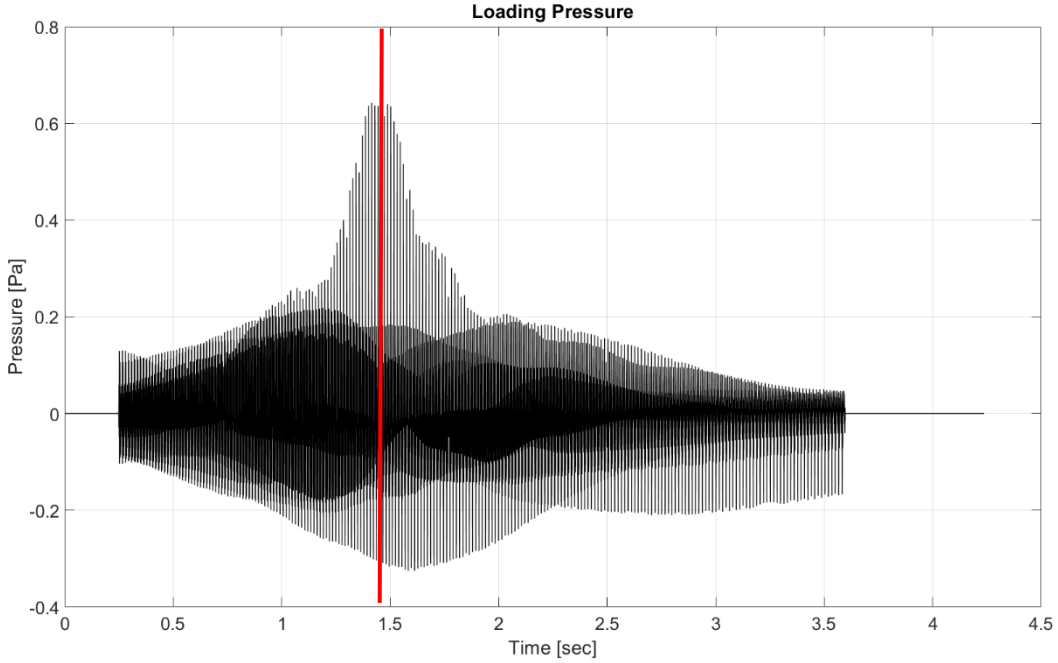

Figure 8.15 Loading noise acoustic pressure variation for flyover case

8.3 Multi-rotor sample and acoustic analysis

One of the most considerable contributions of this study is providing high fidelity and accuracy, full rotorcraft trim and simulation as well as full rotorcraft acoustic analysis of the booming e-VTOL multi-rotor configurations. In order to test the developed capability for such coupled and interacting configuration, a representative multi-rotor rotorcraft is generated with 2 co-axial, 2 prop-rotor and 2 propellers as illustrated in Figure 8.16 and Figure 8.17.

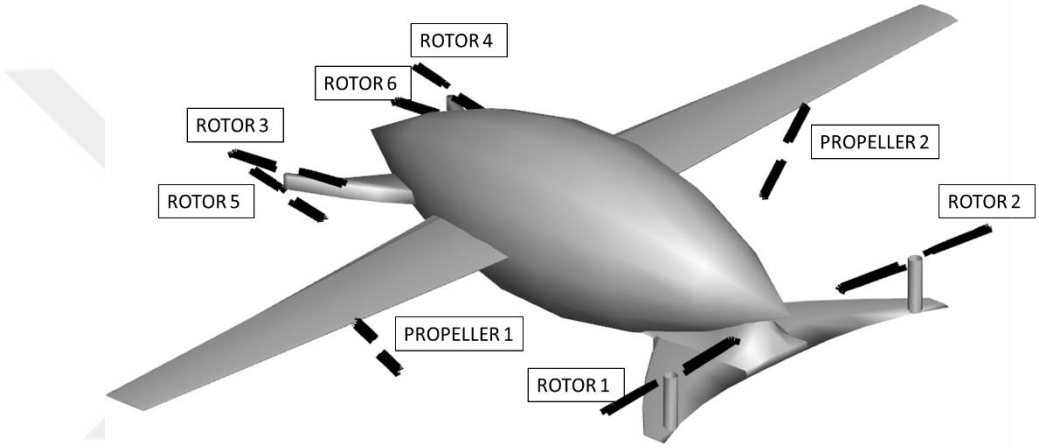

Figure 8.16 Multi-rotor analysis model for demonstration

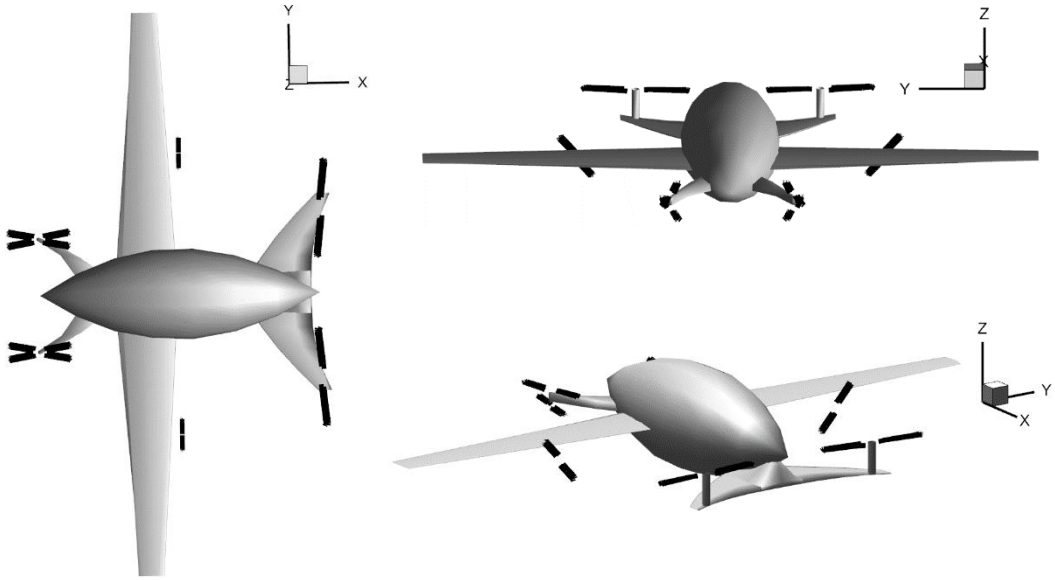

Figure 8.17 Multi-rotor analysis model for demonstration

The feasibility of the multi-rotor model is not prioritized, instead, on the other hand the capability for modeling, analysis and trim calculation of a complex configuration including wings, propellers, prop-rotors and co-axial rotors simultaneously operating and interacting with each other is assessed in this study. In this scope, trim analyses are performed for hover, 20, 50 and 100 Knots level forward speeds. Wake geometries are studied in terms of particle distributions, vorticity iso-surfaces and vorticity contours in cross-planes over converged simulations.

8.3.1 Hovering Flight Condition

At hover, co-axial rotors located on the front and prop-rotors located on the back of the model are operating. Propellers located on the wings are not operating since zero forward speed is targeted. Vortex particles colored in particle strengths and vorticity iso-surfaces colored in total airspeed are illustrated in Figure 8.18.

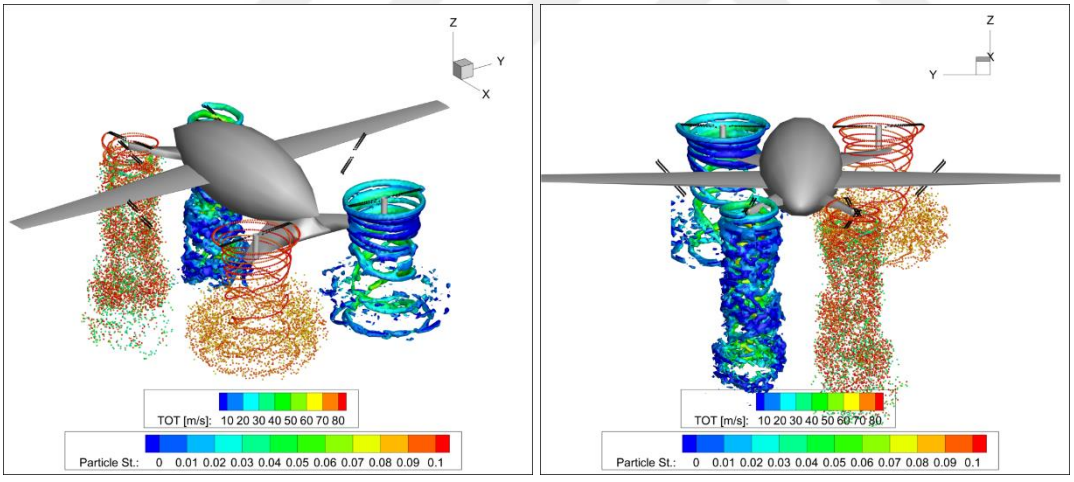

Figure 8.18 Multi-rotor hover trim, vortex particles and vorticity iso-surface

Vorticity contour is plotted in Figure 8.19 in cross-plane to illustrate tip vortices trajectory, contraction, and interaction. For a trim condition, all rotor configurations are expected to generate the same thrust levels in order to have an overall force & moment balance. In this scope, having smaller diameter and higher disc loading, co-axial rotors are producing larger downwash with stronger tip vortices as expected.

Similarly, having larger diameter, prop-rotors located at the back the platform are generating lower downwash velocity, with weaker tip vortices.

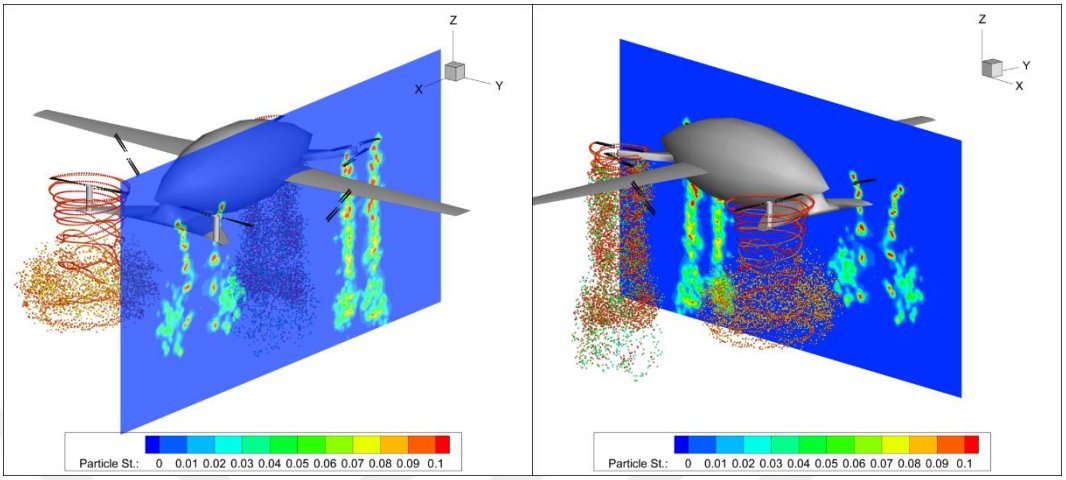

Figure 8.19 Multi-rotor hover trim vorticity contour in cross-plane

Thrust and power convergence variation with simulation step for rotors located on the port side i.e. rotor 1, rotor 3 and rotor 5 are plotted in Figure 8.20 and Figure 8.21. It is observed that, total thrust generated by co-axial rotors are equal to thrust generated by the prop-rotors located at the back of the configuration.

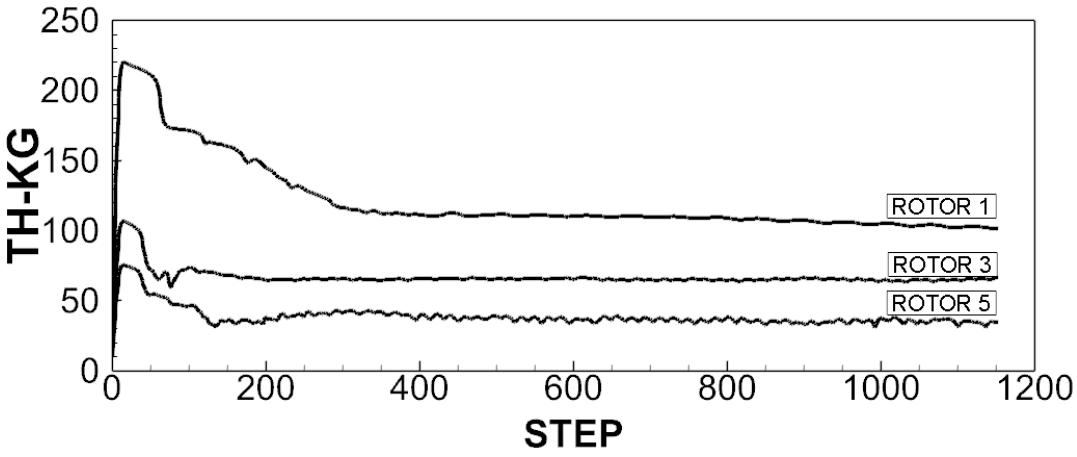

Figure 8.20 Thrust convergence variation with simulation step

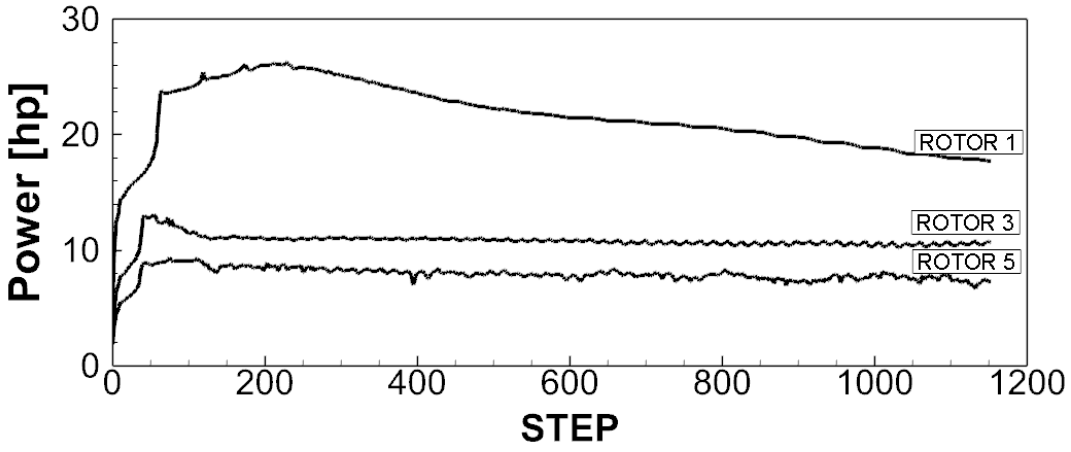

Figure 8.21 Power convergence variation with simulation step

8.3.2 20 knots transition flight

20 knots forward speed is considered a low speed transition flight condition, as all rotors and wings are operating whereas, as the dynamic pressure is low, the wings are not producing enough lift for level flight. Therefore, co-axial and prop-rotors are still generating high level of thrust operating near hover condition. Wake formations interacting with each other in terms of particle distributions, vorticity iso-surfaces and vorticity contours in cross-plane are illustrated in Figure 8.22 and Figure 8.23.

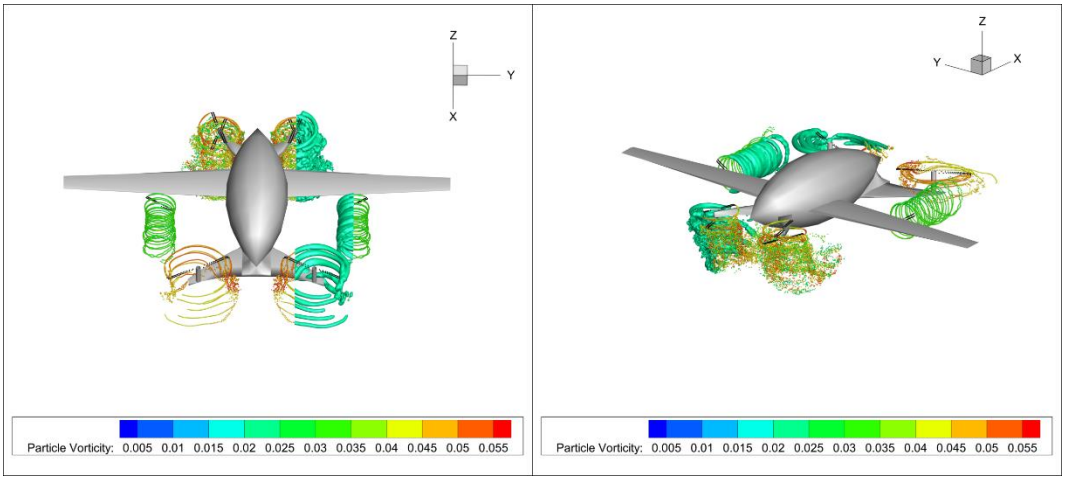

Figure 8.22 Multi-rotor 20 knots trim, vortex particles and vorticity iso-surface

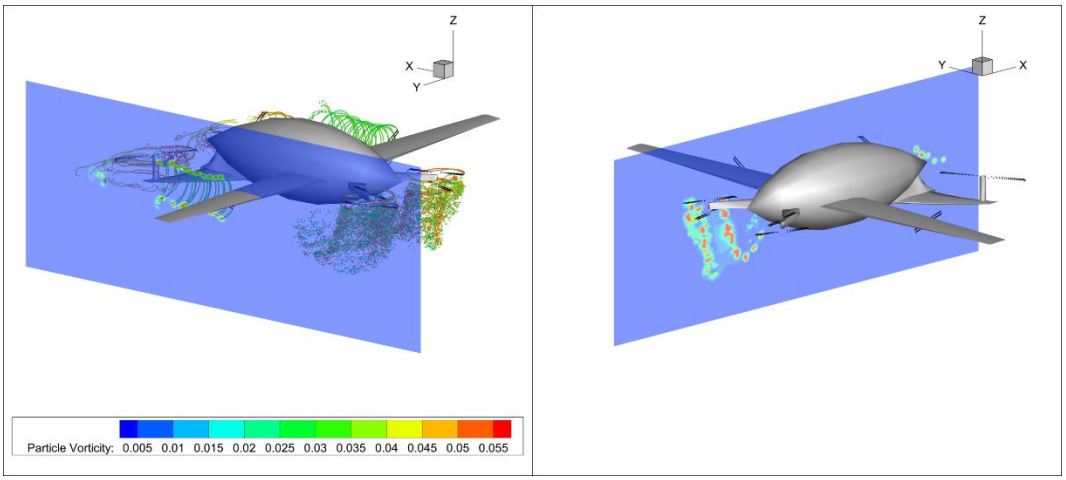

Figure 8.23 Multi-rotor 20 knots trim vorticity contour in cross-plane

Thrust and power convergence variation with simulation step for rotors located on the port side i.e. rotor 1, rotor 3, rotor 5 and propeller 1 are plotted in Figure 8.24 and Figure 8.25.

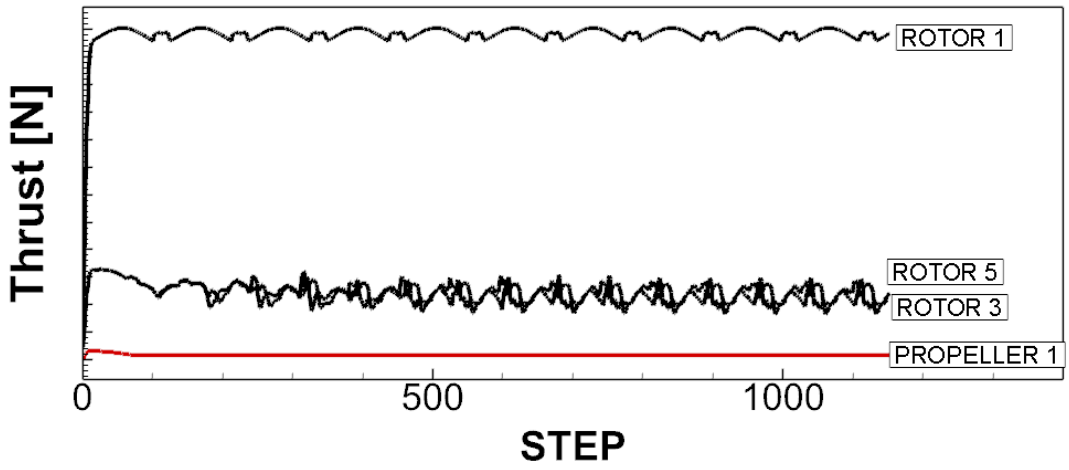

Figure 8.24 Thrust convergence variation with simulation step

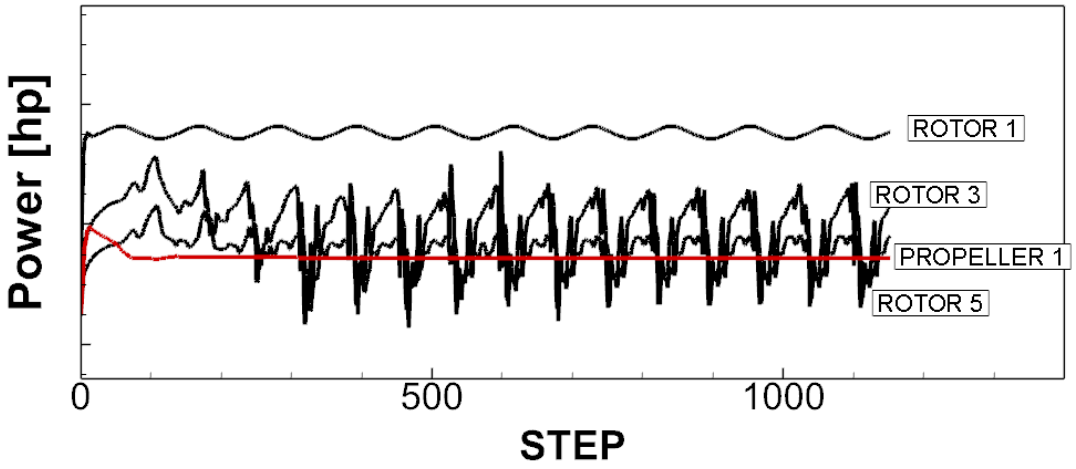

Figure 8.25 Power convergence variation with simulation step

8.3.3 50 knots post-transition flight

50 knots forward speed is considered as a post-transition flight condition as the wings are almost generating required lift for level flight whereas for a longitudinal moment balance and generate the small shortage of lift, the co-axial rotors located at the front of the model are required to operate at low thrust levels. Propellers are operating at moderate thrust levels to produce required propulsive force to attain forward speed. Vorticity iso-surfaces colored with total air speed, in-plane and cross plane vorticity contours, and streamlines are illustrated with Figure 8.26 and Figure 8.27.

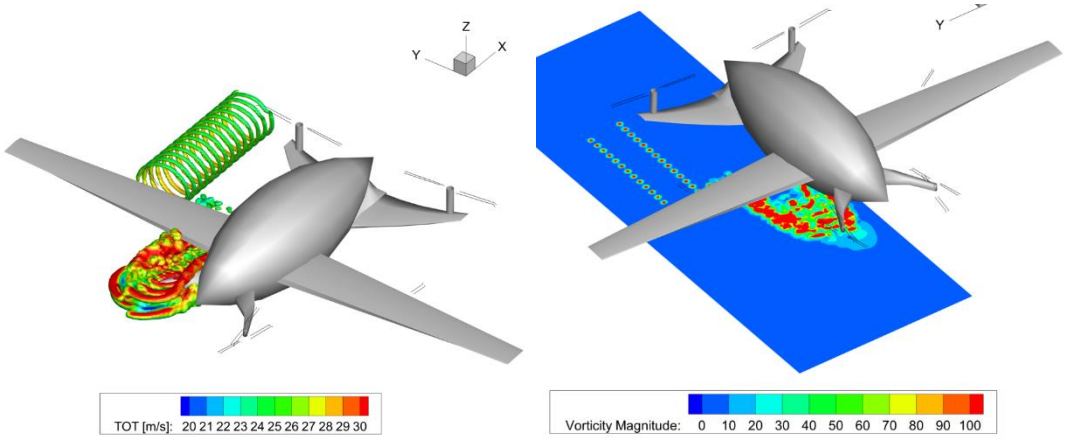

Figure 8.26 Multi-rotor 50 knots trim vorticity iso-surface and vorticity contour over in-plane

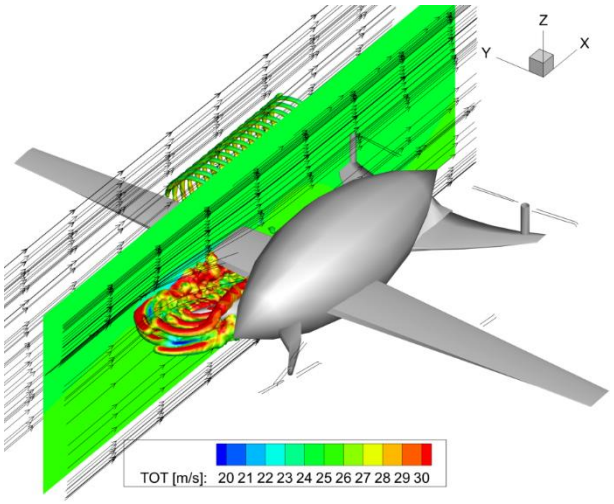

Figure 8.27 Multi-rotor 50 knots trim vorticity iso-surface and streamlines

8.3.4 100 knots fixed-wing mode

100 knots trim condition represents the fixed-wing or airplane mode as the wings generate all the required lift while the propellers are operating at high thrust levels to produce all the required propulsive x-force. For longitudinal moment balance, co-axial rotors are operating at minimal thrust levels. Wake formations of propellers in terms of particle distributions, vorticity iso-surface and in-plane & cross-plane vorticity contours are presented in Figure 8.28 and Figure 8.29.

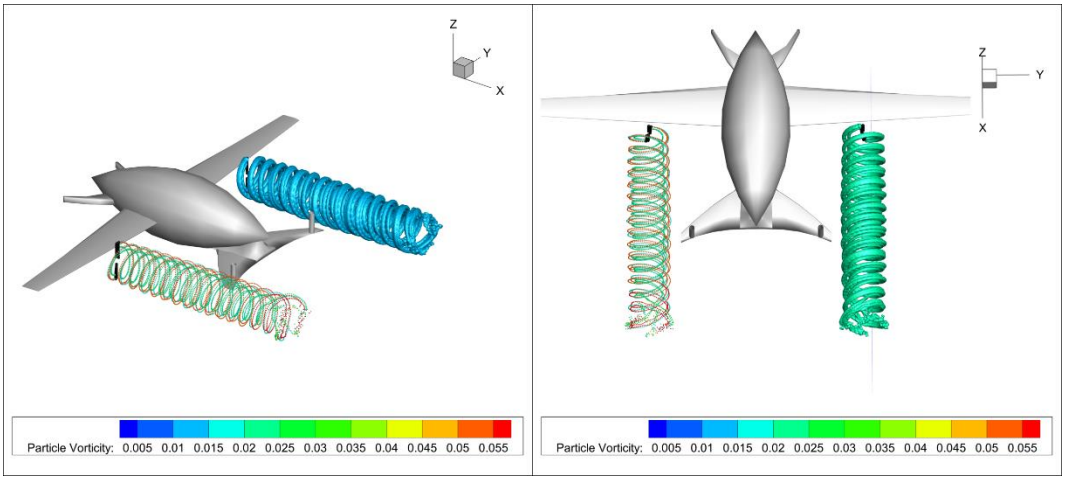

Figure 8.28 100 knots trim, vortex particles and vorticity iso-surface

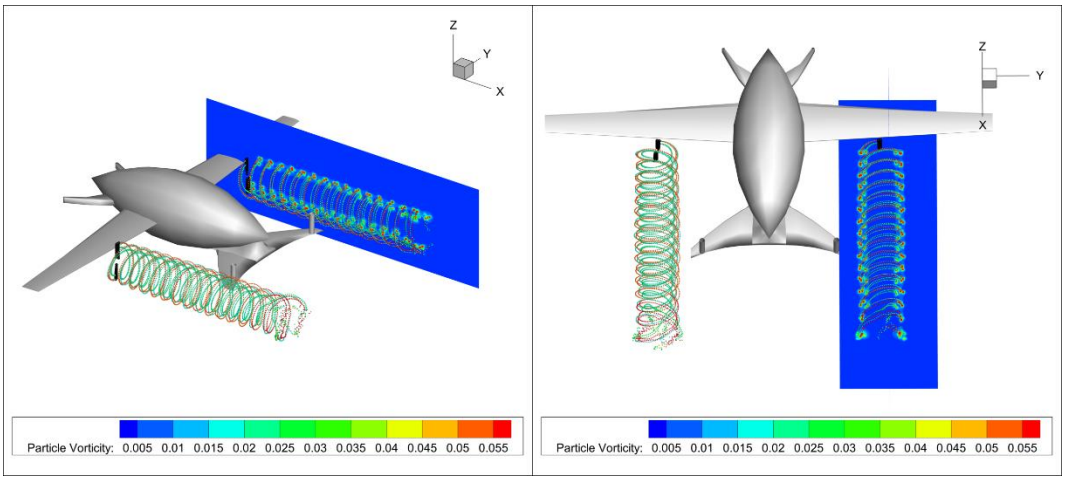

Figure 8.29 100 knots trim, in-plane & cross-plane vorticity contours

8.3.5 Acoustic Analysis for Hovering Flight Condition

For further testing the VVPAM, acoustic analysis for the hovering flight condition is performed and the acoustic sphere is generated. Then, for an observer location illustrated in Figure 8.30, acoustic pressure variations with time are studied. It is observed that, rotor 1 & rotor 2 (the prop-rotors located at the back of the configuration) and rotor 3, rotor 4, rotor 5 and rotor 6 (co-axial rotors located at the front of the configuration) are generating the same acoustic pressure signal with a slight lag resulting from the different distance vectors to the observer location. As discussed before, having smaller radius with larger disc loading, the co-axial rotors producing higher downwash velocities and operating at a higher blade loading produce larger acoustic pressure fluctuations, as expected.

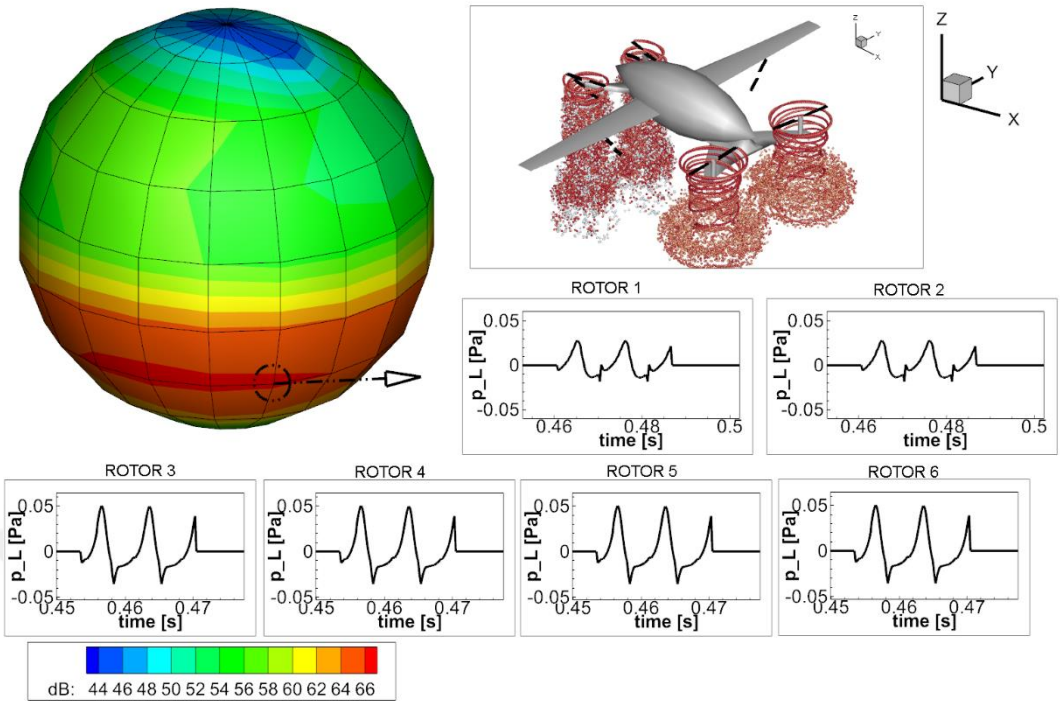

Figure 8.30 Multi-rotor acoustic analysis

8.4 Trajectory optimizations

8.4.1 Jump Take-off and Acceleration

One of the contributions of this thesis is to develop the capability for performing transient acoustic simulations. In order to further test and evaluate this feature, a take-off and acceleration mission is defined for a typical conventional helicopter and model predictive control with trajectory optimization approach is utilized to accomplish the mission steps, while noise model determined the instantaneous and total averaged noise levels on ground surface. In order to test the boundaries, the mission is generated with utmost severe three following steps:

1- Jump Take-off
2- Vertical climb to 300m at maximum climb rate with constant heading
3- Acceleration to 100 knots with maximum rate

The MPC simultaneously optimized the trajectory with mission concerns only and produced the optimal control inputs to track the generated trajectory. Flight profile/path for the jump take-off is illustrated with Figure 8.31 and Figure 8.32.

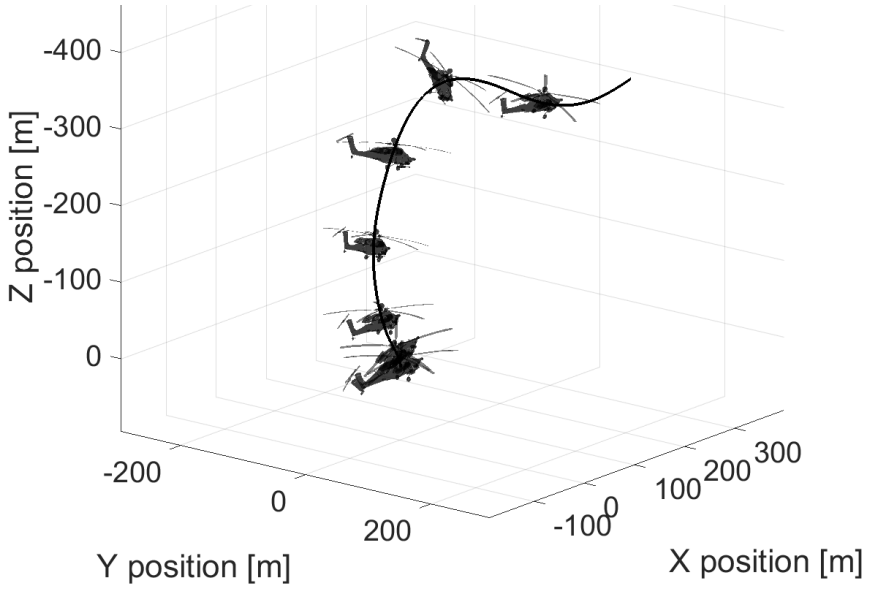

Figure 8.31 Jump Take-off and acceleration flight path

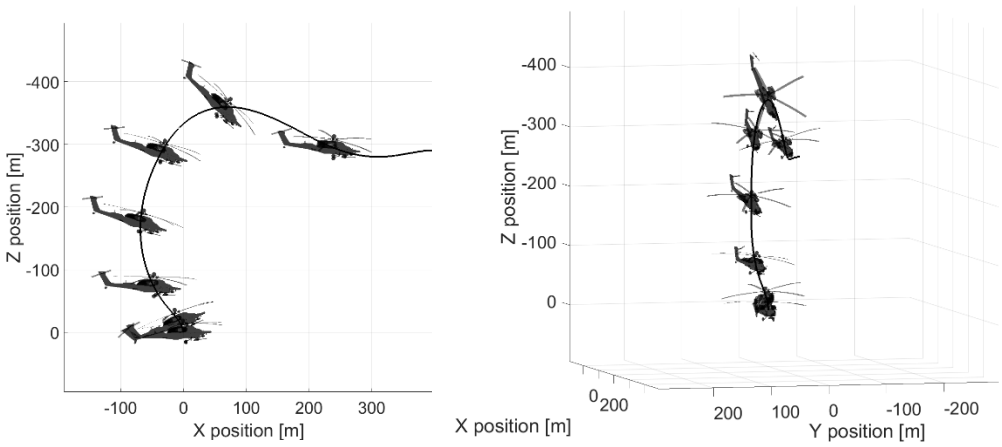

Figure 8.32 Jump Take-off and acceleration flight path

Throughout the take-off and acceleration maneuver, SEL contour on the arbitrary ground surface is calculated as illustrated in Figure 8.33. It is observed from the averaged noise levels that, the maximum noise impact occurs below and forward of the flight profile whereas minimum impact occurs port side of the flight profile. Such simulations would yield better understanding of noise directivity specific for desired maneuvers or flight conditions. Such evaluations can even be utilized in heliport designs or take-off and landing corridors for legacy heliports for minimal community annoyance. Control input, air speed, Euler angle and rates histories are further presented in Figure 8.35 and Figure 8.36 for completeness.

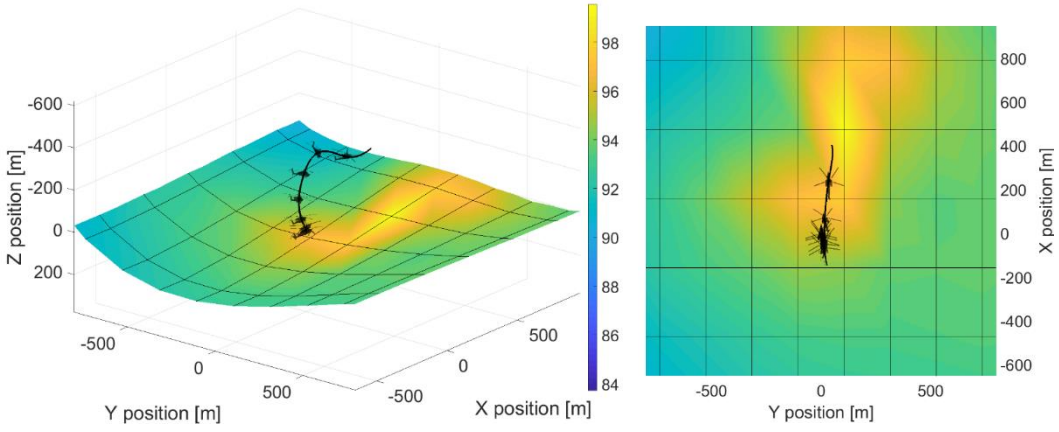

Figure 8.33 Jump take-off total SEL contour on ground

SPL contour can be determined either on a arbitrary ground surface as depicted in Figure 8.33 or on a city 3-D model as depicted in Figure 8.34.

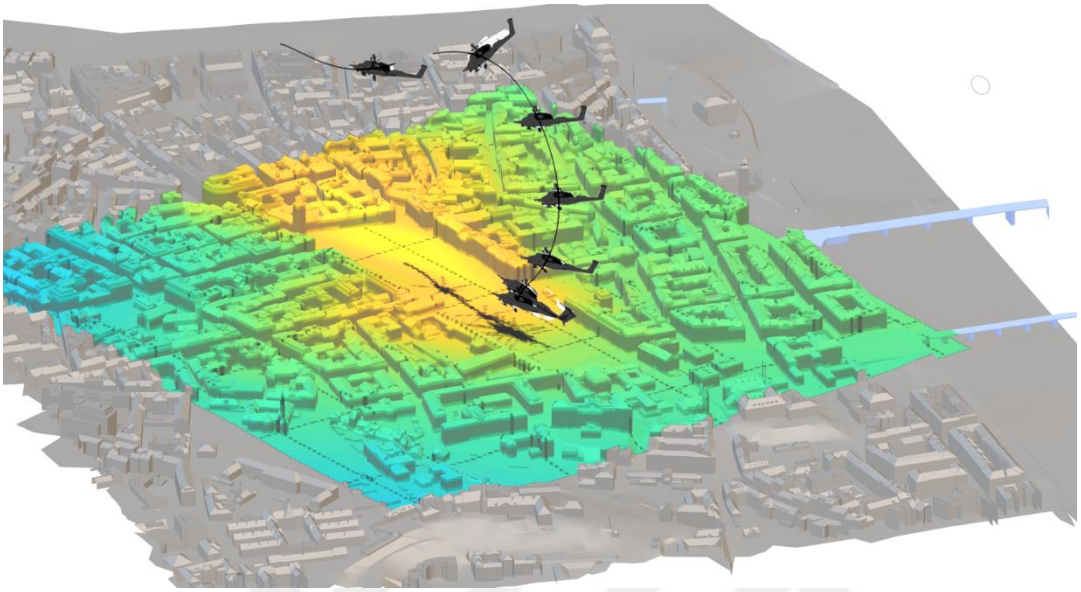

Figure 8.34 Jump Take-off SPL contour on city model

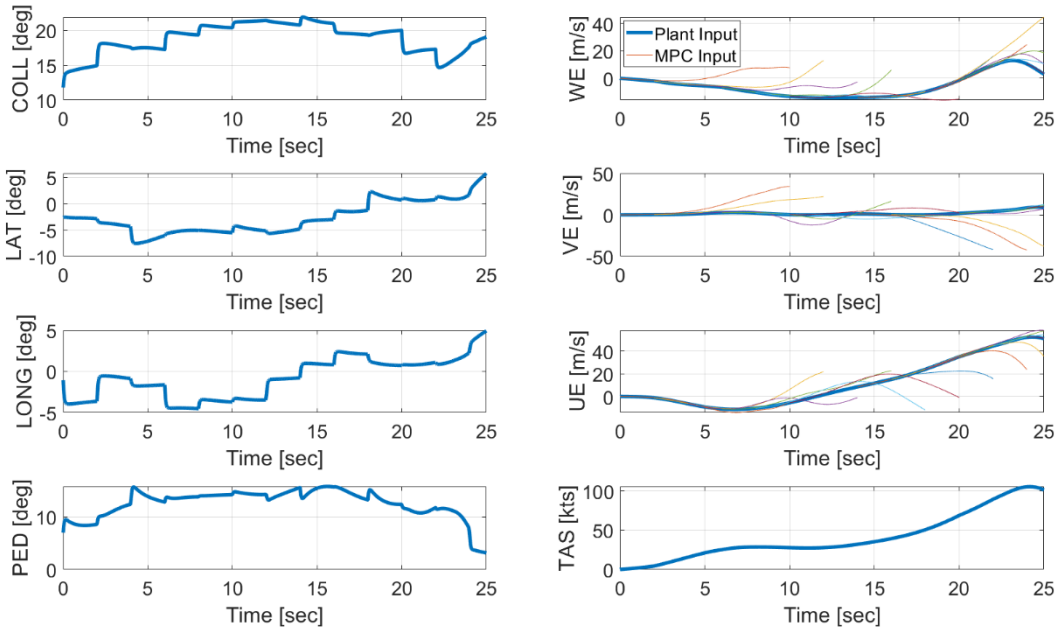

Figure 8.35 Jump take-off control inputs and NED velocity histories

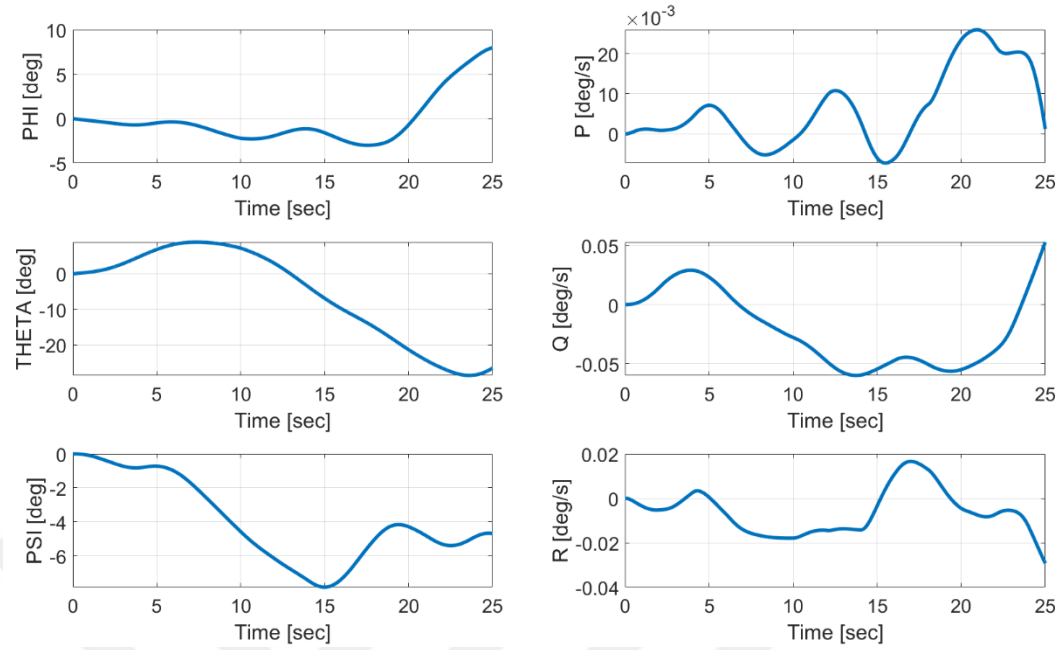

Figure 8.36 Jump take-off Euler angle and rates history

8.4.2 360 Turn

Further MPC trajectory optimization and track simulation is performed for 360 degrees turn course. Mission is defined with four waypoints oriented at 90 degrees azimuths of a circular path. In order to test the performance of trajectory generation and track, simulations are performed with mission concern only. Initially, the helicopter is trimmed at 70 knots level forward flight at [0 0 0] coordinates. Then the helicopter passes from four waypoints with bumper margins of 50m as imposed by the mission objective/cost as depicted in Figure 8.37. Instantaneous acoustic sphere calculations are continuously performed throughout the path as illustrated with Figure 8.38.

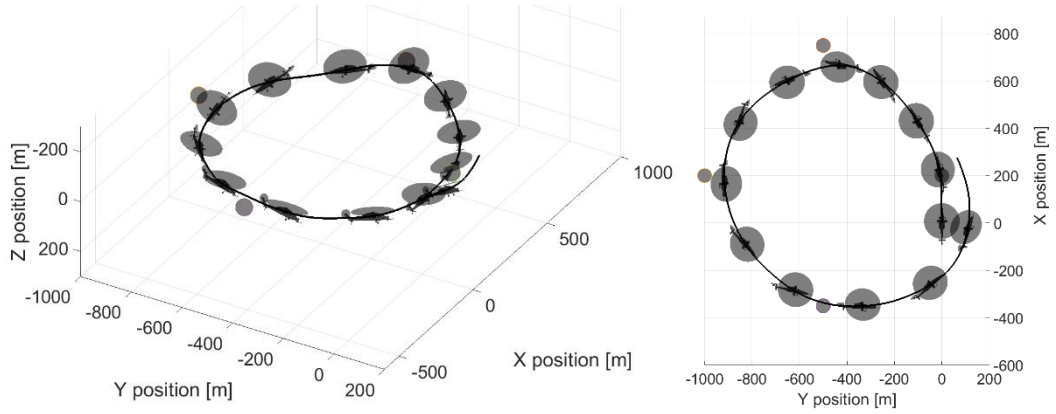

Figure 8.37 360 turn trajectory optimization and track results

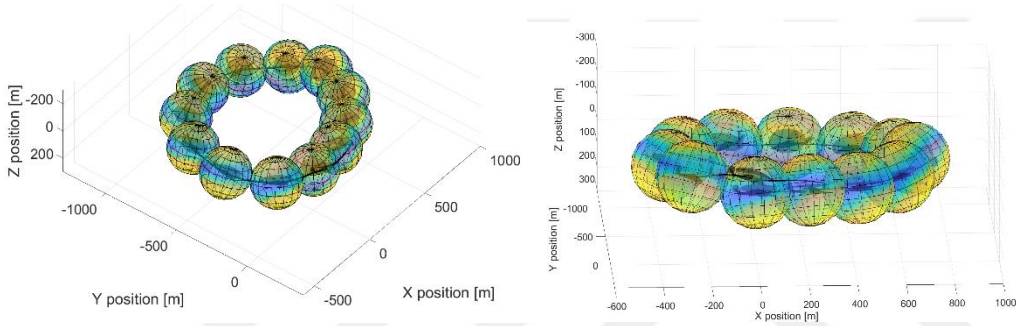

Figure 8.38 Acoustic spheres for 360 turn

Having only mission cost active, resulted in a waypoint track with all other concerns such as acoustics, performance, fuel consumption, safety, comfort as well as constraints such as maximum speed, roll and pitch angles, ignored. Although a good waypoint tracking performance is achieved, as depicted in Figure 8.39 and Figure 8.40, helicopter is continuously gaining speed, which results in harsher maneuver requirements, inputs, state and state rates. This reveals the necessity of a comprehensive objective function when working with an MPC only especially when the SAS is off. Rotorcrafts are inherently coupled and complex platforms, therefore a single channel controller or a single objective with all other concerns ignored may lead the rotorcraft to have uncontrollable boundaries. Therefore, even with supplementary and basic cost functions added to the overall objective related with speed, altitude, states, and rates of states the objective can be transformed into a comprehensive target having a complete set of optimization definition. Nevertheless,

360 turn study revealed the success, accuracy and capability of trajectory optimization and track framework developed in this thesis.

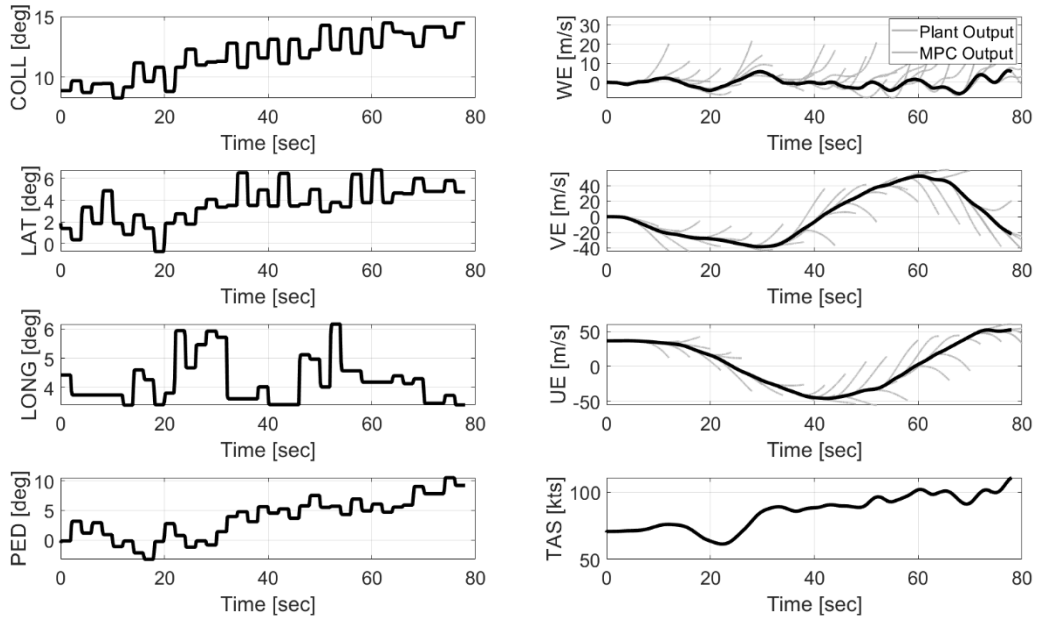

Figure 8.39 360 turn control inputs and NED velocity histories

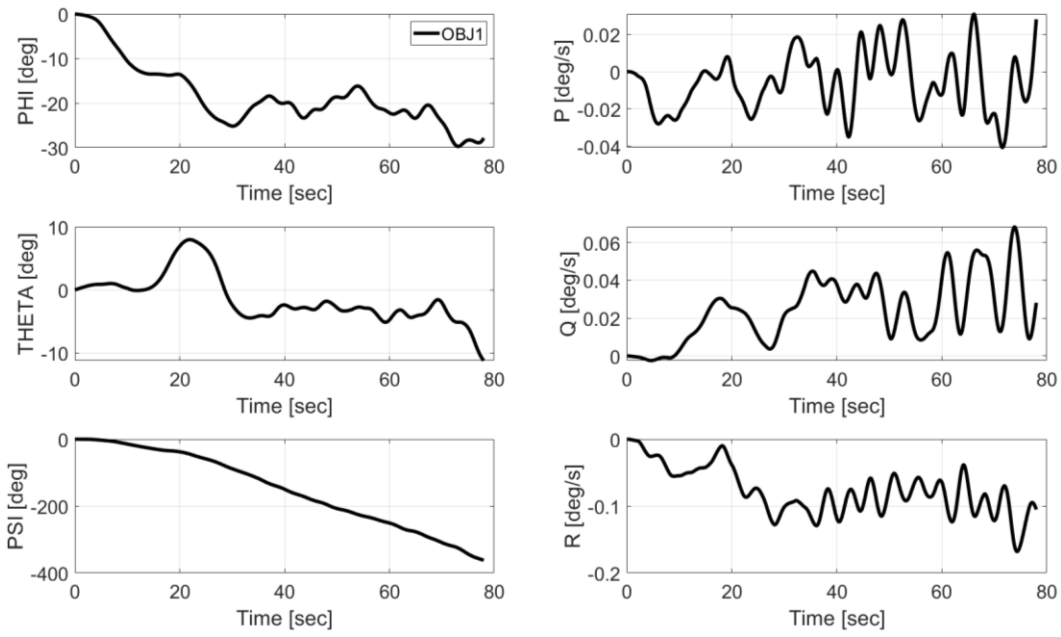

Figure 8.40 360 turn Euler angle and rates history

8.5 Green Trajectory optimizations

8.5.1 Accelerate and Flyover Mission

The noise minimal and green trajectory optimization and track framework developed in this study is tested for an acceleration and flyover condition. Acoustic contour over a terrain 3km x 4km is determined where noise sensitive region is located at x:1500m y:1500 coordinates. Initially, the helicopter is trimmed at 70 knots level flight condition. Mission is defined as to fly at over 110 knots with a flight path angle free in terms of climb/descent but zero in terms of sideslip. In other words, the helicopter is required to fly to North the whole time, whit a minimum noise level at the noise sensitive region and with minimum fuel consumption. Simulations are performed with three different weighting matrices, QQ, of the objective function given in equation (114) with acoustic off, acoustic on and "green objective" combinations.

$$F = J_{Overall}\, QQ\, J_{Overall}{}^{T} + u\, RR\, u^{T} \qquad (113)$$

OBJ1, first objective function, is constituted by zeroing acoustic and performance terms. OBJ2, second objective function, is constituted by setting acoustic contribution to on. OBJ3, the third objective function i.e. the green objective, is constituted by setting fuel consumption to on generate both minimal noise and fuel consumption, in other words "green" trajectory.

SEL contours determined for the overall simulation for each of the objective function are presented with Figure 8.41, Figure 8.42 and Figure 8.43. It is observed that, when acoustic concern is included in the objective, the optimization benefits from the directivity characteristics of the rotorcraft noise and directs the maximum noise impact away from the observer location, which was exactly on the observer location when acoustic concern is off. When fuel concern is further included in the overall objective, the optimization still directs the maximum noise impact away from the

observer whereas, this time with lower altitude variation, which eventually lead to less fuel consumption.

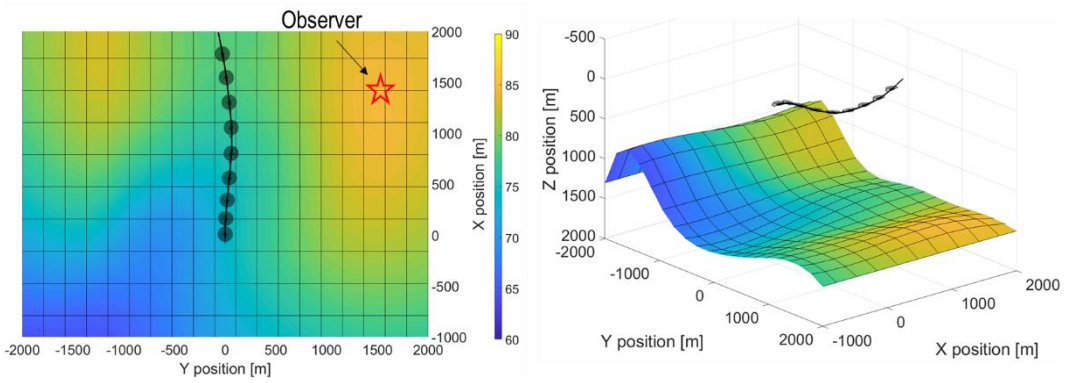

Figure 8.41 SEL contour with OBJ1 for acceleration and flyover mission

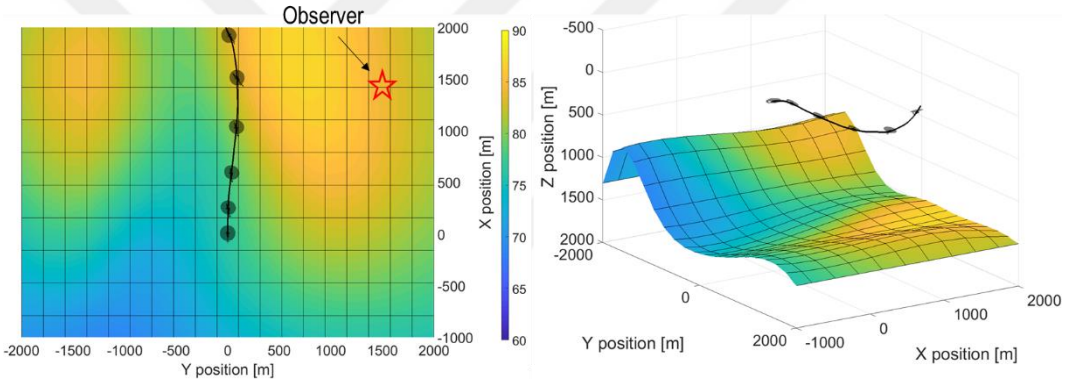

Figure 8.42 SEL contour with OBJ2 for acceleration and flyover mission

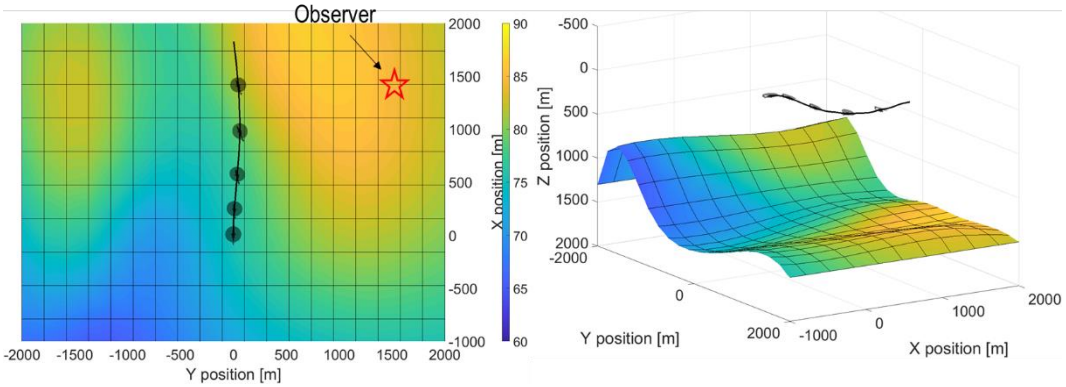

Figure 8.43 SEL contour with OBJ3 for acceleration and flyover mission

In order to assess how much the overall trajectory varied when acoustic and fuel concerns are included, the flight profiles are plotted together and compared as illustrated in Figure 8.44 and Figure 8.45.

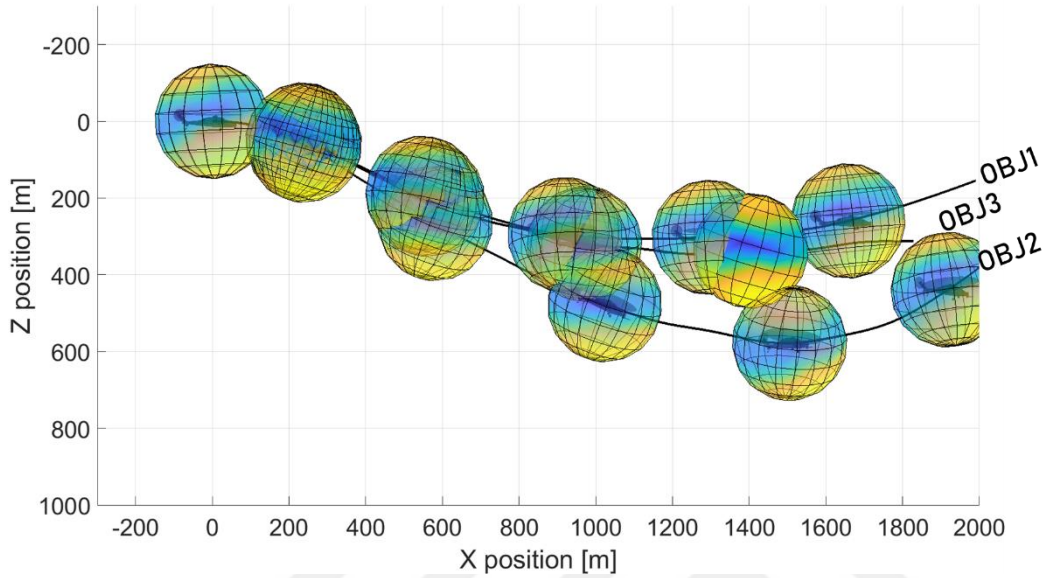

Figure 8.44 Optimized trajectories with OBJ1, OBJ2 and OBJ3 for acceleration and flyover mission

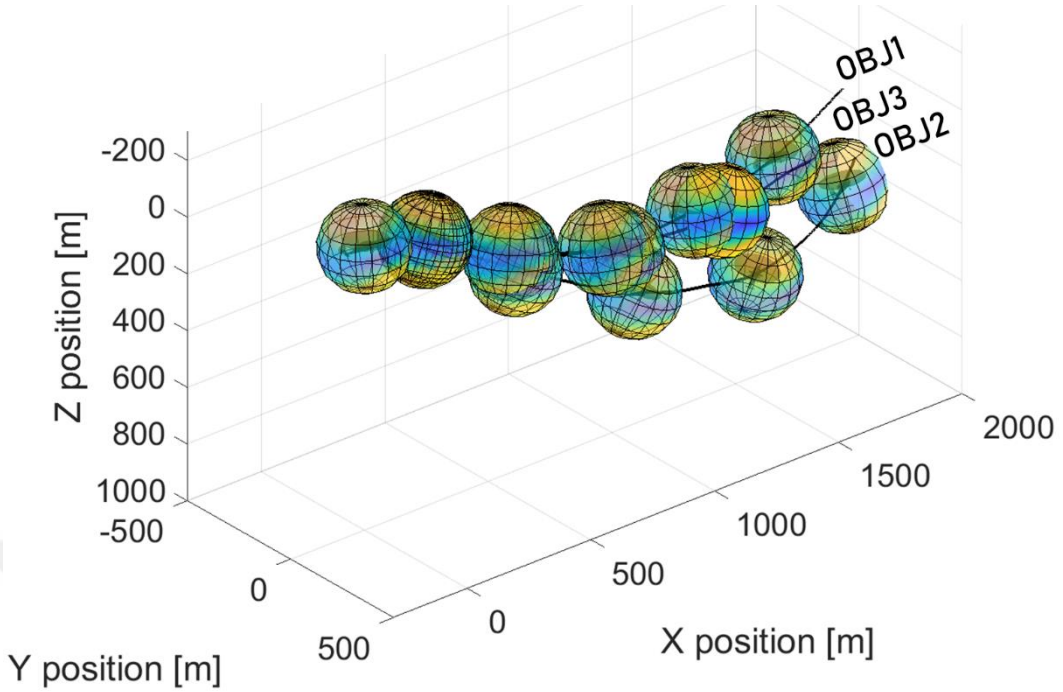

Figure 8.45 Optimized trajectories with OBJ1, OBJ2 and OBJ3 for acceleration and flyover mission

Overall SELdB values and instantaneous SPLdB variation throughout the trajectories for each of the objective is plotted in Figure 8.46. It is observed that, with the inclusion of acoustic concern in the objective function (OBJ2) a 2.5dB in the overall SEL is achieved while SPL throughout the simulation is always lower than the acoustic concern of trajectory (OBJ1). Moreover, inclusion of fuel consumption concern in the optimization function (OBJ3) still benefits of around 2.25 dB decrease in overall SEL, while SPL throughout the simulation stay close to OBJ2.

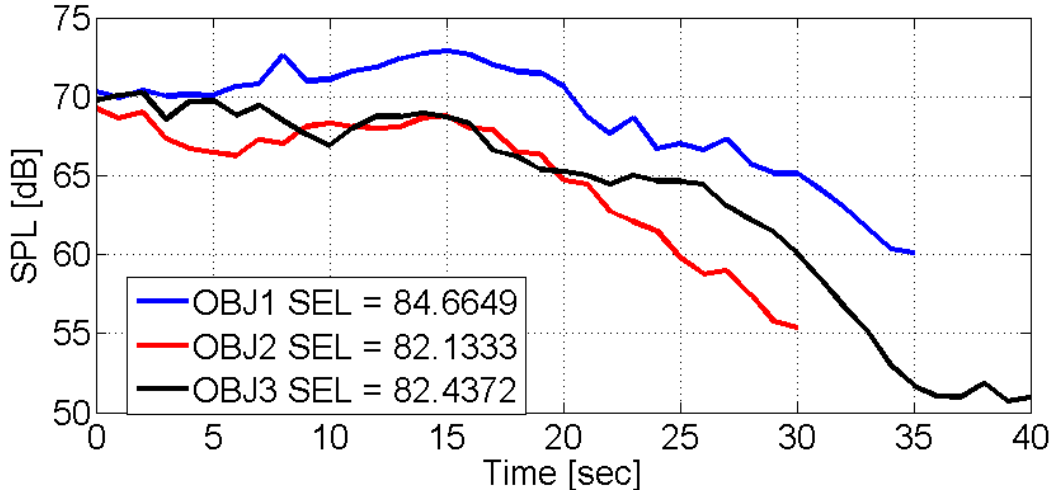

Figure 8.46 SELdB and SPLdB with OBJ1, OBJ2 and OBJ3 for acceleration and flyover mission

Acoustic improvement of a trajectory over another is calculated through the SPLdB definition and utilization of inverse logarithm formulation given in equation (114).

$$\frac{OBJ1_{acoust}}{OBJ2_{acoust}} = 10^{\frac{dB_1 - dB_2}{20}} \tag{114}$$

Consequently, defining the OBJ1 trajectory as the reference, improvements achieved with OBJ2 and OBJ3 as well as the overall trade-offs of the trajectory optimization are summarized in Table 8.2. It is concluded that, with the inclusion of acoustic concern in the optimization algorithm, at least %25 improvement in noise impact is achieved. Moreover, inclusion of performance/fuel consumption concern in the optimization algorithm can reduce consumed fuel by 3%. As safety & comfort assessment is a non-dimensional evaluation, relative variation is defined in Table 8.2. Finally, waypoint track performance for all three objective functions is at least in %2.5 accuracy.

Table 8.2 Optimization trade-off results for accelerate and flyover mission

Trade-offs	OBJ1	OBJ2	OBJ3
SELdB at observer	84.67	82.13	82.43
Acoustic Improvement	100%	75%	77%
Fuel Cons. Improvement	100%	102%	97%
Safety & Comfort	Ref.	Lower	Lower
Waypoint Track	98.00%	97.40%	98.20%

Control input, NED speed components, Euler angles and rate histories for all of the optimized trajectories are given in Figure 8.47 and Figure 8.48. It is observed that, although introducing additional oscillations or pilot workload, acoustic and fuel achievements are significant and remarkable.

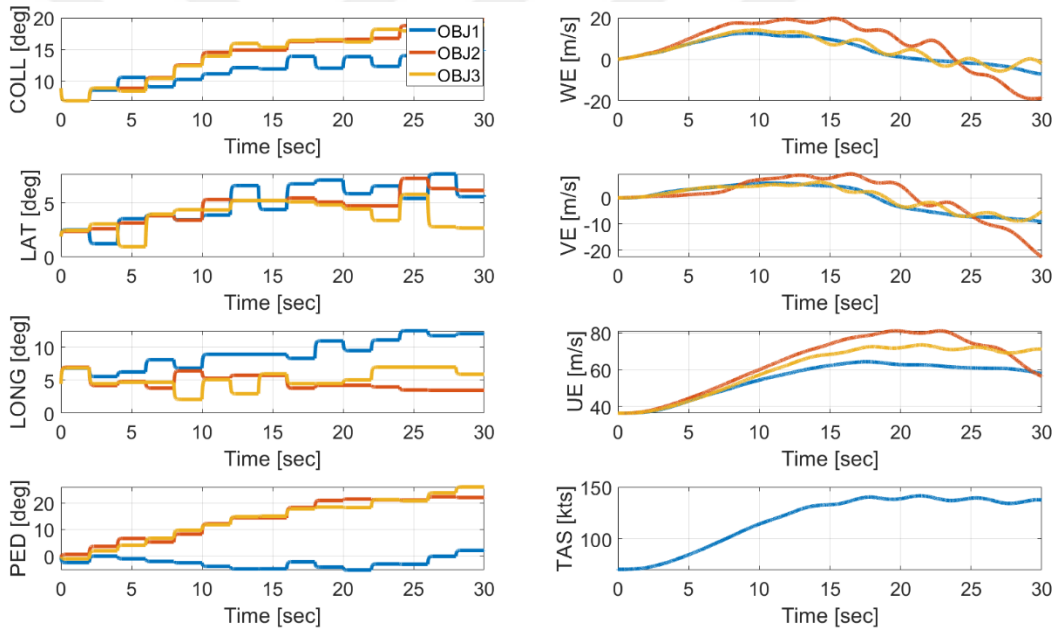

Figure 8.47 OBJ1, OBJ2 and OBJ3 control inputs and NED velocity histories for acceleration and flyover mission

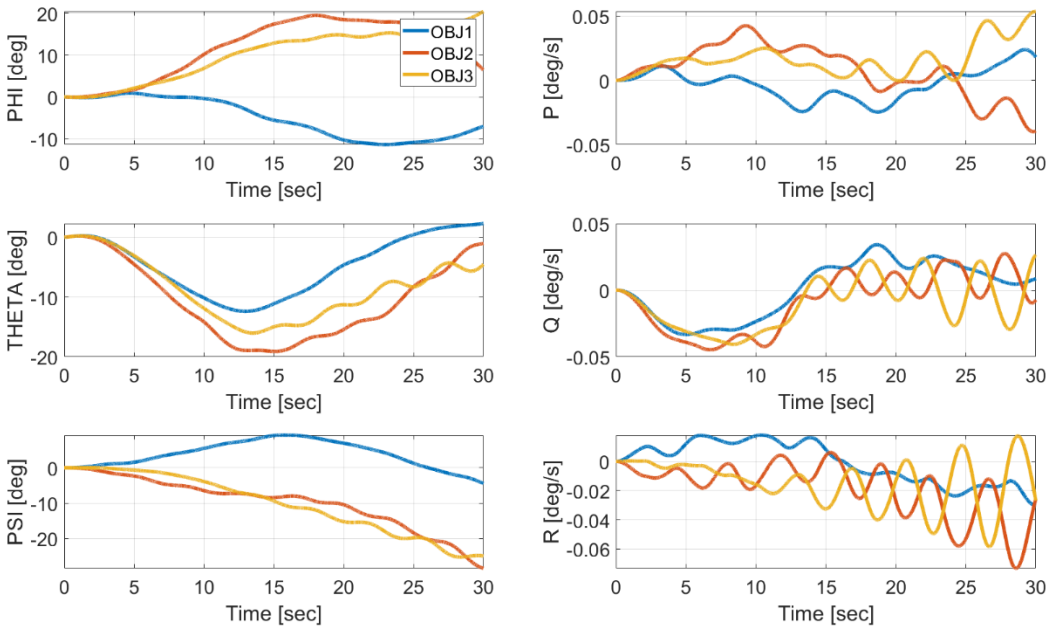

Figure 8.48 OBJ1, OBJ2 and OBJ3 Euler angle and rates history for acceleration and flyover mission

8.5.2 Horseshoe Turn and climb Mission

Another application to further test the noise minimal and green trajectory optimization and track framework developed in this study is done with a horseshoe turn mission profile over a noise sensitive region. Simulations are performed with three different objective functions through different weighting matrices, QQ, of the objective function given in equation (114). Initially, the helicopter is trimmed at 50 knots level flight. Mission is defined to perform a 180° starboard turn then gain 250 m altitude. Acoustic contour over a terrain 3km x 4km is determined, where noise sensitive region is located at x:1500m y:1500 coordinates as illustrated in Figure 8.49 and Figure 8.50. OBJ1, first objective function, is constituted by zeroing acoustic and performance terms. OBJ2, second objective function, is constituted by setting acoustic contribution to on. OBJ3, the third objective function i.e. the green objective, is constituted by setting fuel consumption to on and increasing acoustic importance in overall objective even further to generate both minimal noise and fuel consumption, in other words “green” trajectory.

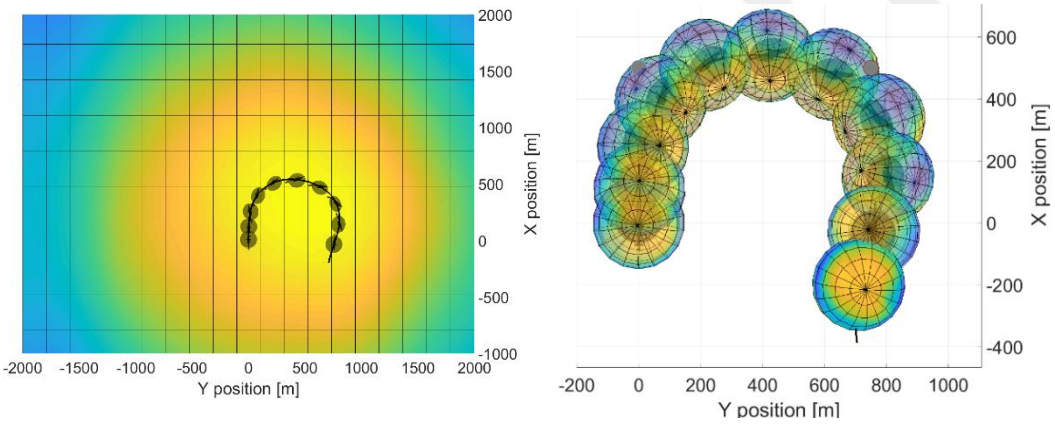

Figure 8.49 Horseshoe turn and climb mission

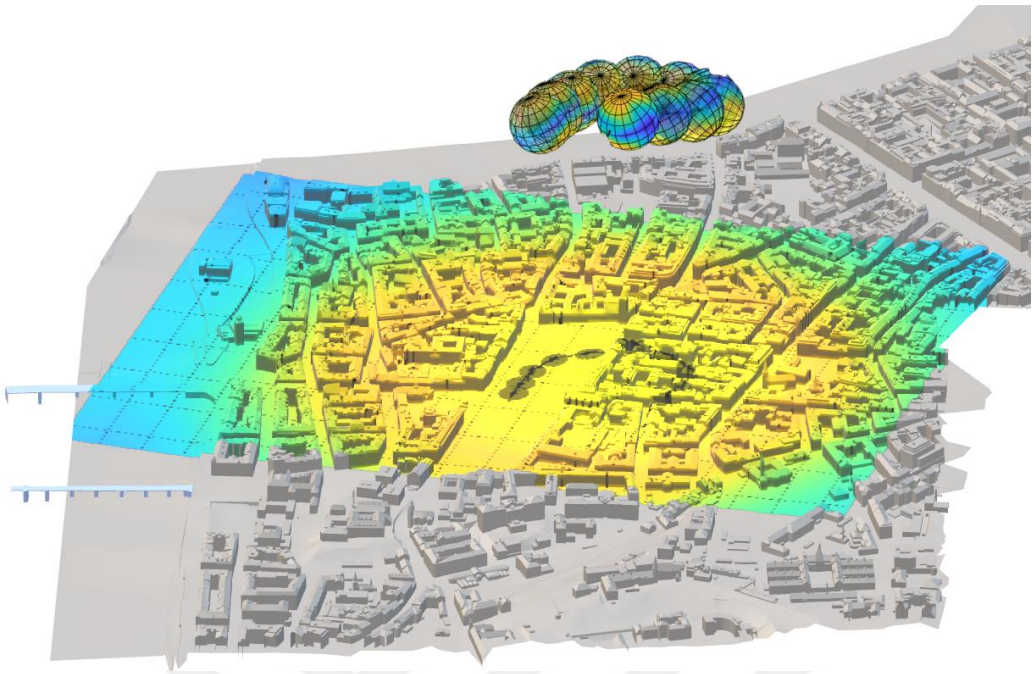

Figure 8.50 Horseshoe turn and climb mission acoustic contour on city model

Acoustic contours and flight profiles determined with all three objective functions (OBJ1, OBJ2 and OBJ3) are given in Figure 8.51 and Figure 8.52. Then SPL time variation and overall SEL values at the observer location are compared in Figure 8.53.

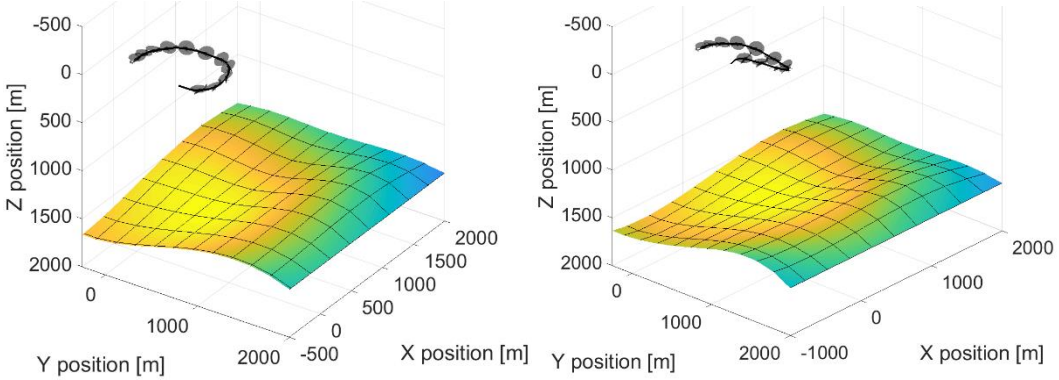

Figure 8.51 Acoustic contour and flight profile for OBJ1 and OBJ2

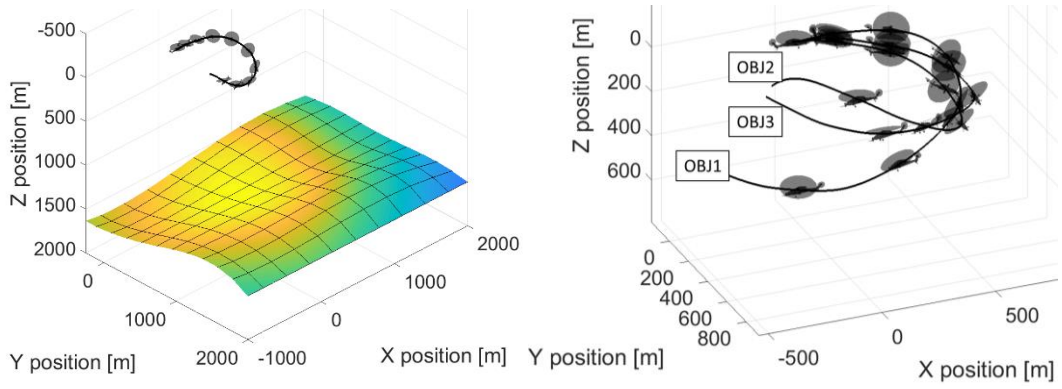

Figure 8.52 Acoustic contour and flight profile for OBJ3

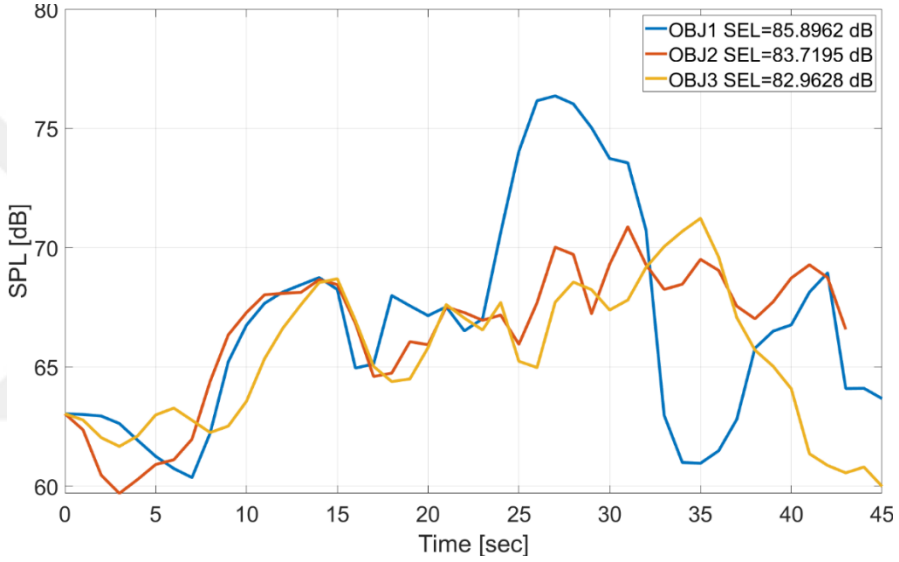

Figure 8.53 Comparison of SPL time variation and SEL at observer location

It is observed that, flight profile determined with all three objectives are similar during the 180° turn, whereas they deviate from each other at the climb. It is important to examine that, although the flight profiles seem similar, when the Euler angles, rates and velocity components are studied as given in Figure 8.54 and Figure 8.55, differences resulting in improved acoustic and fuel consumption characteristics can be noticed. OBJ1, having mission only concerns, provides the sharpest turn with highest roll angle, then increases speed during turn up to 140 knots and clears off the mission at high speed and climb rate flight condition with high acoustic impact at observer location and fuel consumption. OBJ2, having acoustic only concerns,

provides an intermediate turn with altitude loss to reduce acoustic impact at observer location, then clears off the mission at a high rate oblique climb, resulting in reduced overall noise signature without fuel concern. OBJ3, having green trajectory concern, on the other hand, performs the smoothest turn with speed gain lowering fuel consumption and acoustic impact at observer location and clears off the mission at a balanced speed and climb rate in terms of performance, noise and mission time.

Acoustic improvement of a trajectory over another is calculated through equation (114). Consequently, defining the OBJ1 trajectory as the reference, improvements achieved with OBJ2 and OBJ3 as well as the overall trade-offs of the trajectory optimization are summarized in Table 8.3. It is concluded that, with the inclusion of acoustic concern in the optimization algorithm, at least %25 improvement in noise impact is achieved. Moreover, inclusion of performance/fuel consumption concern in the optimization algorithm can reduce consumed fuel by 4%. As safety & comfort assessment is a non-dimensional evaluation, relative variation is defined in trade-off. Finally, waypoint track performance for all three objective functions is at least in %5 accuracy.

Table 8.3 Optimization trade-off results for horseshoe turn and climb

Trade-offs	OB1	OBJ2	OBJ3
SELdB at observer	85.90	83.72	82.96
Acoustic Improvement	100%	77%	71%
Fuel Cons. Improvement	100.0%	99.7%	96.3%
Safety & Comfort	Ref.	Lower	Lower
Waypoint Track	94.00%	98.50%	99.30%

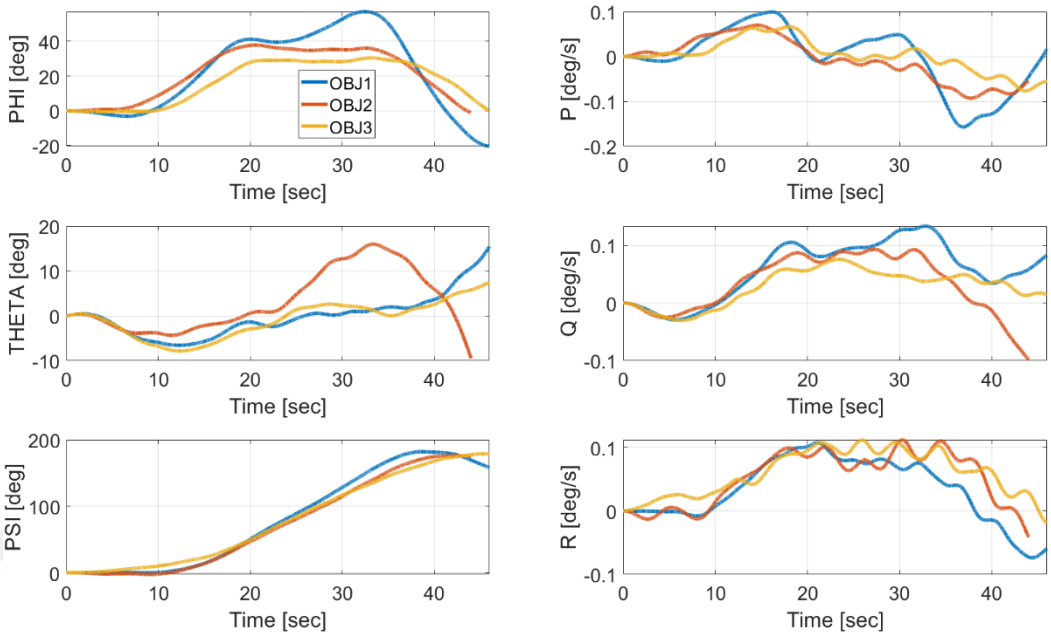

Figure 8.54 Euler angles and rates for horseshoe turn and climb mission

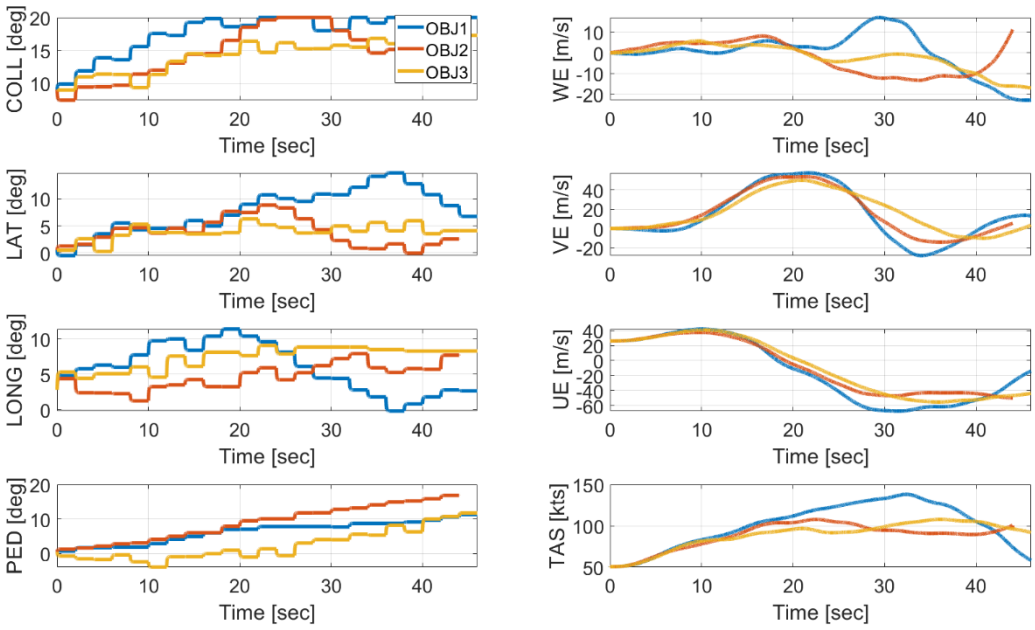

Figure 8.55 Control angles and velocity components for horseshoe turn and climb mission

CHAPTER 9

CONCLUSION

To conclude, whether it is a conventional or unconventional, a multi-rotor or compound; a noise minimal and green trajectory optimization and track framework for rotorcrafts is developed with this study. Developed approach combines multiple disciplines such as aerodynamics, aeroacoustics, flight dynamics and control and is built on high fidelity and accuracy comprehensive rotorcraft modeling basis. A model predictive control (MPC) loop is implemented over the simulation model to provide optimal trajectory and control to track the generated trajectory. Built on optimal control principles, MPC considers acoustic characteristics specific to the rotorcraft configuration, terrain information and mission requirements and generates optimal trajectories in terms of noise impact on noise sensitive regions, performance, fuel consumption, safety, and comfort. The methodology is developed under four modules, each of which can operate as either tightly coupled or individual models. Conclusions and remarks for each module are given separately under related sub-headings in this chapter.

Aerodynamics Module

A viscous vortex particle model (VVPM) specific to rotorcrafts is developed, providing high fidelity and accuracy rotor loads and wake dynamics with blade-vortex, rotor-wake and rotor-rotor interactions included. A rotor dynamics model is coupled with the VVPM providing steady or unsteady blade dynamic response under any flight and operating condition. Developed VVPM computes for isolated trim or full rotorcraft trim as it is coupled with rotorcraft mathematical model. VVPM provides the required high fidelity, accurate and high-resolution aeromechanical data including airloads and blade kinematic information for further comprehensive modeling or aeroacoustics calculations. Developed VVPM provides trimmed steady or unsteady, transient maneuver, analyses capability, with fully interacting i.e. blade-

vortex, rotor-wake and rotor-rotor, wake dynamics. Conclusions for the aerodynamics module are summarized as:

- Utilization of the Lagrangian approach eliminates the artificial diffusion drawback of grid based CFD methods. This enables the usage of vortex particles with significantly larger volume then the minimum mesh size of grid based CFD, without dispersing the tip vortex for desired number of revolutions.
- VVPM proposes significant improvement in terms of spanwise load distribution over free-wake methods. Even though the total integrated loads are same, spanwise distribution estimated with VVPM is more compliant with the test data, which is believed to stem from the better representation of the wake structure and its evolution and absence of empiric tuning parameters related with tip vortex location, core radius, core radius growth, roll-up process, near-far wake characteristics and vortex-wake-blade interactions.
- Typically implementing a VVPM approach requires decision/selection of a regularization kernel from a group of alternatives, which have been studied extensively for applications other than rotorcraft modeling purposes. A regularizing core is required for Biot-Savart induction law, as well as viscous diffusion through particle strength exchange. Kernels tending to return zero towards vortex center thought cut-off functions or high order algebraic functions are available in terms of regularization. In this study, it is experienced that, a Gaussian regularization/distribution for both Biot-Savart kernel and viscous diffusion provides superior configuration in terms of rotorcraft comprehensive modeling purposes.
- As empirical based parameters are absent in VVPM, it is attractive to study unconventional configurations for which experimental data is lacking. The single input parameters defined by the user is the resolution parameter for flow field.
- The VVPM algorithm requires at least N2 calculations (N being the number of vortex particles) which becomes computationally expensive with increasing resolution. However, the nature of the calculations makes the approach

exceedingly appropriate for parallelization or implementation of machine learning algorithms.

- The computational cost may significantly be improved with modern fast multi-pole algorithms and octree data structure. Yet, even with a simple cut-off function operates on vorticity magnitude, total computational cost through convergence can be decreased 10-20 times without effecting estimated rotor total thrust & torque levels i.e. aerodynamic performance. Vorticity contour and vorticity iso-surfaces for a rotor at hover with vorticity cut-off function off and on having same total thrust and torque levels at same collective input setting are illustrated with Figure 9.1 and Figure 9.2. The vorticity cut-off function acts as a barrier eliminating vortex particles with a strength below some arbitrary limit, therefore significantly decreases total particle number in the domain. As the inboard vortex sheet is generally at a weaker strength than the tip vortices, cut-off function eliminates the whole inboard vortex sheet while without changing rotor total estimated aerodynamic characteristics. Furthermore, the implementation methodology provides the potential for parallelization.

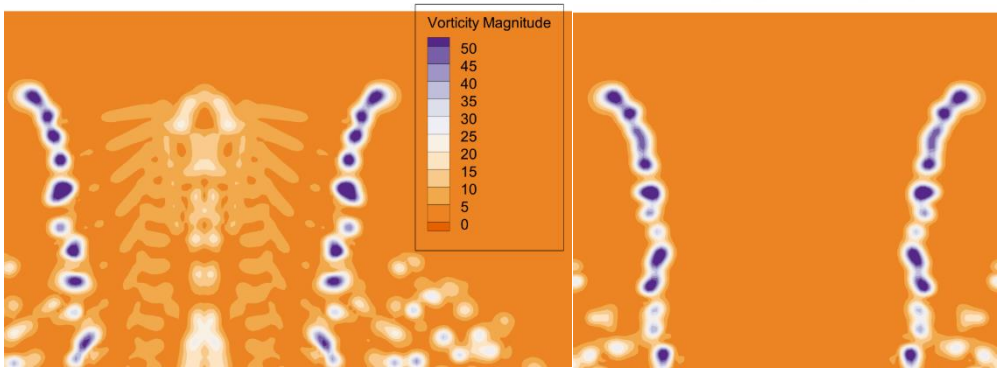

Figure 9.1 Cross-plane vorticity contour for a typical rotor

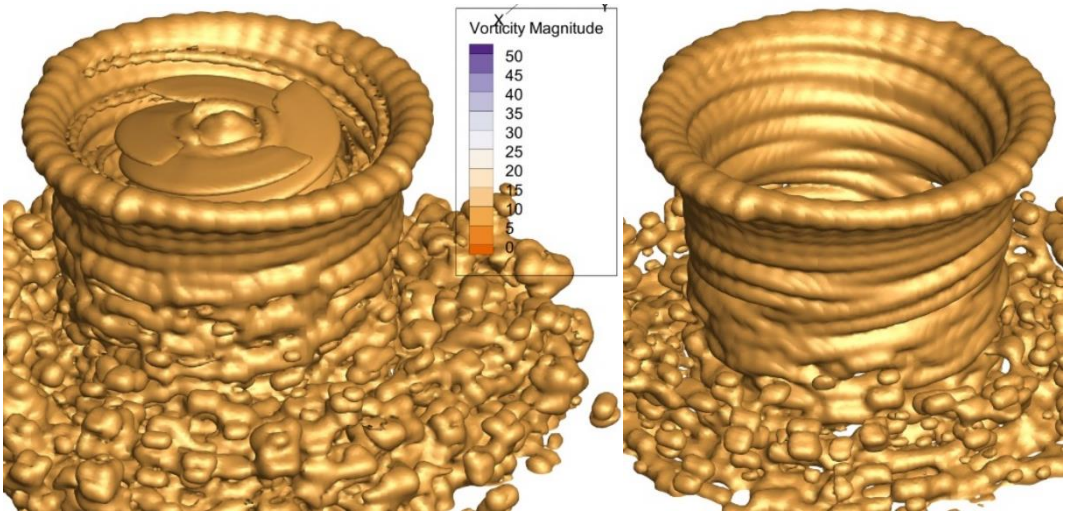

Figure 9.2 Vorticity iso-surface for a typical rotor

- As Stock (Stock, 2007) suggests, the vortex stretching might generate high local vorticities, which produces unrealistic results and discontinuities in the flow field. This was also experienced in this study. Diffusion acts as a physical mechanism due to viscosity to distribute localized high vortices and is essential to include in the governing equations. From a set of viscous diffusion methods present in the literature, a commonly utilized “Particle Strength Exchange” (PSE) method is implemented. Inclusion of viscous diffusion leads vortices to unite around strong vorticity regions such as tip vortex and provides longer existence for tip vortices. The effect of including viscous diffusion in the analysis is illustrated with Figure 9.3 and Figure 9.4 where same analysis is performed with viscous diffusion is on and off. The effect of viscous diffusion is observed in tip vortices i.e when included, results in more structured and regular wake geometry whereas when ignored, results is premature dissipation for tip vortices.

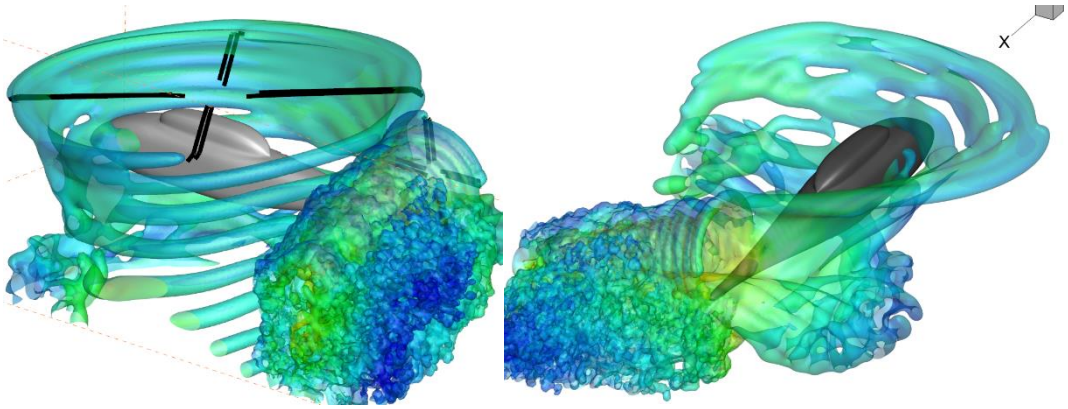

Figure 9.3 Solution with viscous diffusion on (left) and off (right)

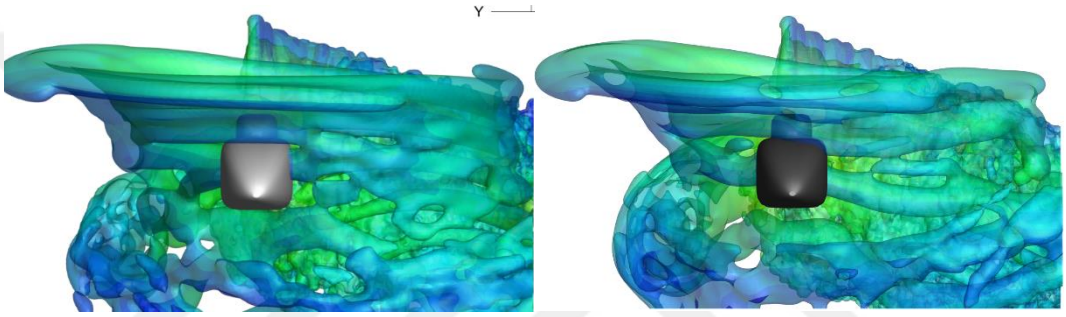

Figure 9.4 Solution with viscous diffusion on (left) and off (right)

- Increasing interest in coaxial/lift offset rotors leads industry and research focus on aeromechanical modeling of such configurations. Utilization of legacy free wake methods or finite state inflow models require additional tuning parameters specific to the configuration and introduces additional challenges to provide accurate induced velocity estimations especially at different separation distances between rotors. VVPM approach inherently can solve interaction/cooperation between any rotors operating at the same domain therefore is evaluated as a powerful alternative for multi-rotor comprehensive analyses.
- At the state of today's technology, in terms of comprehensive rotorcraft modeling, it is beneficial to lean on methodologies at high fidelity, accuracy and providing interactional aerodynamics, such as the VVPM developed in this study. The comprehensive modeling approach developed in this study provides fully interacting rotor-wake dynamics for multiple rotor configurations. VVPM

evaluated as a powerful alternative for legacy free/prescribed wake-based rotor modeling and is potentially a “game-changer” in terms of comprehensive analysis through the capability to estimate wake dynamics and unsteady rotor/blade loads in high fidelity, accuracy and resolution. The fact that VVPM does not require any empiric/analytic tuning parameter unlike legacy free wake methods, finite state inflow models or dynamic wake models which require numerous parameters for wake distortion, vortex core, tip vortex location, blade-wake and rotor-rotor interactions, reveals potential for further rotorcraft applications. Further improvements can be implemented for ground effect and ship wake solutions.

Aeroacoustics Module

The aeroacoustics module developed in this study covers comprehensive model interface including a proposed pressure distribution method and an algorithm that increase wake resolution, and the aeroacoustics solver, TACO, that had been developed within industry-academy co-operation program by Prof. Özyörük from Middle East Technical University (Özyörük et al., 2017) funded by Turkish Aerospace Industries, is coupled with the comprehensive analysis methodology developed in this study. The interface developed in this study distributes the spanwise concentrated load distribution determined through comprehensive analysis and VVPM over the real blade geometry in terms of surface pressure. Utilization of airfoil Cp distribution enables force to pressure transformation both in chordwise and spanwise directions. Then, TACO performs the acoustic analysis with forward time integration scheme. Coupling with comprehensive modeling approach provides a platform for aeroacoustics analysis of any complex configuration including co-axial, intermesh, prop-rotor and multirotor.

- Aeroacoustics signature of a rotor is a single performance parameter depending on complex, coupled and multi-disciplinary overall operating condition. A measured or calculated SPL is strongly influenced by blade planform, profile, airloads, wake dynamics, blade-vortex and blade-wake interaction, blade

complex kinematic motion, elasticity, operating environment, collected data resolution, data post-process etc... Estimation of acoustic pressure time variation requires a coupled and complex calculation process built on high fidelity, accurate and high order approaches covering aerodynamics, aeroelastic and aeroacoustics phenomena. An excellent example of how can estimated SPL can vary depending on calculation methodology is revealed by a co-operative international workshop with worldwide renowned institutes (van der Wall et al., 2014): German Aerospace Center (DLR), US Army AFDD and NASA Langley (US), Konkuk University of South Korea (KU), Office National d'Etudes et Recherches A´erospatiales of France (Onera) and University of Maryland (UM). Approaches utilized by the institutes include both in-house developed and commercial CFD-CSD coupled approaches, free-wake solvers, multi-body elastic blade solvers, aeroacoustics tools. HART-II wind tunnel test is selected as the test case, which is also utilized in this study, and results determined by all those five institutes are compared. In Figure 9.5, test data, results of the five institutes and results determined with the VVPAM tool developed in this study are compared. It is observed that, although the accuracy and resolution vary over a broad range, VVPAM provides significantly comparable results.

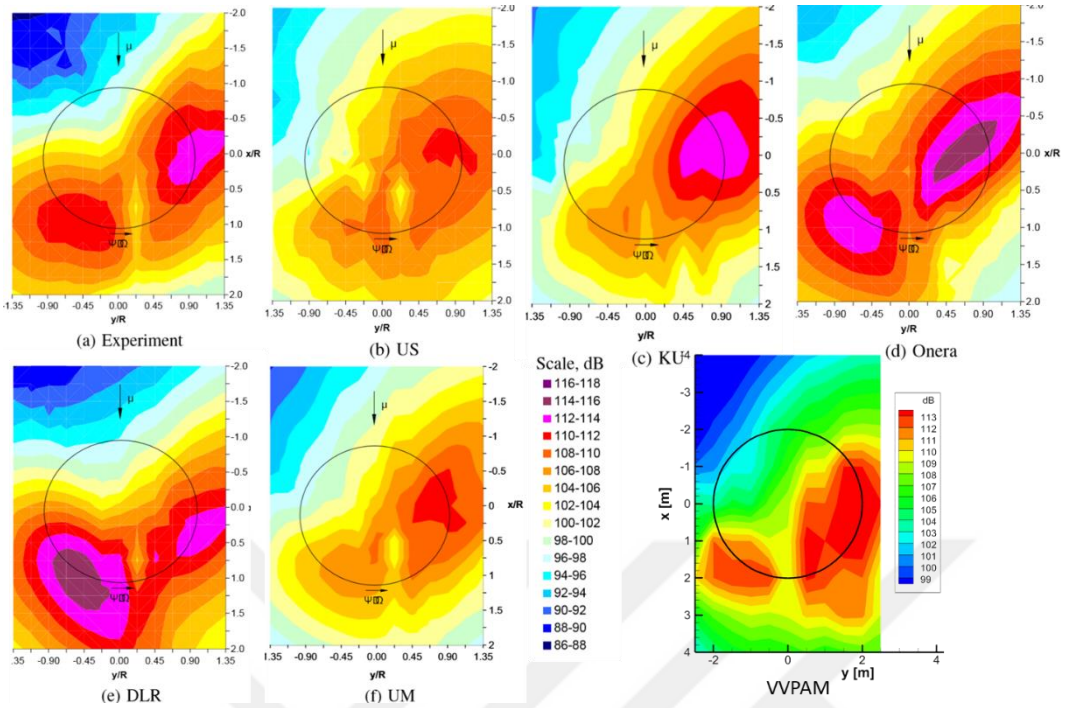

Figure 9.5 Comparison of acoustic analysis results of 5 different institutes, VVPAM and test data

- Another comparison is performed for the blade load variation at a section 87% of the blade span. The fact that aeroacoustics signature of a rotor influenced by the success of the airloads solution, an accurate aeromechanical simulation is essential. HART-II test data is compared with the results of specified 5 institutes plus Georgia Institute of Technology (GIT) and the results determined with the VVPM tool developed in this study as depicted in Figure 9.6.

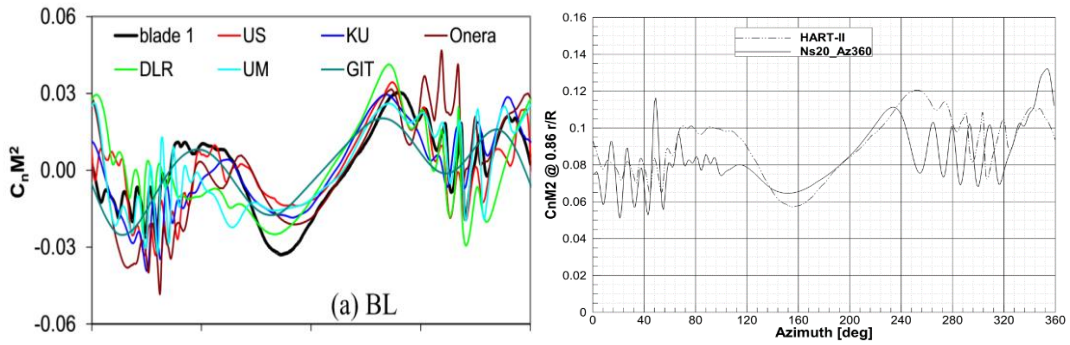

Figure 9.6 Blade loads comparison with test data (left: 5 institutes vs test, right: VVPM vs test)

It is revealed by the comparisons performed in terms of acoustic noise levels and rotor loads; results can vary broadly according to the simulation approach. Compared with the results of worldwide renown institutes, codes and tools, the VVPAM approach developed in this study provides airloads and aeroacoustics modeling at high resolution and accuracy.

- Comprehensive modeling is an essential tool for rotorcraft aeromechanics, which studies not only rotor aerodynamic performance, efficiency, loads, vibration but also rotor aeroacoustics. In this study therefore, the performance of VVPM to provide foundation to rotorcraft aeroacoustics through generation of high resolution and accuracy time dependent blade aerodynamic loads and motion data, is assessed. Such high-resolution aeromechanics data requires a significant computation time. Therefore, a variable time step calculation capability is developed and implemented which provides the capability to vary solution time step i.e. azimuth step for rotor of interest during analysis to increase data resolution.
- In general, there are two integration schemes for FWH integral equations i.e. retarded time and forward time. In retarded time algorithms, integral solution is performed at observer time, provides equally spaced acoustic signal at observer locations however requires root finding backward in time to determined noise emitting time. In forward time integration schemes, source time is the primary time domain, resulting in unequally spaced acoustic signal at observer location, therefore requires an interpolation i.e. a re-sampling computation to determine the final signal. In general, both algorithms require similar computational effort as already discussed in the literature. As discussed in the related chapter, retarded time is impractical, unless the source motion is quite simple and observer is not moving. In forward time schemes, the observer is not required to be fixed. Moreover, for maneuvering rotorcrafts where multiple rotors exist and longtime simulations are required, forward time integration scheme becomes more efficient, accurate and simple. For those reasons discussed in detail at

chapter 5.2, forward time integration is proper for trajectory optimization, multiple rotors and maneuvering rotorcraft applications.

- In general, comprehensive modeling of a rotor leans on spanwise concentrated loads determined with a high quality of wake dynamics and blade airloads as pressure distribution are not concern. Yet, for aeroacoustics calculations and applications a time dependent pressure distribution over the source surface is essential. The methodology proposed with this section to distribute the concentrated airloads over the blade geometry as chordwise and spanwise pressure distribution demonstrated to give accurate and practical acoustic response. Moreover, when integrated and compared with the comprehensive code results, negligible accuracy loss in observed. When compared with test data and benchmark commercial tools, it is evaluated that, the methodology proposed with this thesis provides sufficient accuracy and resolution in terms of aeroacoustics applications.

Simulation Module

Simulation module covers the rotorcraft mathematical model, surrogate noise model and terrain model, providing real-time simulation capability with SAS and actuator models included. Rotorcraft mathematical model is a generic, comprehensive analysis environment with a modular structure enabling modeling of any rotorcraft configuration including multi-rotors, tiltrotors, co-axial etc… A SAS is developed over the mathematical model to stabilize the non-linear plant as desired. The mathematical model operates real time and provides required flight dynamics data for further acoustics calculations. As the high fidelity VVPAM solver cannot be implemented as a real time simulation model, a surrogate noise model is developed. Noise model is comprising pre-compiled acoustic spheres generated specifically to a steady flight condition for all individual rotors and full rotorcraft and a three-dimensional interpolation routine to determine instantaneous effective acoustic sphere depending on the rotorcraft operating condition and environment. Through noise model, real time acoustic calculations can be performed at large number of observers. The noise model is coupled with a terrain model. Terrain model covers

the ground surface geometry, and urban areas, cities and noise sensitive regions exist on the landform. Whenever desired, noise model determines the acoustic response of the rotorcraft over the surface mesh covering the terrain while considering atmospheric and spherical losses. Coupled all together, simulation model including rotorcraft mathematical model, noise model and terrain model operates real time, provides an environment to perform non-linear time simulations starting from a trimmed flight condition with the pilot in the loop, with instantaneously calculated control inputs or with pre-defined control history. The conclusion and remarks deducted in terms of simulation model are summarized as:

- Having a modular structure for modeling coupled with a modular and flexible trimmer is essential for unconventional rotorcraft analysis. Moreover, for unconventional configurations where complex wake dynamics or aerodynamic interactional effects are dominant, coupling mathematical model with VVPM provided unlimited modeling capability. Such as the case of the sample multi-rotor simulated in this study, rotorcraft configuration with combination of any rotor/propeller type is “analyzable”. “Analyzable” means unlike “classical” comprehensive models having various empiric tune parameters and method-based limitations, such a mathematical model developed in this study, any rotorcraft with unconventional configurations can be modeled and simulated.
- It is experienced that, the Jacobian calculated with simplified dynamic inflow model for rotorcraft trim is still sufficient to trim the rotorcraft when VVPM is involved. This eliminates the need to generate another the sensitivity matrix for VVPM which significantly improved the computational cost. It is concluded that for a trim with VVPM, it is suggested that first perform a trim analysis with simplified inflow models then utilize the same Jacobian for further VVPM trim. It is evaluated that, the airloads dynamics is much faster than the wake dynamics. Generating a correcting control input at each time step with the Jacobian provides a smooth continuous convergence to trim targets. As long as the cost decrease direction i.e. the search direction, for the Jacobian is consistent with VVPM, the convergence can be achieved.

- The noise model developed in this study provides acoustic map on ground surface at 100 Hz with significant accuracy. Therefore, to study noise impact of a rotorcraft for long time durations, such a noise model is extremely beneficial.
- Unlike general trend in the literature, a full sphere database instead of a hemi-sphere contour is implemented in this study. As the purpose is generating optimal trajectories and flight profiles over long duration and distances, utilization of a full sphere eliminates the need for potential extrapolation especially in case of high Euler angles.
- Instead of storing only the SPL contour on the acoustic sphere, full frequency spectrum is stored which enables utilization of more sophisticated atmospheric attenuations models.

Trajectory Optimization and Track Module

The trajectory optimization and track approach developed in this study is basically a framework, combining multiple disciplines such as aerodynamics, aeroacoustics, flight dynamics and control. A model predictive control approach built on optimal control basics, is implemented in this study. Such approach utilizes a prediction model to estimate future dynamics and response of the plant. As the main aim of this study is to generate optimal trajectories in terms of reduced noise impact and fuel consumption while ensuring safety, comfort and mission objectives, the most feasible and practical approach is to simulate and iterate the trajectory separately from the plant to provide optimality. This scope can be completely provided with the MPC approach. Conclusions and remarks deducted from development of such a trajectory optimization and track framework are summarized as:

- It is observed that in terms of optimization nearly all the literature work concentrates on unmanned air vehicles with well-defined mission definition, obstacles, and controlled environment without any unforeseen disturbances. In terms of modeling, generally simplified mathematical models are utilized as plant such as point mass or linear models with rigid rotor configurations and most of the literature work is for UAVs with inherently decreased

aeromechanical complexity. For UAVs, the much higher ratio of the main rotor mass to fuselage mass and having very stiff main rotors without flapping hinges leads the inertial effects of the main rotor become the dominant component influencing the rotational dynamics which simplifies the coupled dynamic and aerodynamic response of the rotors. However, as the civil airspace are covered with full-size helicopters and when noise levels are the concern, the trajectory generation and track mechanism must be capable of coping with complex full-size helicopter aeromechanic environment. Besides as the success of the trajectory generation and track depends on how well the mathematical model represents the plant, a fully non-linear mathematical model with capability of determining rotor dynamic and aerodynamic response is essential for this study. Consequently, the better the simulation model is the more accurate and successful the trajectory optimization can be performed.

- Rotorcrafts are highly coupled and complex systems. For a fully controlled and optimized flight profiles, a comprehensive and overall optimization objective function is essential. Otherwise, the contradicting objectives or the trade-off between the disciplines might result in violation of each other and constraints. Therefore, for MPC applications, the objective function should be carefully generated and tuned. Auto improvements or optimization of the objective function can be performed which is left as a future extension of this study.
- While developing the safety and comfort cost for the overall objective function, it is experienced that, envelope protection algorithms can easily be established with such an MPC approach developed in this study. This might be a future extension of this study.
- Currently constant optimization frequency is utilized throughout this study. An adaptive frequency for optimization can be implemented to pass non-essential optimization stages which may significantly decrease overall computational cost especially for long simulations.
- The developed framework is applicable to rotorcraft flight route generations. Currently all flight routes, flight profile and all types of procedures are not

optimized but rather generic for all types of rotorcrafts. The methodology developed in this study can be utilized for new flight path development, specific to each rotorcraft design, which will generate a solution specific to each rotorcraft with best contribution to decrease public annoyance.

CHAPTER 10

FUTURE WORKS

A trajectory optimization and track framework covering various disciplines has been studied in this dissertation. Therefore, future works and potential improvement fields can be defined for each of the sub aspects. However only overall comprehensive future works are summarized in this chapter.

- The accuracy and fidelity of the optimized trajectory depends on the overall objective which is the combination of cost functions from various disciplines, that often contradict with each other. The trade-offs between the costs are left to the user currently, yet for a comprehensive overall objective, an outer optimization loop is planned to optimize the weights of each of the cost according to the desired mission.
- The accuracy and fidelity of the optimized track controls depends on the fidelity of the simulation model. Having VVPM coupled with the rotorcraft mathematical model provides utmost fidelity for comprehensive modeling purposes, yet, computational cost is required to be improved for further long simulations. Implementation of an octree algorithm and parallelization in GPU is planned to significantly improve the computational cost of VVPM coupled rotorcraft comprehensive mathematical model.

REFERENCES

Advanced Rotorcraft Technology. (2008). *FLIGHTLAB Theory Manual*.

Alvarez, E. J., & Ning, A. (2018). Development of a vortex particle code for the modeling of wake interaction in distributed propulsion. *2018 Applied Aerodynamics Conference*. https://doi.org/10.2514/6.2018-3646

Alvarez, E. J., & Ning, A. (2019). Modeling Multirotor Aerodynamic Interactions Through the Vortex Particle Method. *AIAA Aviation Forum*. https://doi.org/10.2514/6.2019-2827

Anderson, J. D. (2012). Fundamentals of Aerodynamics — Fifth edition. In *The Aeronautical Journal* (Vol. 116, Issue 1176). https://doi.org/10.1017/S000192400000676X

Atalay, M. M., Şenipek, M., & Yücekayalı, A. (2019). Assessment of maneuver airloads with model predictive control. *10th AIAC - Ankara International Aerospace Conference, 10th*.

Atalay, M. M., Yücekayalı, A., Şenipek, M., & Özyörük, Y. (2019). Main Rotor – Tail Rotor Interactional Noise. *8th Asian/Australian Rotorcraft Forum*, 1–11.

Avera, M. (2017). Vortex Particle Analysis of Side-by-Side Overlapping Rotors in Forward Flight. *73rd AHS Forum*, 2017.

Bacchini, A., & Cestino, E. (2019). Electric VTOL configurations comparison. *Aerospace*, *6*(3). https://doi.org/10.3390/aerospace6030026

Baslamisli, U., Ayan, E., & Yücekayalı, A. (2014). Tail rotor aerodynamic performance improvement with a gurney flap design. *40th European Rotorcraft Forum*, *40th*(September 2-5).

Beddoes, T. S. (1985). A Wake Model for High Resolution Airloads. *2nd International Conference on Basic Rotorcraft Research*.

Behr, R. D., & Reindel, E. M. (2008). Helicopter Noise Analysis for University of California San Francisco Mission Bay Hospital Site. *Esa*, *302300*.

Bernardini, G., Anobile, A., Serafini, J., Hartjes, S., & Gennaretti, M. (2015). Methodologies for helicopter noise footprint prediction in maneuvering flights. *22nd International Congress on Sound and Vibration, ICSV 2015*, *July*, 12–16.

Bottasso, C. L., Croce, A., Leonello, D., & Riviello, L. (2004). Optimization of critical trajectories for rotorcraft vehicles. *Annual Forum Proceedings - American Helicopter Society*, *1*(April), 816–835. https://doi.org/10.4050/1.3092853

Bramwell, A. R., Done, G. T., & Balmford, D. (2001). *Bramwell's Helicopter Dynamics* (2nd ed.). American Institute of Aeronautics.

Brentner, K. S., & Farassat, F. (1994). Helicopter Noise Prediction: The Current Status and Future Direction. *Journal of Sound and Vibration*, *170*(1).

Brentner, K. S., & Farassat, F. (2003). Modeling aerodynamically generated sound of helicopter rotors. *Progress in Aerospace Sciences*, *39*(2–3), 83–120. https://doi.org/10.1016/S0376-0421(02)00068-4

Bres, G. A., Brentner, K. S., Perez, G., & Jones, H. E. (2004). Maneuvering rotorcraft noise prediction. *Journal of Sound and Vibration*, *275*(3–5), 719–738. https://doi.org/10.1016/j.jsv.2003.07.005

Calabretta, J. (2010). A Three Dimensional Vortex Particle-Panel Code for Modeling Propeller-Airframe Interaction. In *Thesis at California Polytechnic State University* (Issue June).

Calabretta, J. S., & McDonald, R. A. (2010). A three dimensional vortex particle-panel method for modeling propulsion-airframe interaction. *48th AIAA Aerospace Sciences Meeting Including the New Horizons Forum and Aerospace Exposition*, *January*. https://doi.org/10.2514/6.2010-679

Caradonna, F. X., Tung, C., Field, M., & California, U. S. A. (1980). EXPERIMENTAL AND ANALYTICAL STUDIES OF A MODEL HELICOPTER ROTOR IN HOVER. *European Rotorcraft and Powered Lift Aircraft Forum*, *6*.

Casalino, D. (2003). An advanced time approach for acoustic analogy predictions. *Journal of Sound and Vibration*, *261*(4), 583–612. https://doi.org/10.1016/S0022-460X(02)00986-0

Castillo, C. L., Moreno, W., & Valavanis, K. P. (2007). Unmanned helicopter waypoint trajectory tracking using model predictive control. *2007 Mediterranean Conference on Control and Automation, MED*. https://doi.org/10.1109/MED.2007.4433726

Castles, W., & de Leeuw, J. H. (1953). *The Normal Component of the Induced Velocity in the Vicinity of a Lifting Rotor and Some Examples of Its Application*.

Chatelain, P., Duponcheel, M., Caprace, D. G., Marichal, Y., & Winckelmans, G. (2016). Vortex Particle-Mesh simulations of Vertical Axis Wind Turbine flows: From the blade aerodynamics to the very far wake. *Journal of Physics: Conference Series*, *753*(3). https://doi.org/10.1088/1742-6596/753/3/032007

Chen, R. T. N. (1990). A survey of nonuniform inflow models for rotorcraft flight dynamics and control applications. *Nasa Technical Memorandum*, *14*(2), 147–184. http://www.csa.com/partners/viewrecord.php?requester=gs&collection=TRD&recid=A9038521AH

Chen, R. T. N., & Zhao, Y. J. (1996). *Optimal Trajectories for the Helicopter in One-Engine-Inoperative Terminal-Area Operations*. *NASA TM 110400*, 1–34.

Chorin, A. J. (1973). Numerical study of slightly viscous flow. *Journal of Fluid Mechanics*, *57*(4), 785–796. https://doi.org/10.1017/S0022112073002016

Chorin, A. J. (1980). Vortex Models and Boundary Layer Instability. *Journal of Scientific and Statistical Computing*, *1980*(1), 1–21.

Conlisk, A. T. (2001). Modern helicopter rotor aerodynamics. *Progress in Aerospace Sciences*, *37*, 419–476.

Cruz, L., Massaro, A., Melone, S., & D'Andrea, A. (2012). Rotorcraft multi-objective trajectory optimization for low noise landing procedures. *38th European Rotorcraft Forum 2012, ERF 2012*, *2*, 1056–1068.

Cvetkovic, D., Kostic, I., Caslav, M., & Bengin, A. (2002). Numerical Model of Single Main Rotor Helicopter Dynamics. *ICAS 2002 Congress*, 1–10.

Dauer, J. C., Faulwasser, T., Lorenz, S., & Findeisen, R. (2013). Optimization-based feedforward path following for model reference adaptive control of an unmanned helicopter. *AIAA Guidance, Navigation, and Control (GNC) Conference, August 2013*. https://doi.org/10.2514/6.2013-5002

DENG, J., FAN, F., LIU, P., HUANG, S., & LIN, Y. (2019). Aerodynamic characteristics of rigid coaxial rotor by wind tunnel test and numerical calculation. *Chinese Journal of Aeronautics*, *32*(3), 568–576. https://doi.org/10.1016/j.cja.2018.12.026

Dose/Effect–, & WG2. (2002). *European Comission, Position paper on dose response relationships between transportation noise and annoyance*.

Dugar, V., Choudhury, S., & Scherer, S. (2017). Smooth trajectory optimization in Wind: First results on a full-scale helicopter. *Annual Forum Proceedings - AHS International*.

Dülgar, P. A., Yücekayali, A., Güngör, O., & Ortakaya, Y. (2019). Rotor Stall Onset Assessment. *8th Asian/Australian Rotorcraft Forum*.

Egolf, T. A., & Landgrebe, A. J. (1982). A Prescribed Wake Rotor Inflow and Flow Field Prediction Analysis - User's Manual and Technical Approach. *NASA Contractor Reports, Contractor*(June).

Erez, T., Lowrey, K., Tassa, Y., Kumar, V., Kolev, S., & Todorov, E. (2013). An integrated system for real-time model predictive control of humanoid robots. *IEEE/RAS International Conference on Humanoid Robots*, 292–299. https://doi.org/10.1109/HUMANOIDS.2013.7029990

Ezertaş, A., & Yücekayali, A. (2013). Hover performance assessment of 3 meter radius rotor on whirl tower. *39th European Rotorcraft Forum*, *39*.

Federal Aviation Administration (FAA). (2004). *Report To Congress: Nonmilitary Helicopter Urban Noise Study*.

Federal Aviation Administration (FAA). (2019). *Helicopter Flying Handbook*. http://www.amazon.com/Helicopter-Handbook-Federal-Aviation-Administration/dp/162087492X/ref=sr_1_2?ie=UTF8&qid=1397128668&sr=8-2&keywords=helicopter+books

Fletcher, T. M., & Brown, R. E. (2010). Helicopter tail rotor thrust and main rotor wake coupling in crosswind flight. *Journal of Aircraft*, *47*(6), 2136–2148. https://doi.org/10.2514/1.C031018

Freeman, Carl. E., & Mineck, R. E. (1979). *Fuselage Surface Pressure Measurements of a Helicopter Wind-Tunnel Model With a 3.15-Meter Diameter Single Rotor*.

Gatzke, B. T. (2010). *Trajectory Optimization for Helicopter Unmanned Aerial Vehicles (UAVs)*. https://doi.org/10.1090/dimacs/029/20

Gennaretti, M., Colella, M. M., & Bernardini, G. (2009). Analysis of helicopter vibratory hub loads alleviation by cyclic trailing-edge blade flap actuation. *Aeronautical Journal*, *113*(1146), 549–556. https://doi.org/10.1017/S0001924000003201

Georges-henri cottet. (2001). Vortex Methods: Theory and Practice. In *Measurement Science and Technology* (Vol. 12, Issue 3). https://doi.org/10.1088/0957-0233/12/3/704

Gläßel, H., Kahl, J., Dieterich, O., & Rudolph, S. (2004). Neural Networks for BVI System Identification. *European Rotorcraft Forum*.

Goulos, I. (2016). An improved analytical approach for modeling the effect of rotor wake curvature using finite-state induced flow models. *Journal of the American Helicopter Society*, *61*(3). https://doi.org/10.4050/JAHS.61.032010

Greenwood, E. (2017). Helicopter Flight Procedures for Community Noise Reduction. *73rd AHS International Annual Forum*.

Güngör, O. (2019). Fidelity and Performance Assessment of CFD Simulation Methodologies for Hovering Rotor. *7th Asian/Australian Rotorcraft Forum, ARF*.

Hairer, E., Norselt, Syvert. P., & Wanner, G. (1993). *Solving Ordinary Differential Equations* (8th ed.). Springer Verlag Berlin Heidelberg.

Hartjes, S., & Visser, H. G. (2019). Optimal control approach to helicopter noise abatement trajectories in nonstandard atmospheric conditions. *Journal of Aircraft*, *56*(1), 43–52. https://doi.org/10.2514/1.C034751

He, C., Syal, M., Tischler, M. B., & Juhasz, O. (2017). State-space inflow model identification from viscous Vortex Particle Method for advanced rotorcraft configurations. *Annual Forum Proceedings - AHS International*, 1846–1875.

He, C., & Zhao, J. (2009). Modeling rotor wake dynamics with viscous vortex particle method. *AIAA Journal*, *47*(4), 902–915. https://doi.org/10.2514/1.36466

Heffley, R., & Mnich, M. (1988). Minimum-Complexity Helicopter Simulation Math Model. In *NASA Contractor Reports* (Vol. 177476).

Hilbert, K. (1984). a Mathematical Model of the UH-60 Helicopter. In *Nasa Technical Memorandum* (Vol. 85890, Issue 1).

Hirschberg, A., & Rienstra, S. W. (2004). *An introduction to aeroacoustics* (Issue july 18).

Ho, J. C., & Yeo, H. (2017). Comparison of Calculated and Measured Blade Loads of the Tilt Rotor Aeroacoustics Model (TRAM). *73rd AHS Forum*, 2017.

Holden, J., & Goel, N. (2016). *Fast-Forwarding to a Future of On-Demand Urban Air Transportation*. 1–98. https://www.uber.com/elevate.pdf

Hu, H., Gu, B., Zhang, H., Song, X., & Zhao, W. (2015). *Hybrid Vortex Method for the Aerodynamic Analysis of Wind Turbine*. *2015*.

Huh, K. (1988). HELICOPTER ROTOR BLADE LOADING CALCULATIONS USING AN AXISYMMETRIC VORTEX SHEET AND THE FREE WAKE METHOD. In *MIT*. https://doi.org/10.7868/s0367676513090172

IKAIDA, H., TSUCHIYA, T., ISHII, H., GOMI, H., & OKUNO, Y. (2010). Numerical Simulation of Real-Time Trajectory Optimization for Helicopter Noise Abatement. *Journal of Mechanical Systems for Transportation and Logistics*, *3*(2), 415–430. https://doi.org/10.1299/jmtl.3.415

Jepson, D., Moffitt, R., Hilzinger, K., & Bissel, J. (1983). Analysis and Correlation of Test Data From an Advanced Technology Rotor System. *NASA Contractor Reports, August*.

Johnson, W. (1980). Performance and Loads Data From a Wind Tunnel Test of a Full-Scale Rotor with Four Blade Tip Planforms. *NASA Technical Memorandum, 81229*.

Johnson, W. (1988a). *A Comprehensive Analytical Model of Rotorcraft Aerodynamics and Dynamics, CAMRAD/JA Volume I*.

Johnson, W. (1988b). *A Comprehensive Analytical Model of Rotorcraft Aerodynamics and Dynamics, CAMRAD/JA Volume II*.

Johnson, W. (1994). *Helicopter Theory*. Dover Publications.

Johnson, W. (2013a). A history of rotorcraft comprehensive analyses. *Annual Forum Proceedings - AHS International*, *69*, 685–706.

Johnson, W. (2013b). *Rotorcraft Aeromechanics*. Cambridge University Press.

Joulain, A., Desvigne, D., Alfano, D., & Leweke, T. (2017). Numerical investigation of the vortex roll-up from a helicopter blade tip using a novel fixed-wing adaptation method. *CEAS Aeronautical Journal*, *8*(2), 245–260. https://doi.org/10.1007/s13272-016-0234-z

Khardi, S. (2014). Aircraft Flight Path Optimization . The Hamilton-Jacobi-Bellman considerations. *Applied Mathematical Sciences*, *6*(25), 1221–1249.

Klesa, J. (2008). *Increasing of Aircraft Propeller Efficiency by Using Variable Twist Propeller Blades*.

Kunz, K., Huck, S. M., & Summers, T. H. (2013). Fast Model Predictive Control of Miniature Helicopters. *European Control Conference*, 1377–1382.

Kunze, P. (2013). Parametric fuselage geometry generation and aerodynamic performance prediction in preliminary rotorcraft design. *39th European Rotorcraft Forum 2013, ERF 2013*, 100–102.

Landgrebe, A. (1971). An Analytical and Experimental Investigation of Helicopter Rotor Performance and Wake Geometry Characteristics. *Usaamrdl Technical Report*.

Lapp, T., & Leena, S. (2004). Model predictive control based trajectory optimization for nap-of-earth flight including obstacle avoidance. *American Control Conference*, 891–896.

Leishman, J. G. (2006). *Principles of Helicopter Aerodynamics*. Cambridge University Press.

Lighthill, M. J. (1952). On sound generated aerodynamically, I: general theory, Proceed. *Proceedings of the Royal Society A211*, 564–587.

Liu, H. (2008). Interfacing Comprehensive Rotorcraft Analysis With Advanced Aeromechanics and Vortex Wake Models Interfacing Comprehensive Rotorcraft Analysis With Advanced Aeromechanics and Vortex Wake Models. *Time*, *April*.

Luca Vigano, G. M. (2006). Acausal Modeling of Helicopter Dynamics for Automatic Flight Control Applications. *Modelica*, *May*, 377–384.

Ma, X. D., Zhang, Y., & Wei, P. (2018). VPM/CFD-based research on rotor performance and loads of individual blade control rotor system. *Tehnicki Vjesnik*, *25*(3), 694–700. https://doi.org/10.17559/TV-20180201121301

Majhi, J. R., & Ganguli, R. (2008). *Modeling Helicopter Rotor Blade Flapping Motion Considering Nonlinear Aerodynamics*. *27*(1), 25–36.

Martinussen, K. Å. (2010). *Prediction of Noise Generated by a Small Helicopter Rotor*. *June*.

Masarati, P. (2017). *MBDyn Theory and Developer's Manual Version 1.7.1*.

Miller, M., & Narkiewicz, J. (2006). Tiltrotor modeling for simulation in various flight conditions. *Journal of Theoretical and Applied Mechanics*, *44*(4), 881–906.

Mishra, A., Mavriplis, D., & Sitaraman, J. (2016). Time-dependent aeroelastic adjoint-based aerodynamic shape optimization of helicopter rotors in forward flight. *AIAA Journal*, *54*(12), 3813–3827. https://doi.org/10.2514/1.J054962

Morgans, A. S., Karabasov, S. A., Dowling, A. P., & Hynes, T. P. (2005). Transonic helicopter noise. *AIAA Journal*, *43*(7), 1512–1524. https://doi.org/10.2514/1.6679

Morris, R., Johnson, M., & Venable, K. B. (2015). Optimizing rotor craft approach trajectories with acoustic and land use models. *AAAI Workshop - Technical Report*, *WS-15-05*, 35–40.

Munzinger, C. (1998). Development of a Real-Time Flight Simulator for an Experimental Model Helicopter. *Georgia Institute of Technology*, *December*.

Neunert, M., de Crousaz, C., Furrer, F., Kamel, M., Farshidian, F., Siegwart, R., & Buchli, J. (2016). Fast nonlinear Model Predictive Control for unified trajectory optimization and tracking. *Proceedings - IEEE International Conference on Robotics and Automation*, *2016-June*(ICRA), 1398–1404. https://doi.org/10.1109/ICRA.2016.7487274

Ngo, T. D., & Sultan, C. (2016). Model predictive control for helicopter shipboard operations in the ship airwakes. *Journal of Guidance, Control, and Dynamics*, *39*(3), 574–589. https://doi.org/10.2514/1.G001243

Noise Sensitive Areas. (n.d.). Retrieved April 16, 2020, from https://www.tuolumnecounty.ca.gov/374/Noise-Sensitive-Areas

Okulov, V. L., Sørensen, J. N., & Wood, D. H. (2014). The rotor theories by Professor Joukowsky : Vortex theories. *Progress in Aerospace Sciences*, 1–28. https://doi.org/10.1016/j.paerosci.2014.10.002

OKUNO, Y., & Kawachi, K. (1994). Optimal Control of Helicopters Following Power Failure. *Journal of Guidance, Control, and Dynamics*, *14*(1).

Opoku, D. G., Triantos, D. G., Nitzsche, F., & Voutsinas, S. G. (2002). Rotorcraft Aerodynamic and Aeroacoustic Modeling Using Vortex Particle Methods. *ICAS 2002 Congress*, *1*, 299.1-299.11.

Ortun, B., Bailly, J., des Rochettes, H. M., & Delrieux, Y. (2014). Recent advances in rotor aerodynamic optimization, including structural data update. *American Helicopter Society International - 5th Decennial AHS Aeromechanics Specialists' Conference 2014: Current Challenges and Future Directions in Rotorcraft Aeromechanics*, 462–474.

Özyörük, Y., Ünal, A., & Yüksel, A. O. (2017). Noise predictions of helicopter rotors in hover and forward flight. *23rd AIAA/CEAS Aeroacoustics Conference, 2017*, *June*, 1–15. https://doi.org/10.2514/6.2017-3529

Padula, S. L., Burley, C. L., Boyd, D. D., & Marcolini, M. A. (2019). *Design of Quiet Rotorcraft Approach Trajectories* (Issue June 2009).

Peters, D., Boyd, D. D., & He, C. (1987). Finite-State Induced-Flow Model for Rotors in Hover and Forward Flight. *AHS 43rd*.

Peters, D., & He, C. (1989). Correlation of Measured Induced Velocities with a Finite State Wake Model. *AHS 45th*.

Peters, D., & He, C. (1995). inite State Induced Flow Models Part II: ThreeDimensional Rotor Disk. *Journal of Aircraft*, *32*(2).

Prieur, J., & Splettstoesser, W. R. (1999). ERATO – An ONERA-DLR Cooperative Program on Aeroacoustic Rotor Optimisation. *Proceedings of the 25th European Rotorcraft Forum*.

Putnam, T. W. (1975). *Review of Aircraft Noise Propagation: Vol. NASA TM X-*.

Rajmohan, N., Sankar, L., & Costello, M. (2011). Effect of Inflow Modeling on Coupling between Rotor Flight Mechanics and Aeromechanics. *49th AIAA Aerospace Sciences Meeting Including the New Horizons Forum and Aerospace Exposition*, *January*, 1–18. https://doi.org/10.2514/6.2011-1192

Ramasamy, M., Gold, N. R., & Bhagwat, M. J. (2010). Rotor hover performance and flowfield measurements with untwisted and highly-twisted blades. *36th European Rotorcraft Forum, ERF 2010*, *2*, 770–783.

Reddy, K. R., & Stewart, C. J. (2009). Simulation, a valuable tool in the estimation of helicopter flight dynamic characteristics. *18th World IMACS/MODSIM Congress*.

Salazar, T. (2010). Mathematical model and simulation for a helicopter with tail rotor. *International Conference on Computational Intelligence, Man-Machine Systems and Cybernetics - Proceedings, August*, 27–33.

Sankar, L. N. (2001). *Computational Studies of Horizontal Axis Wind Turbines*.

Şenipek, M. (2017). *DEVELOPMENT OF AN OBJECT-ORIENTED DESIGN, ANALYSIS AND SIMULATION SOFTWARE FOR A GENERIC AIR VEHICLE*. https://doi.org/10.13140/RG.2.2.24882.15042

Şenipek, M., Yücekayali, A., & Ortakaya, Y. (2019). Agility Assessment of Utility and Attack Configurations. *8th Asian/Australian Rotorcraft Forum, 8th*.

Şenipek, M., Yücekayali, A., & Ortakaya, Y. (2015). Multi-variable Aerodynamic Planform Optimization of Helicopter Main Rotor for Hover and Forward Flight Design Objectives. *8th AIAC Ankara International Aerospace Conference, September 10-12*.

Şenipek, M., Yücekayalı, A., & Kutay, A. T. (2017). Application of Generic Air Vehicle Simulation Model for Real-Time Aeroacoustic Noise Computation of Propeller Aircrafts. *9th AIAC Ankara International Aerospace Conference*.

Shen, J. (2003). COMPREHENSIVE AEROELASTIC ANALYSIS ANALYSIS OF HELICOPTER ROTOR WITH TRAILING-EDGE FLAP FOR PRIMARY CONTROL AND VIBRATION CONTROL. In *University of Maryland*.

Shinoda, P. (1996). Full-Scale S-76 Rotor Performance and Loads at Low Speeds in the NASA Ames 80- by 120- Foot Wind Tunnel. *NASA Technical Memorandum, 110379*, 238.

Singh, P., & Friedmann, P. P. (2018a). A computational fluid dynamics-based viscous vortex particle method for coaxial rotor interaction calculations in hover. *Journal of the American Helicopter Society*, *63*(4). https://doi.org/10.4050/JAHS.63.042002

Singh, P., & Friedmann, P. P. (2018b). Application of vortex methods to coaxial rotor wake and load calculations in hover. *Journal of Aircraft*, *55*(1), 373–381. https://doi.org/10.2514/1.C034520

Stock, M. J. (2007). Summary of Vortex Methods Literature (a living document rife with opinion). *Transport*, 1–114.

Stock, M. J., Gharakhani, A., & Stone, C. P. (2010). Modeling rotor wakes with a hybrid OVERFLOW-vortex method on a GPU cluster. *28th AIAA Applied Aerodynamics Conference*, *1*(June). https://doi.org/10.2514/6.2010-4553

Szymendera, C. J. (2002). Computational Free Wake Analysis of a Helicopter Rotor. In *The Pennsylvania State University: Vol. M.Sc* (Issue May). http://www.personal.psu.edu/~lnl/theses/chris_thesis_lq.pdf

Takahashi, M. D. (1990). A Flight-Dynamic Helicopter Mathematical Model with a Single Flap-Lag-Torsion Main Rotor. *NASA Technical Memorandum 102267*, 1–118. https://ntrs.nasa.gov/search.jsp?R=19910009728

Talbot, P. D., Tinling, B. E., Decker, W. a, & Chen, R. T. N. (1982). A mathematical model of a single main rotor helicopter for piloted simulation. *Nasa Technical Memorandum*, *84281*(September), 46.

Tamer, A., Yücekayali, A., & Ortakaya, Y. (2011). Design and Optimization of Helicopter Rotor for Minimum Power Required. *6th AIAC Ankara International Aeropsace Conference, September 14-16*.

Tamer, A., Yücekayali, A., & Ortakaya, Y. (2010). Helikopter Rotoru Aerodinamik ve Yük Analizleri İçin Pal Aeroelastik Çırpma Modelinin Geliştirilmesi. *3. Ulusal Havacilik ve Uzay Konferansı, September 16-18*.

Tan, J. F., & Wang, H. W. (2013). Simulating unsteady aerodynamics of helicopter rotor with panel/viscous vortex particle method. *Aerospace Science and Technology*, *30*(1), 255–268. https://doi.org/10.1016/j.ast.2013.08.010

The MathWorks, Inc. (2012). *MATLAB-fmincon* (Revision: 1.1.6.28). The MathWorks, Inc.

Theodore, C., & Celi, R. (2002). Helicopter flight dynamic simulation with refined aerodynamics and flexible blade modeling. *Journal of Aircraft*, *39*(4), 577–586. https://doi.org/10.2514/2.2995

Todorov, M. (2011). Aeroelastic Modeling of Hingeless Helicopter Blade in Forward Flight. *Faculty of Transport*, 2–6.

Tsuchiya, T., Ishii, H., Uchida, J., Ikaida, H., Gomi, H., Matayoshi, N., & Okuno, Y. (2009). Flight trajectory optimization to minimize ground noise in helicopter landing approach. *Journal of Guidance, Control, and Dynamics*, *32*(2), 605–615. https://doi.org/10.2514/1.34458

van der Wall, B. G., Lim, J. W., Smith, M. J., Jung, S. N., Bailly, J., Baeder, J. D., & Douglas Boyd, D. (2014). The HART II international workshop: An assessment of the state-of-the-art in comprehensive code prediction. *CEAS Aeronautical Journal*, *4*(3), 223–252. https://doi.org/10.1007/s13272-013-0077-9

van Rees, W. M., Leonard, A., Pullin, D. I., & Koumoutsakos, P. (2011). A comparison of vortex and pseudo-spectral methods for the simulation of periodic vortical flows at high Reynolds numbers. *Journal of Computational Physics*, *230*(8), 2794–2805. https://doi.org/10.1016/j.jcp.2010.11.031

Vermeer, L. J., S, J. N., & Crespo, A. (2013). Wind turbine wake aerodynamics. *Progress in Aerospace Sciences*, *39*(October 2003), 467–510. https://doi.org/10.1016/S0376-0421(03)00078-2

Visser, H. G., Pavel, M. D., & Tang, S. F. (2009). Optimization of rotorcraft simultaneous noninterfering noise abatement approach procedures. *Journal of Aircraft*, *46*(6), 2156–2160. https://doi.org/10.2514/1.39763

Vladimir, C., Horia, D., Florin, F., & Alexandru, D. (2006). Determination of angle of attack for rotating blades. *Wind Energy Proceedings of the Euromech Colloquium*, *4*(2), 37–42. https://doi.org/10.13111/2066-8201.2012.4.2.4

Wall, B. G. van der. (2003). *2nd HHC Aeroacoustic Rotor Test (HART II) - Part I: Test Documentation*.

WANG, F., XU, G., & SHI, Y. (2018). Efficient prediction of ground noise from helicopters and parametric studies based on acoustic mapping. *Chinese Journal of Aeronautics*, *31*(2), 273–284. https://doi.org/10.1016/j.cja.2017.11.013

Wang, H. B. (2017). Influence analysis of propeller location parameters on wings using a panel / viscous vortex particle hybrid method. *Journal of Aircraft*, *September*, 1–21. https://doi.org/10.1017/aer.2017.109

Wang, Y., & Boyd, S. (2010). Fast Model Predictive Control Using Online Optimization. *Control Systems Technology, IEEE Transactions On*, *18*(2), 267–278. https://doi.org/10.1109/TCST.2009.2017934

Williams, F. J. E., & Hawkings, D. L. (1969). Sound Generation by Turbulence and Surfaces in Arbitrary Motion. *Philosophical Transactions of the Royal Society London*, *264*(1151), 321–342.

Winckelmans, G., & A., L. (1993). contributions to vortex particle methods for the computation of three dimensional incompressible unsteady flows. *Journal of Computational Physics*, *109*, 247–273.

Worthmann, K. (2012). Estimates of the prediction horizon length in MPC: A numerical case study. *4th IFAC Nonlinear Model Predictive Control Conference*, *4*. https://doi.org/10.3182/20120823-5-NL-3013.00037

Yilmaz, D. (2008). Evaluation and Comparison of Helicopter Simulation Models with Different Fidelities. In *Master Thesis*.

Young, L. a. (1997). *Vortex Core Size in the Rotor Near-Wake*. http://hdl.handle.net/2060/20040082235

Yücekayali, A. (2011). *Development of a Comprehensive and Modular Modeling, Analysis and Simulation tool for Helicopters*.

Yücekayali, A., Ayan, E., & Ortakaya, Y. (2014). Acoustic Assesment of 3 Meter Radius Rotor With Whirl Tower Test and Analysis. *70th AHS American Helicopter Society Forum*, *70th*(May 20-22).

Yücekayali, A., Baslamisli, U., & Ayan, E. (2014). Rotor Test Kulesinde Hafif Sinif Helikopter Ana Rotoru Akustik Ölçüm Testleri ve Pal Kalinlik Gürültüsü Analiz Araci Geliştirilmesi. *5. Ulusal Havacilik ve Uzay Konferansi*, *September 8-10*.

Yücekayali, A., Ezertaş, A., & Ortakaya, Y. (2013). Whirl Tower Testing and Hover Performance Evaluation of a 3 Meter Radius Rotor Design. *7th AIAC Ankara International Aerospace Conference*, *7*(September 11-13), 1-.

Yücekayali, A., & Ortakaya, Y. (2015a). A Parametric Study on Main Rotor Tip Shape to Reduce Blade-Vortex Interaction Noise. *8th AIAC Ankara International Aerospace Conference*, *September 10-12*, 1–8.

Yücekayali, A., & Ortakaya, Y. (2010). Girdap Teorisi ve Pal Elemanlari Metodu ile Helikopter Rotorunun Aerodinamik Modellenmesi. *3. Ulusal Havacilik ve Uzay Konferansı*, *September 16-18*.

Yücekayali, A., & Ortakaya, Y. (2015b). Helicopter Main Rotor Noise Computation from Pre-compiled Acoustic Hemisphere With Atmospheric Propagation Model. *5th AIAC, Ankara International Aerospace Conference*, *5th*, 1–9.

Yücekayali, A., & Ortakaya, Y. (2019). Viscous Vortex Particle Method Explored for Main Rotor-Tail Rotor Interaction. *8th Asian/Australian Rotorcraft Forum*, *8th*(October 30-November 2).

Yücekayali, A., Şenipek, M., & Kutay, A. T. (2017). Optimal Guidance Model for Green Trajectory Generation of Helicopters. *9th AIAC, September*, 1–9.

Yücekayali, A., Şenipek, M., & Ortakaya, Y. (2015). Main Rotor Aeroacoustic Analysis & Validation with Test Data and Favorable Planform Design for Minimal Aerodynamic Noise. *41st European Rotorcraft Forum*, 1–12.

Yücekayali, A., Şenipek, M., & Ortakaya, Y. (2019). Agility assessment of helicopter main rotor design. *The Vertical Flight Society - Forum 75: The Future of Vertical Flight - Proceedings of the 75th Annual Forum and Technology Display*.

Yücekayali, A., Şenipek, M., & Ortakaya, Y. (2018). Development of CFD embedded rotor actuator surface simulation model. *7th Asian/Australian Rotorcraft Forum, ARF 2018, October 30-November 1*.

Yücekayali, A., Şenipek, M., Ortakaya, Y., & Özyörük, Y. (2019). TACO: Helicopter noise predictions. *7th Asian/Australian Rotorcraft Forum, ARF 2018*, *7th*(October).

Yucekayali, A., Şenipek, M., Özyörük, Y., & Ortakaya, Y. (2019). Comprehensive Rotorcraft Aeroacoustics: Investigation of Surface Pressure Distribution Methods. *45th European Rotorcraft Forum 2019, ERF 2019, 45th*, 1–10.

Zhao, J., & He, C. (2012). Enhancement of viscous vortex particle method for fundamental rotor wake dynamics simulation. *50th AIAA Aerospace Sciences Meeting Including the New Horizons Forum and Aerospace Exposition*, *January*, 1–11. https://doi.org/10.2514/6.2012-1196

Zhao, Y., Jhemi, A. A., & Chen, R. T. N. (1996). Optimal Vertical Takeoff and Landing Helicopter Operation in One Engine Failure. *Journal of Aircraft*, *33*(2).

APPENDICES

A. Greens function

Determination of the relationship between particle representation of the vorticity field and velocity field is summarized from Winckelmans (Winckelmans & A., 1993) in this chapter. The particle representation of the vorticity field is given with equation (115).

$$\vec{\omega}_\sigma = \sum_{p=1}^{N} \alpha_p(t)\zeta_\sigma\left(\vec{x} - \vec{x}_p(t)\right) \tag{115}$$

The regularization $\zeta_\sigma = \frac{1}{\sigma^3}\zeta\left(\frac{|\vec{x}|}{\sigma}\right)$ function is a radially symmetric function with the normalization given with equation (116).

$$4\pi \int_0^\infty \zeta(\rho)\rho^2 d\rho = 1 \tag{116}$$

where σ is smoothing radius and ρ is non dimensional distance parameter defined as $\rho = \frac{|\vec{x}-\vec{x}_p(t)|}{\sigma}$. Defining the Green's function $G(\rho)$ as equation (117).

$$-\zeta(\rho) = \nabla^2 G(\rho) = \frac{1}{\rho^2}\frac{d}{d\rho}\left(\rho^2 \frac{dG}{d\rho}\right) = \frac{1}{\rho}\frac{d^2}{d\rho^2}\left(\rho G(\rho)\right) \tag{117}$$

Then utilization definition of curl of streamfunction given in equation is (118) utilized to obtain relationship between streamfunction and Green's function given in equation (119) and (120).118118118

$$\nabla^2 \psi_\sigma(x,t) = -\omega_\sigma(x,t) \tag{118}$$

$$\psi_\sigma(x,t) = G(x) * \omega_\sigma(x,t) = G_\sigma(x) * \omega(x,t) \tag{119}$$

$$\psi_\sigma(x,t) = \sum_{p=1}^{N} G_\sigma\left(\vec{x} - \vec{x}_p(t)\right)\alpha_p(t) \tag{120}$$

where $G_\sigma(x) = G\left({}^{|\vec{x}|}/_{\sigma}\right)/\sigma$. If a $q(\rho)$ function is defined such as in equation (121), useful relations between $\zeta(\rho)$, $G(\rho)$ and $q(\rho)$ can be obtained which eventually leads to velocity field formulation.

$$q(\rho) = \int_0^\rho \zeta(t)t^2 dt \tag{121}$$

The normalization condition given with equation (116) leads to equation (122).

$$\frac{1}{\rho^2}\frac{d}{d\rho}q(\rho) = \zeta(\rho) \tag{122}$$

Then from the definition of Green's function $G(\rho)$ and $q(\rho)$,

$$q(\rho) = \int_0^\rho \zeta(t)t^2 dt = -\int_0^\rho \frac{d}{dt}\left(t^2\frac{d}{dt}G(t)\right)dt = -\rho^2\frac{d}{d\rho}G(\rho) \tag{123}$$

Equation (124) is determined as

$$-\frac{1}{\rho}\frac{d}{d\rho}G(\rho) = \frac{q(\rho)}{\rho^3} \tag{124}$$

The from equation (122), equation (125) is determined.

$$-\frac{1}{\rho}\frac{d}{d\rho}\left(\frac{q(\rho)}{\rho^3}\right) = \frac{1}{\rho^2}\left(\zeta(\rho) - 3\frac{q(\rho)}{\rho^3}\right) \tag{125}$$

Finally, the velocity field is determined through equations (126), (127) and (128).

$$\vec{u}_\sigma(\vec{x},t) = \nabla \times \vec{\psi}(\vec{x},t) \tag{126}$$

$$\nabla \times \vec{\psi}(\vec{x},t) = \sum_{p=1}^{N} \nabla\left(G_\sigma\left(\vec{x} - \vec{x}_p(t)\right)\right) \times \alpha_p(t) \tag{127}$$

$$\vec{u}_\sigma(\vec{x},t) = -\sum_{p=1}^{N} \frac{q_\sigma\left(\vec{x} - \vec{x}_p(t)\right)}{\left|\vec{x} - \vec{x}_p(t)\right|^3}\left(\vec{x} - \vec{x}_p(t)\right) \times \alpha_p(t) \tag{128}$$

where $q_\sigma = q\left(|\vec{x}|/\sigma\right)$

B. Lighthill's Acoustic Analogy

The main intention behind the Lighthill's analogy is derive a homogenous wave equation from exact mass continuity and conservation of momentum equations given with equations (129) and (130).

$$\frac{\partial \rho}{\partial t} + \frac{\partial \rho u_i}{\partial x_i} = 0 \tag{129}$$

$$\frac{\partial \rho u_i}{\partial t} + \frac{\partial \rho u_i u_j}{\partial x_j} = -\frac{\partial P_{ij}}{\partial x_j} + f_i \tag{130}$$

where $\rho$is the fluid density, u_i is the velocity component, f_i is the force field such as gravitational field and P_{ij} is the net force acting on the surface of the infinitesimal volume element given with equation (131).

$$P_{ij} = p\delta_{ij} - \sigma_{ij} \tag{131}$$

Further derivation is performed through taking time derivative of the mass continuity equation and subtracting divergence of the momentum equation to determine equation (132).

$$\frac{\partial^2 \rho}{\partial t^2} = \frac{\partial^2}{\partial x_i \partial x_j}\left(P_{ij} + \rho u_i u_j\right) - \frac{\partial f_i}{\partial x_i} \tag{132}$$

Then re-writing the equation (132) in perturbation form such as $p' = p - p_0$ and $\rho' = \rho - \rho_0$, adding $\frac{1}{c_0^2}\frac{\partial^2}{\partial t^2}p'$ to both sides and defining Lighthill's stress tensor as $\sigma_{ij} = p\delta_{ij} - P_{ij}$, Lighthill's analogy given with equation (133) is determined.

$$\frac{1}{c_0^2}\frac{\partial^2 p'}{\partial t^2} - \frac{\partial^2}{\partial x_i^2} = \frac{\partial^2}{\partial x_i \partial x_j}\left(\rho u_i u_j - \sigma_{ij}\right) - \frac{\partial f_i}{\partial x_i} + \frac{\partial^2}{\partial t^2}\left(\frac{p'}{c_0^2} - \rho'\right) \tag{133}$$

C. Validation of Aeroacoustics Solver with Commercial Tools

The aeroacoustics solver utilized in this study has been validated with commercial comprehensive rotorcraft modeling tool, CHARM, before being coupled with the developed viscous vortex particle method by the author. HART-II wind tunnel test case is utilized for validation study. In this scope, first, aeromechanical analysis is performed with CHARM and PSU-WOPWOP, commercial rotorcraft aeroacoustics solver, is utilized to determine the acoustic pressure variation at the observer location and compared to test data. Then, same aeromechanical data is operated through the pressure distribution approach proposed with this study and the aeroacoustics solver, TACO, is utilized to determine the acoustic pressure variation and compared to test data. It is observed that, the aeromechanical data resolution that CHARM outputs to external user is lower than the aeromechanical data that CHARM provides to PSU-WOPWOP for acoustic analysis purposes. Therefore, the reconstructed high-resolution data provided by CHARM to PSU-WOPWOP is utilized for further TACO analysis and results are compared. It is observed that, initialized with the same aeromechanical data, PSU-WOPWOP and TACO calculates similar acoustic signature which is also comparable to the test data.

First, wind tunnel trim analysis for the rotor configuration given with Figure 11.1 is performed with CHARM.

Specifications	Values
Blade Span	2m
Rotational Speed	1041 rpm
Blade Twist	-8° linear
Precone Angle	2.5°
Root cut out	22 %
Number of blades	4

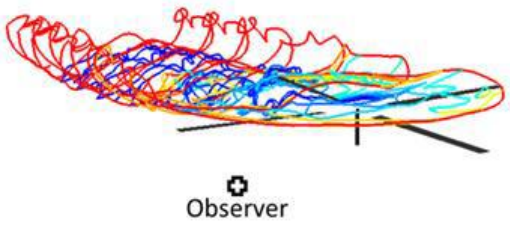

Figure 11.1 HART-II test case configuration and CHARM wake output

Then aeroacoustics analysis is performed for an observer, i.e. Microphone 11 illustrated in Figure 11.1 and acoustic pressure variation is compared with the test data as depicted in Figure 11.2.

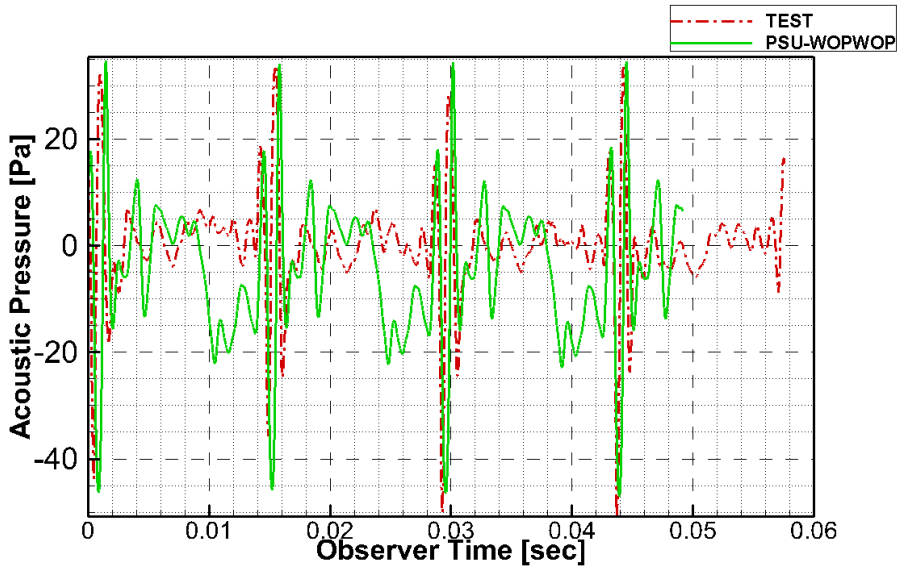

Figure 11.2 Test vs PSU-WOPWOP comparison

It is observed that, acoustic signature of the test case can be determined accurately through the commercial tools. Then, same acoustic analysis is performed with CHARM standard output with TACO, and result is compared with test data as depicted in Figure 11.3.

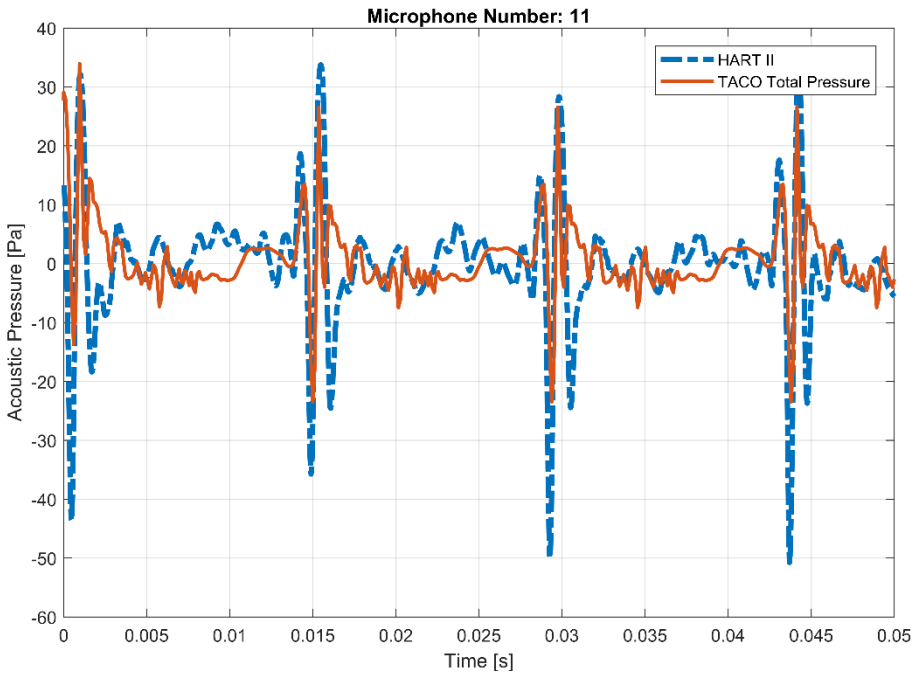

Figure 11.3 Test vs TACO initial comparison

It is observed that, although the wave form of the acoustic signature is similar with the measured data, TACO failed to estimate peak acoustic pressure values. Through further investigation, it is observed that, CHARM, being already commercially coupled with PSU-WOPWOP, provides higher resolution airloads data for acoustic analysis purposes by an additional reconstruction stage after the solution is converged as illustrated in Figure 11.4.

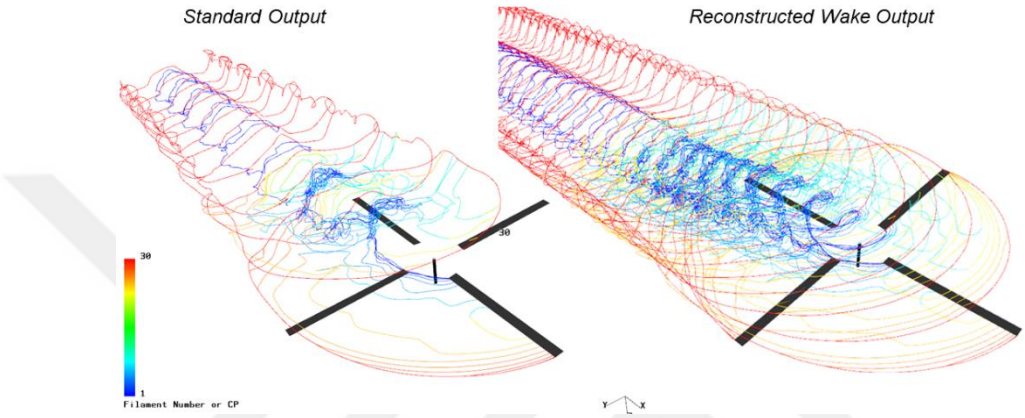

Figure 11.4 Wake re-construction

Then the re-constructed aeromechanical data generated by CHARM is utilized with the pressure distribution methodology and TACO, acoustic analysis is performed and result is compared in Figure 11.5.

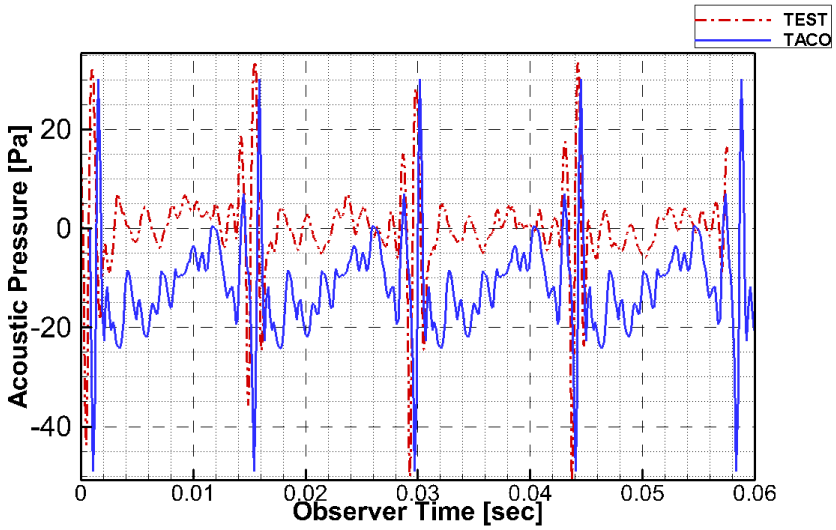

Figure 11.5 Test vs TACO + CHARM validation

It is observed that, TACO can capture both pressure peaks and signature waveform as accurately as commercial PSU-WOPWOP aeroacoustics solver.

This study revealed the importance of the high resolution and fidelity aeromechanical solution which is the essential input for the aeroacoustics analysis. The viscous vortex particle method coupled comprehensive solver developed in this study provides such high fidelity, accuracy and resolution airloads data without a necessity of an additional reconstruction stage as the validation study, chapter 5.5, reveals. Furthermore, coupled with rotorcraft mathematical model, aeroacoustics evaluations for multiple rotor full rotorcraft free flight and maneuvering conditions are achievable at practical computational cost. Besides, the study reveals the potential of the developed VVPAM, VVPM coupled aeroacoustics solver, in terms of evaluation and developing a better understanding for maneuvering rotorcraft noise signature.

D. Model Predictive Control for SAS

An alternative approach for a closed-loop stabilization (SAS) over the non-linear mathematical model is developed with utilization of model predictive control. Damping of the disruptive rates is achieved through implementing rates of states of the rotorcraft as an additional cost/penalty in the overall optimization function. Utilization of MPC for a SAS is established easily in the prediction stage through a Ricatti equation utilizing instantaneous rotorcraft inputs and states. Gust simulation for a conventional helicopter at hover is performed with MPC-SAS on and off, and platform dynamic response is illustrated with Figure 11.6 and Figure 11.7.

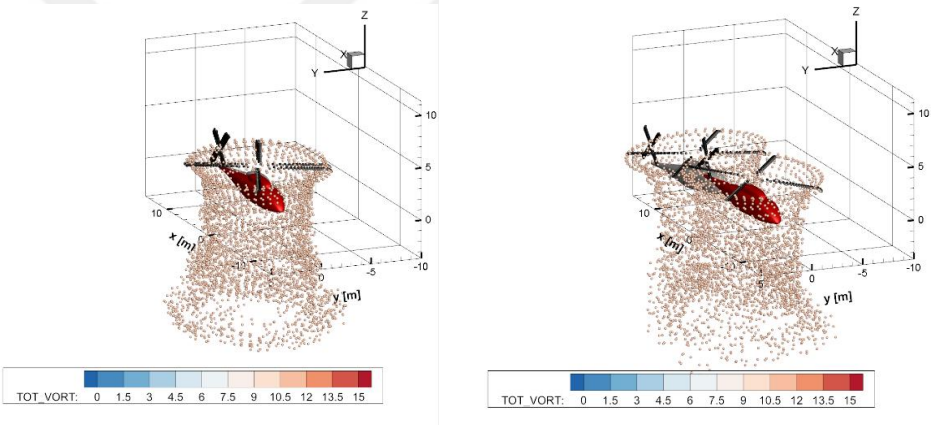

Figure 11.6 Gust simulation at hover. SAS is off for grey, SAS is on for red helicopters. Left : t=0 seconds, Right: t=1.0 seconds

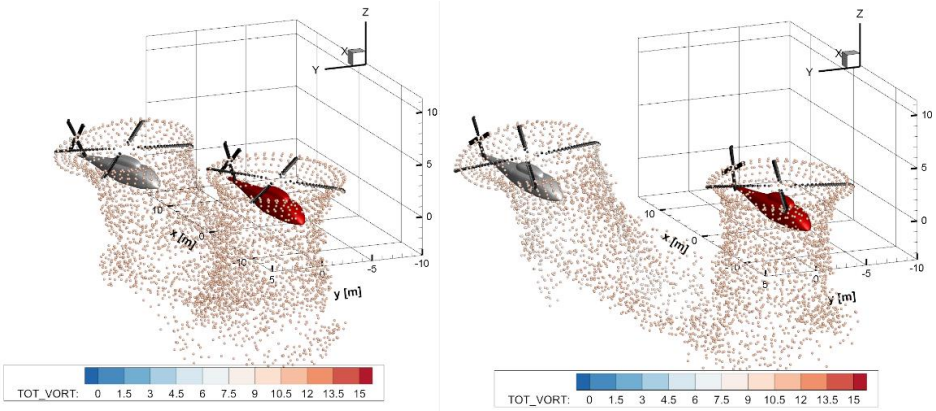

Figure 11.7 Gust simulation at hover. SAS is off for grey, SAS is on for red helicopters. Left : t=2.0 seconds, Right: t=3.0 seconds

E. VVPM for fuselage interaction

One of the most important interaction problem for rotorcrafts is rotor-fuselage interaction. Rotor produces extra download on the fuselage and results alteration of rotorcraft trim states. An essential extension of the VVPM approach developed in this study is solution of rotor-fuselage interaction. As VVPM is capable of calculating air velocity vector at any location in the domain, it can be utilized to determine local or average air flow on fuselage. A sample illustration of rotor induced air velocity distribution over the fuselage for a conventional configuration helicopter at an arbitrary forward fight is given in Figure 11.8

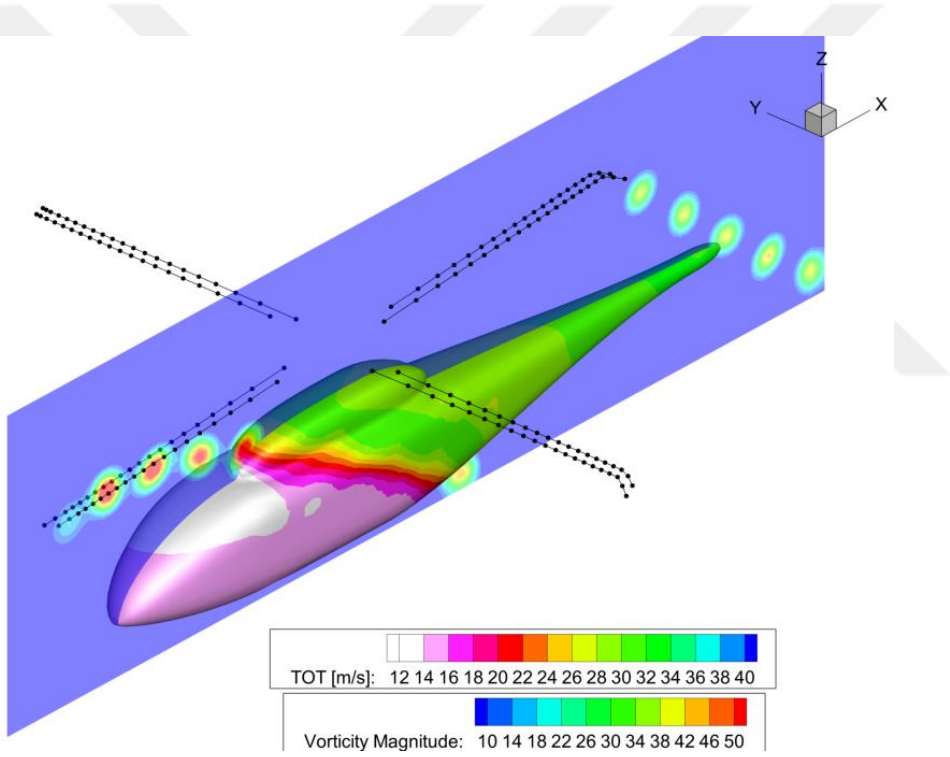

Figure 11.8 Local air speed distribution of rotor induced airflow on fuselage

F. Trajectory Optimization for Multiple Rotorcraft

The simulation model developed in this study is implemented as a library into the trajectory optimization environment. This basically gives the capability to model, simulate, and perform optimization for multiple rotorcrafts simultaneously. A sample trajectory optimization and track simulation are performed for two conventional helicopters. One is at hover and the other is performing a pirouette maneuver around the hovering helicopter. Both helicopters are always facing to each other. Simulation results are illustrated with Figure 11.9 and Figure 11.10.

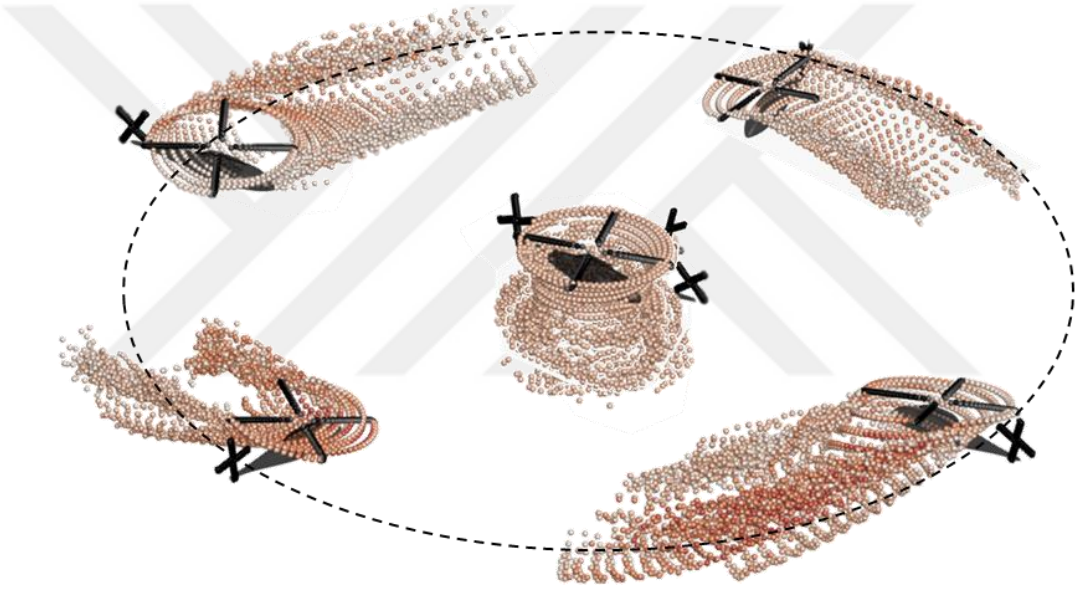

Figure 11.9 Multiple helicopter trajectory optimization – pirouette maneuver

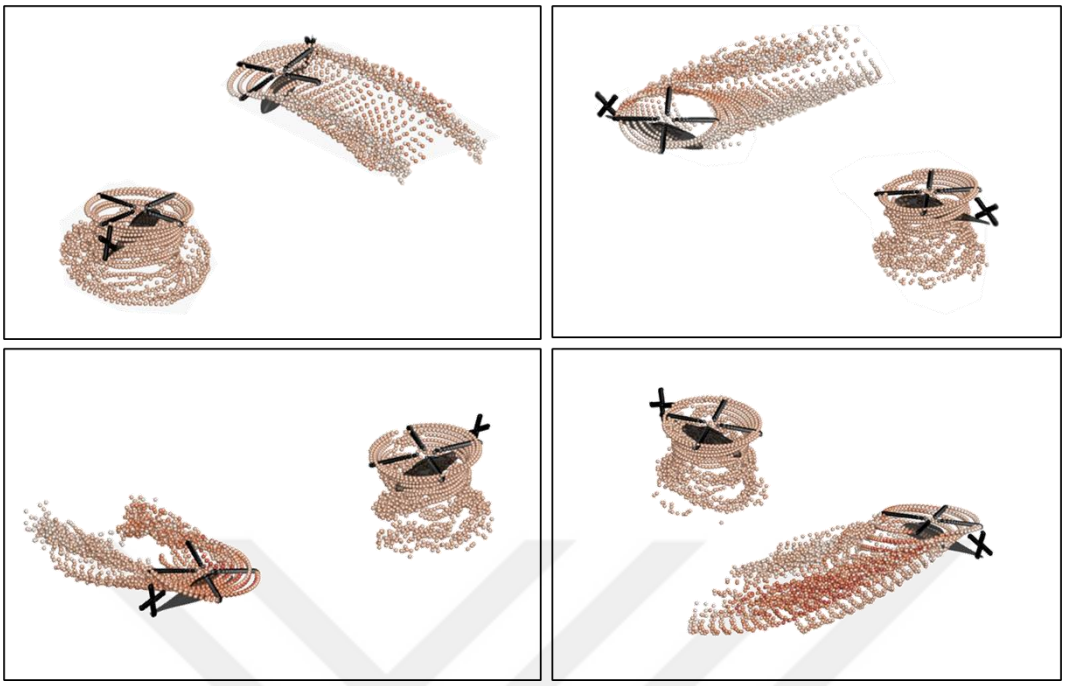

Figure 11.10 Multiple helicopter trajectory optimization – pirouette maneuver

CURRICULUM VITAE

PERSONAL INFORMATION

Surname, Name: Yücekayalı, Arda
Nationality: Turkish (TC)
Date and Place of Birth: 04 September 1986, Ankara
Marital Status: Married
Phone: +90 555 400 5490
email: Yucekayali.arda@gmail.com

EDUCATION

Degree	Institution	Year of Graduation
MS	METU Aerospace Engineering	2011
BS	METU Aerospace Engineering	2008
High School	Gazi Anadolu Lisesi, Ankara	2003

WORK EXPERIENCE

Year	Place	Enrollment
2008-Present	Turkish Aerospace Ind.	Chief Engineer

FOREIGN LANGUAGES

Advanced English, Basic French

PUBLICATIONS

1. Yücekayali, A., and Ortakaya, Y., Viscous Vortex Particle Method Explored for Main Rotor - Tail Rotor Interaction, 8th ARF - Asian/Australian Rotorcraft Forum, Ankara, Turkey, 30 Oct- 1 Nov 2019
2. Kalkan, U., Senipek, M., and Yücekayali, A., Markovian Approach for Learning Based Flight Condition Recognition Methods, 8th ARF - Asian/Australian Rotorcraft Forum, Ankara, Turkey, 30 Oct- 1 Nov 2019
3. Arslan, P., Güngör, O., Yücekayali, A., and Ortakaya, Y., Rotor Stall Onset Assessment 8th ARF - Asian/Australian Rotorcraft Forum, Ankara, Turkey, 30 Oct- 1 Nov 2019.

4. Senipek, M., Yücekayali, A., and Ortakaya, Y., Agility Assessment of Utility and Attack Configurations, 8th ARF - Asian/Australian Rotorcraft Forum, Ankara, Turkey, 30 Oct- 1 Nov 2019.
5. Atalay, M., M., Senipek, M., Yücekayali, A., and Prof. Özyörük, Y., Main Rotor - Tail Rotor Interactional Noise, 8th ARF - Asian/Australian Rotorcraft Forum, Ankara, Turkey, 30 Oct- 1 Nov 2019.
6. Atalay, M. M., Şenipek, M., Yücekayali, A., Assessment of Maneuver Airloads with Model Predictive Control, 8th AIAC, Ankara, Turkey, September 2019.
7. Şenipek, M., Yucekayali, A., Ortakaya, Y., and Özyörük, Y., Comprehensive Rotorcraft Aeroacoustics: Investigation of Surface Pressure Distribution Methods for Rotor Noise, 45th European Rotorcraft Forum, Warsaw, Poland, 17-20 September 2019.
8. Yücekayalı, A., AGILITY ASSESSMENT OF HELICOPTER MAIN ROTOR DESIGN, 75th Vertical Flight Society Annual Forum, Philadelphia, USA, 13-16 May 2019
9. Yücekayalı, A., Senipek, M, Ortakaya, Y., DEVELOPMENT OF CFD EMBEDDED ROTOR ACTUATOR SURFACE SIMULATION MODEL, 7th Asian/Australian Rotorcraft Forum, Jeju Island, Korea, Oct 30-Nov 1, 2018.
10. Yücekayalı, A., Senipek, M, Ortakaya, Y., and Özyörük, Y., TACO: HELICOPTER NOISE PREDICTIONS, 7th Asian/Australian Rotorcraft Forum, Jeju Island, Korea, Oct 30-Nov 1, 2018.
11. Yücekayalı, A., Ezertas, A. and Ortakaya, Y., DYNAMIC STALL MODEL OPTIMIZATION WITH CFD AND ASSESSMENT WITH COMPREHENSIVE APPROACH FOR IMPROVED BLADE DESIGN, 44th European Rotorcraft Forum, Delft, Netherlands, September 2018.
12. Yücekayalı, A., Şenipek, M., Kutay, A., T., OPTIMAL GUIDANCE MODEL FOR GREEN TRAJECTORY GENERATION OF HELICOPTERS, 9th AIAC Conference, Ankara, Turkey, September 2017.
13. Şenipek, M., Yücekayalı, A., Kutay, A., T., APPLICATION OF GENERIC AIR VEHICLE SIMULATION MODEL FOR REAL TIME AEROACOUSTIC NOISE COMPUTATION OF PROPELLER AIRCRAFTS, 9th AIAC Conference, Ankara, Turkey, September 2017.
14. Yücekayalı, A., Senipek, M., Ortakaya, Y., MAIN ROTOR AEROACOUSTIC ANALYSIS & VALIDATION WITH TEST DATA AND PLANFORM DESIGN FOR MINIMAL AERODYNAMIC NOISE, 41th European Rotorcraft Forum, Munich, Germany, September 2015.
15. Yücekayalı, A., Ortakaya Y., HELICOPTER MAIN ROTOR NOISE COMPUTATION FROM PRE-COMPILED ACOUSTIC HEMISPHERE

WITH ATMOSPHERIC PROPAGATION MODEL, 8th Ankara International Aerospace Conference, AIAC, Ankara, Turkey, September 2015.
16. Senipek, M., Yücekayalı, A., Ortakaya, Y., MULTI-VARIABLE AERODYNAMIC PLANFORM OPTIMIZATION OF HELICOPTER MAIN ROTOR FOR HOVER AND FORWARD FLIGHT DESIGN OBJECTIVES, 8th Ankara International Aerospace Conference, AIAC, Ankara, Turkey, September 2015.
17. Yücekayalı, A., Senipek, M., Ortakaya, Y., DEVELOPMENT OF FLIGHT CONDITION RECOGNITION ALGORITHMS BASED ON ROTORCRAFT SIMULATOR, 8th Ankara International Aerospace Conference, AIAC, Ankara, Turkey, September 2015.
18. Yücekayalı, A., Ortakaya, Y., A PARAMETRIC STUDY ON MAIN ROTOR TIP SHAPE TO REDUCE BLADE-VORTEX INTERACTION NOISE, , 8th Ankara International Aerospace Conference, AIAC, Ankara, Turkey, September 2015.
19. Yücekayalı, A., Ayan, E., Ortakaya, Y., ACOUSTIC ASSESSMENT OF 3 METER RADIUS ROTOR WITH WHIRL TOWER TEST AND ANALYSIS, 70th AHS Annual Forum, American Helicopter Society, Montreal, Quebec, Canada, May 20-22, 2014.
20. Baslamisli, U., Ayan, E., Yücekayalı, A., TAIL ROTOR AERODYNAMIC PERFORMANCE IMPROVEMENT WITH A GURNEY FLAP DESIGN, 40th European Rotorcraft Forum, Southampton, UK, 2-5 September 2014.
21. Yücekayalı, A., Ezertaş, A.,Ortakaya, Y., WHIRL TOWER TESTING AND HOVER PERFORMANCE EVALUATION OF A 3 METER RADIUS ROTOR DESIGN, AIAC-2013-142, VII. Ankara International Aerospace Conference, METU, Ankara, Turkey, 11-13 September 2013.
22. Ezertaş, A., Yücekayalı, A., Ortakaya,Y., HOVER PERFORMANCE ASSESSMENT OF 3 METER RADIUS ROTOR ON WHIRL TOWER, 39th ERF European Rotorcraft Forum, Moscow, Russia, September 3-6, 2013.
23. Tamer, A., Yücekayalı, A., Ortakaya, Y., DESIGN AND OPTIMIZATION OF HELICOPTER ROTOR FOR MINIMUM POWER REQUIRED, AIAC-2011-088, VI Ankara International Aerospace Conference, METU, Ankara, Turkey, 14-16 September 2011
24. Baslamisli, U., Yücekayalı, A., "GURNEY FLAP İLE HELİKOPTER KUYRUK ROTOR PERFORMANSININ İYİLEŞTİRİLMESİ ", 5th UHUK, Kayseri, Turkiye, 8-9 September 2014.
25. Okcu, I., D., Yücekayalı, A., "HC-1 İnsansız Helikopter Kontrol Edilebilirlik, Statik ve Dinamik Kararlılık Değerlendirmesi", 5th UHUK, Kayseri, Turkiye, 8-9 September 2014.

26. Yücekayalı, A., Başlamişli, U., Ayan, E., “Rotor Test Kulesinde Hafif Sınıf Helikopter Ana Rotoru Akustik Ölçüm Testleri ve Pal Kalınlık Gürültüsü Analiz Aracı Geliştirilmesi”, 5th UHUK, Kayseri, Turkiye, 8-9 September 2014.
27. Tamer, A., Şen, S., Yücekayalı, A., Ortakaya, Y., HELİKOPTER ROTORU AERODİNAMİK ve YÜK ANALİZLERİ İÇİN PAL AEROELASTİK ÇIRPMA MODELİNİN GELİŞTİRİLMESİ, UHUK, III. ULUSAL HAVACILIK VE UZAY KONFERANSI, Eskişehir, Turkiye, 16-18 September 2010.
28. Yücekayalı, A., Ortakaya, GİRDAP TEORİSİ VE PAL ELEMANLARI METODU İLE HELİKOPTER ROTORUNUN AERODİNAMİK MODELLENMESİ, UHUK-2010, III. ULUSAL HAVACILIK VE UZAY KONFERANSI, Eskişehir, Turkiye, 16-18 September 2010